Active Tectonics and Geomorphology of the central South Island, New Zealand: Earthquake Hazards of Reverse Faults

A thesis submitted in partial fulfilment of the requirements for the degree of Doctor of Philosophy in Geology at the University of Canterbury by

Timothy Stahl

June 2014

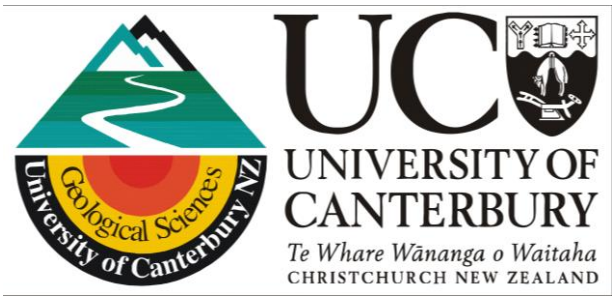

FRONTISPIECE

"We started from a lonely valley, down which runs a stream called Forest Creek. It is an ugly, barren-looking place enough — a deep valley between two high ranges....We went up a little gorge, as narrow as a street in Genoa, with huge black and dripping precipices overhanging it, so as almost to shut out the light of heaven. I never saw so curious a place in my life."

-Samuel Butler, on the basis for the landscape in his novel *Erewhon*

(A First Year in the Canterbury Settlement)

"First there is a mountain, then there is no mountain, then there is."

-Donovan, on tectonic geomorphology
("There is a Mountain")

ABSTRACT

Oblique continental collision between the Pacific and Australian Plates in the central South Island of New Zealand (between c. 44 and 46°S) results in distributed reverse faulting. Only a few of these faults have been studied in detail, highlighting a major knowledge deficit in the earthquake behaviour, magnitude potential and contribution to seismic hazard for many faults in this part of the orogen. Three reverse faults are investigated in detail in this thesis: the Moonlight Fault Zone (MFZ), the Fox Peak Fault and the Forest Creek Fault. Geochronologic approaches, including Schmidt hammer exposure-age dating, radiocarbon dating, and optically stimulated luminescence dating, are combined with paleoseismic trenching, fault surface trace mapping, analysis of GPS and LiDAR survey data, and numerical modelling to characterise the rupture behaviour of these faults.

A new Schmidt hammer chronofunction based on over 7000 clast analyses is developed that relates rebound value (R-value) to age for river terraces. The rapid, inexpensive, non-destructive, and statistically valid nature of this technique makes it widely applicable for age dating here and globally. I use Schmidt hammer exposure-age dating along with other geochronologic and surveying methods to show that stranded post-last glacial lake shorelines of Lake Wakatipu are undeformed and at a uniform elevation across the MFZ. This indicates an absence of uplift across the MFZ since c. 13 ka and suggests that this fault may be inactive or subject to long periods of interseismic quiescence despite its location in the active orogen. This result also challenges the long-held hypothesis that lake shorelines throughout central NZ are tilted due to isostatic rebound.

Three segments of the Fox Peak Fault are identified through field mapping and surveying. Slip rates at over 50 locations along the 36.5 km total length of the fault (c. 1.5 mm yr^{-1} maximum) co-vary with the bounding range topography and exhibit large gradients near intersecting NW-striking faults. Four paleoseismic trenches were excavated to determine if these segment boundaries represent barriers to earthquake rupture propagation. Evidence of 3-4 earthquakes since c. 16 ka on the two end segments with overlapping age uncertainties indicates that the recurrence interval of the fault is 2000-3000 years. The most recent event (MRE) occurred at c. 2.5 ka. Large single event displacement to length ratios on these segments and a single event scarp on the central segment indicate that while the segment boundaries control on-fault slip gradients, they are not likely to impede through-going ruptures in an earthquake. This is a relatively recent development from the long-term tectonic geomorphology, which is suggestive of range growth on separate faults.

A trench on the range-bounding Forest Creek Fault, located in the hanging wall of the Fox Peak Fault, has had two to three earthquakes in the last c. 6 ka, with MRE and penultimate event ages overlapping those on the Fox Peak Fault. A Monte Carlo simulation that incorporates a distance-based probability for fault-to-fault rupture, fault geometry from field data and 3D modelling, and uncertainty in average slip is used to calculate probability density functions of moment magnitudes for the Fox Peak-Forest Creek fault system. Increased Coulomb stresses on the Forest Creek Fault from slip on the Fox Peak Fault are within the range reported for historic earthquake stress drops and confirm the feasibility of coeval rupture of these two imbricate faults. The results suggest that earthquakes 50-100% stronger than those predicted by empirical scaling laws need to be considered for the Fox Peak-Forest Creek system.

The 2010 Darfield (Canterbury) M_W 7.1 earthquake caused coseismic landsliding in the Harper Hills in the eastern foothills of the Southern Alps. Mapping, surveying, ground penetrating radar and trenching across the landslide head scarp indicate that failure was accommodated by combined bedding-controlled translation and toppling of decoupled basalt blocks. The lack of evidence for prior slip events over a time period that is likely to exceed the return period (1000–2500 years) of peak ground accelerations at the site suggests that failure in the Harper Hills may be related to the fault-specific seismic source dynamics experienced in the Darfield earthquake.

This thesis offers a new understanding of the chronology, slip distributions, rupture behaviour, and geomorphic impacts of late Quaternary earthquakes sourced from active reverse faults in New Zealand.

CONTENTS

TABLE OF FIGURES

ACKNOWLEDGMENTS

During my Ph.D. study I was supported by a University of Canterbury Doctoral and International Doctoral Scholarships, for which I am grateful. My research was funded by the New Zealand Earthquake Commission, the Royal Institute of Chartered Surveyors (UK) and UC Mason Trust Grants.

First and foremost, I must thank my supervisory team for their guidance, friendship and timely reviews of my research. Mark Quigley provided valuable field training and feedback throughout, while allowing me to build this project from the ground up and always challenging me to do better. Mark, thanks for everything. It has been a pleasure to work with you and learn from you over the past four years.

Discussions in the field and office with Stefan Winkler provided valuable insights into Quaternary geomorphology and geochronology. Mark Bebbington tolerated my ambitious statistical schemes and helped mould them into useful tools in MatLab. Kari Bassett assisted with interpretation of trench logs. David Nobes assisted with GPR processing and interpretation.

I thank my office mates Brendan Duffy and Eric Bilderback for being excellent mentors, collaborators and friends. Ashton McGill, Sam McColl, Simon Cook and Tom Brookman all dedicated a week or more to field work on the Fox Peak, Forest Creek and Moonlight Faults. Their time and efforts were invaluable. Sharon Hornblow, Narges Khajavi, Travis Horton, David Nobes, Jarg Pettinga, Tristram Irvine-Finn, Matt Cockcroft, Josh Blackstock, Stefano the Italian, and Greg De Pascale all assisted with work in the field, which could not have been done without them.

This research benefitted from many useful discussions with colleagues at GNS and elsewhere, namely Phil Tonkin, David Barrell, Russ Van Dissen, Simon Cox, John Beavan, Simon Brocklehurst and Andy Nicol. The scientific extravaganza following the September 4th Darfield earthquake was memorable, due in part to being able to work with the quality crew of Nicola Litchfield, Pillar Villamor, Kevin Furlong, Chris Massey and others listed above.

The technical and secretarial staff at UC, namely Pat Roberts, Janet Warburton, Cathy Higgins, Vanessa Tappenden, Matt Cockcroft, Sacha Baldwin-Cunningham, Rob Spiers and Kerry Swanson, are fantastic and allowed my Ph.D.to run smoothly. Thank you for putting up with my frantic requests for field equipment, map laminations and various payments. Useful discussions with Tim Davies, Eric Brogt and Travis Horton, as well as a great bunch of students, made a heavy teaching load infinitely more enjoyable.

The landowners of the Canterbury and Otago High Country have been wonderfully receptive and I thank them for allowing me access to their lands. In particular, the Aubreys of Ben McLeod Station, the Brays of Lilydale Station and the Murdochs of Cloudy Peaks Station were kind to allow several months of access over the past four years. The Cochranes of Hunter Valley Station and the Dennises of the Harper Hills kindly provided access on many occasions. It was a pleasure to deal with people as passionate about their land as I am.

I thank Ningsheng Wang at Victoria University of Wellington's OSL Laboratory and Rafter Radiocarbon Laboratory at GNS for their efforts in dating my samples. Marco Olmos of the Queenstown Lakes District council kindly provided LiDAR of the Lake Wakatipu area. The editorial staffs and reviewers of three articles submitted for publication at *GSA Bulletin*, *Earth Surface Processes and Landforms*, and *Geomorphology* greatly improved the quality of the material presented in this thesis. Fault plane solutions were derived using Fault Kin5, Rick Allmendinger's brainchild.

My friends David McConnel, Ashton McGill, Tom Brookman, Sam McColl, Mark Quigley, Narges Khajavi, Sharon Hornblow, Ben Mackey, Nick Riordan, Simon Cook, Brendan Duffy and Eric Bilderback helped keep me sane throughout, or, at least, I am indebted to their efforts.

Last, but certainly not least, many thanks to my partner Hazel and my family in the USA for their love and moral support over the past four years. I couldn't have done this without you.

THESIS PROLOGUE

Aims

On September 4th, 2010, at 4:30 a.m., an earthquake initiating on a blind reverse fault approximately 40 kilometres west of central Christchurch shook the city's residents awake. The rupture jumped from the reverse Charing Cross Fault to strike-slip and oblique-normal fault segments before triggering another blind reverse fault rupture 20 seconds into the sequence (Holden et al. 2011; Beavan et al. 2012; Elliot et al. 2012; Bradley 2012). Widespread liquefaction in Christchurch, along with rock falls and 'jumping' boulders in the Port Hills, a landslide in the Harper Hills, and one of the best examples of strike-slip surface rupture ever recorded were all evident in the ensuing hours and days (Quigley et al. 2012; Bradley et al. 2012; Khajavi et al. 2012; Quigley et al. 2013; Stahl et al. 2014). Five months later, another oblique-reverse fault ruptured under the Port Hills, causing shaking that led to the deaths of 185 people and several tens of billions worth of damage to the city. The sources of the Darfield and Christchurch earthquakes were unknown to scientists before the events. It was first-hand experience of the importance of identifying and characterising active faults, including reverse faults in the New Zealand landscape.

The paucity of paleoseismic and geomorphologic data on reverse faults is not unique to New Zealand. Reverse faults are often blind, have discontinuous surface traces and contain zones of distributed, secondary faulting (c.f. Officers of the Geological Survey 1983; Rubin 1996; McCalpin 2009) that make surface studies difficult. There are relatively few historical, continental thrust and reverse faulting events with which to derive empirical scaling laws (e.g. Rubin 1996; Wesnousky 2008; Field et al. 2013). Geologically-derived slip rates often disagree with geodetic estimates due to fault trace obscurity in high relief landscapes and distributed deformation in the ranges adjacent to the fault (e.g. Wallace et al. 2007; Cox et al. 2012). Subsurface geometries can be complex, making fault traces and slip distributions at the surface appear relatively irregular compared to strike-slip ruptures. Additionally, seemingly unrelated faults at the surface may be linked at depth or be strongly influenced by regional stress fields, affecting the occurrence, and possibly concurrence, of earthquakes in a fault system (Lin and Stein 2004; Pollitz et al. 2003; Freed 2005).

This thesis is devoted to better understanding the earthquake hazards and paleoseismicity of reverse faults. *How and with what tools can geologists better study the paleoseismicity of reverse faults? Can geologic and geodetic slip rates be reconciled? How does an earthquake on one fault influence the seismic hazard on others?* These questions are explored utilizing the natural laboratory of the central South Island of New Zealand. In developing a variety of tectonic geomorphologic tools

to improve the scientific community's understanding of reverse faults, I have also attempted to conduct primary source characterisation with the goal of providing robust data for inclusion in the New Zealand national seismic hazard model. Research questions and study sites were chosen accordingly.

Scientific Context

Relative motion between the Australian and Pacific plates in the central South Island of New Zealand is predominantly accommodated by slip on the Alpine Fault (Walcott 1998; Berryman et al. 2002). Geodesy and geology indicate that c. 75% of the 40-50 mm yr^{-1} oblique convergence is accommodated by slip on the Alpine Fault (Norris and Cooper 2001; Wallace et al. 2007; DeMets et al. 2010). With an average recurrence interval of 329 ± 68 years, and most recent event (MRE) of 1717 AD, the probability of an Alpine Fault rupture in the next 50 years is approximately 30% (Rhoades and Van Dissen 2003; Berryman et al. 2012). Expected magnitudes for a full-length rupture are M_W 8.1 (De Pascale and Langridge 2012). More proximal known faults and distributed seismicity contribute a higher component to the seismic hazard for the major population centres of the South Island (e.g. Stirling et al. 2008). In South Canterbury and Otago, this deformation and resulting contribution to seismic hazard are dominated by slip on NE-striking reverse faults.

Although there is clear geomorphic evidence of reverse faults preserved in the central South Island landscape, the geologic data collected thus far, with notable exceptions (Officers of the Geological Survey 1983; Van Dissen et al. 1994; Litchfield and Lian 2004; Amos et al. 2007; Amos et al. 2010; Amos et al. 2011) have been largely insufficient to validate presupposed slip rates, recurrence intervals and moment magnitudes. Geodesy has been invaluable in testing these assigned values but yields slip rates inconsistent with geologic studies where available (Wallace et al. 2007, Amos et al. 2010, this study). Moment magnitudes have mostly been assigned based on empirical scaling laws and not validated through paleoseismic trenching (e.g. Berryman et al. 2002). Recurrence intervals are also calculated based on scaling laws that have been primarily developed for oblique and strike-slip faults (Berryman et al. 2002; Stirling et al. 2013). Additionally, the probabilities of segmented fault ruptures are specified a priori and often informed by mapping alone. More work is required to test these critical parameters of the national seismic hazard model (NSHM).

There are three principal field sites examined in this thesis (Fig. P.1). Each represented a significant knowledge gap in the New Zealand paleoseismic record prior to this thesis. The Moonlight Fault in Southland and Otago (Fig. P.1A) is a major reverse-oblique fault with previously unknown late Quaternary activity. Its location in the Lake Wakatipu basin allows for the utilisation of stranded lake shorelines as strain markers over the latest Pleistocene to present. The Fox Peak and Forest Creek Faults in South Canterbury (Fig P.1B) are intersecting, range-bounding reverse faults. The close

proximity of the two faults and remarkable surface expression make this fault system an excellent place to test models of fault interaction and segment linkage. The fault system that ruptured in the Darfield earthquake (the Hororata Anticline, Greendale and Charing Cross Faults shown in Fig. P.1C) provided an excellent modern analogue of fault segment interaction. Coseismic ground cracks in the Harper Hills provided information on the return period of regional strong ground motions and the paleoseismicity of the Darfield earthquake sources. I have asked the following research questions regarding these faults (Table P.1):

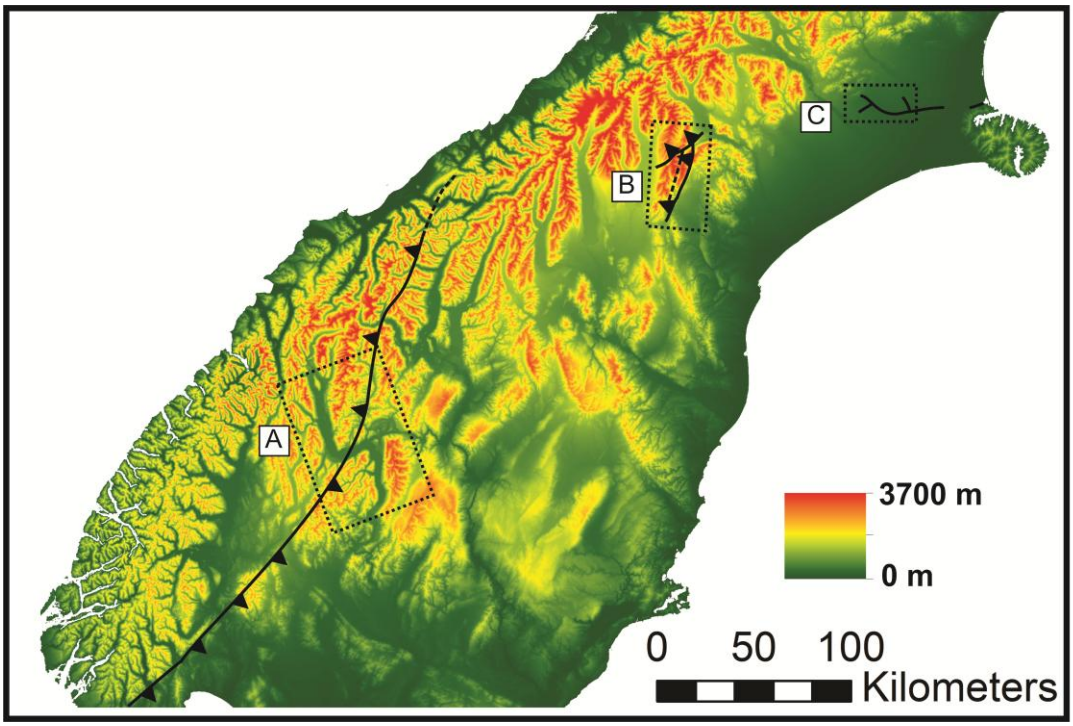

Figure P.1: Principal field sites within this thesis. (A) The Lake Wakatipu Basin in central Otago (with Moonlight Fault crossing the centre of basin); (B) The Fox Peak and Forest Creek Faults in South Canterbury; (C) The Harper Hills and Darfield earthquake source faults. Compare with strain rates, strain rate uncertainty and locations of previous geologic work in Fig. P.2.

Goal/Scientific Contribution	Research Questions	Relevant Chapter(s)
Obtain slip rates to identify segments and recent fault activity on the **Fox Peak Fault**	How can the required age control be obtained for sequences of offset geomorphic markers?	Chapter 1
	How are discontinuous geomorphic markers correlated and their offset measured across a fault?	Chapter 2
	Is the paleoseismicity of a group of fault segments related to long-term range growth, and what are the implications for future seismic hazard?	Chapter 3
	Are geologically-derived slip rates consistent with current geodetic models of fault slip rates in the central South Island?	Chapters 2 & 3
Obtain ages and single-event displacements of earthquakes on fault segments to identify the recurrence interval and magnitude potential of reverse fault systems	How can estimates of seismic hazard be improved by integrating field data into fault segmentation and fault-to-fault rupture scenarios?	Chapter 3
	How reliable are secondary (fault-induced) and indirect (off-fault, shaking-induced) records for determining the paleoseismicity of the **Fox Peak Fault** and **Darfield earthquake source?**	Chapters 3 & 5
Investigate earthquake interaction and secular modulation of slip rates on reverse faults	Is the **Moonlight Fault** active? What is the nature of strain heterogeneity and fault episodicity in Otago, and is it influenced by glaciations?	Chapters 2 & 5
	Does activity on the **Fox Peak Fault** influence the timing of earthquakes on the **Forest Creek Fault?**	Chapter 3 & 4

Thesis Format

Chapter 1 investigates the utility of applying Schmidt hammer exposure-age dating (SHD) to fluvial terraces and outwash plains of New Zealand's South Island. Studying reverse faults in the eastern Southern Alps of New Zealand presents the challenge of having few options for constraining absolute ages of features traversed by a fault. Detrital charcoal for radiocarbon is sparse and often washed out of fluvial systems during deposition, and luminescence requires well-exposed outcrops of (typically) fine material for dating. Cosmogenic dating is widely used, but requires either an impractical amount of samples from all offset features, or age-correlated features at all study sites. In a dynamic range-front environment, short-term variations in stream power make climatic or tectonic age-correlation of alluvial fans, landslides and river terraces unrealistic.

SHD is widely used in geomorphology, and when carefully calibrated, can provide meaningful ages for a range of landforms. It has never been used on river terraces prior to this thesis. The Schmidt hammer is ideal for obtaining ages from New Zealand river terraces for several reasons:

(i) Most of the New Zealand Southern Alps are comprised of relatively homogeneous Torlesse greywacke sandstone (e.g. Mackinnon 1983). A lack of significant lithologic variation is imperative for measuring the mechanical degradation of rocks through time via the Schmidt hammer.

(ii) Large, rounded cobble and boulders of greywacke sandstone are often preserved at the surfaces of abandoned river terraces. The location of these terraces in the high energy environments of the Southern Alps ensures enough 'surface clasts' of suitable size are available for Schmidt hammer testing.

(iii) The known order of terraces in a sequence provides input data that can be used to further constrain ages (as opposed to other landforms, where relative order may be more ambiguous).

(iv) The lack of datable material in many eastern New Zealand river terraces has led to widespread usage of weathering-rind dating (e.g. Chinn 1981; Whitehouse et al. 1986; Knuepfer 1984, 1988; McSaveney 1992; Nicol and Campbell 2001). While proven effective, weathering-rind dating is destructive, time-intensive, requires surface clasts that can be removed to analyse rind thickness variability, and requires some subjectivity in what constitutes a rind. Additionally, rinds are often inexplicably absent from many boulders on a surface. SHD is non-destructive, conducted on in-situ surface clasts, and requires subjectivity only in that clasts must not move, break, or have evident shallow discontinuities during sampling.

I have calibrated the Schmidt hammer on terrace surfaces of known age and produced a new chronofunction for use in Torlesse greywacke. Chapter 1 explores the use of the technique in different sub-groups of Torlesse greywacke and weathering regimes in the South Island. Statistical protocols are developed for processing SH data and converting to SH values to absolute (numerical) ages.

Chapter 2 incorporates SHD (as well as absolute dating techniques), field mapping, surveying, and LiDAR analysis to study the post-Last Glacial Maximum (LGM) activity of the Moonlight Fault in central Otago. The fault is situated in a zone c. 50-100 km from the plate boundary and stranded lake shorelines of Lake Wakatipu present ideal strain markers for studying the tectonic evolution of the basin. Studying their deformation is important for several reasons:

(i) The Moonlight Fault Zone (MFZ) cuts across the centre of Lake Wakatipu and its late Quaternary activity is uncertain. The MFZ has proposed late Quaternary traces and offsets (Wellman 1979; Turnbull 2000) but is mapped as inactive in GNS's active fault database. Wallace et al. (2007) allow for 1 mm yr^{-1} convergence across the Moonlight Fault Zone in their geodetic model. The NSHM assigns a recurrence interval of c. 6 ka and expected magnitude of M_W 7.6 for two separate MFZ segments. Thus, there are conflicting views on its activity. It is essential for the future development of Queenstown and the Otago region to consider the hazard posed by the MFZ.

(ii) Eastern Otago faults have irregular recurrence intervals (Beanland and Berryman 1989; Berryman and Beanland 1991; Litchfield and Lian 2004; Norris and Niccols 2004). This

implies that strain is heterogeneously distributed in space and/or time throughout Otago. The high relief and depth of schist exhumation surrounding Wakatipu suggests that the area has had higher rock uplift rates than ranges to the East in the past. The shorelines of Lake Wakatipu, New Zealand longest lake in an orientation sub-perpendicular to the plate boundary, should reliably record the pattern of recent uplift for comparison.

(iii) Glacial loading and unloading have been shown to be mechanisms for the modulation of fault slip rates (Mörner 1978; Thorson 1996; Tsuboi et al. 2000; Stewart et al. 2000; Sauber and Molnia 2004; Hetzel and Hampel 2005; Hampel et al. 2009; Hampel et al. 2010). Given that Wakatipu contained a c. 1 km thick valley glacier as part of the Southern Alps ice-cap in the LGM (Barrell 2011), and is crossed by the MFZ, one could expect a glacially-modulated earthquake history to be recorded in the landscape.

I surveyed the lake shorelines using a combination of differential GPS (dGPS), real-time kinematic GPS (RTK), and existing Light Detection and Ranging (LiDAR) datasets. Dating was accomplished by calibrating SHD with optically stimulated luminescence (OSL) ages and an existing radiocarbon date of river terraces that correlate with the lake shorelines. I developed a numerical technique to correlate discontinuous shorelines observed in the LiDAR and dGPS from site to site to confirm my field observations of deformation. The results show that the shorelines have not been offset or tilted in the last c. 13-17 ka, revealing broad implications for the regional tectonics.

Chapter 3 investigates the paleoseismicity of the Fox Peak and Forest Creek fault systems in South Canterbury. These two intersecting faults have long been recognised as having evidence of recent activity but have not been investigated in detail. The faults provide the ideal opportunity to study reverse fault development, segmentation and interaction. I used field mapping, surveying, trenching, dating and Monte Carlo modelling in MatLab to derive baseline fault parameters (length, sense, slip rates, recurrence intervals, single event displacements and segmentation) for the Fox Peak Fault. Slip rates and topographic analysis revealed discrete fault segments, which were subsequently trenched to obtain the ages of recent earthquakes. The results show that the structural development of the Fox Peak and Forest Creek Faults through time has increased the potential for large (M_W 7+) earthquakes.

Chapter 4 presents a Monte Carlo simulation approach for calculating moment magnitude probability distributions for fault-to-fault earthquakes on imbricate reverse faults. I used data from the Fox Peak and Forest Creek Faults as input data into the model. Coulomb stress modelling was used to show the feasibility of these earthquakes which could be 50% to 100% larger than those predicted by empirical scaling laws. Employing this type of procedure is particularly important for reverse faults,

which have demonstrated a capacity, and perhaps the tendency, to jump onto arrays of nearby faults (e.g. Officers of the Geological Survey 1983; Rubin 1996; Lin and Stein 2004; Xu et al. 2009; Parsons et al. 2012; Field et al. 2013).

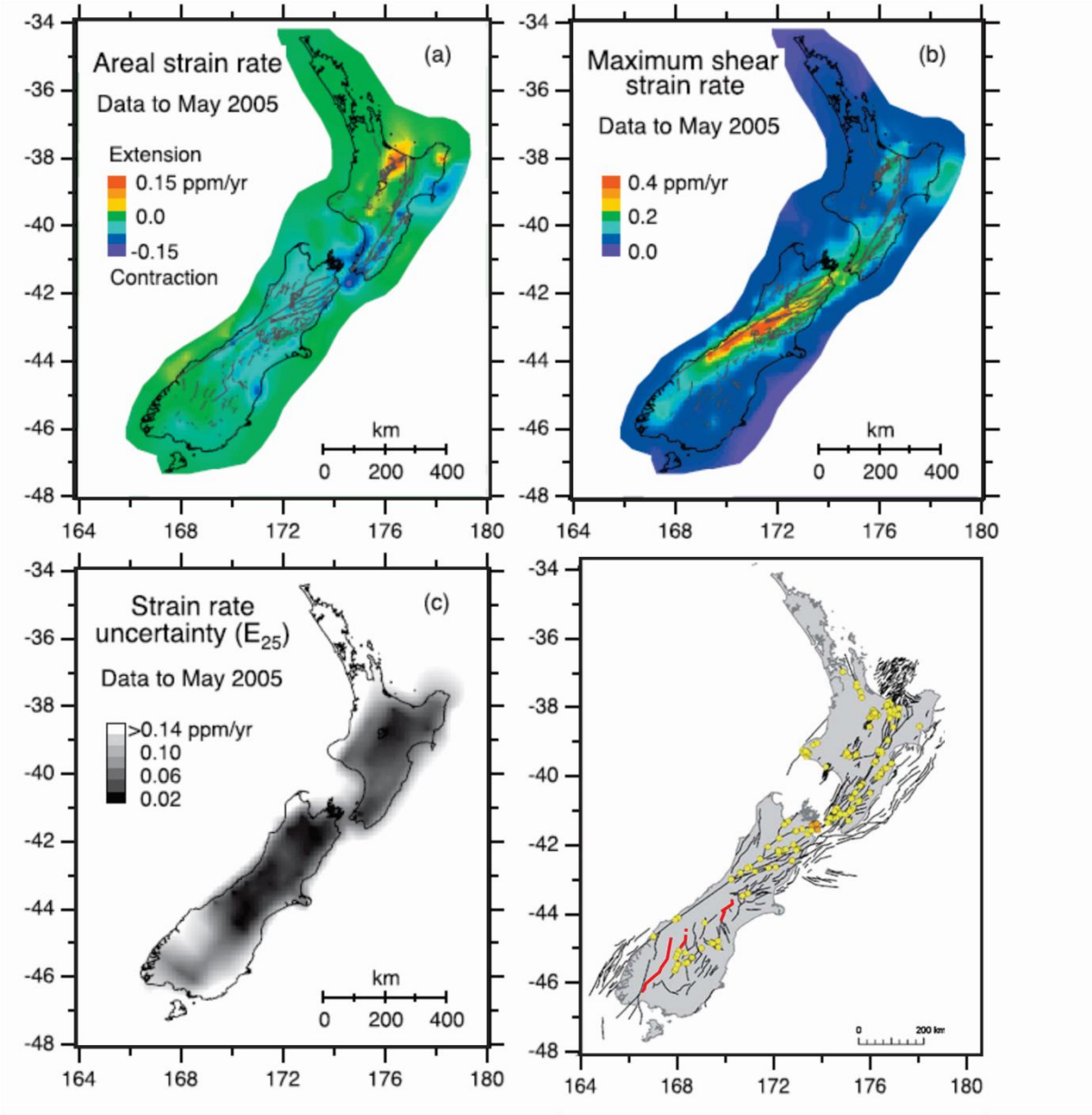

Figure P.2: (a) Areal strain rate, (b) Maximum shear strain rate, and (c) strain rate uncertainty of Beavan et al. (2007). In the bottom right, the New Zealand Active Fault Database from Stirling et al. (2012) is shown with locations of geologically constrained paleoseismic data in yellow. Faults discussed in this thesis are shown in red (the Nevis-Cardrona Fault - a small segment NE of the Moonlight Fault - and the Lake Heron Fault - continuation of the Forest Creek Fault - are briefly discussed in Chapter 6). Note the lack of geologic data/high strain rates for the Fox Peak and Forest Creek Faults, and lack of geologic data/high strain rate uncertainty for the Moonlight Fault.

Chapter 5 presents the findings of research on the coseismic Harper Hills landslide that occurred during the Darfield earthquake. The aim was to document and monitor the landslide as well as provide insight into the paleoseismicity of the region and utility of secondary (i.e. non-seismogenic) features in paleoseismology. I used GPR, structural and geomorphic mapping and trenching to characterise the kinematics and history of the landslide. The activation of the landslide was most likely related to source kinematics and dynamics that cannot be predicted by peak ground accelerations (PGAs) alone, highlighting the uncertainties in predicting earthquake impacts based on PGA return times from the NSHM. The required ground motion parameters for failure may be tied to the paleoseismicity of the Greendale and Hororata Anticline faults.

Chapter 6 summarises the main conclusions of this thesis. Preliminary data on high priority active reverse faults are presented for further development of the central South Island reverse fault paleoseismic catalogue.

Appendices are included for individual chapters where appropriate and a Digital Supplementary Information file has been included for large spreadsheets (e.g. SHD data, survey shapefiles and regression statistics, slip and slip rates).

Logistical explanation for thesis structure

This is perhaps an unusual thesis in that a range of geologic phenomena are addressed and the field areas are separated by hundreds of kilometres. The topics move from Quaternary geochronology and numerical modelling, to short-term fault segmentation and paleoseismology, to long-term tectonic geomorphology and structure. How did such a thesis come to be?

I initially accepted an offer to complete a PhD on the paleoseismicity of the Fox Peak and Forest Creek Faults in early 2010. After initial reconnaissance and mapping, it was apparent that any research on fault segmentation would require a large number surface ages (and slip rates) outside the scope of site-to-site map correlations and outside the budget of the PhD. I enlisted my supervisor Stefan Winkler to assist with developing a calibrated-dating tool that could handle embedded surface clasts on river terraces. Over the course of several field trips and my own supervision of a University of Canterbury Summer Scholarship, I was able to produce new chronofunctions for Schmidt hammer exposure-age dating, and started putting them to use on the Fox Peak Fault in 2011.

One of the questions central to my Fox Peak /Forest Creek fault work was whether one could find paleoseismic evidence of fault interaction or earthquake clustering due to deglaciation. While the surface expressions of the Fox Peak and Forest Creek faults seemed promising for the former, the glacial history of the Rangitata catchment at the time was dubious enough to limit useful research into the latter. In 2011, I was invited onto a multi-faceted research project with Sam McColl and Simon

Cook to look at the glacial history of the Lake Wakatipu basin. The work on the Moonlight Fault stemmed from 3 weeks in the field with Sam and Simon, followed by a fortuitous acquisition of LiDAR on shorelines I had already surveyed in the field.

The September 2010 Darfield earthquake had many impacts on the Canterbury landscape that required immediate documentation to ensure the quality of scientific data was not lost. My own involvement focused on the initial mapping of the surface trace and investigations into landslides in the Harper Hills and Banks Peninsula. Upon finding a null result in trenching of the landslide head scarp, I realised that this had broader implications for the paleoseismology of reverse faults, and decided to include the work in this thesis.

Scientific contributions arising from this PhD and related work

At the time of submitting this thesis, Chapters 1 and 5 have been published in peer-reviewed journals (Stahl et al. 2013; Stahl et al. 2014). Chapter 2 has been submitted and publication is pending a second stage of peer review. Some appendices in articles for publication have been moved into the main text of this thesis. The contents of all chapters have been widely presented at conferences, seminars and undergraduate lectures/laboratory sessions. I have co-authored and contributed to numerous other papers during my Ph.D. study involving the Darfield earthquake and surface rupture of the Greendale Fault (Quigley et al. 2010; Van Dissen et al. 2011; Barrel et al. 2011b; Quigley et al. 2012; Villamor et al. 2012; Duffy et al. 2013; Cook et al. 2013).

Originality

The material presented in this thesis has benefitted from many useful discussions with my supervisors, co-authors and collaborators. In Chapter 1, Stefan Winkler and Daniel Duke assisted with the work in the field. Mark Bebbington assisted with MatLab codes and statistical framework for this and other chapters. In Chapter 2, Sam McColl and Simon Cook assisted with field work, some figures and initial phases of the writing. The final text is all my own work, though some background geomorphologic framework was originally provided by Sam McColl. In Chapter 3, several supervisors and students assisted with trenching, but it is otherwise all my own work. Eric Bilderback Mark Quigley and David Nobes helped with the Harper Hills field work and interpretation of data. My primary supervisor, Mark Quigley, engaged in scientific discussions and provided editorial assistance for all of the thesis chapters. Apart from these exceptions, the field work conducted, techniques developed, interpretations, and presentation of data constitute my own personal research.

Deputy Vice-Chancellor's Office
Postgraduate Office

UNIVERSITY OF CANTERBURY
Te Whare Wānanga o Waitaha
CHRISTCHURCH NEW ZEALAND

Co-Authorship Form

This form is to accompany the submission of any thesis that contains research reported in co-authored work that has been published, accepted for publication, or submitted for publication. A copy of this form should be included for each co-authored work that is included in the thesis. Completed forms should be included at the front (after the thesis abstract) of each copy of the thesis submitted for examination and library deposit.

Please indicate the chapter/section/pages of this thesis that are extracted from co-authored work and provide details of the publication or submission from the extract comes:

Chapter 1: Schmidt hammer exposure-age dating (SHD) of late Quaternary fluvial terraces in New Zealand; Publication of same name in Earth Surface Processes and Landforms, 2013.

Please detail the nature and extent (%) of contribution by the candidate:

Research was performed under the guidance of Stefan Winkler and Mark Bebbington. Writing and scope benefitted from revisions with Mark Quigley and Brendan Duffy. All ideas, execution of research, text and figures are those of the candidate, with input from coauthors. Estimated candidate contribution 90%.

Certification by Co-authors:

If there is more than one co-author then a single co-author can sign on behalf of all

The undersigned certifys that:

- The above statement correctly reflects the nature and extent of the PhD candidate's contribution to this co-authored work
- In cases where the candidate was the lead author of the co-authored work he or she wrote the text

Name: *PD Dr. Stefan Winkler* Signature: 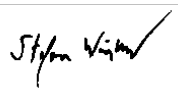 Date:1 4.05.2014

Deputy Vice-Chancellor's Office
Postgraduate Office

UNIVERSITY OF CANTERBURY
Te Whare Wānanga o Waitaha
CHRISTCHURCH NEW ZEALAND

Co-Authorship Form

Please indicate the chapter/section/pages of this thesis that are extracted from co-authored work and provide details of the publication or submission from the extract comes:

Chapter 2: Post-glacial tectonic history of the Lake Wakatipu Basin and Moonlight Fault; Submitted to Lithosphere, April 2014.

Please detail the nature and extent (%) of contribution by the candidate:

Estimated contributions in components of research:

Field work (planning, project aims, scope, execution): 50%

Analysis (survey processing, dating, modelling, other): 90%

Writing, literature review, formatting, revising: 90%

Certification by Co-authors:

If there is more than one co-author then a single co-author can sign on behalf of all

The undersigned certifys that:

- The above statement correctly reflects the nature and extent of the PhD candidate's contribution to this co-authored work
- In cases where the candidate was the lead author of the co-authored work he or she wrote the text

Name: *Sam McColl* Signature:  Date: *15/05/2014*

Deputy Vice-Chancellor's Office
Postgraduate Office

UNIVERSITY OF CANTERBURY
Te Whare Wānanga o Waitaha
CHRISTCHURCH NEW ZEALAND

Co-Authorship Form

Please indicate the chapter/section/pages of this thesis that are extracted from co-authored work and provide details of the publication or submission from the extract comes:

Chapter 5-Coseismic landsliding during the 2010 Mw 7.1 Darfield (Canterbury) Earthquake: Implications for paleoseismic studies of landslides; Accepted for publication under same name in Geomorphology, 2014

Please detail the nature and extent (%) of contribution by the candidate:

Field work (planning, execution): 70%

Analysis of data: 80-90%

Writing: 90%

Eric Bilderback initiated landslide monitoring and mapping, and assisted with analysis. Mark Quigley helped with mapping and trenching. David Nobes performed GPR and helped with interpretation/writing of that section.

Certification by Co-authors:

If there is more than one co-author then a single co-author can sign on behalf of all

The undersigned certifys that:

- The above statement correctly reflects the nature and extent of the PhD candidate's contribution to this co-authored work
- In cases where the candidate was the lead author of the co-authored work he or she wrote the text

Name: *Mark Quigley* Signature: 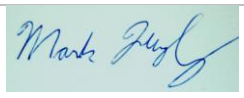 Date: *15/5/14*

CHAPTER 1. SCHMIDT HAMMER EXPOSURE-AGE DATING OF LATE QUATERNARY FLUVIAL TERRACES

1.1 Abstract

Schmidt hammer rebound values (R-values) are reported for surface clasts from numerically dated Holocene and Pleistocene fluvial terraces in the South Island of New Zealand. R-values are combined with previously obtained weathering rind, radiocarbon, terrestrial cosmogenic nuclide and luminescence terrace ages to derive SH R-value chronofunctions for greywacke clasts from four distinct locations. The results show that different weathering rates affect the form of the SH R-value vs. Age curve; however, a fundamental dependency between the two remains constant over timescales ranging from 10^2 to 10^5 years. Power law scaling constants suggest changes in clast weathering rates are primarily affected by climatic (precipitation and temperature) and sedimentologic variables (source terrane petrology). Age uncertainties of c. 22% of the surface age suggest that Schmidt hammer exposure-age dating (SHD) is a reliable calibrated-age dating technique for fluvial terraces.

1.2 Introduction

Geomorphic studies frequently utilise age dating of fluvial terraces and glacial outwash plains (e.g. Bull and Knuepfer 1987; Molnar et al. 1994; Amos et al. 2007, 2010; Barrell et al. 2011). Isotopic and radiogenic techniques have the ability to provide numerical ages but are typically expensive and labour intensive. River deposits that lack suitable organic material for radiocarbon dating, have complex mixing, burial and/or exposure histories that complicate terrestrial cosmogenic nuclide dating (TCND) or contain detritus that was not completely 'bleached' prior to deposition for luminescence dating may be challenging to date using these techniques.

Clasts exposed at or near the surface weather by chemical, physical and biological processes that collectively reduce the mechanical strength of the rock (e.g. Birkeland and Noller 2000; Walker 2005). Time-dependent variables like rock weathering rind thickness (e.g. Chinn 1981; Knuepfer 1988; McSaveney 1992; Oguchi and Matsukura 1999; Laustela et al. 2003), surface roughness (e.g. Benedict 1985), P-wave velocity (Crook and Gillespie 1986) and clast density (Maizels 1989) may be used to derive relative-ages for populations of surface clasts. The weathering-induced reduction of rock strength can also be measured using the Schmidt hammer (hereafter SH).

The SH was originally developed for concrete testing but has been widely used as a field test of rock hardness and relative-dating technique for over three decades (Schmidt 1951; Day and Goudie 1977; Day 1980; Matthews and Shakesby 1984; McCarroll 1991a, 1994; Goudie 2006; Shakesby et al. 2006, 2011). SH rebound value (R-value) tests rock hardness at the surface by measuring the percentage rebound of a hammer mass in a controlled impact against the test surface (Goudie 2006; Shakesby et al. 2006). A number of workers have shown that decreasing SH R-values, and thus a decrease in rock mechanical strength, correspond with an increase in rock surface exposure age (e.g.,

Matthews and Shakesby 1984; McCarroll 1989, 1991b,c; Winkler 2005; Shakesby et al. 2006, 2011; Matthews and Winkler 2012).

A geomorphic feature with independent, numerical age control can be used to quantify the relationship between SH R-values and exposure age. R-values of a population of surface clasts reflect the time-dependent mechanical degradation of the rock, and thus an approximate time since a presently stable surface was abandoned following erosion or aggradation. If numerical ages exist for a sequence of two or more features, then a chronofunction that relates SH R-values to surface exposure ages may be derived and used to estimate the surface ages for other undated deposits within the sequence (Shakesby et al. 2006; Winkler 2009; Matthews and Owen 2010). Geomorphic studies coupled with SH analyses have been used to produce calibrated-age curves for glacial, periglacial, mass movement, and alluvial fan deposits (e.g. McCarroll 1991a; Nesje et al. 1994a, b; White et al. 1998; Aa et al. 2007; Kellerer-Pirklbauer et al. 2008; Rode and Kellerer-Pirklbauer 2011; Shakesby et al. 2011), and polished bedrock surfaces (e.g. Gupta et al. 2009; Matthews and Owen 2010).

Previous studies have yielded strong correlations between average SH R-values and surface exposure ages within the Holocene (McCarroll 1987; Nicholas and Butler 1996; Winkler 2005; Matthews and Owen 2010; Shakesby et al. 2011). Only a few studies have applied SH exposure-age dating (SHD) to pre-Holocene surfaces, with variable results (e.g. White et al. 1998; Engel 2007; Sánchez et al. 2009). Shakesby et al. (2006) and White et al. (1998) are the only studies to apply SHD to fluvial deposits.

Fresh, fluvially-polished rock tends to yield the highest R-values for any given lithology (Ericson 2004; Gupta et al. 2009) and rounded clasts have the highest R-values of all sediment morphologies (McCarroll 1989; Shakesby et al. 2006), possibly as a result of minimal surface roughness (Williams and Robinson 1983; McCarroll 1989). Given the relatively high initial strength and low initial surface roughness of the lithologies and clasts present in New Zealand's fluvial terraces (Read et al. 1999), SHD may be useful over a longer (pre-Holocene) timescale than commonly attempted.

In this chapter, SHD is applied to surface clasts on fluvial terraces for the first time. SH analyses are combined with published luminescence, radiocarbon, weathering rind and TCND ages to construct age-calibration curves for a suite of terraces in New Zealand's South Island. Climatic and petrologic data are used to compare weathering rates between study sites and predict chronofunction parameters.

1.3 Study Sites

The four study sites in the central South Island of New Zealand (Fig. 1.1A and B) were chosen because they contain well-dated Holocene and Pleistocene terraces, have similar clast lithologies and they span a range of contemporary climates. The ages used to calibrate SHD in this study are the best estimates of abandonment ages for the terraces. Terraces formed by lateral incision into pre-existing fan deposits, without subsequent aggradation or leaving a veneer of gravel prior to abandonment, may yield exposure ages older than the abandonment of the terrace tread (i.e. skewed to the age of deposition of the fan gravel). Weathering rind exposure-ages for terrace treads, as well as local terrace stratigraphy, suggest episodes of minor aggradation prior to abandonment for all of the terraces in this study (e.g. Bull 1990).

The Saxton River terraces (Fig. 1.1C) have been extensively studied in attempts to calculate slip rates on the cross-cutting Awatere Fault (Knuepfer 1988; McCalpin 1996; Mason et al. 2006). The site consists of six previously mapped terraces incised into a late Pleistocene (c. 16 ka) fan. For the purposes of our investigation, I differentiated between two terraces (T5a & T5b), previously mapped as T5, and separated by a c. 1 m riser. This was done to test the resolution of the SH in distinguishing between terraces formed in a short time period. All of the terraces except for T3 and T5a have been previously dated using weathering rinds, which produce consistently reliable results in New Zealand's well-indurated Torlesse greywacke (Chinn 1981; Whitehouse et al. 1986; Knuepfer 1984, 1988; McSaveney 1992; Nicol and Campbell, 2001). Ages were inferred for terraces where maximum and minimum age control was available from adjacent terraces.

Weathering rind ages are used in conjunction with numerical dating. McCalpin (1996) obtained a radiocarbon age of 1186 ± 110 cal. years BP (2012) for the Saxton T6 terrace overbank silts. This minimum age of abandonment for the terrace tread is younger than but consistent with Knuepfer's (1988) weathering rind age of 2000 ± 500 years for abandonment of T6, which is adopted in this study. Mason et al. (2006) have extensively dated the oldest terraces T1 and T2 with multiple radiocarbon and OSL dates. Their preferred age of T1 terrace abandonment was an OSL age of 14,500 ± 1500 years derived from fluvial silts capping the terrace gravels. A discrepancy between Mason et al.'s (2006) OSL age for T1 (see Fig. 1.1) and a younger weathering rind age (9410 ± 1570 years; Knuepfer 1988) was attributed to deflation of a silt cover that previously covered the exposed gravel (Mason et al. 2006). This was interpreted to have reduced the surface exposure time and hence the weathering rind age. I therefore use Mason et al.'s (2006) OSL ages for the abandonment of T1 and T2 in this analysis as the best estimate of true surface age.

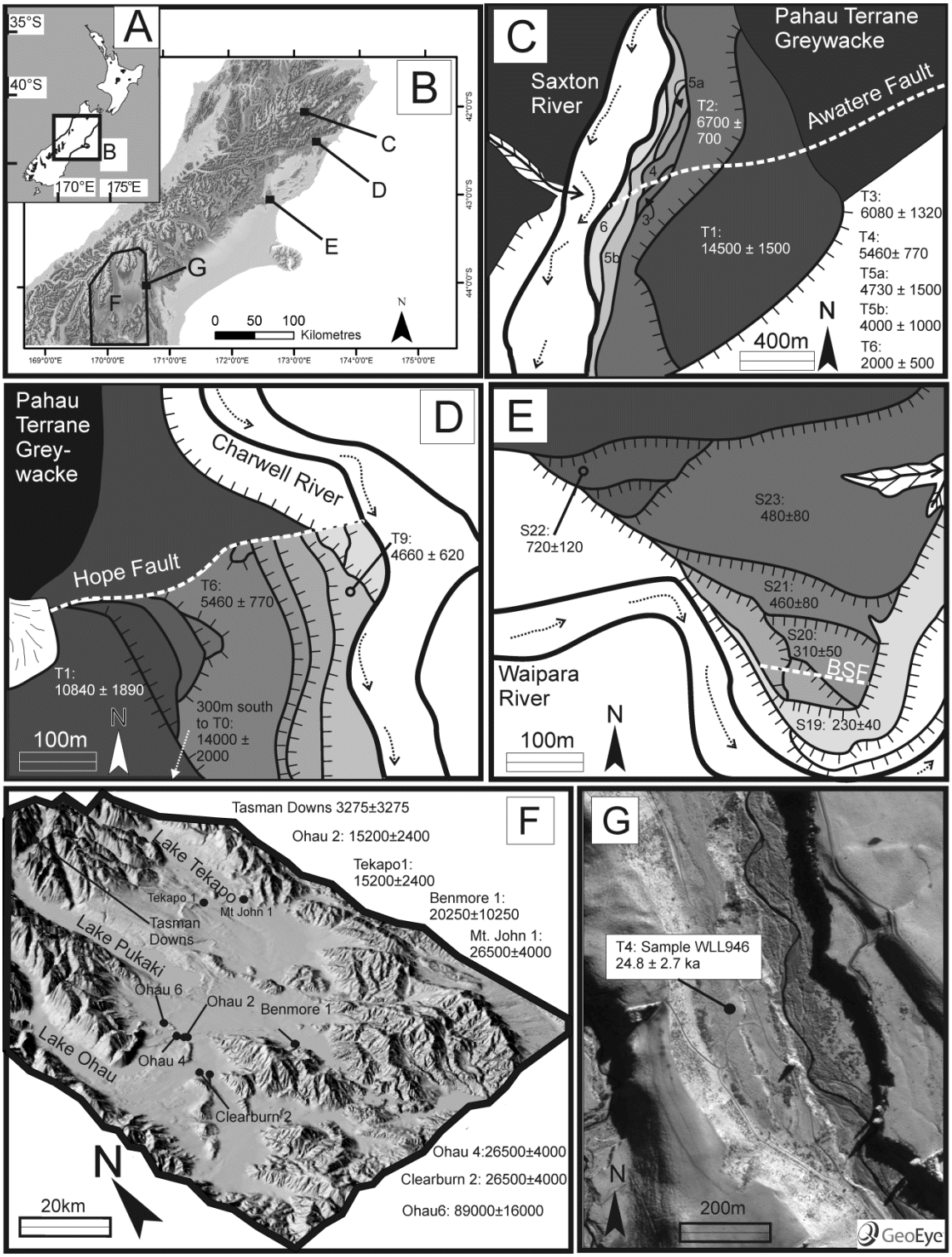

Figure 1.1: Location map of SHD study sites around South Island, New Zealand (A & B) and generalised geomorphic maps of study sites. All ages are given in years unless otherwise specified. (C) Saxton River terraces (modified after Mason et al. 2006); (D) Charwell River terraces (modified after Knuepfer 1984); (E) Waipara River terraces (modified after Nicol and Campbell 2001); (F) 15m Digital Elevation Model (3x vertical exaggeration) of the Mackenzie basin and sites selected for sampling. (G) GeoEye aerial imagery of the Cloudy Peaks test site, showing location of OSL sample and paired fluvial terraces incised by stream flowing N-S in image. References for ages in (C-G) and Schmidt hammer data are given in Table 1.1.

Table 1.1: Terrace names by study site, the amount of SH measurements (n) taken, SHN mean/median values and references for terrace ages given in Fig. 1.1. See text for discussion.

Site	SH_N mean	SH_N median (SH_R)	Reference for numerical age given in Fig. 1.1
SAXTON RIVER			
T1 (n=150)	39.0	38	Mason et al. (2006)
T2 (n=100)	40.6	40.5	Mason et al. (2006)
T3 (n=50)	43.3	44	Inferred from Mason et al. (2006) and Knuepfer (1988)
T4 (n=100)	43.2	43	Knuepfer (1988)
T5a (n=100)	45.6	47	Inferred from Knuepfer (1988)
T5b (n=100)	47.0	48	Knuepfer (1988)
T6 (n=50)	51.3	52	Knuepfer (1988) and McCalpin (1996)
Modern (n=50)	60.9	61.5	
CHARWELL RIVER			
T0 (n=50)	33.9	33	Bull and Knuepfer (1987)
T1 (n=100)	35.1	35	Knuepfer (1988)
T6 (n=50)	39.1	38	Knuepfer (1988)
T9 (n=100)	42.9	44	Knuepfer (1988)
Modern (n=50)	56.0	55.5	
WAIPARA RIVER			
S22 (n=50)	44.0	44	Nicol and Campbell (2001)
S23 (n=100)	46.1	45.5	Nicol and Campbell (2001)
S21 (n=50)	47.4	47.5	Nicol and Campbell (2001)
S20 (n=50)	49.3	48.5	Nicol and Campbell (2001)
S19 (n=50)	54.2	55	Nicol and Campbell (2001)
Modern (n=50)	60.9	62	

The Charwell River study site consists of a flight of twelve post-14ka terraces along the Hope Fault-bounded range front (Fig. 1.1D). The terraces were formed by incision into late Pleistocene gravel and greywacke bedrock, and are capped with a veneer of younger aggradational gravels (Bull and Knuepfer 1987). The oldest and highest surface was not mapped by Knuepfer (1984) and I assume this surface, named here as T0 to keep consistent terminology, is the apex of the 14ka aggradation event described by Bull and Knuepfer (1987). Terraces younger than T0 were dated by Knuepfer (1988) using weathering rinds calibrated with radiocarbon and with other studies. Of these eleven, three were selected for SHD- most terraces were only subtly preserved in the landscape and lacked surface clasts. Although predominantly Torlesse greywacke (Pahau sub-terrane), the modern

stream also contains boulders of trachybasalt, either from the local Gridiron/Lookout Formations (Suggate 1958; Challis 1966) or from an unmapped volcanic member of the Torlesse greywacke. The weathering pattern of both lithologies is similar in surface clasts on abandoned terraces with the trachybasalt representing a relatively low proportion of the total clast count.

Table 1.1 (continued): Terrace names by study site, the amount of SH measurements (n) taken, SH_N mean/median values and references for terrace ages given in Fig. 1.1. See text for discussion.

Site	SH_N mean	SH_N median (SH_R)	Reference for numerical age given in Fig. 1.1
MACKENZIE BASIN			
Tekapo1 (n=100)	46.0	46	Amos et al. (2007) and (2010); Barrell et al. (2011)
Benmore1 (n=100)	45.2	45.5	Inferred from Barrell and Cox (2003)
Ohau2 (n=100)	46.5	47	Amos et al. (2007) and (2010)
Ohau4 (n=100)	42.3	41.5	Amos et al. (2007) and (2010)
Mt. John1 (n=100)	41.5	42	Amos et al. (2007) and (2010); Barrell et al. (2011)
Clearburn1 (n=100)	40.2	39.5	Amos et al. (2007) and (2010); Barrell et al. (2011)
Ohau6 (n=50)	31.7	31.5	Amos et al. (2007) and (2010)
Tasman Downs (n=50)	58.0	60	Inferred from Schaefer et al. (2009)
Modern (n=50)	60.2	62	
CLOUDY PEAKS			
T4	39	40.13	This study

The Waipara River study site consists of between 5 cut-in-fill terraces that are all younger than 1 ka and are displaced by the Bobys Stream Fault ('BSF' in Fig. 1.1E) (Nicol and Campbell 2001; Campbell et al. 2003). The terraces consist primarily of a Torlesse greywacke gravel veneer (undifferentiated Pahau and Esk Head Melange sub-terranes) overlying a late Pleistocene outwash gravel strath surface. Nicol and Campbell (2001) used weathering rinds to date five of the terraces on site, as well as several others in the area with reliable results. Locally derived clasts of coarse-grained, Tertiary sandstone were identified on the three oldest terraces. On younger terraces and in the modern stream, coarse limestone boulders were readily identifiable. Some greywacke surface clasts on these terraces were coated with a calcium-carbonate film from the weathering limestone.

The Mackenzie basin is an intermontane basin located in the central South Island (Fig. 1.1F). The study sites are dispersed across the basin where low relief moraines, glacial lakes, and

glaciofluvial outwash plains predominate. Glacial and periglacial features have been numerically dated using various techniques including OSL and TSL (thermally stimulated luminescence), TCND, and radiocarbon (Barrell and Cox 2003; Amos et al. 2007, 2010; Schaefer et al. 2009; Barrell 2011; Barrell et al. 2011). The ages of these features range from the 'Little Ice Age' to at least 100-150ka. Outwash plains are exceptionally preserved due to the dry climate and distance from the Main Divide, which allows reliable mapping of correlative deposits and features (e.g. Maizels 1989; Amos et al. 2007 and 2010; Barrell et al. 2011). Surface clasts are all Torlesse greywacke (Rakaia sub-terrane). Outwash plains in this study fall into five categories based on numerical ages: marine isotope stage (MIS) 5 or 6 (89 ± 16 ka); early MIS 2 (26.5 ± 4 ka); mid MIS 2 (inferred as 20.25 ± 10.25 ka); late MIS 2 (15.2 ± 2.3 ka); and Holocene (3.275 ± 3.275 ka) (Fig. 1.1F). Efforts were taken to sample where previously numerically dated samples had been taken; however, some samples were taken in locations of unknown age that have been mapped and correlated with dated units elsewhere (Amos et al. 2007, 2011; Barrell et al. 2011). Where minimum or maximum numerical ages were obtained, the age and error inferred for the surface was conservatively set midway between bounding units/surfaces of known age (Table 1.1). In addition to these four study sites, a test site at Cloudy Peaks, on the edge of the Mackenzie basin, was selected for comparison between OSL and SHD techniques. An OSL age of 24.8 ± 2.7 ka (Fig. 1.1G; Table 1.2) was obtained from fluvial silts overlying river gravel in a terrace located approximately 40m above stream level. Surface clasts used for SHD consist of Rakaia sub-terrane greywacke rocks.

Table 1.2: Optically stimulated luminescence results for T4 at the Cloudy Peaks test site- measured a-Value, Equivalent Dose, Cosmic Doserate, Total Doserate, and OSL Age.

Sample[a]	Lat/Long	a Value	D_e[b] Gyr	dD_c/dt[c] Gyr/ka	dD/dt[d]	OSL Age (ka)	Field Code
WLL946	-44.017, 170.693	0.05 ±0.01	88.74 ± 8.70	0.2162 ± 0.0108	3.57 ± 0.17	24.8 ± 2.7	T49611

[a]*Sample preparation and measurements performed at the School of Earth Sciences, Victoria University of Wellington, Wellington, New Zealand*

[b]*Equivalent dose*

[c]*Contribution of cosmic radiation to the total doserate*

[d]*Total doserate*

Table 1.2 (continued): OSL Sample description, water content and radionuclide content

Deposit	Water Content (%)	K (%)	U (ppm) from ^{234}Th	U (ppm) from ^{226}Ra, ^{214}Pb, ^{214}Bi	U (ppm) from ^{210}Pb	Th (ppm) from ^{208}Tl, ^{212}Pb, ^{228}Ac
T4 sandlens	17.3	1.97 ± 0.04	2.69 ± 0.21	2.49 ± 0.12	2.08 ± 0.16	10.53 ± 0.12

1.4 Methodology

An N-type *SH* (hereafter SH_N) with a calibrated impact energy of 2.207 N·m (Proceq SA 2012) was used in this study. Control of potential instrument error was constrained by pre- and post-sampling checks of correct calibration using a test anvil in order to detect instrumental deterioration during the measurement campaign. One *SH* impact was delivered on each clast for a minimum of 50 clasts per surface (e.g. Matthews and Shakesby 1984, Winkler 2005). This provides a statistically significant sample size and produces similar results to much larger sample sizes (Niedzielski et al. 2009). Although recently developed test designs with multiple sub-samples and an overall largely increased number of clasts measured at one site can significantly tighten the instrumental error margins (e.g. Shakesby et al. 2011, Matthews and Winkler 2012), the restricted availability of clasts suitable for testing and the character of my test sites preclude such attempts.

Where possible, two independent sets of 50 clasts were sampled on each surface to test for data consistency, as has been suggested for weathering rind studies (McSaveney 1992). A third test, during which the SH_N operator was selective to sample only clasts with geomorphic stability indicators (i.e. rock varnish, raised quartz veins, lichen cover), was conducted in instances where the surrounding geomorphology visibly suggested reworking or secondary deposition (e.g. T1 at the Saxton River site). This method weighted the dataset towards clasts with a more reliable exposure history without discarding data that may be relevant to the surface exposure age.

To avoid the effects of rock moisture content (Sumner and Nel 2002) and instrumental inconsistencies due to humidity causing corrosion/rust inside the *SH*, sampling was carried out in dry conditions. The clast surfaces were not brushed clean or smoothed prior to *SH* sampling so that the full weathering rind and clast surface roughness were preserved. The sampled surfaces were lichen free and any obvious mineral veins or structural discontinuities were avoided (Ozbek and Gul 2011). The *SH* was held as vertically as possible on horizontal to sub-horizontal clast surfaces to avoid biased *R*-values created by varying impact angles and protruding mineral grains on rebound (André 1996; Ericson 2004; Shakesby et al. 2011, Proceq 2012). If small particles were chipped off during sampling or the sound of the *SH* impact was not resonant (indicating possible cracks invisible below

the surface), an additional attempt was made to resample the clast surface from another impact point. If the same problem was encountered, the clast was omitted from the dataset.

Clasts with less than 15 cm of rock exposed at the surface were avoided during sampling. Although ideally larger clasts/boulders are preferred with SH studies, the limited availability of clasts precluded an increase in this minimum size. While there is little constraint on subsurface clast geometry and edge effects in clasts of this size in the present study, I consider the chosen minimum of 15 cm exposed rock reasonable on the following bases:

i) Demirdag et al. (2009) showed in a series of tests that rocks from various lithologies with a minimum edge dimension greater than 11 cm yield consistent L-type *SH R*-values. The L-type *SH* has a lower impact energy than the SH_N, and thus the minimum edge dimension required for consistent results is likely somewhat higher for a SH_N. Nevertheless, the present cut off value of 15 cm is larger than suggested by Aydin (2009) for International Society of Rock Mechanics standards (100 mm at the point of impact for SH_N), and is equivalent to those suggested in the ASTM (2005) (minimum 15 cm).

ii) The terrace gravels I observed in outcrop rarely contained disk-shaped or 'platy' clasts, which typically have much smaller edge dimensions than required for sampling.

iii) Every boulder was kicked before sampling to check for stability, and clasts that moved during sampling were considered unsuitable. Additionally, if a clast was chipped during sampling, or the SH sounded flat rather than resonant, indicative of a shallow discontinuity (as with disk-shaped clasts), the *R*-value was omitted from the dataset.

iv) Some of the impact energy during sampling may have been dissipated within the underlying soil as opposed to wholly within/on the clast being sampled. These effects are thought to be minimal, as most clasts sampled were firmly encased in soil. So long as the effect is constant (i.e. the average clast size and mechanical soil properties remain unchanged from site to site) the results should be internally consistent.

v) The SH_N was chosen over devices with less impact energy (e.g. Equotip) due to significantly smaller *R*-value variance (Viles et al. 2011) and a much more frequent usage in geomorphology in both New Zealand and elsewhere.

When different lithologies could be identified in the terraces and active stream bed (e.g. the Waipara River), care was taken to sample only the Torlesse greywacke. Where the weathering of two similar lithologies on older terraces made identification of Torlesse greywacke difficult (such as volcanic rocks in the Charwell River), both lithologies were sampled in the modern stream.

Catchment lithologies and proportional contributions to the fluvial system are assumed not to have changed over time.

For surface clasts with a simple exposure history, *SH R*-values are expected to be normally distributed (Winkler 2005, 2009) and the mean *R*-value from a series of measurements is the most often used proxy for the surface exposure age (e.g. Goudie 2006). In this study, slight differences were sometimes observed in the individual *R*-value distributions and dataset means when comparing individual tests on the same surface (n=50 per test) to each other and/or the combined dataset. Niedzielski et al. (2009) found that using the median increased *R*-value consistency and reduced the required sample size for a range of rock types. The median *R*-value (hereafter SH_R) is less affected by statistical outliers than the mean and is preferred in this study. Both mean and median values for the study sites are listed in Table 1.1.

A Kruskal-Wallis analysis of variance (ANOVA) test (Kruskal and Wallis 1952) was used to test for significant differences among SH_R. The analysis was run as a multiple comparisons test (comparing each median to every other median) at the 1σ level using a Dunn-Sidak correction (Sidak 1967). This is a much more conservative approach than identifying significant differences in a dataset *sensu stricto* but less conservative than multiple comparison tests with other adjustment techniques (e.g. Abdi 2007).

Age-SH_R correlations are derived for the Saxton River terraces (Fig. 1.1C), Charwell River terraces (Fig. 1.1D), Waipara River terraces (Fig. 1.1E), and Mackenzie basin outwash plains (Fig. 1.1F), with published age errors and 95% standard errors reported for age and SH_R, respectively.

Climate data for the study sites were compiled along with petrologic information from Torlesse greywacke sub-terranes (Table 1.3). This was done to investigate possible changes in weathering rates due to differences in precipitation, temperature and source rock composition. Maximum temperature (°C) and precipitation data (mm) were downloaded from the National Institute of Water and Atmospheric Research (NIWA) CliFlo database as monthly averages over a thirty year time period. Climate stations that were nearest to the study sites (maximum 55 km) and in similar microclimates were chosen. For the Charwell River, Saxton River and Cloudy Peaks sites, temperatures were adjusted using an average New Zealand lapse rate of 0.5 °C/ 100 m (Norton 1985). Thirty year averages for each month were extrapolated to full year values (i.e. multiplied by 12) to obtain a range of possible annual precipitations (MAP_{month}) and maximum mean temperatures (MAT_{month}). These are preferred over mean annual temperature and precipitation because the latter give no indication of climate fluctuations sub-annually. More importantly, the exponential dependence of chemical

weathering rates on temperature illustrates that climate extremes control long-term rates more so than lower average values (e.g. Velbel 1990).

Petrologic data for the Torlesse sub-terranes were compiled from a variety of sources and are reported as Quartz-Feldspar-Lithics (QFL) modal percentages (Table 1.3). For the Rakaia sub-terrane, averages were calculated from MacKinnon's (1983) Petrofacies 1 through 4. The modal percentages of Petrofacies 5 (MacKinnon 1983; Roser and Korsch 1999) were used for the Pahau terrane, and supported by Barnes' (1990) data. QFL percentages from greywacke within the Esk Head Melange are more difficult to quantify, but data from the greywacke blocks in the melange proper (Botsford 1983) and gradational contact into the Pahau terrane (Feary 1979) were taken as representative modal percentages.

Table 1.3: Thirty-year monthly averages of maximum temperature (°C) and precipitation (mm) extrapolated for a full year (MAT_{month} and MAP_{month}, respectively). The data range is from 1981-2010, except for the Cloudy Peaks site/Fairlie weather station, where the only available data range was from 1951-1980. Petrologic data are given as modal percentages of Quartz-Feldspar-Lithics (QFL) for Torlesse greywacke sub-terranes.

Site	Climate station	Distance to study site (km)	Elevation Difference (m)	MAT_{Jan}	MAP_{Jan}	MAT_{Feb}	MAP_{Feb}	MAT_{Mar}	MAP_{Mar}
Saxton	Molesworth	9	70	21	521	20.9	548	18.5	586
Charwell	Kaikoura Aws	28	300	18.9	468	18.5	622	17.2	710
Waipara	Waipara West	3	0	23.8	691	23.7	491	21.6	544
Mackenzie	Lake Tekapo, Air Safaris	Variable; <55	Variable, not adjusted	21.6	624	21.3	396	18.8	564
Cloudy Peaks	Fairlie	14	200	20.6	708	20.4	564	18.6	888

Table 1.3 (continued)

Site	MAT_{Apr}	MAP_{Apr}	MAT_{May}	MAP_{May}	MAT_{Jun}	MAP_{Jun}	MAT_{Jul}	MAP_{Jul}	MAT_{Aug}	MAP_{Aug}
Saxton	15.1	572	11.5	649	8.0	706	6.6	649	8.3	574
Charwell	14.7	666	12.7	679	10.5	900	9.4	1103	10.2	803
Waipara	19	672	15.6	434	12.8	635	12	646	13.4	755
Mackenzie	14.9	672	10.7	720	7	600	5.8	624	8.2	648
Cloudy Peaks	15.7	624	11.9	852	9.3	540	8.3	612	10	588

Table 1.3 (continued)

Site	MAT Sep	MAP Sep	MAT Oct	MAP Oct	MAT Nov	MAP Nov	MAT Dec	MAP Dec	Sub-terrane	*Q*	*F*	*L*
Saxton	11.4	634	13.5	830	15.8	595	18.4	695	Pahau	.26	.34	.40
Charwell	12.2	682	13.8	757	15.5	703	17.6	563	Pahau	.26	.34	.40
Waipara	15.8	756	17.7	472	19.8	719	22.1	628	Pahau/Esk Head	.40	.20	.40
Mackenzie	11.9	636	14.5	612	17.2	624	19.4	576	Rakaia	.30	.50	.20
Cloudy Peaks	13.3	528	15.5	756	17.4	720	19.1	804	Rakaia	.30	.50	.20

1.5 Results

1.5.1 SH Data

SH_R values for all study sites decrease with an increase in terrace age (Fig. 1.2). In all three curves, SH_R can be correlated with age using a power law function of the simple form

$$SH_R = a * (age)^b \qquad \textit{(Eqn. 1.1)}$$

where *a* and *b* are statistically estimated constants (Fig. 1.2A-C). The power law describes the SH_R – age relationship over timescales ranging from 10^2 yr (Waipara) to 10^5 yr (Mackenzie basin) timescales. The curves are generally defined by a rapid decrease in SH_R values from clasts within the modern stream to clasts in the youngest terrace, followed by conformity to the power law (Eqn. 1.1). This implies that a short period (ca. 10^2 - 10^3 years for the study sites considered herein) of relatively rapid weathering occurs during and/or after the transfer of alluvium from an active channel into an 'inactive' terrace.

To test if the curves have a common slope, I used the statistical package (S)MATR and fit curves with a Major Axis (MA) regression (see Warton et al. 2006 for a full review). This was chosen in place of Ordinary Least Squares (OLS) fitting for the following reasons:

i) MA fitting uses a maximum likelihood estimation (MLE) of slope when deriving a common slope among different groups (e.g. different study sites). Using a MLE reduces Type 1 error (rejection of a potentially true hypothesis of common slope) and does not assume constant SH_R variance with age (homoscedasticity) (Warton et al. 2006; Shakesby et al. 2011). This enables comparison of terraces spanning three orders of magnitude of ages and errors.

ii) MA fitting accounts for uncertainty in numerical age as well as SH_R. An MA fitted line optimises residuals perpendicular from the curve at the data point, as opposed to solely in the *y* (SH_R) direction.

iii) MA is better suited to describing theoretical relationships between two variables; OLS is more appropriate when the goal is to predict *y* from *x* (Warton et al. 2006). The interest in this study is the former.

iv) In this study, MA yields values that generally agree with, but lie between the extremes of, OLS and standardised major axis fitting (Warton et al. 2006).

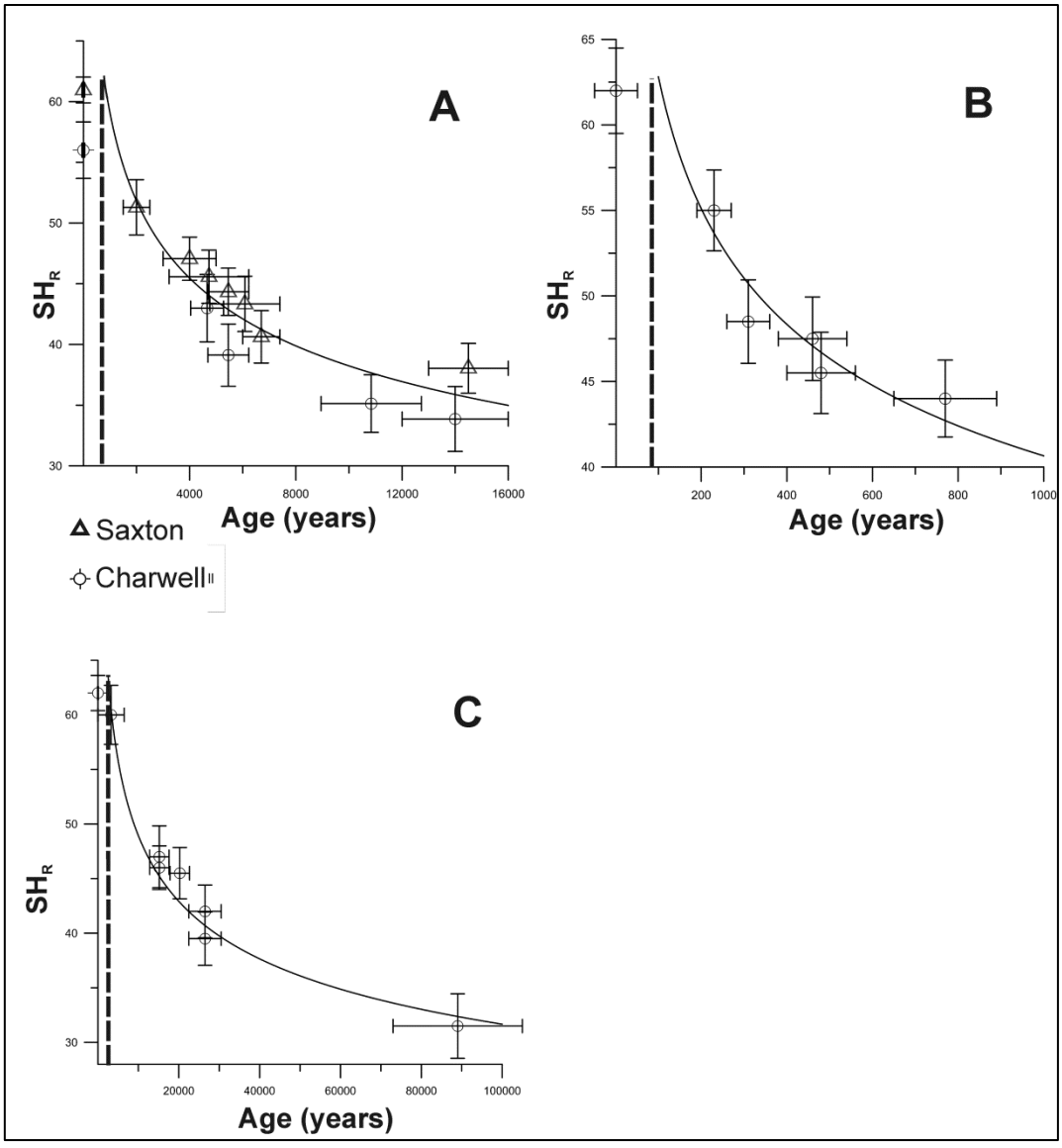

*Figure 1.2: SH_R-Age curves for **(A)** Saxton and Charwell River terraces; **(B)** Waipara River terraces; **(C)** Mackenzie basin outwash plains. Standard error of the median is approximated as 1.25 times the standard error of the mean (Hojo 1931). Vertical asymptote is drawn through the age with a corresponding SH_R value equal to that of the modern stream.*

A common slope (*b*-value in Eqn. 1.1) of -0.189 was determined with high statistical significance ($p = 0.678 > .05$). The *a*-value of each curve was then computed using nonlinear least squares with the fixed, common *b*-value. Table 1.4 shows the results of these tests and curve fitting. The *a*-value for the Cloudy Peaks test site was determined by rearranging Eqn. 1.1 ($a = 264$).

Table 1.4: Statistically estimated power law constants (with 95% confidence intervals) for Eqn. 1.1. The p-value (0.678) obtained for testing if the datasets had a common slope (b-value) was much higher than the critical value (0.05). See text for discussion.

Site	*a*-value	*b*-value	Lower threshold of power law behaviour (SH_R; Age_{min})	R^2 to lower threshold
Saxton and Charwell	217^{+7}_{-7}	$-0.189^{+0.0316}_{-0.0375}$	52; 2000	0.854
Waipara	150^{+3}_{-4}	$-0.189^{+0.0316}_{-0.0375}$	55; 230	0.951
Mackenzie	281^{+5}_{-6}	$-0.189^{+0.0316}_{-0.0375}$	60; 3275	0.9826

The power law constants control different aspects of the chronofunction form. The *a*-value, or scaling constant, controls the 'position' of the SH_R-age line in logarithmic space (Fig. 1.3). It is interpreted as being inversely related to weathering rate. The power law slope, *b*-value, is common to all sites and indicates that there is a ubiquitous *change* of weathering rates through time, despite orders of magnitude differences in the rates themselves. A linear function drawn between the modern stream and the youngest terrace results in a smooth transition from linearity to power law (in logarithmic space), but is only an assumption due to lack of data in that time range (curved fine-dotted lines in Fig. 1.3).

A Kruskal-Wallis ANOVA test shows that most terraces have statistically significant differences among their medians (Fig. 1.4). It is rare for two terraces to have statistically indistinguishable SH_R when their numerical age errors do not overlap. The results show that *SHD* is ideal for relative-age dating of Pleistocene outwash plains- in the Mackenzie basin, *R*-value datasets that cannot be differentiated are from surfaces that are the same age. Calibrated-age dating of Holocene fluvial terraces at the other three sites is more prone to statistical 'overlap', though this is rare in the present study.

Predicted age uncertainties were computed using the 95% confidence interval of *a*-values and the residuals of actual age to regression age. These values yield an average 22% uncertainty with respect to terrace age. This approach to predicting age uncertainty (or more specifically *equation* error) is preferred in this study for its simplicity. Predicted age errors for linear regressions involving

SH measurement error are discussed in full by Shakesby et al. (2011). Because SH_R is related to age by a power law in this study, both SH_R and age are logarithmically transformed in the regression procedure, which simultaneously transforms the errors. Thus straight-forward age error distributions using SH_R are not possible, but the double transformation reduces the increasing variability in age observed by Shakesby et al. (2011).

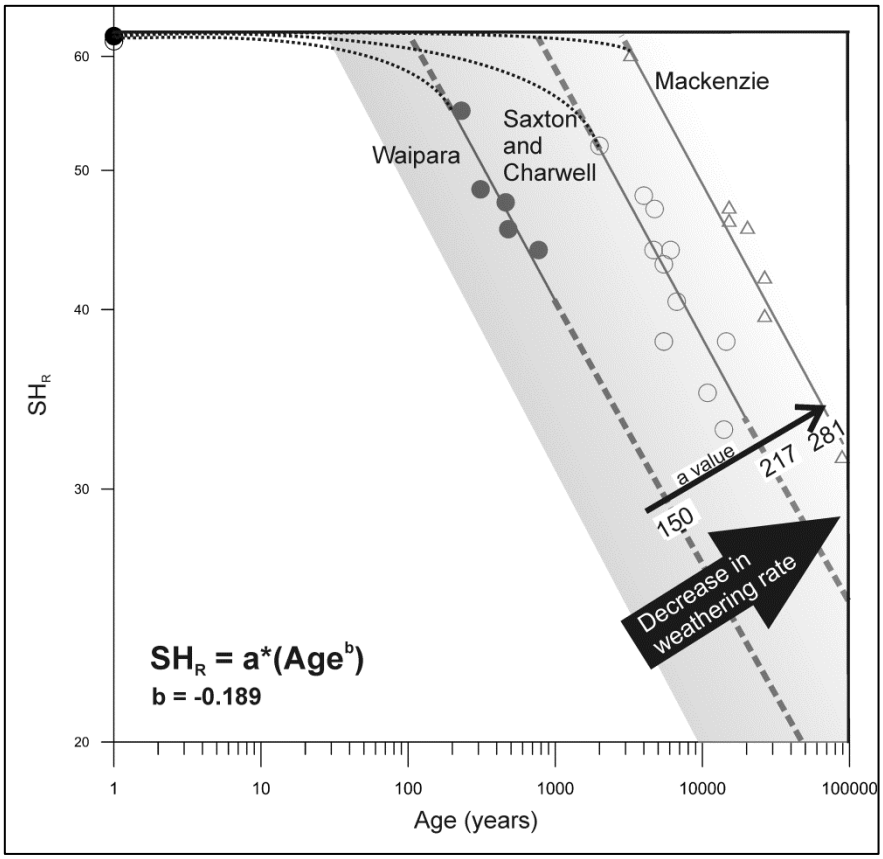

Figure 1.3: SH_R-Age data on a logarithmic scale for the three curves shown in Fig. 1.2A-C.Dark lines (solid for known data and dashed for assumed continuation) show the maximum likelihood estimation of a common slope (b-value) for the three groups. The line position is determined by a-value in Eqn. 1.1, which increases with decreasing weathering rate. The fine-dotted lines are linear interpolations (curved when plotted on logarithmic axes) between the modern stream values and the youngest surface.

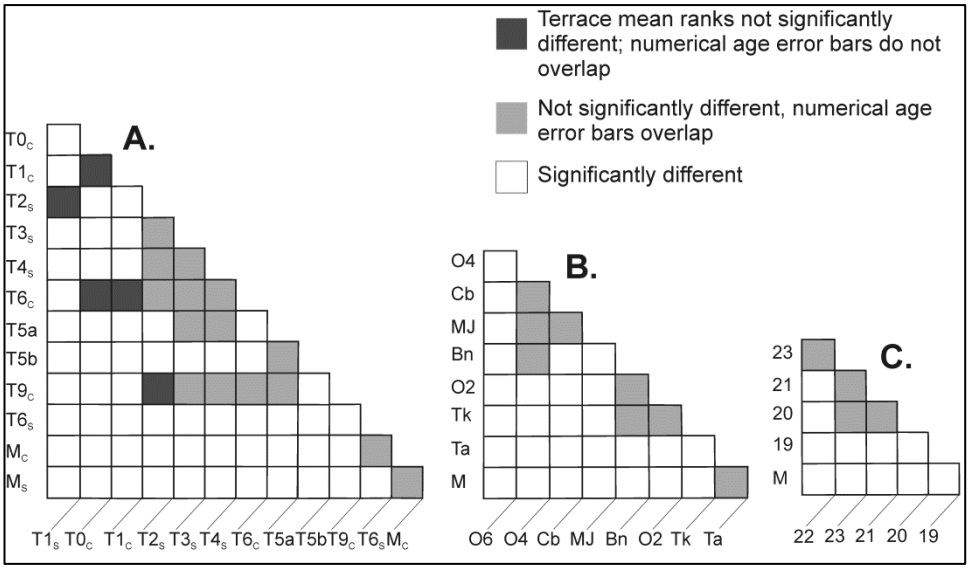

Figure 1.4: Matrix of Kruskal-Wallis test results for SHD data. A) Saxton and Charwell River terraces; B) Mackenzie basin outwash plains; C) Waipara River terraces. In A) $_S$ indicates Saxton, $_C$ indicates Charwell, M= modern stream tests. In B), O=Ohau, Cb=Clearburn1, MJ=Mt. John1, Bn=Benmore, Tk=Tekapo1, Ta=Tasman Downs. See text for discussion.

1.5.2 Climate and lithology data

The weathering rate from dissolution of a silicate mineral is often expressed with the Arrhenius equation:

$$R_x = A * exp\left(-\frac{E_a}{RT}\right) \qquad \textit{(Eqn. 1.2)}$$

where R_x is weathering rate, E_a is the activation energy (kJ mol^{-1}), R is the gas constant, T is the temperature (°K), and A is a pre-exponential factor related to mineral surface area and reactivity (Riebe et al. 2004). White and Blum (1995) modified this equation to include precipitation and empirically predict chemical weathering flux at the watershed scale

$$Q_x = (c * P) * exp\left[-\frac{E_a}{R}\left(\frac{1}{T} - \frac{1}{T_0}\right)\right] \qquad \textit{(Eqn. 1.3)}$$

where Q_x is the chemical weathering flux (mol*ha^{-1}*yr^{-1}) of a solute, P is annual precipitation (mm), T_0 is a reference temperature, and c is the slope of a linear correlation between precipitation and Q_x (set as c = .45, after White and Blum 1995). MAT and MAP for each month (Table 1.3) were used to calculate ranges of Q_x for the four study sites (Fig. 1.5A). E_a was set to 60 kJ mol^{-1}, which is within range reported for the dissolution of common silicate minerals (e.g. feldspars: E_a = 45-85 kJ mol^{-1}; White and Blum 1995; Brady and Carroll 1994; Riebe et al. 2004) and the solution obtained for SiO_2 from a global dataset of granitoid rocks used by White and Blum (1995) (E_a = 59.4 kJ mol^{-1}). A reference temperature of 288.15 °K (15 °C) was used, which is near the average MAT_{month} (15.8 °C).

Because the interest in this study is comparison of *in situ* clast weathering rates, values are not normalised for watershed size and scale is arbitrary (i.e. flux and rate are interchangeable terms).

Other authors have modified Eqn. 1.3 to account for other influences on chemical weathering rate (e.g. denudation rate; Riebe et al. 2004) with an additional dimensionless term on the right side of Eqn. 1.3. In Torlesse greywacke, chemical weathering occurs predominantly along intergranular boundaries, joints, and microcracks (Watters et al. 1981). Thus, to incorporate the influence of petrologic differences on the availability of fluid pathways for weathering, I multiply by the proportion of lithic fragments in the Torlesse sub-terrane (L) over a reference proportion (L_0= .5) to obtain an adjusted chemical weathering rate (W_x) for each site:

$$W_x = (c * P) * exp\left[-\frac{E_a}{R}\left(\frac{1}{T}-\frac{1}{T_0}\right)\right] * \left(\frac{L}{L_0}\right) \qquad \textit{(Eqn. 1.4)}$$

Fig. 1.5B shows the relationship of power law a-value to L for the study sites and the Cloudy Peaks test site, with the inset QFL ternary diagram showing scatter in L for the different sub-terranes. $W_{x\,min}$, $W_{x\,max}$, $W_{x\,median}$, and $W_{x\,avg}$ (the dataset mean weighted to the highest 50% of the values) are reported in Table 1.5. Fig. 1.5C shows a-values plotted against these measures of W_x.

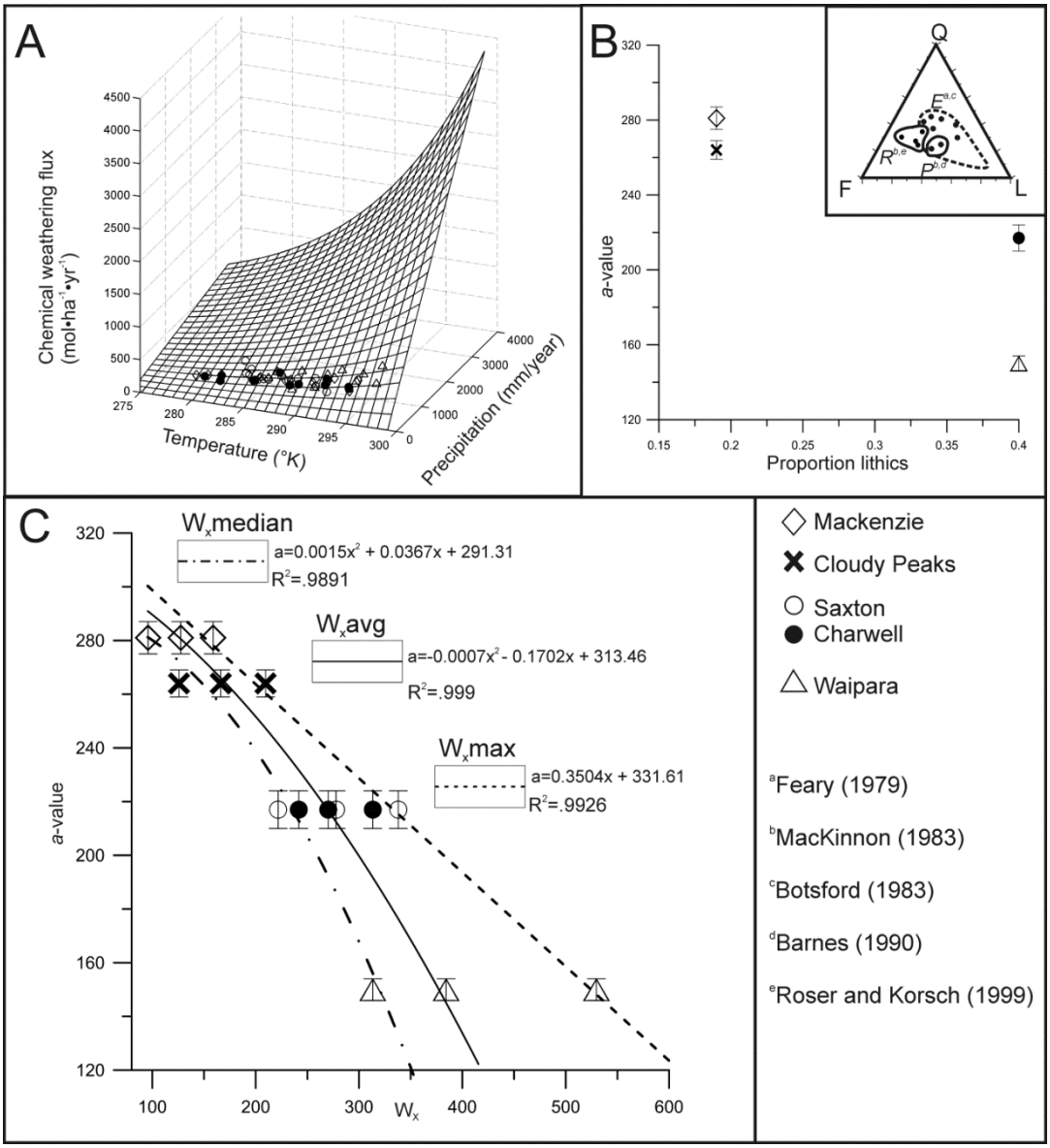

Figure 1.5: Climate and petrographic data for SHD study sites (A) Chemical weathering fluxes calculated by MAT_{month} and MAP_{month} for all four study sites. (B) Representative proportion of lithics in Torlesse sub-terrane vs. a-value for the four study sites and Cloudy Peaks test site. Inset ternary diagram shows distribution of QFL percentages for R (Rakaia sub-terrane), P (Pahau sub-terrane) and E (Esk Head Melange sub-terrane). (C) Adjusted chemical weathering rates vs. a-value and best-fit regressions for the four study sites. Data for the Cloudy Peaks test site is plotted but not included in the regression analysis. The key in the lower right applies to all three sub-figures.

Table 1.5: Minimum, median, weighted average and maximum values of adjusted chemical weathering flux. 95% confidence interval for a-value at Cloud Peaks is an estimate from previous results.

Site	$W_{\chi min}$	$W_{\chi median}$	$W_{\chi avg}$	$W_{\chi max}$	*a*-value
Saxton	111.13	221.72	277.80	337.99	217^{+7}_{-7}
Charwell	191.6	241.72	270.24	313.306	217^{+7}_{-7}
Waipara	166.93	313.34	384.24	529.63	150^{+3}_{-4}
Mackenzie	45.15	95.86	127.56	158.84	281^{+5}_{-6}
Cloudy Peaks	56.45	125.85	166.18	209.59	264^{+5}_{-5}

1.6 Discussion

1.6.1 Time dependence of SH_R

Previous studies have suggested that the mean *R*-value chronofunction is linear through time. Shakesby et al. (2011) recently confirmed this for the Holocene in relatively resistant granite boulders, but indicated that over a longer timescale (i.e. beyond the Late Glacial re-advances) weathering, and thus *R*-values, must inevitably reach a dynamic equilibrium. *SH* studies of 10^4-10^5 timescale features have pointed towards curvilinear relationships (White et al. 1998; Engel 2007; Sánchez 2009; Černá and Engel 2011), as well as some SH studies on 10^2-10^3 year timescales (McCarroll and Nesje 1993; Betts and Latta 2000; Awasthi et al. 2005; Kellerer-Pirklbauer et al. 2008). Curvilinear correlations on such short timescales could be due to comparatively small datasets, uncertainty in absolute ages, exceptionally fast weathering conditions or coincidental, non-age related variations in rock surface hardness between study sites (Shakesby et al. 2011).

The data show that the relationship between SH_R and age is curvilinear in all instances regardless of timescale. OLS fitting of a linear regression produces reasonable results for the Waipara terraces, but even fitting of a second-order polynomial produces a higher correlation coefficient. Linear regressions at the other sites can only be obtained by excluding data from older terraces.

For numerous time-dependent weathering processes, there is laboratory and field-based evidence that the fundamental processes governing weathering follow a power law. Busenberg and Clemency (1976) noted that the kinetic dissolution of feldspars follows a power law for some stages

of weathering in the laboratory. Harden (1987) found a power law relationship for the accumulation of clay content through time in soils ranging from 10 ka to 3 Ma. Taylor and Blum (1995) compared the relative proportions of cations in unweathered parent material for a glacial chronosequence and obtained a power law relationship with age. They remarked '*the explanation for the power law relationship is probably a combination of several mechanisms, including changes in mineral surface area, depletion of reactive minerals, and exhaustion of rapidly weathered minerals'* (p. 981). Simple and modified power laws are commonly used for weathering rind thickness chronofunctions in New Zealand (Chinn 1981; Whitehouse et al. 1986; Knuepfer 1984, 1988).

Vance et al. (2009) reviewed the decrease in chemical weathering rate of silicate minerals with time. They show that there is a common dependence of weathering rate on time (common power law slope, *b*-value) for samples from different climates and rock-types, despite weathering rate change over several orders of magnitude (changing power law *a*-value). White and Brantley (2003) similarly reviewed weathering rates of common minerals (plagioclase, K-feldspar, biotite, and hornblende) and drew the same conclusions. These results are reflected in the current study. The trend in decreasing SH_R values with time is common among all sites, but the absolute rate varies, presumably, with small changes in lithology and/or climate. Thus, the chemical weathering of minerals provides a feasible mechanism to explain the observed power law decrease of SH_R with time as well as variations in *a*-value.

1.6.2 Relationship of *a*-value to climate and lithology

Modern chemical weathering rates are precipitation and temperature dependent (Eqn. 1.3; White and Blum 1995). Fig. 1.5A shows that chemical weathering fluxes, Q_x, are all relatively low for my study sites. More importantly, the clustering of points shows that there are only small variations in Q_x from one site to another. These variations cannot fully explain the differences in *a*-value. Since chemical weathering in Torlesse greywacke is in large part limited by the fluid pathways (e.g. intergranular boundaries) available in the rock (Watters et al. 1981), differences in source terrane lithic content *L* should show a relationship with *a*-value for the sites. Fig. 1.5B shows that there is a general negative correlation between *a*-value and increasing lithic content. Sites with the same lithic content but vastly different *a*-values (Waipara and Saxton/Charwell, Mackenzie basin and Cloudy Peaks), however, suggests that lithic content alone does not control chemical weathering rate.

Fig. 1.5C shows the relationship of adjusted chemical weathering rate, W_x, to *a*-value for the four study sites. The data for the Cloudy Peaks test site is plotted for comparison but not included in determination of the regressions or correlation coefficients. The data show that the highest weathering rates at a site have a strong correlation with *a*-value; the regression is linear for $W_{x\,max}$ and a second-order polynomial for $W_{x\,avg}$ and $W_{x\,median}$. $W_{x\,min}$ does not show a useful correlation with *a*-value due to

the relatively restricted range of climate fluctuations at Charwell (see Table 1.3) and so is not plotted in Fig. 1.5C. At Cloudy Peaks, *a*-values determined from absolute age control conform with those that would be predicted by the three separate measures of W_x. This suggests that absent independent age control, climate and petrologic information can be used to estimate *a*-value in Torlesse greywacke sub-terranes.

I note that this empirical approach does not seek to fully describe a fundamental relationship between W_x and *a*-value. There are undoubtedly other variables, such as vegetation and site-specific chemistry differences that affect chemical weathering rates. Additionally, chemical weathering rates in paleo-climates are not addressed- it is assumed that all sites are affected equally by past climate change, though the orders of magnitude timescale differences considered here mean that this is not the case (e.g. Vance et al. 2009). However, the high correlation coefficients and predictive capability of the regression equations imply that these effects are small compared to the climatic extremes and petrologic variables for which W_x accounts.

1.6.3 Relationship of chemical weathering to Schmidt hammer rebound

Using several geotechnical indices, Hodder and Hetherington (1991) showed that there is a quantifiable relationship between chemical weathering indices and rock strength (using *SH*, Shore hardness, and Point load tests) for Torlesse greywacke in New Zealand. The mechanism by which chemical alteration leads to a reduction in *SH* rebound requires an explanation which is considered here.

Weathering rinds are a product of chemical alteration on the outer edges of surface boulders (Whitehouse et al. 1986; Oguchi and Matsukura 1999; Birkeland and Noller 2000). Oguchi and Matsukura (1999) found that Vickers microhardness was useful in distinguishing different zones within a weathering rind profile. Laustela et al. (2003) found a linear relationship between weathering rind thicknesses and *SH R*-value for rock glacier surfaces in the Swiss Alps. Likewise, SH_R and modal weathering rind thicknesses are positively co-variant at three of the study sites and best defined by linear regressions (Fig. 1.6). This relationship indicates that an increase in weathering rind thickness occurs concurrently with a drop in mechanical strength that is measurable by the *SH* on timescales of c. 15ka or less. Since the slope of the SH_R-modal weathering rind thickness line changes from one area to the next, however, SH_R must be measuring another property within or on the clast.

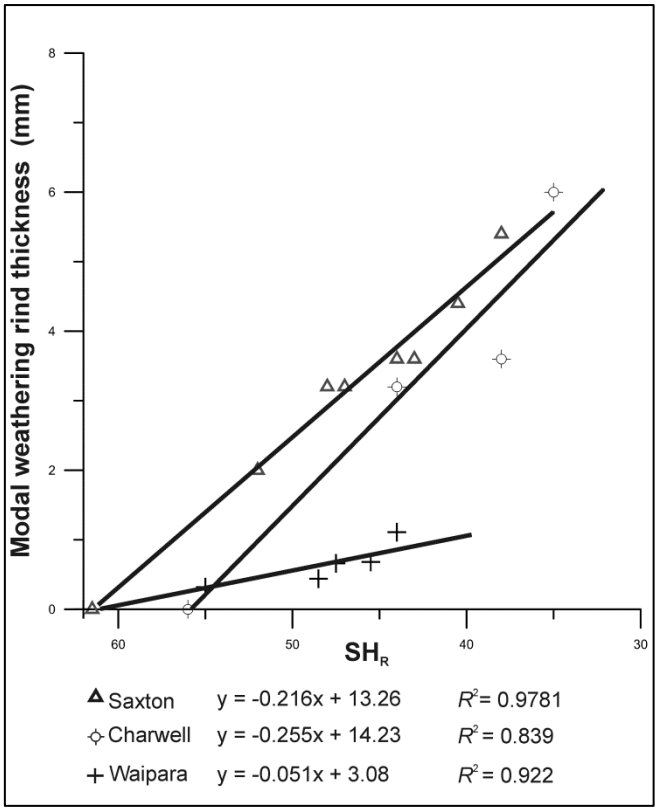

Figure 1.6: Relationship of SH_R to modal weathering rind thickness for the Charwell, Saxton, and Waipara River sites. References for weathering rind data are the same as for ages at respective study sites in Table 1.1.

The 'other' aspect of clast weathering could have any number of underlying chemical or physical mechanisms. Studies have outlined how rock properties that vary with surface exposure time, such as P-wave velocity (Crook and Gillespie 1986; Sharma et al. 2011), rock density (Maizels 1989; Hodder and Hetherington 1991; Basu et al. 2007), and surface roughness (Benedict 1985; McCarroll 1989; André 1996; Ericson 2004; Gupta et al. 2009) also affect *SH R*-values. Exactly how chemical weathering is coupled to each of these properties is not presently well constrained, though a decrease in reactive surface area with increasing surface roughness and/or precipitation of soft, authigenic clay minerals in or on the clast likely facilitate at least some of the reduction in *SH R*-value.

1.6.4 Applicability of SHD to fluvial terraces

SHD is capable of differentiating exposure-ages of surface clasts on fluvial terraces. Eqn. 1.1 and *b*-values reported in Table 1.4 can be used to derive *a*-values for other terraces with Torlesse greywacke surface clasts and at least one age control point. An empirical relationship between *a*-value and climatic/petrologic-dependent weathering rates is suggested. At a test site, *a*-values derived using this relationship yielded similar results to solving with independent age control. Average age uncertainties of 22% of the terrace age are consistent with those of weathering rind studies (Knuepfer 1988; 5-40%). Care should be taken in applying curves from this study to lithologies other than

Torlesse greywacke, as the *b*-value and/or chronofunction may not be applicable. For other calibrated-age studies where absolute ages are not available, similar methods of adjusting constants for chemical weathering rates may be useful regardless of the form of the equation.

1.7 Conclusions

Schmidt hammer exposure-age dating is a useful calibrated-age dating technique for outwash plains and fluvial terraces. In New Zealand, Schmidt hammer median *R*-values are a power law function of exposure age (Eqn. 1.1, Fig. 1.3). The power law exponent, or *b*-value, for Torlesse greywacke is the same irrespective of study site (Table 1.4). The power law scaling constant, or *a*-value, scales with intrinsic petrologic variations between Torlesse sub-terranes and extrinsic climatic variables, and can be directly solved for using a minimum of one age control point. Empirical relationships for predicting *a*-value without absolute age constraints are suggested. Estimates of predicted age uncertainties (c. 22% of terrace age) are similar to those of weathering rind studies. Modal weathering rind thicknesses are correlated to Schmidt hammer *R*-values, though the changing slope of the regression from one area to the next indicates that there must be other time-related factors that influence *R*-values. If sufficient measures are taken to reduce time-independent *R*-value variability from site to site, use of *SHD* offers a sound alternative to absolute and other calibrated-age techniques for dating fluvial terraces over late Quaternary timescales.

CHAPTER 2. POST-GLACIAL TECTONIC HISTORY OF THE LAKE WAKATIPU BASIN AND MOONLIGHT FAULT

2.1 Abstract

The South Island of New Zealand straddles the transpressional Australian-Pacific plate boundary, providing an excellent opportunity to document the on-shore distribution of uplift and active faulting. I surveyed and dated stranded lake shorelines of Lake Wakatipu in the southern South Island to assess the magnitude and timing of post-glacial tectonic deformation in this part of the orogen. Shoreline ages were assessed using a combination of SHD and optically stimulated OSL dating of river terraces directly correlated with stranded shorelines. Survey data and OSL ages indicate formation of the lake and the highest, most prominent preserved shoreline occurred shortly after 17.1 ± 2.6 ka. Gradual lowering of the lake level occurred between terrace-forming episodes from c.13 ka to 2 ka, followed by accelerated lowering to or just below modern levels. GPS mapping and LiDAR survey data indicate that correlative shoreline elevations are consistent across the 80 km-long lake. Numerical cross-correlation of shoreline elevations identified in the LiDAR datasets reinforces my preferred shoreline correlations. The results show no differential tectonic and/or glacial-rebound induced uplift in the last c. 13 ka recorded by stranded shorelines of Lake Wakatipu, despite proximity to the Pacific-Australian plate boundary, the Moonlight Fault, and a large Last Glacial Maximum (LGM) glacial ice load. The Moonlight Fault has not been active in the last c. 13 ka, despite the National Seismic Hazard Model and geodetic modelling allowing for a 1 mm yr^{-1} slip rate and M_W 7.6 earthquake every c. 6 ka. Any deformation resulting from tectonics or glacial-rebound may have been distributed throughout the region or onto structures adjacent to the Wakatipu basin. This pattern is consistent with time-varying partitioning of strain and seismic hazard on faults in southern New Zealand, but not with glacially-modulated fault activity observed elsewhere in the world.

2.2 Introduction

Characterising the spatio-temporal distribution of strain at plate boundaries is a crucial part of assessing seismic hazard. Geodetic measurements of shortening and uplift rates provide a baseline with which to compare to longer-term measurements from geologic studies (Dixon et al. 2003; Papanikolaou et al. 2005; Nicol and Wallace 2007; Amos et al. 2013). Earthquake and slip rate histories from many fault systems around the world, however, indicate that slip rates on a fault vary with time and that strain is not distributed homogeneously throughout a fault system (Norris and Nicolls 2004; Dolan et al. 2007; Oldow and Singleton 2008; Oskin et al. 2008). Variability in slip rates on a fault can be caused by stress changes between structural domains within a plate margin (e.g. Dolan et al. 2007), ductile shear zone weakening (Oskin et al. 2008), surface loading and unloading (e.g. Stewart et al. 2000), fault interaction and triggering (e.g. Freed 2005), and volcanism (Villamor et al. 2007).

In obliquely-convergent settings, partitioning of slip into plate-parallel and normal components displays along-strike variability (e.g. Jones and Wesnousky 1992; Pettinga and Wise 1994; Norris and Cooper 2001). Plate boundary geometry and kinematics are also influenced by surface processes such as erosion, sediment mass transfer and fluctuations in glacial ice loads (Stewart et al. 2000). There is increasing evidence for the timing of fault activity being modulated by changes in ice loads via glacial isostatic adjustment (GIA) mechanisms (e.g. Stewart et al. 2000; Sauber and Molnia 2004; Hetzel and Hampel 2005; Hampel et al. 2009). It is thus necessary to consider any role that surface processes may have played when trying to understand the spatio-temporal distribution of tectonic strain.

Stranded lake shorelines represent ideal strain markers and are common in locations that have experienced extensive and repeated phases of glaciations. Shorelines have the capacity to record deformation over the scale of a single fault rupture (Caskey and Ramelli 2004; Oldow and Singleton 2008) to broad-wavelength deformation from GIA, volcanic and tectonic uplift (McMartin 2000; Schaetzl et al. 2002, Caskey and Ramelli 2004; Oldow and Singleton 2008; Pierce et al. 2007). Accurate quantification of this deformation is important for assessing natural hazards in susceptible regions, but is complicated by the challenges of obtaining absolute ages for surfaces and correlating often poorly-preserved features. Subjective interpretation of survey data to identify paired shorelines between sites can introduce additional uncertainty into the dataset.

In this study, I use measurements of stranded shoreline ages and elevations to deduce the post-Last Glacial Maximum (LGM) deformation history of the Lake Wakatipu basin in southern New Zealand. A shoreline chronology is established using new ages derived from OSL and SHD, and existing radiocarbon ages. Shoreline elevation correlations from GPS-surveyed sites around the lake are corroborated by numerical analysis of LiDAR data. The results have important implications for strain partitioning in southern New Zealand and the glacial modulation of fault slip rates observed elsewhere.

2.3 Geological background

New Zealand is situated at the convergent margin between the Australian and Pacific plates. In the central and southern South Island (Fig. 2.1A), approximately 75% of the c. 30-50 mm yr^{-1} relative plate motion is accommodated by oblique-right lateral slip on the Alpine Fault (Norris and Cooper 2001; Sutherland et al. 2006; DeMets et al. 2010). The remaining 25% is taken up on predominantly reverse, strike-slip and oblique faults in Canterbury and Otago (Norris et al. 1990, Berryman and Beanland 1991; Walcott 1998; Sutherland et al. 2006). At its southwestern margin, the Alpine Fault transitions into almost pure strike-slip requiring the partitioning of strain on NE-striking reverse faults in a wide zone of deformation throughout Otago and the Australian plate (Norris and Cooper 2001; Barnes et al. 2005; Wallace et al. 2007; Barth et al. 2013).

Using field and GPS data, Sutherland et al. (2006) calculated that faults within an 80 km zone SE of the southern Alpine Fault must accommodate cumulative 7-8 mm yr^{-1} plate-parallel and 7-11 mm yr^{-1} shortening rates in the absence of vertical axis block rotations. On the eastern and western peripheries of the plate boundary, shortening rates decrease to 3-8 mm yr^{-1} cumulatively (Sutherland et al. 2006), with Beavan and Haines (2001), Berryman et al. (2002), Norris and Nicolls (2004), and Wallace et al. (2007) deriving c. 2-4 mm yr^{-1} contraction in central and eastern Otago from GPS data.

Geologically observed slip rates on individual Otago faults appear to vary with time (Beanland and Berryman 1989; Beanland and Berryman 1991; Litchfield and Lian 2004; Norris and Nicolls 2004) but have been sufficient to uplift and sustain asymmetric, anticlinal ranges and intervening basins (e.g. Jackson et al. 1996). Topographic relief of the topography and bedrock deformation increases to the West, indicating that the highest rates of uplift and erosion have been concentrated toward the plate boundary since the initiation of oblique-compression at c. 6.4 Ma BP (Walcott 1998; Norris and Cooper 2001). Paleoseismic studies, however, reveal an irregular pattern of earthquakes over the late Quaternary, with faults east of the highest topography showing the most activity over the latest Pleistocene (cf. Norris and Nicolls 2004). Strain rates of Beavan and Haines (2001) show that contemporary strain has been concentrated in eastern Otago. Fig. 2.1B shows slip rates and timing of most recent events of faults in Otago.

Lake Wakatipu, New Zealand's longest lake, occupies a glacially-deepened trough (e.g. Cook and Swift 2012) surrounded by several > 2000 m peaks. The lake begins c. 50 km SE of the Alpine Fault and is approximately 80 km long, 60 km of which is oriented roughly perpendicular to the plate boundary. Mechanical models of long-wavelength vertical velocities across the region show uplift decreasing from c. 4 to 2 mm yr^{-1} from NW to SE along the lake (Upton et al. 2009), which may result from coupling on the plate boundary. Geodetically-derived shortening rates derived of Beavan and Haines (2001) and Wallace et al. (2007) are poorly constrained due to poor spatial coverage across the lake, though strain rates of Beavan and Haines (2001) show that contraction in minimal. Historical seismicity is relatively low, but focal mechanisms are typically consistent with reverse and oblique-dextral motion (Leitner et al. 2001).

Ak: Akatore Fault | MREs:1200 BP, <3800 BP, >125 ka BP|SR: 0.8-2.3 mm/yr (late Holocene);
Ti: Titri Fault | MRE: 90-150 ka BP | SR: Unknown;
BM: Blue Mountain Fault | MRE: <7310 BP | SR_v: 0.1-0.2 mm/yr (since ~100 ka);
Sp: Spylaw Fault | MREs:<10 ka, ~5 events<39 ka BP | SR_v: 0.1-0.3 mm/yr (since ~40 ka);
TaR: Taieri Ridge Fault(s) | MRE: <7140 BP | SR_v: 0.6 mm/yr (Holocene);
RP: Rock and Pillar Range [Hyde Fault] | MRE: <4260 BP | SR_v: 0.15 mm/yr (mid Holocene)
Ro: Rough Ridge [Gimmerburn Fault] | MRE: Unknown | SR_v: 0.27 (late Holocene)
Ra: Raggedy Range [Blackstone Hill Anticline]: Unknown (Quaternary activity)
Du: Dunstan Fault | MRE: 1,000-5,000 BP | SR_v: 0.5 mm/yr (late Pleistocene)
Pi: Pisa Fault | MRE: >23 ka BP | SR_v: 0.08 mm/yr (late Pleistocene)
NCF: Nevis-Cardrona Fault | MREs: <9760 BP, 9760-20.5 ka BP, >20.5 ka BP | SR_v: 0.3 mm/yr (late Pleistocene)

Figure 2.1: Overview of study area in Otago South Island of New Zealand with the ice extent in the LGM (after Barrell 2011) in grey and eastern Otago faults dashed. (B) Simplified map and location of eastern Otago faults. Data for most recent event(s) (MREs) and slip rates/vertical slip rat rates (SR_V) shown in box below. References for Ak: Litchfield and Norris (2000); Litchfield and Lian (2004); Ti: Litchfield and Lian (2004); BM: Pace et al. (2005); Sp: Pace et al. (2005); TaR: Norris and Nicolls (2004); RP: Norris and Nicolls (2004); Ro: Norris and Nicolls (2004); Ra: Berryman et al. (2002); Du: Berryman et al. 2002; Pi: Beanland and Berryman (1989), Berryman et al. (2000); NCF: Beanland and Barrow-Hurlbert (1986), Berryman et al. (2000). (C) Lake Wakatipu basin, with approximate LGM ice extent (based on Turnbull 2000), location of the Moonlight (MFZ) and southern Nevis-Cardrona (NCF) faults, and selected locations referred to in text. (a) Bible Terrace; (b) Blanket Bay; (c) Greenstone River fan; (d) Meiklejohns Bay; (e) Bob's Cove beds; (f) Queenstown; (g) Frankton; (h) Jack's Point; (i) Kingston; (j) Glen Nevis station. Dashed boxes are extents of Fig. 2. 3, 2.4, and 2.6.

The Moonlight Fault, which strikes NE-SW and crosses the middle of the lake (Fig. 2.1B, C) has been deemed inactive (Turnbull 2000), despite proposed offsets on apparent fault traces near the lake that suggests recent activity (Turnbull et al. 1975; Turnbull 1980). The more broadly defined Moonlight Tectonic or Fault Zone (MFZ) consists of several sub-parallel faults in a 20 km wide zone crossing Lake Wakatipu. The fault length is 100-200 km long, depending on mapping north and south of Lake Wakatipu. Based on the distribution of the outlying Tertiary Bob's Cove Beds, the vergence of the Moonlight Fault has been inferred to switch across the lake ('scissors', after Turnbull et al.,1975) so that uplift on the west and east sides of the fault increases to the north and south of the lake, respectively. Wallace et al. (2007) include a shortening rate of 1 mm yr^{-1} across the MFZ in their GPS models. The National Seismic Hazard Model assigns a slip rate of 1 mm yr^{-1} and expected moment magnitude (M_W) of 7.6 for each of the MFZ segments to the North and South of Lake Wakatipu (Stirling et al. 2012).

The N-S striking Nevis-Cardrona Fault (NCF) passes c. 20 km to the east of Queenstown and 10 km SE of Kingston (Fig 1B). The fault is considered active, having a recurrence interval of c. 3.6 to <10 ka and with evidence for at least one Holocene rupture (Beanland and Barrow-Hurlbert 1988; Berryman and Beanland 1991). Southeast of Kingston, throw per event is estimated at 0.25-0.4 m with the total throw of 1.3 m reflecting faulting since 18 ka (Beanland and Barrow-Hurlbert 1988). Cumulative throws increase towards the centre of the fault to c. 3-7 m over the last c. 18 ka. Mapping on the southwestern-most extent of the fault indicates that motion transitions into strike-slip (Kerr et al. 2000) and topography on the hanging wall is more subdued. GPS modelling by Wallace et al. (2007) indicates that the summed slip rate across the NCF and adjacent faults east of Wakatipu (i.e. the Dunstan and Pisa faults) could be 2.5-7 mm yr^{-1}, higher than those calculated in geologic studies.

The basement rocks of the Wakatipu basin are predominantly comprised of the Caples and Rakaia terrane greywacke and their metamorphic equivalents (e.g. Haast Schist) (Turnbull 2000). The basin also includes an outlier of late Oligocene limestone, mudstone, sandstone, conglomerate and breccia (Bobs Cove Beds) infaulted along the Moonlight Fault.

The glacial trough in which Lake Wakatipu is situated is known to have experienced at least four major glaciations (Barrell 1994; 2011), with the most recent glaciation culminating some 18 ka (Fig. 2.1). The depth of ice during these glaciations, including during the LGM (c. 28 - 18 ka) may have exceeded 1 km in thickness (Barrell 2011). Much of the Southern Alps of New Zealand may have been covered by ice-caps at this time (Fig. 2.1A).

During the LGM, drainage of the Wakatipu catchment was through the terminal moraine at Kingston (Fig. 2.1 & 2.3). Lake Wakatipu developed as the Wakatipu Glacier drew back from this maximum position. It is thought that Lake Wakatipu existed at a height of approximately 43 m above the present level for a sufficient time to form a prominent high-stand shoreline around many parts of the lake (Thomson 1996). This shoreline has been cut into bedrock, moraine and alluvial fan surfaces (e.g. Fig. 2.3 & 2.4). Lacustrine sediments, assumed to have been deposited mostly during the lake level high-stand, are preserved in road cuttings near Frankton (Fig. 2.4b). Wood has been extracted from lake silts at several construction sites in the area around Frankton and Queenstown (Fig. 2.4) and yield radiocarbon ages of c. 6-9 ka (Bell 1992). The oldest of these (with a radiocarbon age of 8930 ± 91 years BP) was obtained from lake sediments below a shoreline cut at 26 m above present lake level, and represents a minimum age for the formation of the lake and a maximum age for the formation of that shoreline surface.

The age of the high-stand (c. +43 m), most prominent shoreline is unknown but Bell (1992) suggested that it formed shortly (i.e. < 1000 years) before formation of the + 26 m shoreline. At some point in the past, drainage switched from the outlet in the south at Kingston (at c. 352 m a.s.l.) to the east through the Kawarau River (Fig. 2.1) (Thomson 1996). This probably occurred with the connection of the Kawarau River to Lake Wakatipu via westward head-ward incision into sediments SE of Morven Hill by a tributary of the Kawarau River (Fig. 2.4) (Bell 1992; Thomson 1996). Following drainage capture, the lake level dropped episodically, as shown by the numerous smaller shorelines below the high-stand shoreline; some of these are below the present-day lake level indicating a more recent increase in the water level (Fig. 2.4). Since drainage capture, the lake level is likely to have fluctuated in response to continued incision of the outlet, shifts in the position and size of the Shotover River delta and occasional landsliding in the Kawarau gorge (Thomson 1985; Barrell 1994; Thomson 1996).

2.4 Methodology

2.4.1 Survey Data

Transects of lake level markers (shorelines and alluvial terraces) were field-surveyed using Real-Time Kinematic (RTK) GPS and differential GPS (dGPS) at five locations (Fig. 2.3, 2.5, 2.6 & 2.7, Appendix 1). Light Detection and Ranging (LiDAR) data were acquired by New Zealand Aerial Mapping for Queenstown Lakes District Council and available in three locations around Lake Wakatipu (Fig. 2.3, 2.4 & 2.6). LiDAR data were collected using an Optech ALTM3100EA system at a height of 1200 m with a 42° field of view. The pulse repetition frequency (PRF) was set at 70 kHz. The accuracy of the dataset was verified on the ground using dGPS and a regional network of geodetic reference marks. Automatically classified ground returns were manually processed to remove vegetation and hydrologic features. The processed LiDAR point clouds were gridded into 1x1 m digital elevation models (DEMs) (Appendix 1). Elevation transects were extracted in locations where multiple shorelines were readily identifiable (at Kingston and Glenorchy).

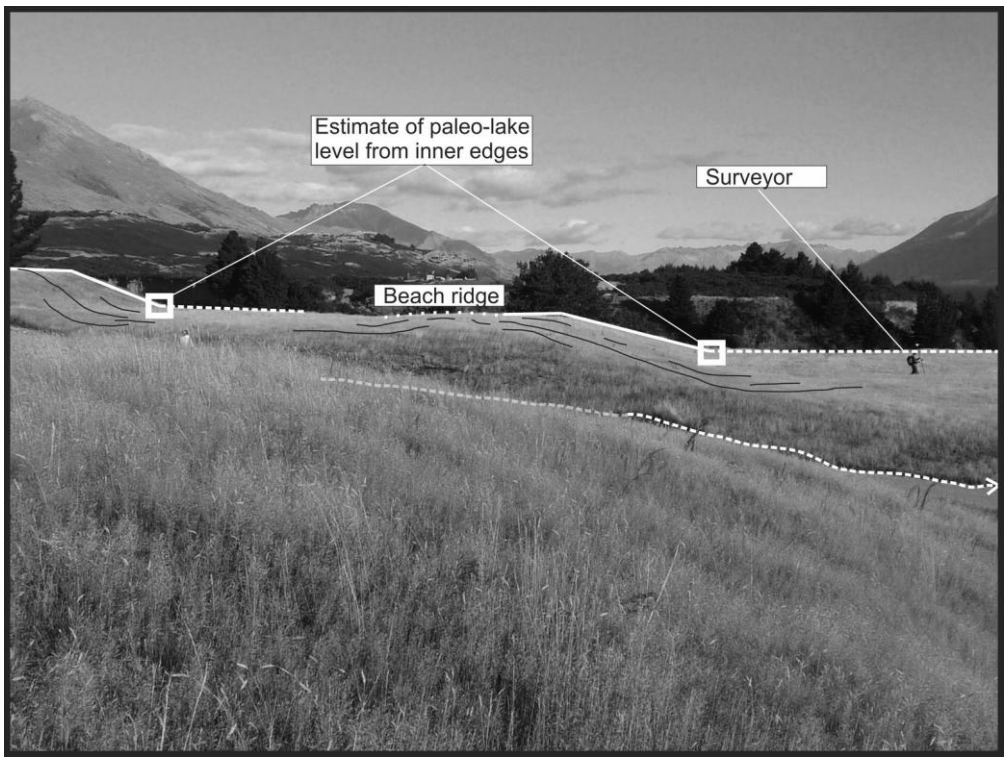

Figure 2.2: Field photo of shoreline terraces at Blanket Bay, with a beach ridge on the mid-level terrace and paleo-lake levels indicated by white dashed lines (see text for discussion). Author surveying with the RTK GPS rover. In the Frankton/Shotover fan LiDAR data, only the prominent high-stand surface could be reliably identified. An elevation for the high-stand surface was measured by spot-sampling at 18 locations on the southern side of Frankton Arm and the Kawarau river (Fig. 2.4), producing an average elevation of 351.3 m (standard deviation (δ) = 0.8 m). The spot heights chosen were in locations where the shoreline feature was well defined, undisturbed by engineering works, and where it appeared to be an erosional feature (rather than an aggradational feature, which is deemed to be the case for a surface of a similar elevation in proximity to the Shotover River fan).

2.4.2 Identification of shoreline elevations

Individual shorelines exist wherever low gradients were observed in shoreline profiles (e.g. Fig. 2.2). For all survey techniques employed and for all sites except the Greenstone River fan, representative shoreline elevations were identified on the basis of the estimated mean lake level (MLL) being near the inner edge of each terrace (Fig. 2.2). Slope inflection points at the bases of terrace risers but down-slope of the tops of colluvial fill at their bases were considered to best represent MLL. Observation of the modern shoreline morphology and water levels were consistent with this interpretation. At the Greenstone River fan (Fig. 2.5), the surfaces measured (fluvial terrace treads) approximate the level of the lake at time of formation but are likely to be slightly higher because of (a) small amounts of aggradation prior to abandonment of the fluvial surface and (b) an increase in elevation of the river terraces away from the paleo delta-lake interface (i.e. base-level). To adjust for (a), terrace elevations were taken from the lowest point along the terrace tread, usually in paleochannels. The depth of channels was consistent along the tread and I take this as indicative of removal of a thin boulder lag prior to abandonment of the predominantly degradational terraces. Several transects were needed to survey the laterally discontinuous terraces and adjust for (b). The average down-fan gradient (0.0058) was calculated from elevations of correlative terraces along the three transects. Terrace elevations were projected down-fan as necessary to better estimate the elevation of the lake interface. Beach ridges on the outer edges of some terrace treads indicate that the position of the delta has not shifted significantly through time and that the terrace surfaces closely approximate the lake level at the time of their formation.

2.4.3 Shoreline correlations

Preserved shorelines at Lake Wakatipu are discontinuous, formed in different materials (thus having different degrees of shoreline development and preservation), have sparse radiocarbon material for dating, and have non-uniform soil development that is insufficient for the purposes of relative dating. Initial correlations of these spatially isolated shoreline features were based primarily on matching of shorelines with similar geomorphology between sites. Correlation of shorelines between sites was conducted by first matching the prominent high-stand shoreline at each site and systematically correlating the equivalent lower shorelines between each site to achieve the best fit.

To support the field-based identification and correlation of lake-shorelines, I first employed a method of identifying shorelines for sites with high point densities (LiDAR and continuous dGPS), similar to that of Demoulin et al. (2007). The identification stage assumes that a histogram of elevations for any swath or profile across a flight of shorelines will contain more observations per bin width for flatter surfaces than for steeper terrain. That is, since elevation does not change significantly over the width of a terrace tread, elevation bins on terrace treads will be more populous than those on

sloping terrace risers. This relationship depends on the histogram bin width chosen for elevation; bin width is selected to be small enough to maximise variations in slope but larger than the natural increments in the raw data. For LiDAR data, elevation data are extracted by area (swath) (e.g. Fig. 2.3 & 2.6) and for dGPS data it is extracted from points recorded along a paced transect with an average point spacing of 1 m after processing.

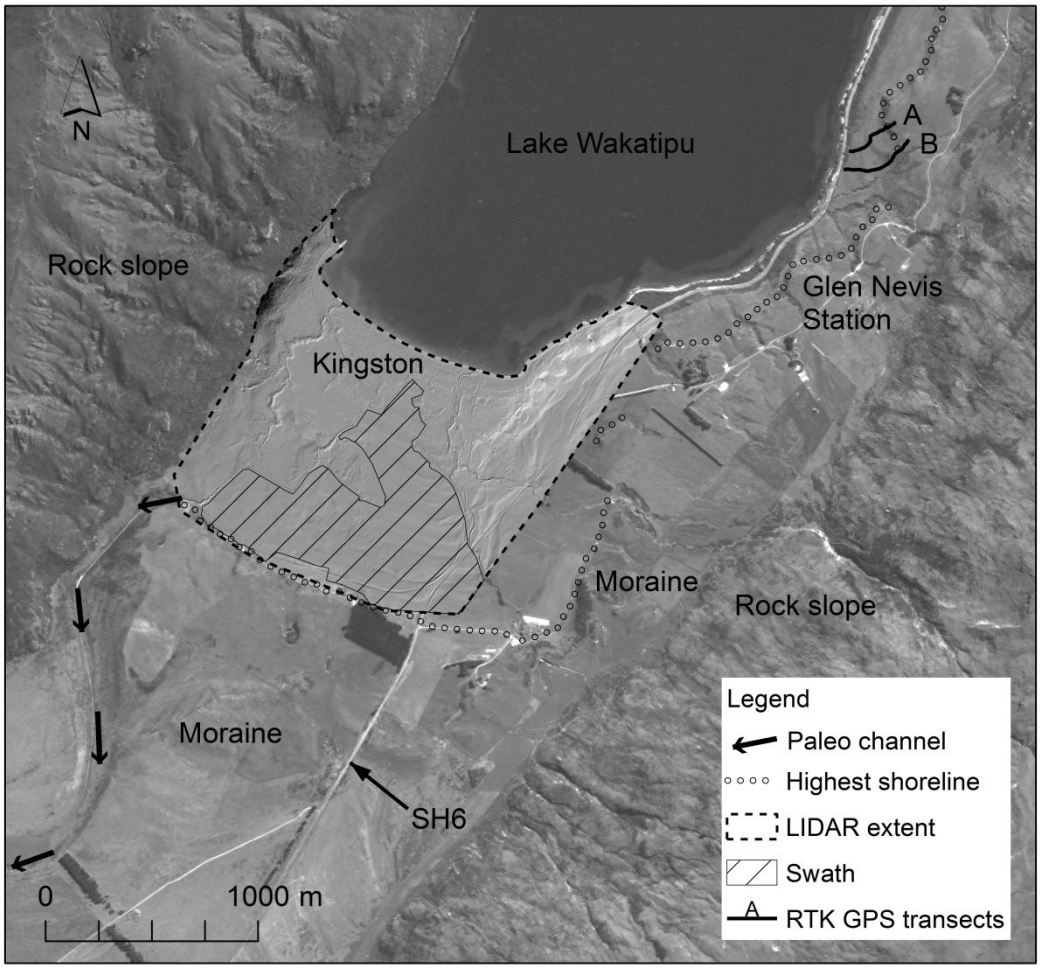

Figure 2.3: LiDAR (dashed extent) and SPOT imagery of Kingston township at the southern end of Lake Wakatipu, with terminal moraine and the former outlet from Lake Wakatipu shown. The prominent high-stand shoreline is shown here cut into moraine. See Fig. 2.1 for location reference.

The histogram is converted into a probability density function (PDF) and evaluated at 0.2 m intervals using a non-parametric fit smoothed with a Gaussian kernel. A minimum probability density threshold is chosen so that all values above the threshold are representative of terrace treads. This threshold is chosen based on field evaluation of what constitutes a discrete shoreline. Linear discriminant analysis is then used to separate terrace treads from risers whereby peaks above the pre-set threshold are assigned a value of 1 (terraces) and values below the threshold 0 (not terraces). Differentiation of peaks is achieved by setting 'troughs' that lie above the threshold (i.e. moderately

sloping risers between closely spaced terrace treads) equal to zero in the new 'step' function (Appendix 2). This method is disadvantaged by using the entire width of a terrace tread to compare elevations, as opposed to more accurate measures of MLL (see above). However, it allows for objective identification of shorelines without interpreting the position of the inner edge and yields similar results (see discussion).

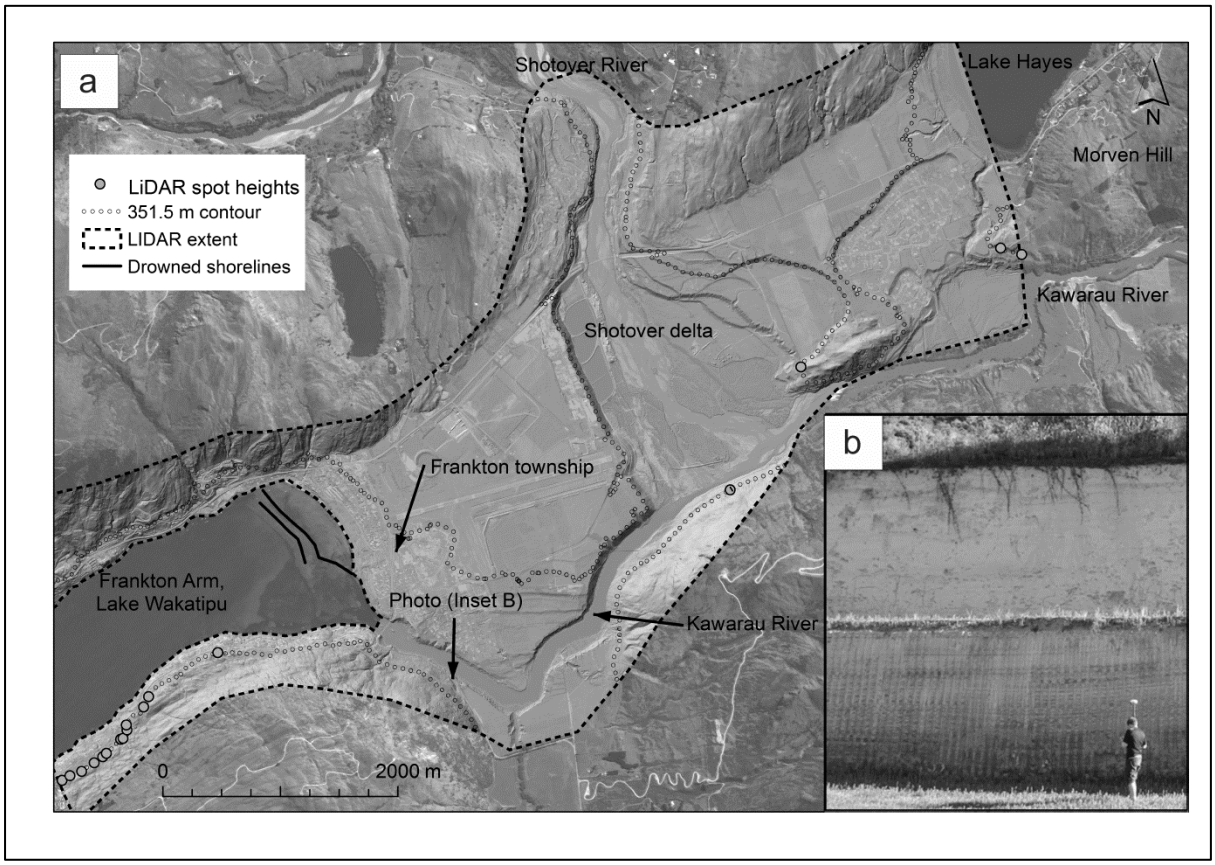

Figure 2.4: LiDAR and SPOT imagery of the Shotover delta area of Lake Wakatipu. a) The prominent high-stand shoreline cut into bedrock is shown here in the position of the 351.5 m contour mapped on to SPOT satellite imagery and LIDAR data. b) shows a road-cut exposure of lacustrine sediments deposited by Lake Wakatipu when the lake level was higher. Lake Hayes and Lake Wakatipu were once connected, prior to drainage capture by the Kawarau River. See Fig.2.1 for location reference.

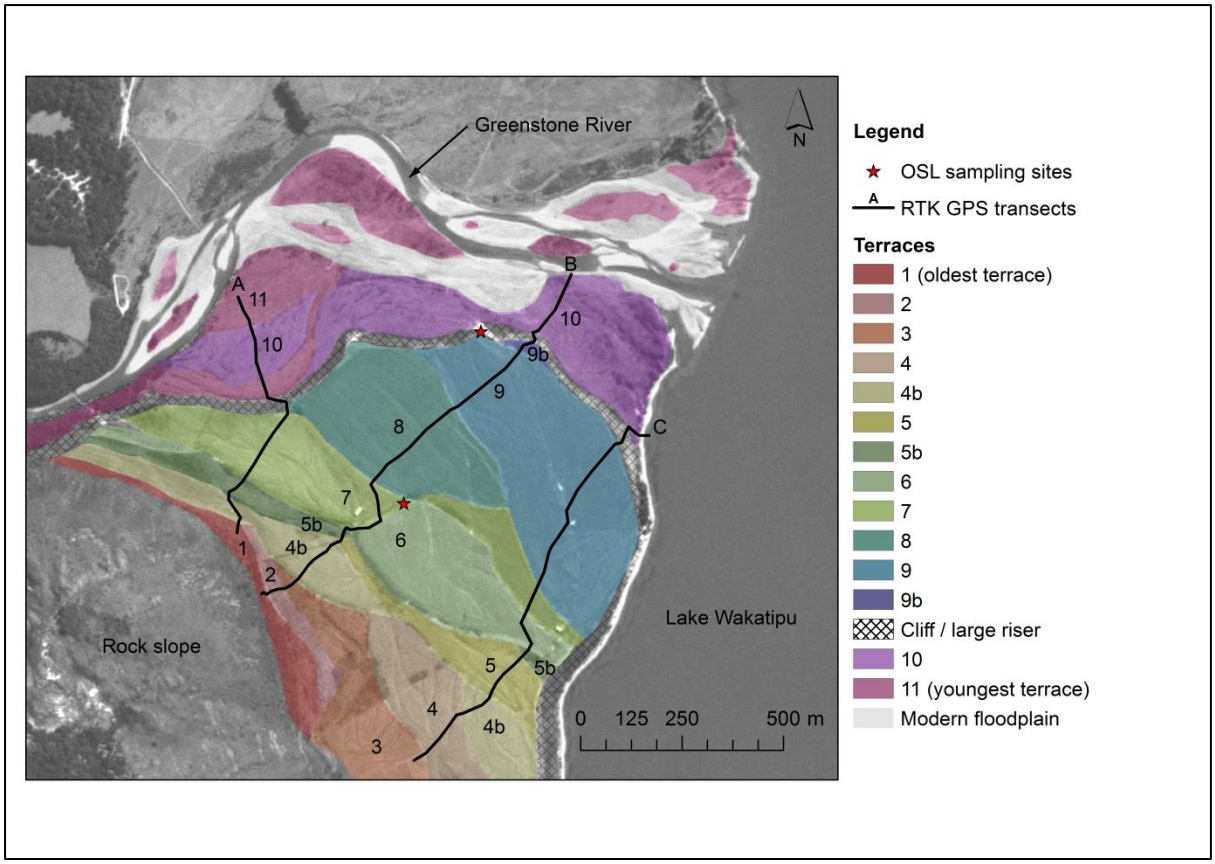

Figure 2.5: SPOT imagery, RTK GPS data, OSL sampling locations, and terrace designations at the Greenstone River fan. See Fig. 2.1 for location reference.

A numerical test for offset, tilt, and quality of correlation between sites was conducted. Input data are the step functions derived from PDFs of terrace elevations. The cross-correlation 'score' is the sliding dot product of two discrete functions, f and g:

$$(f \star g)[n] \stackrel{\text{def}}{=} \sum_{m=-\infty}^{\infty} f^*[m]g[m+n] = F^* \cdot G \qquad \textit{(Eqn. 2.1)}$$

where the cross-correlation $(f \star g)$ at an 'elevation shift' n is defined as the sum of the products at all values within the functions of the complex conjugate of f (f^*) and g. The formula slides the function g along the x-axis summing the product between it and values in f^*. At elevation shifts where 'peaks' and 'troughs' in the two functions align, the cross-correlation is at a maximum. It is equivalent to the product of the Fourier transforms of the two functions, F^* and G, which is used for computational purposes (e.g. Kammler 2007). I calculate cross-correlation in discrete elevation windows to find the maximum value over a range of possible elevation shifts (i.e. offsets between two flights of terraces) (Appendix 2). The result is an objective identification of correlative shorelines between two sites and the amount of offset between them.

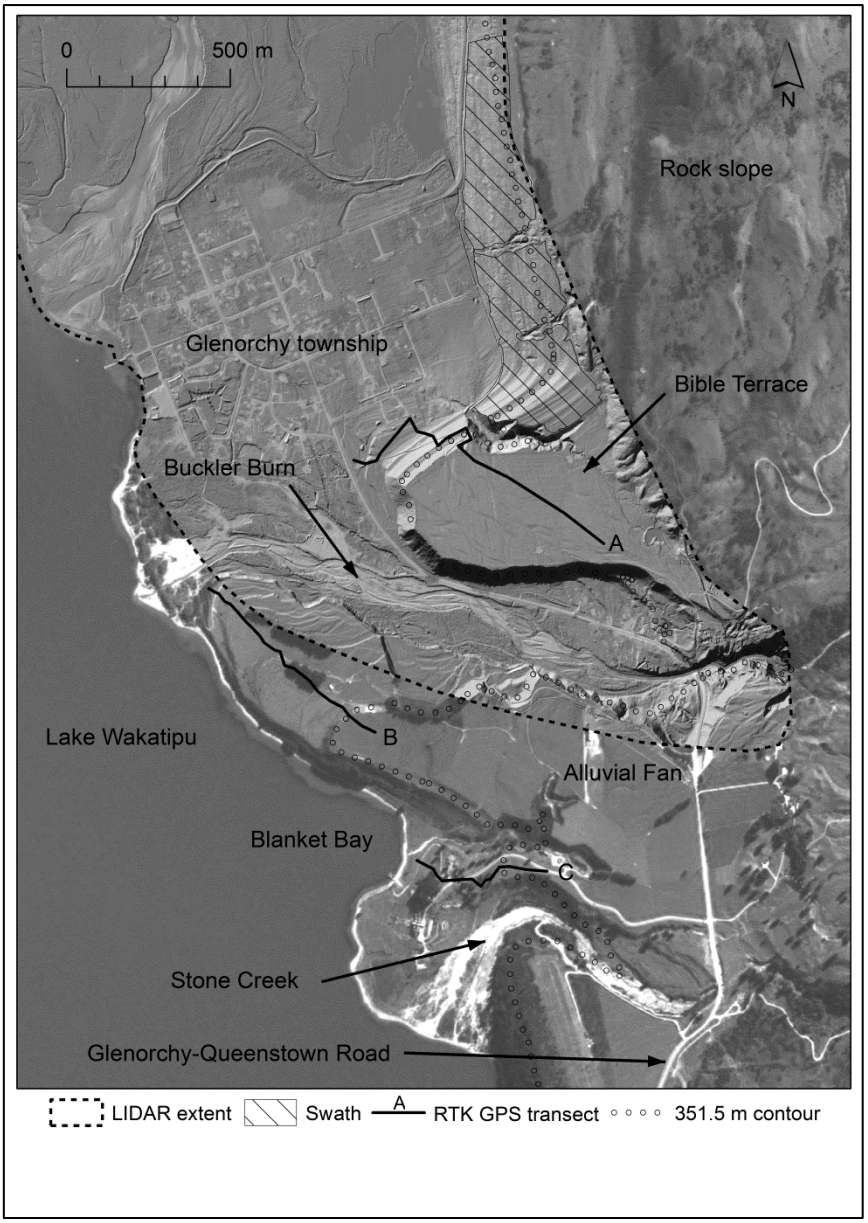

Figure 2.6: SPOT imagery, LiDAR and RTK GPS data collected at Bible Terrace and Blanket Bay. See Fig. 2.1 for location reference.

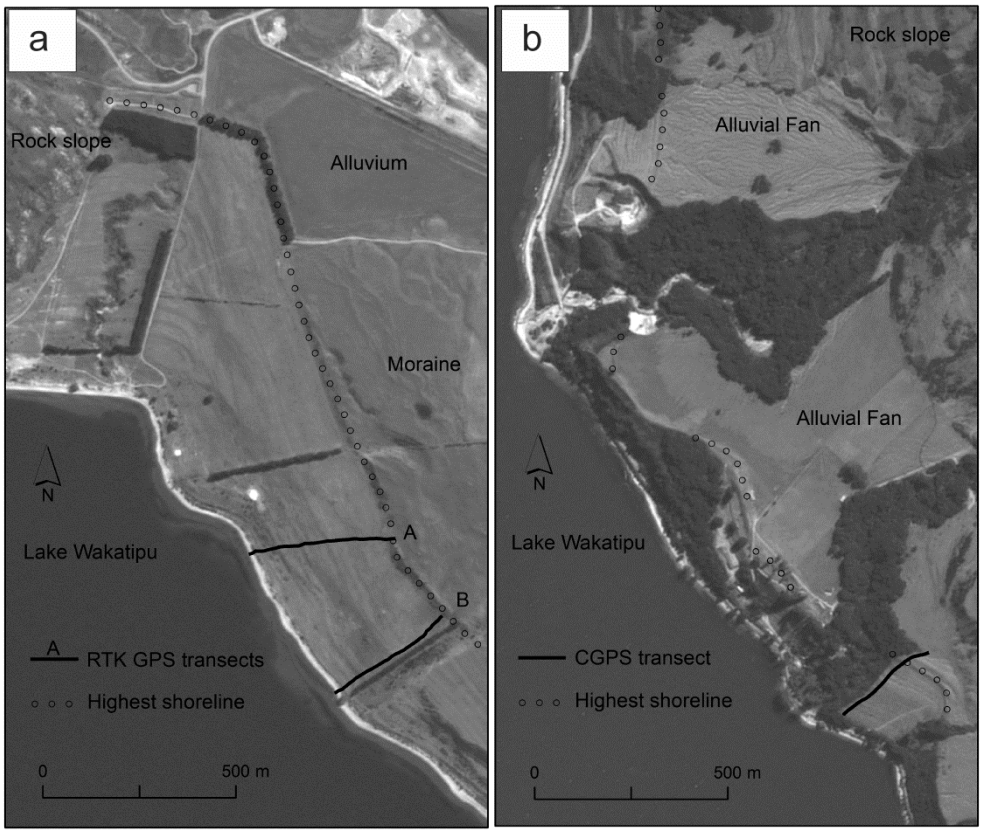

Figure 2.7: SPOT imagery Jack's Point and Meicklejohns Bay a) SPOT imagery, RTK GPS transects at Jack's Point and; b) dGPS transects and spot height at Meiklejohns Bay. dGPS at Jack's Point is overlapped by RTK transect. See Fig. 2.1 for location reference.

2.4.4 Shoreline ages

To obtain age control for the shorelines I used the exposure-age of surface clast populations on river terraces via SHD (Stahl et al. 2013; Chapter 1). SH R-value tests rock hardness by measuring the percentage rebound of a hammer mass in a controlled impact against the surface. Clasts that have been weathering at the surface for a long period of time have lower mechanical strength, and thus lower R-values, than clasts that have only recently been exposed. With some numerical age control, a chronofunction relating SH R-value to exposure-age can be constructed and used to obtain independent exposure-ages of alluvial terraces (Eqn. 1.1)

The Greenstone River fan (Fig. 2.5) was selected for sampling because river terraces are well-preserved and contain greywacke sandstone clasts suitable for SHD in New Zealand. A clast count (n =125) of the modern river floodplain gave an 80% relative abundance of greywacke sandstone. Clasts of other lithologies were avoided in the SH sampling; however, misidentification of clast lithology in the field may have contributed to some age error. The methodology for data collection followed that of Stahl et al. (2013), testing 50 - 100 boulders per surface.

Lithic content of the surface clasts, identified as Momus Sandstone subgroup of Caples terrane greywacke, can range from 35-78% (Turnbull 1980). I use the minimum value of 35% because the modal value and higher (50-78%) yields results inconsistent with absolute dating. A range of *a*-values were then calculated from regressions with modified chemical weathering rates (Fig. 1.5C & 2.8).

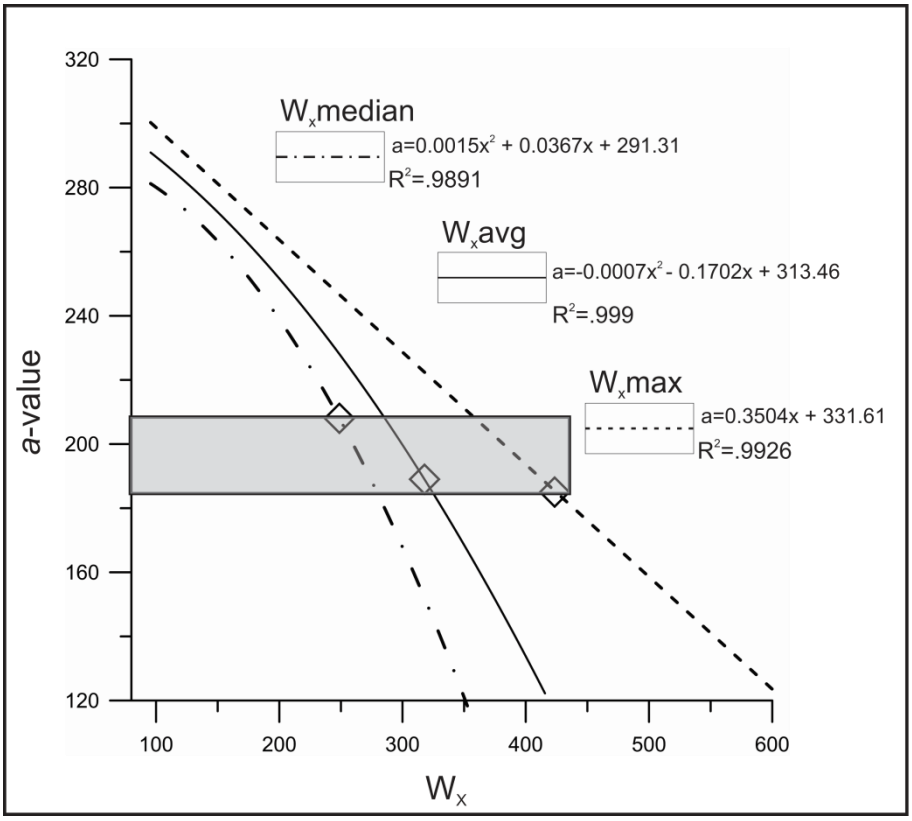

Figure 2.8: Range of SHD a-values for the study site (open diamonds) calculated from empirical relationships (lines) with modified chemical weathering rate (Wx), as defined in Stahl et al. (2013). The a-values derived for different values of Wx are: Wx weighted average = 188.6; Wx median = 207.5; and Wx maximum = 185.2.

To calculate exposure ages and associated errors, I modify the simple age calculation of Stahl et al. (2013) (Eqn. 1.1) to incorporate terrace order, known age constraints and error arising from selection of *a*-values. The algorithm describing this process is illustrated in Fig. 2.9. The programme uses Monte Carlo rejection sampling to reduce the error in the R-value dataset based on terrace chronology. In each iteration, 'final' R-values are accepted only if each sampled R-value obeys the known terrace order, so that all PDFs are constrained simultaneously. A uniform distribution over the possible range of *a*-values (grey box, Fig. 2.8) was used to incorporate inherent uncertainty in its selection. Age distributions were then calculated as in Eqn. 1.1, using distributions of *a*-values and R-value medians (SH_R) assembled from > 100,000 trials.

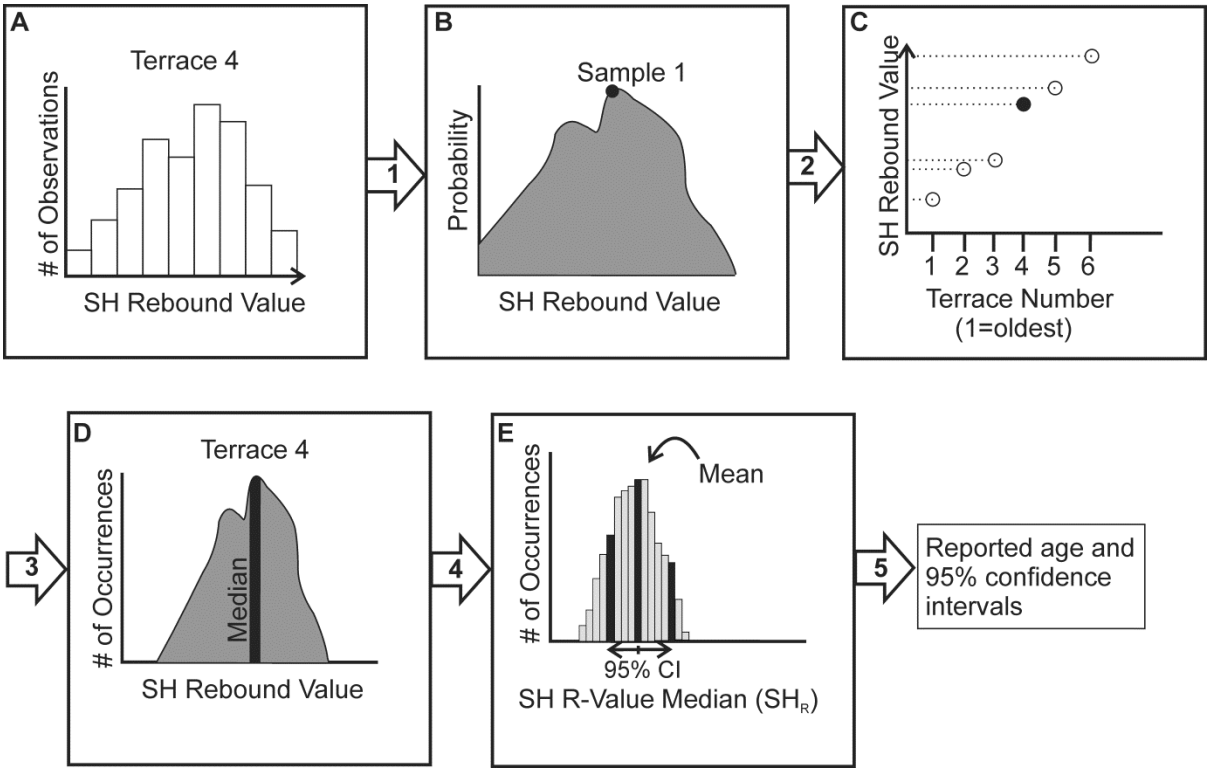

Figure 2.9: Algorithm to calculate SH exposure-age and error using Monte-Carlo rejection sampling : Step 1: Conversion of raw histogram of SH values (A) to a probability distribution (B); Step 2: Random sample selection from B, checked against acceptance/ rejection criteria from known terrace order and absolute age constraints (C); Step 3: Accepted data used to populate a new distribution (D); Step 4: Median of (D) selected over 100,000 trials and used to produce a final distribution (E); Step 5: Calculation of SH exposure age statistics based on distribution (E).

Age control was achieved using optically stimulated luminescence (OSL) ages for three samples collected from deltaic and alluvial terrace sediments at the Greenstone River fan (Fig. 2.5) as well as pre-existing radiocarbon ages. Two OSL samples were taken from a road-cut outcrop beneath T9 (Fig. 2.5 & 2.10). The sediments in this outcrop were interpreted to represent the progression of the Greenstone River delta into Lake Wakatipu, and the subsequent erosion and formation of T9. The 25° dipping gravels, silt and sand lenses exposed at the base of the outcrop are foreset beds deposited during the initial outbuilding and aggradation of the Greenstone River delta into a young Lake Wakatipu (Fig. 2.10a). A medium-grained sand bed 2.2 m below the ground surface and within the foreset beds was selected for sampling (Fig. 2.10b). The age of this sample provides a minimum age for the presence of Lake Wakatipu (i.e. a water body into which the foreset beds were deposited), and a maximum age for the highest preserved terrace at the site (T1).

At the top of the foresets there is a sharp angular unconformity, above which rests a veneer of well-rounded and imbricated gravels (Fig. 2.10a). I interpreted this unconformity and deposition of gravels to have formed from incision of the Greenstone River into its former delta after lake levels

dropped. Disk-shaped (‘platy’) clasts in interbedded gravel and sands lying immediately above the boulder lag and a prominent beach ridge along the outer edge of the T9 tread (Fig. 2.5) confirm that river incision, transitioning to a lake interface, is the most likely mode of deposition. An OSL sample was taken from a sand lens above the boulder lag (Fig. 2.10b) and is representative of the age of abandonment (and thus equivalent to exposure age) of the T9 terrace surface.

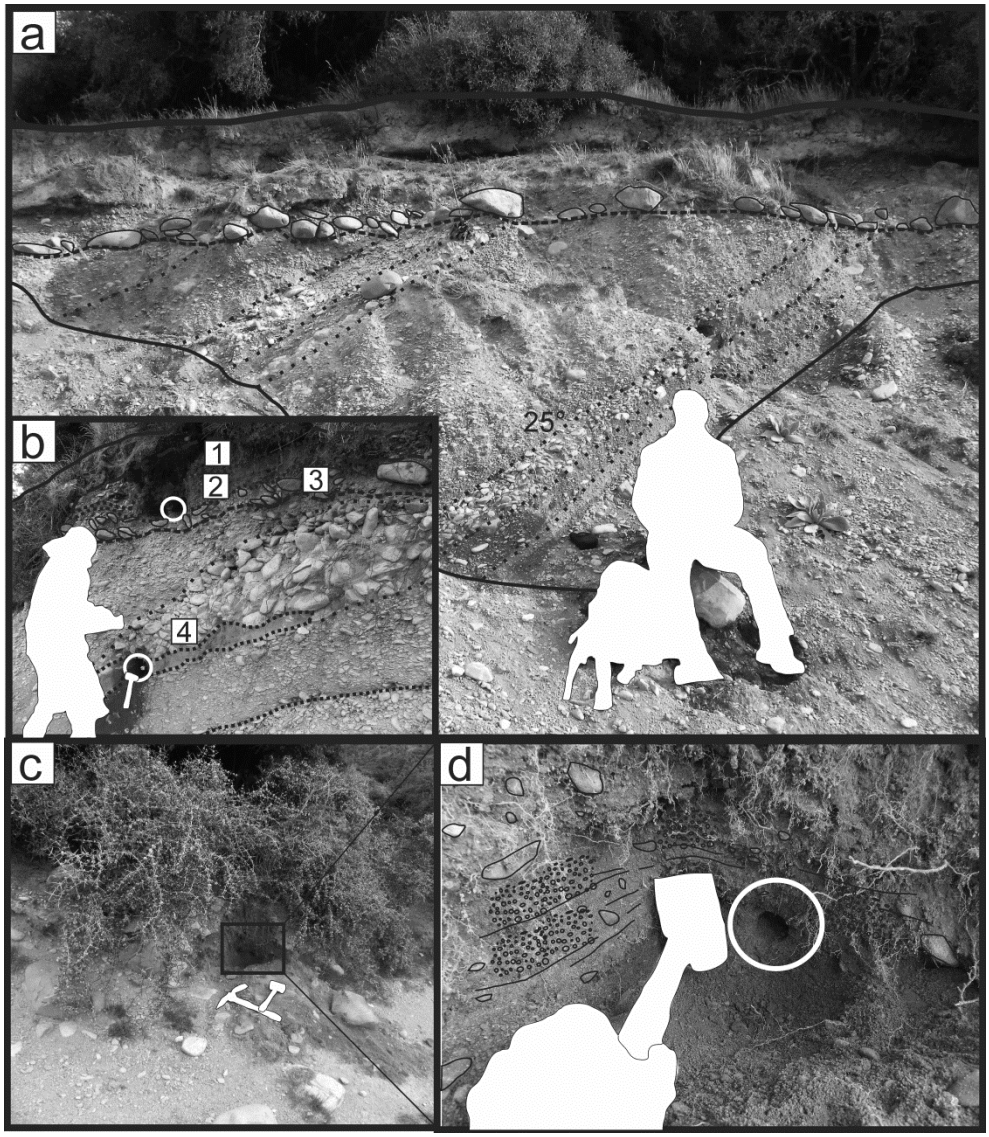

Figure 2.10: OSL sampling locations at the Greenstone River fan. (a) Dipping fan-delta deposits overlain by a degradational boulder-lag deposited during incision of the Greenstone River into its fan. (b) Location of OSL samples and local stratigraphy: (1) Beach gravels, (2) Fluvial sand (Sample WLL1077), (3) Coarse boulder lag, (4) Deltaic gravels and sands (Sample WLL1078). (c) and (d) Location of Sample WLL1079 in deltaic sands and gravels.

A third OSL sample was taken from a smaller road-cut through the riser between T7 and T6 (Fig. 2.10c, d). From the depth beneath the T6 tread (2.75 m), it is inferred that the coarse sands sampled date the initial delta and not the subsequent formation of the terrace. A radiocarbon age of

8930 ± 91 years BP (9734-10277 cal. BP, using CALIB 7.0 and SHCal13 of Hogg et al. 2013) was obtained by Bell (1992) for wood found in lake sediments below a shoreline near Queenstown at the equivalent T6 elevation (+ 26 m lake level) and is used here as a maximum age for the T6 surface.

The OSL samples were processed at Victoria University of Wellington using Multiple Aliquot Additive Dose (MAAD) and Single Aliquot Regenerative Dose (SAR) methods on fine grained (4-11 μm) feldspar. Additionally, the SAR method was used on two of the samples with coarse-grained (125-200 μm) quartz.

Numerical ages and adjusted chemical weathering rates were used to constrain the *a*-value for SHD in Eqn. 1.1.

2.5 Results

2.5.1 Shoreline correlations

Fig. 2.11 shows the results of correlating shorelines of equal elevation at 7 sites around Lake Wakatipu (site locations given in Fig. 2.1). Where two methods were used to survey shorelines, two columns of data points are shown at the site. Methods with close point spacing (LiDAR and dGPS) were typically more useful in detecting subtle changes in slope at terraces, though RTK surveying is considered more reliable than dGPS. Correlations were drawn by extending horizontal boxes around points of similar elevation, and terrace numbers are assigned according to the order at the Greenstone River fan.

The prominent high-stand shoreline is present at c. 351.5 m at 6 of the 7 survey sites. Additionally, it is seen, cut mostly into bedrock, in the LiDAR data at Queenstown/Frankton (Fig. 2.4) at an average elevation of 351.3 m (δ=0.8 m). At Jack's Point, the only site where the prominent shoreline was not easily identified at c. 351.5 m, a surface of 3-4 m higher was measured (shown by the highest elevation points in Fig. 2.11 for profiles G and H). This could be a result of relative uplift of the shorelines there. However, given that it is the only site where the prominent shoreline is significantly different and the prominent shoreline is observed at c. 351.3 m in the LiDAR data at nearby Frankton (Fig. 2.4), a more likely explanation is that the elevation selected to represent this shoreline at Jack's Point is unreliable. At this location the inner most edge may not adequately represent the shoreline elevation because of moraine sediment re-deposited at the base of the large scarp or accumulation of beach gravels deposited by wave action. A position closer to the presumed outer edge of the shoreline at this site is thus considered to give a more representative shoreline elevation, and gives an elevation of c. 352 ± 1 m. Therefore, while uncertain, the elevation of the

prominent shoreline at Jack's Point is probably consistent with the 6 other surveyed sites and elsewhere along the lake.

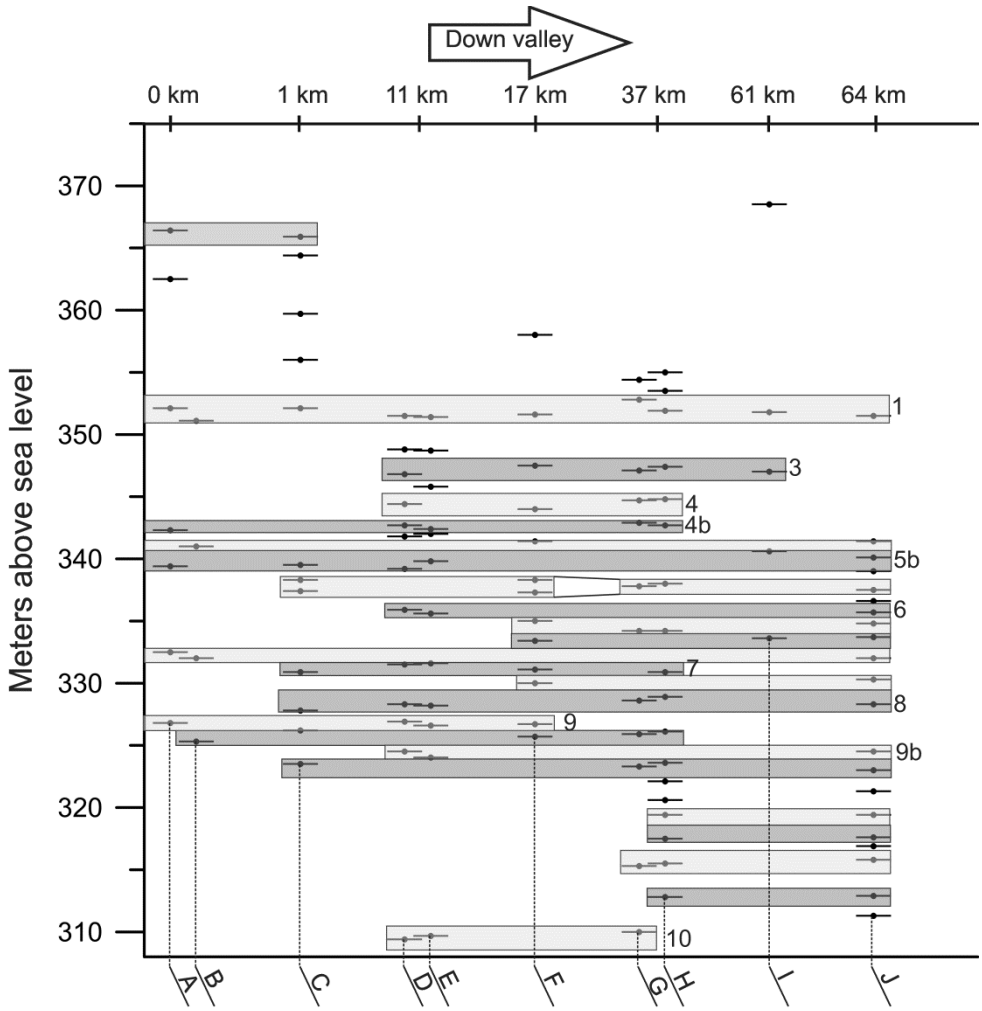

Figure 2.11: Correlation of shorelines for all study sites and survey methods. (A) Bible Terrace LiDAR; (B) Bible Terrace RTK; (C) Blanket Bay RTK; (D) Greenstone fan RTK; (E) Greenstone fan dGPS; (F) Meiklejohns Bay dGPS; (G) Jack's Point RTK; (H) Jack's Point RTK; (H) Jack's Point dGPS; (I) Glen Nevis RTK; (J) Kingston LiDAR. Data point symbols are flat for visualisation, and do not represent any form of error.

Site-to-site correlations are shown in Fig. 2.11 with terrace number labelling given in reference to the Greenstone River terraces (Fig. 2.5). Flat-lying correlation 'envelopes' can explain correlation of 95 (82%) of the shorelines surfaces identified (including surfaces identified from all three surveying methods). The majority (58%) of shoreline correlation envelopes include shoreline surfaces from three or more sites. However, this percentage increases to 74% if the lowest 5 envelopes are excluded; preservation of the youngest shorelines is generally restricted to just two sites where data are not made unreliable by anthropogenic modification and where shoreline formation was more favourable (i.e. eroded into finer materials).

Higher surfaces at several sites (Fig. 2.11) are present above the most prominent shoreline but there are no grounds for correlation of any of these surfaces based on the method of correlation used. These surfaces could possibly be older shorelines that formed during a short-lived higher lake level (possibly of a proto-Lake Wakatipu), but resemble fluvial terraces, fan surfaces and kame terraces and are thus more likely to be non-lacustrine in origin.

2.5.2 Quantitative identification and correlation of shorelines

Elevations selected from survey data (Section 2.4.1) and those from the automated process were plotted against each other (Fig. 2.12). Any large differences in the two datasets should result in deviation from a slope of 1 and/or scatter about a best-fitting line. Terrace elevations were taken from the centre point of the step function at each terrace (Fig. 2.13). Some terraces found in the automated process were not found in the subjective selection and vice-versa. While some 'steps' were found to encompass several more discrete peaks in the PDFs (i.e. small breaks in slope beneath the selection threshold), Fig. 2.12 shows that the terraces identified from the two different methodologies plot on a line with a slope of 1 with an R^2 of 0.99. Thus, while some terraces are grouped together in the automated process, the best defined shorelines at each site are comparable to my field-based interpretations (Fig. 2.11). At Kingston and Glenorchy, the resolution of terrace identification is compromised by the use of swaths (for numerical analysis) and profiles (for field-based analysis), but prominent shorelines are at equivalent elevations.

The results of cross-correlating shorelines for LiDAR swaths at Bible Terrace/Kingston and dGPS profiles at Meiklejohns Bay/Jack's Points are shown in Fig. 2.14a and b, respectively. Both show the strongest correlations at the elevations of the best-defined, overlapping terraces and an elevation shift of zero. The alignment of these correlations suggests that there are no identifiable offsets between the two datasets in each test. The highest terraces in each test show possible (but weakly supported) 2-3 m uplift of Bible Terrace relative to Kingston and 3-5 m uplift of Jack's Point relative to Meiklejohns Bay (orange outlines). Because the cross-correlation is restricted by the common elevation range of the two datasets being compared, it is unknown if these offsets are real or isolated artefacts (discussed fully in Appendix 2). A larger range of common elevations would allow a pattern of offset terraces to be detected. However, an offset of zero is consistent with my interpretations over the entire elevation range, and particularly for the prominent high-stand surface, which makes these apparent offsets likely to be artefacts.

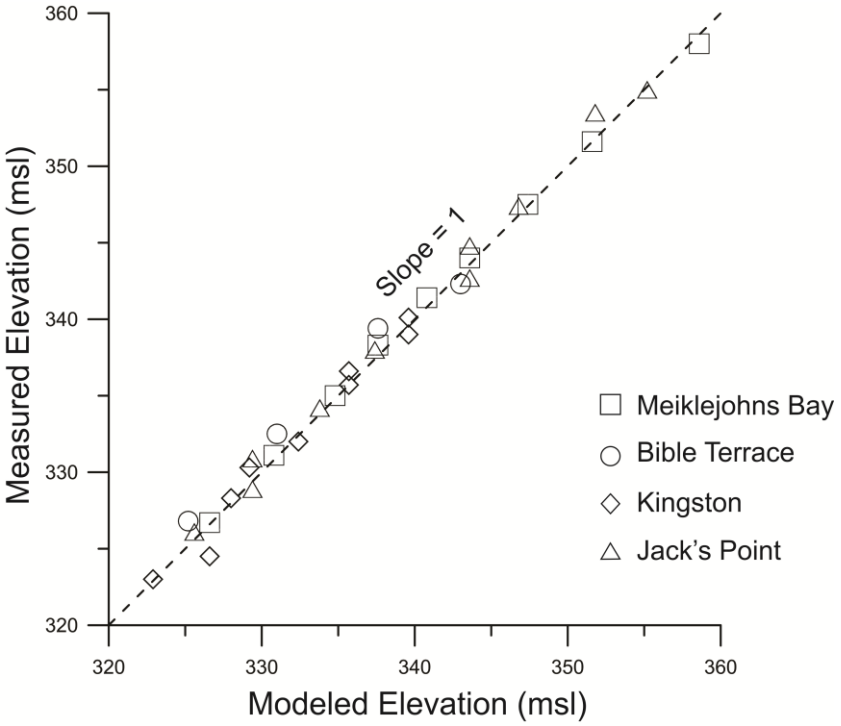

Figure 2.12: Measured vs. modelled shoreline elevations for each site used in the cross-correlation analysis.

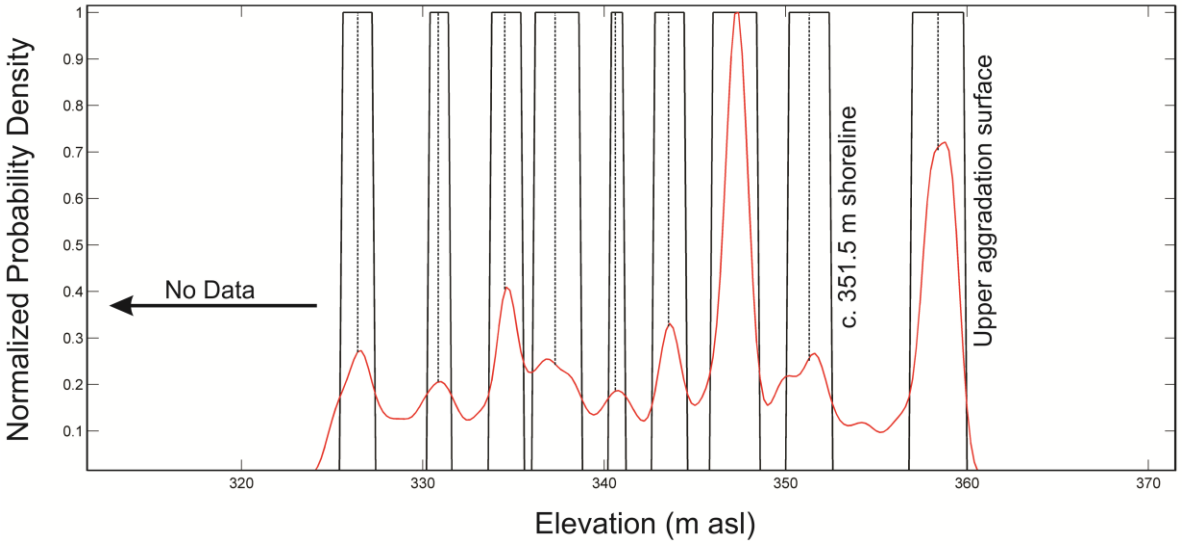

Figure 2.13: Elevation PDF and corresponding step function for Meiklejohns Bay. See Section 2.9 (Appendix 2) for algorithm details.

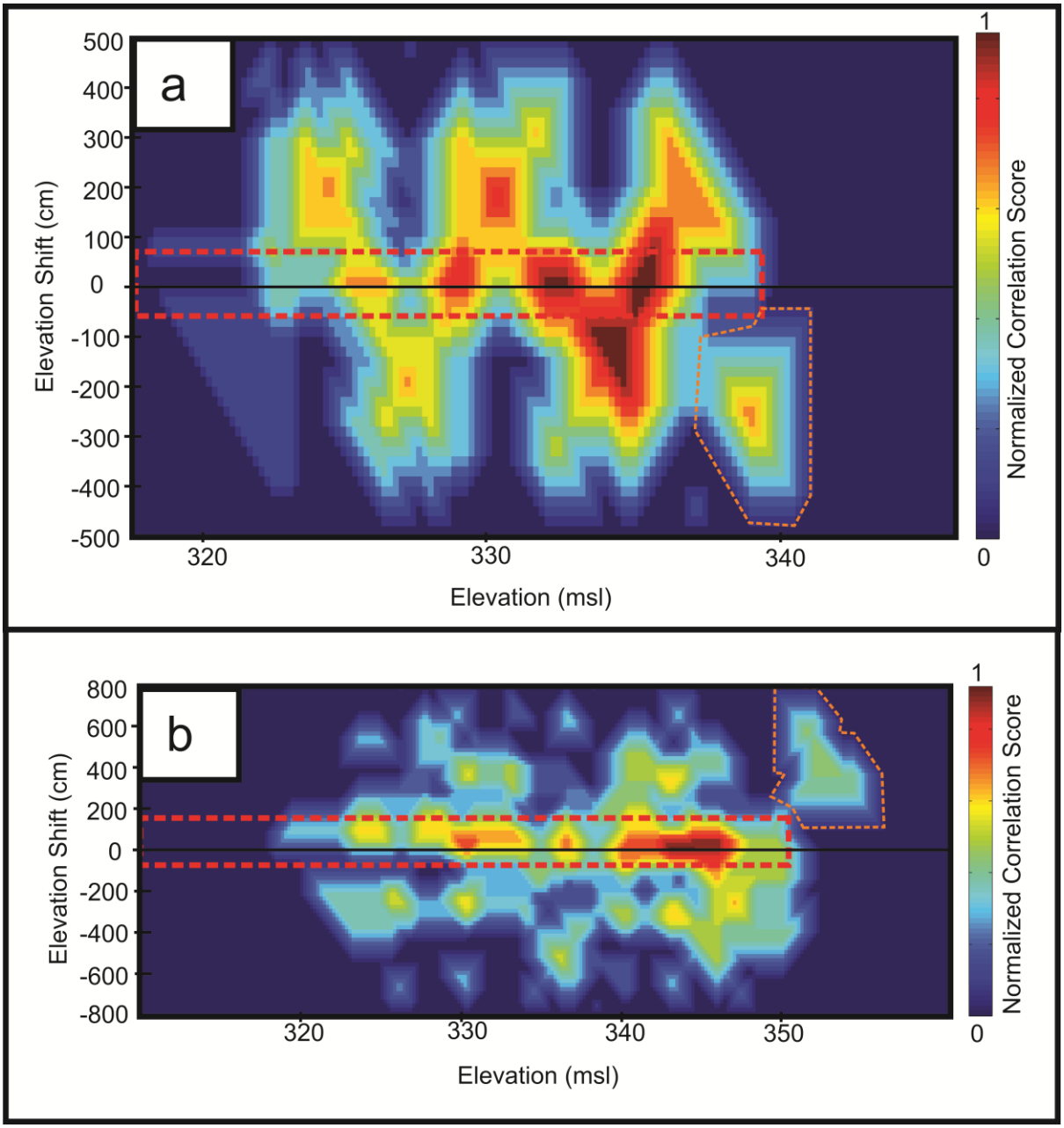

Figure 2.14: Cross-correlation plots for four study sites. a) Cross-correlation plot for Kingston and Bible Terrace LiDAR swaths. b) Cross-correlation plot for Jack's Point and Meiklejohns Bay dGPS transects. Clusters of high correlations at known terrace elevations and at zero elevation shift indicate that a lack of tilt/offset is likely.

2.5.3 Ages of Greenstone River terraces

Five ages are reported for the three OSL samples from the Greenstone River terraces (Table 2.1). Ages for sample WLL1077 (Terrace 9 sand lens) yield results inconsistent with the stratigraphy and known age constraints from the glacial history of the region. Both $WLL1077_{MAAD}$ (feldspar) and $WLL1077_{SAR}$ (quartz) are older than the respective, underlying ages for WLL1078 (fan delta deposits). Furthermore, the MAAD (feldspar) derived age is older than the deglaciation of the Wakatipu valley during the LGM and is inconsistent with the glacial chronology at other central

Otago sites (McKellar 1960; Barrell 2011). Incomplete bleaching of fan delta sediments would explain these older ages, as has been observed in cut-in-fill terrace deposits elsewhere in New Zealand (Little et al. 2010). For these reasons, as well as known difficulties with quartz luminescence in New Zealand (e.g. Preusser et al. 2006), I reject the MAAD OSL age for T9 and SAR (quartz) ages for T9 and the fan delta. The remaining two ages, $WLL1078_{MAAD}$ (16.3 ± 3.4 ka) and $WLL1079_{SAR}$ (17.8 ± 2.2 ka), both date fan sediments, are consistent with the regional geomorphic framework, and have overlapping age errors. As such, I accept the weighted mean of the two (17.1 ± 2.6 ka) as representative of the maximum age for initiation of terrace formation and minimum age for the presence of Lake Wakatipu at the Greenstone River.

Table 2.1: OSL results from the Greenstone River fan.

Sample Number*	*a* value	D_e[†] (Gy)	dD/dt[§] (Gy/ka)	OSL Age (MAAD)	OSL Age (SAR)
WLL1077	0.06 ± 0.03	63.41 ± 5.58	2.64 ± 0.21	24.0 ± 2.8 ka	--
WLL1077 [Quartz]	--	30.21 ± 1.98	2.27 ± 0.07	--	13.3 ± 1.0 ka
WLL1078	0.06 ± 0.03	46.42 ± 8.94	2.85 ± 0.22	**16.3 ± 3.4 ka**	--
WLL1078 [Quartz]	--	29.12 ± 1.34	2.45 ± 0.07	--	11.9 ± 0.7 ka
WLL1079	0.06 ± 0.03	45.07 ± 4.35	2.54 ± 0.21	--	**17.8 ± 2.2 ka**

*Sample preparation and measurements performed at School of Earth Sciences, Victoria University of Wellington, Wellington, NZ

[†]Equivalent dose

[§]Doserate.

MAAD: Multiple Aliquot Additive Dose method; SAR: Single Aliquot Regenerative Dose method.

Table 2.1(continued)

Sample Number*	Deposit	dD_c/dt (Gy/ka)[§]	Water Content (%)	K (%)	U (ppm) from ^{234}Th	U (ppm) from ^{226}Ra, ^{214}Pb, ^{214}Bi	U (ppm) from ^{210}Pb	Th (ppm) from ^{208}Tl, ^{212}Pb, ^{228}Ac
WLL1077	T9 sand lens	0.2002 ± 0.0100	13.7	1.44 ± 0.03	1.68 ± 0.19	1.59 ± 0.12	1.5 ± 0.16	6.21 ± 0.09
WLL1078	delta sand	0.1631 ± 0.0082	7.8	1.54 ± 0.04	**1.97** ± 0.24	1.58 ± 0.15	1.71 ± 0.20	6.08 ± 0.10
WLL1079	delta sand	0.2038 ± 0.0102	13.4	1.33 ± 0.03	1.54 ± 0.24	**1.58** ± 0.15	**1.55** ± 0.20	**6.05** ± 0.11

*Sample preparation and measurements performed at School of Earth Sciences, Victoria University of Wellington, Wellington, NZ

[§]Contribution of cosmic radiation to the total doserate.

Age control points, SH_R, and SH exposure ages are listed in Table 2.2. The results indicate a general decrease in exposure age with decreasing elevation. Errors of c. 35% of the surface age (2σ) are higher than reported in Stahl et al. (2013) and are most likely due to error in predicting *a*-value, lithologic mixing and recent ploughing of the terrace treads for grazing. Two terraces (T4b and T7) do not conform to the constant river down-cutting model and terrace order. Overlapping age errors with the next youngest terrace imply that this discrepancy is attributable to the factors listed above.

Table 2.2: SHD parameters and ages from the Greenstone River fan.

Terrace	Age control	Bootstrapped SH_R	SH Exposure Age (ka) (2σ)
3	<17.1 ± 2.6 ka	34.4	10.0 ± 3.7
4b	< T3	37.8	6.2 ± 2.3
5b	<T4b	37.6	6.3 ±2.3
6	<9.7-10.2 ka	41.2	3.8 ± 1.4
7	<T6	47.2	2.0 ± 0.8
8	<T7	45.3	2.2 ± 0.8
9	<T8	46.3	2.2 ±0.8
10	<T9	55.9	0.8 ± 0.3

2.6 Discussion

2.6.1 Lake level changes and shoreline development

The age data presented here for the formation of the Greenstone River delta and the terraces have provided improved information about the timing of changes in the level of Lake Wakatipu. My reconstruction is presented in Fig. 2.15 and updates that of Thomson (1996). The results show that Lake Wakatipu had formed by c. 17 ka, which implies a rapid retreat of the glacier from its Kingston terminal position at the LGM. The timing of this retreat is consistent with other deglaciation evidence from New Zealand (Barrell 2011) and the rapidity of the retreat is consistent with calving glacier retreat through a glacially deepened trough (Cook and Swift 2012). The level of Lake Wakatipu is thought to have been controlled by the height of the outlet at Kingston (presently c. 352 m) and maintained at this level sufficiently long for the formation of the prominent high-stand shoreline, which in places is cut into bedrock. Abandonment of the equal elevation high-stand shoreline and lake outlet at Kingston must have occurred simultaneously when drainage of Lake Wakatipu was captured by the Kawarau River (Thomson 1996).

The dates indicate that lowering of the lake proceeded after the capture event, lowering 20 m over 10 ka. The possibility of large lake level fluctuations between shoreline forming episodes cannot be dismissed, but I consider this unlikely given the seemingly stable average rate at which the lake has dropped over c. 13 to 2 ka (Fig. 2.15). A tentative age of 13.0 ± 2 ka is assigned for the abandonment of the 351.5 m surface by projecting back a constant rate of lowering from the age of T3 to c. 12 ka and via correlation with a late to post-LGM sediment flux observed elsewhere in the Southern Alps (Alloway et al. 2007).

From an elevation of 327 m at 2.2 ka, there was a more rapid drop to c. 305 m before levels rose by several metres within the last c. 0.5 ka. This apparent rapid lowering is supported with geomorphic evidence: few shorelines are preserved below 325 m except at sites with an abundance of fine-grained beach gravels (i.e. where shorelines were more likely to be preserved during short lake still-stands). The reason for the rapid lowering in the last 2 ka is unknown.

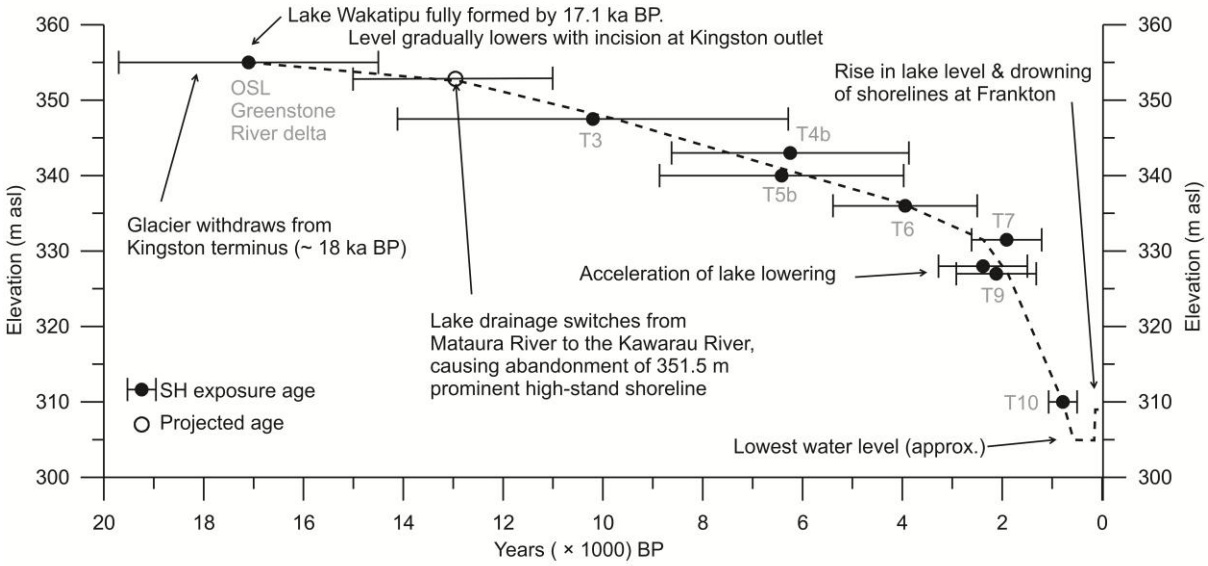

Figure 2.15: Lake level reconstruction for Lake Wakatipu based on elevations and SH exposure-ages for Greenstone River terraces.

The most likely cause for the more recent increase in lake level is thought to be a landslide in the Kawarau gorge, although other possibilities including progradation of the Shotover Delta and uplift on the hanging wall Nevis-Cardrona Fault have also been considered (Thomson 1985). The age I loosely assign for this drowning event is within the last 500 years, following the assumption that it post-dates T10 (777 ± 280 years ago) at the Greenstone River by several hundred years. However, it is possible that T10 is younger than the lowest (drowned) shorelines seen at the Frankton Arm; that is, it

could be that the highest lake level was attained in the drowning event, and T10 has been abandoned following subsequent lowering.

2.6.2 Tilting and offset

No tilt or offset can be detected in the survey data at the sites examined along the length of Lake Wakatipu (Fig. 2.11 & 2.14). The well-defined and widespread high-stand terrace (T1) is at a height of 351.5 m (δ=0.8) at most locations. The elevation for this most accurately represents the elevation of the lake prior to abandonment of this surface, which is likely to have occurred around c. 13 ka. Prior to abandonment, it is possible that lake basin underwent tilting, which may not be recorded in the shoreline elevation. However, I consider this unlikely because the 351.5 m shoreline is well-defined at most locations around the lake, even in locations where it is etched into bedrock, suggesting a stable lake still-stand of considerably long duration. The stated error for the 351.5 m surface (δ=0.8 m) can be explained by error in selection of the elevation representative of mean lake level from site to site, and actual differences in mean lake level due to differences in wave-directions, wind loading, and seiching. Because the high-stand terrace does not show detectable deformation, correlations below the prominent high-stand shoreline are more confidently drawn. It is recognised that if the 351.5 m shoreline is misidentified at a site, the closely-spaced correlations below 351.5 m in Fig. 2.11 could occur by chance.

The cross-correlation (Fig. 2.14) supplemented my field-based correlation by providing a numerical basis for identifying deformation (or lack thereof). A search window of 5-8 m was specified, as this is the likely range of offset for the ages I obtained for the Holocene shorelines, given the likely range of regional uplift rates and recurrence interval of the MFZ (Beavan and Haines 2001; Wallace et al. 2007; Stirling et al. 2012). Larger windows unnecessarily increase the error and incidence of artefacts in the cross-correlation. The resolution of this technique seems to be ±1 m based on tests of surfaces with known offsets (Appendix 2). Therefore, I can rule out deformation of the sequence of shorelines since the early Holocene, even if the interpretation of the 351.5 m surface at each site is incorrect. However, this is unlikely given geomorphic evidence and the consistent elevation of the 351.5 m surface.

The lack of differential uplift of Wakatipu shorelines contradicts previous observations by Wellman (1979) of both tilting and fault activity in the basin. Though Wellman (1979) was not explicit on the magnitude of offset, the results show that over the last c. 13 ka (and probably 12-17 ka), no uplift about a NE-SW axis has occurred. It is possible that older, local high-stand terraces record an uplift signal, but in this study it has not been possible to correlate these isolated surfaces with others along the lake. As probable kame terraces and dissected fan surfaces, they are unlikely to reliably record a basin-wide base level for elevation comparison between sites. However, if these

older surfaces do record a glacial rebound signal, it would imply that all of the rebound response occurred during and within the 1-5 ka following glacial unloading. I suggest that it is more probable that the ice volume and distribution was insufficient to induce differential uplift of the shorelines from NW to SE. The possibility of broad or uniform uplift with a gradient below the resolution resolvable by this study cannot be dismissed.

Lake basins in different tectonic settings in the central South Island for which Wellman (1979) also measured tilting warrant further examination to check whether or not this tilting is demonstrable. Similar approaches to that taken here could be used to quantify the magnitude and rates of tilting (if present) and explore whether there is a gradual decay in uplift rates with time (i.e. a glacial-rebound signal) or with away from the Alpine Fault.

2.6.3 Implications for regional tectonics and earthquake hazards

In the absence of differential isostatic rebound, undeformed lake shorelines offer insights into the tectonics and paleoseismicity of the region. It is not surprising that uplift due to coupling on the Alpine Fault is not expressed at the surface as is measured in the central South Island; coseismic and interseismic off-fault deformation is almost purely plate-parallel in the SW (Norris and Cooper 2001; Berryman et al. 2002; Sutherland et al. 2006). Nonetheless, GPS and mechanical models predict shortening, uplift and uplift gradients east of the Main Divide in Otago (Upton and Koons 2007; Wallace et al. 2007; Upton et al. 2009). Wellman (1979) suggested that uplift in the region is largely controlled by the Moonlight Fault, and that shorelines on the south side of the lake record progressive faulting. If even a tenth of the modelled 2-4 mm yr^{-1} of uplift (Upton et al. 2009) or 1 mm yr^{-1} shortening across the MFZ (Wallace et al. 2007) was occurring, greater than 10 m metres of differential uplift should be observed across Lake Wakatipu since the LGM.

Fault-normal distances of two of the sites in this study, Meiklejohns Bay (10 km to the NW) and Jack's Point (14 km to the SE), both on the 'west-up' side of Lake Wakatipu, are short enough that significant permanent uplift, interseismic elastic strain, or asesimic folding on the Moonlight Fault should be evident. By the same argument, the Nevis-Cardrona Fault, with known <18 ka offsets (Beanland and Barrow-Hurlbert 1988), should show a discernible pattern of uplift-tapering towards the north of the lake (i.e. away from the fault plane on the hanging wall). To consider these two scenarios, I compiled uplift curves for thrust/reverse faulting events from three historical thrust-reverse fault earthquakes: the Kern County earthquake in California (White Wolf Fault), Chi-Chi earthquake in Taiwan (Chelungpu Fault) and the Wenchuan earthquake (Pengguan and Beichuan faults). These faults are considered to be representative of the mechanism and lengths of the MFZ and NCF because they are reverse and oblique events on c. 75-200 km faults (Stein and Thatcher 1981; Stein et al. 1988; Leitner et al. 2001, Yu et al. 2001; Caskey and Ramelli 2004; Qi et al. 2011).

Separate best fitting curves for the hanging wall and footwalls were fit to normalised displacement along a transect crossing the fault (Fig. 2.16). For the NCF, cumulative displacements over c.18 ka were taken from the closest point of measurement along the fault to the study site (Beanland and Barrow-Hurlbert 1988). I consider a 1 m displacement at the MFZ as a minimum, conservative estimate considering observed single-event displacements elsewhere in Otago (Beanland and Barrow-Hurlbert 1988; Litchfield and Norris 2000) and the range of shortening rates and recurrence intervals on these faults (Fig. 2.1). If uplift is less than this due to the vergence switch at the lake, this may be an overestimate; however, data from reverse faults elsewhere indicate that slip need not decrease between segments of opposite dip (e.g. Crone et al. 1992).

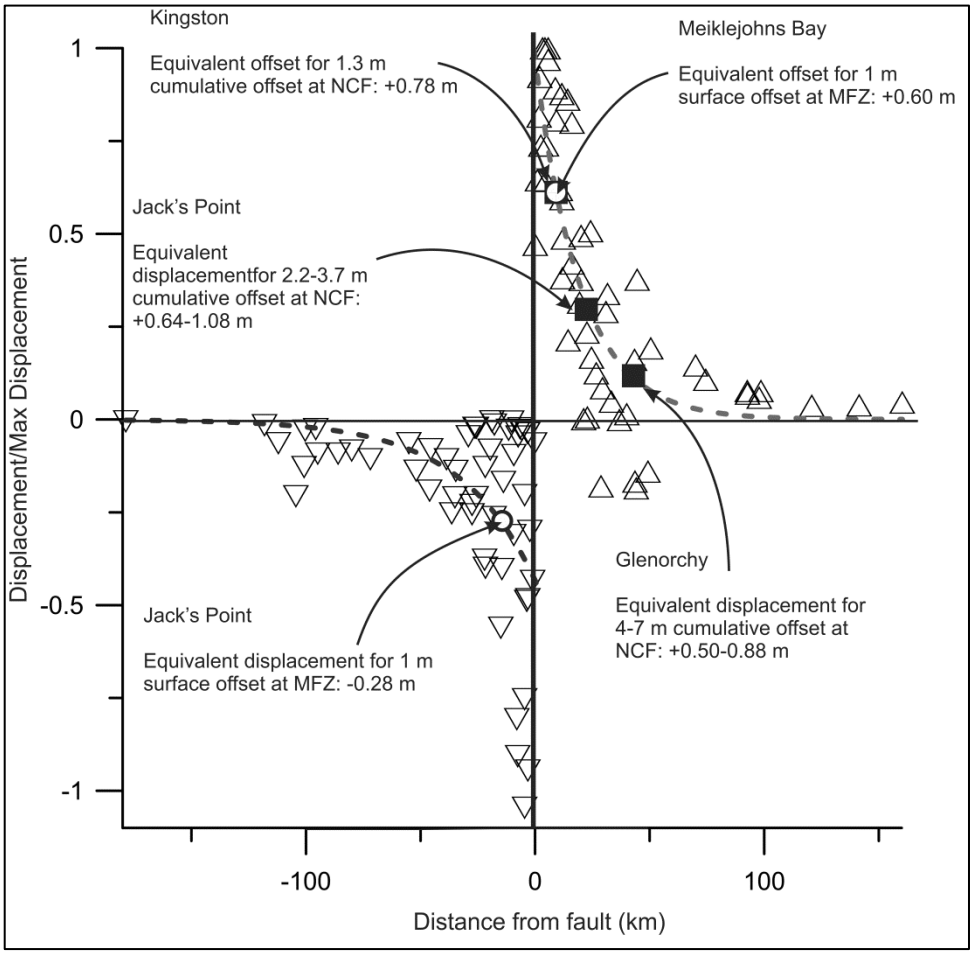

Figure 2.16: Normalised displacement vs. distance from fault for three historical thrust-reverse fault ruptures (Kern County, Chi-Chi and Wenchuan earthquakes, triangles) and faults in the Wakatipu basin. Black and grey dashed lines are the best-fitting curves (exponentials) through data on the foot walls and hanging walls, respectively. Circles and squares mark where sites in this study lie on the best-fitting curve with respect to the Moonlight Fault Zone and Nevis-Cardrona Fault, respectively. Text with arrows show what the displacements would be for each site and fault, relative to an originally horizontal surface.

A 1 m offset on the MFZ should result in c. 90 cm of vertical separation between the two closest sites (Fig. 2.16). There is no evidence of this deformation, and certainly any substantially greater amount of uplift can be ruled out. Even supposing vertical slip rates on the MFZ of some of the slowly uplifting eastern Otago ranges (c. 0.1 mm yr^{-1}, see Fig. 2.1), uplift over 13 ka would be more than that which I test for and should be within the resolution of my shoreline identification.

The lack of differential uplift due to earthquakes on the NCF is also explained through Fig. 2.16. Given the position of the sites along and perpendicular to the fault, there are no significant differences in expected uplift between Kingston, Jack's Point and Glenorchy.

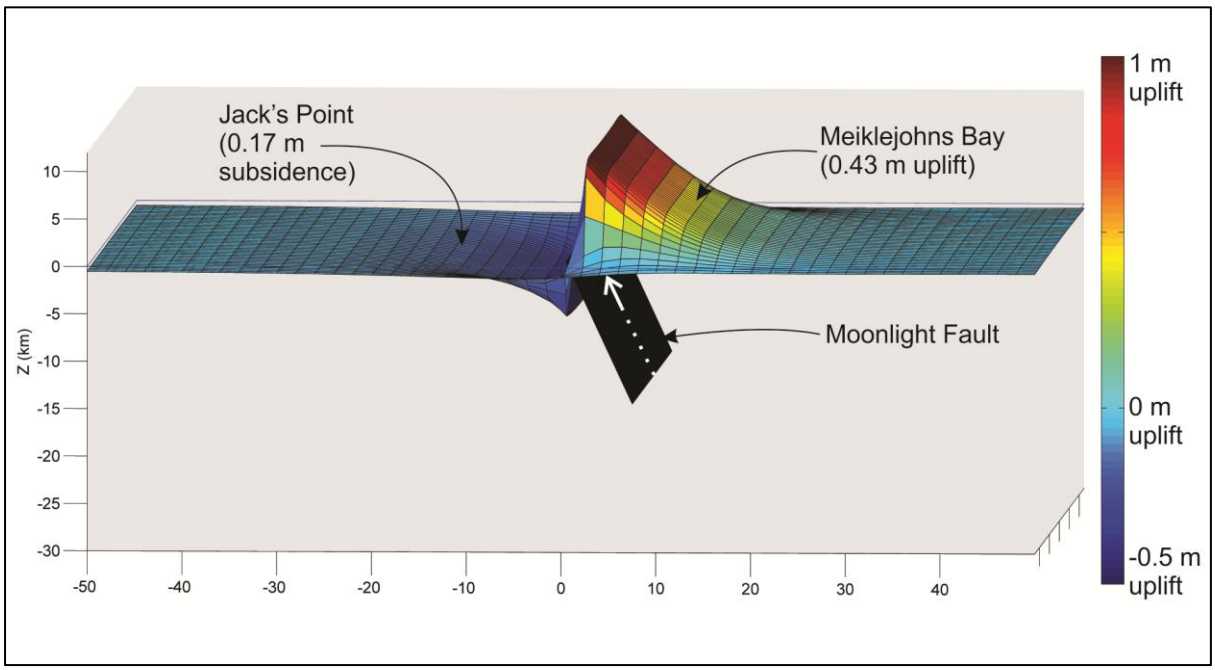

Figure 2.17: Finite element model of displacement on the Moonlight Fault (from Coulomb 3.3). In this model the Moonlight Fault dips at 65° and the fault slips uniformly with 1 m dip slip. Young's modulus= 635000 bar and Poisson's ratio=0.13 (after Brown et al. 1980). The model yields less total displacement (0.6 m) between sites than the empirical model, but is still within the range of detection over two or more earthquake cycles. X and Y axes in km.

Finite element modelling of fault displacement is another approach used to estimate the displacement field associated with an earthquake. Fig. 2.17 shows the results of a simple model constructed to further constrain fault displacement, in case the earthquakes in the empirical model are not representative of earthquakes on the Moonlight Fault. Earthquake displacement, fault dip and sense, coefficient of friction, Young's modulus and Poisson's ratio are specified a priori (Fig. 2.17). The results show a total vertical separation between Meiklejohns Bay and Jack's Point equivalent distances of 0.6 m, which is 0.3 m less than in the empirical model (Fig. 2.16). This is less than the variability in the prominent shoreline elevation and outside the level of detection in the cross-

correlation; however, it is stressed that this separation is likely to be a minimum. Offset over two or more earthquake cycles are even more unlikely.

The results indicate that uplift has occurred evenly, or not at all, over the last c.12-17 ka within a 50-100 km zone SE of the Pacific-Australian plate boundary. This is consistent with the relative lack of contraction measured by Beavan and Haines (2001), but not with other geodetic models. Shortening may be accommodated by homogeneous crustal thickening or long-wavelength folding, but has not contributed to identifiable interseismic or coseismic uplift across any fault system at the surface. East of this zone, faults of eastern Otago (Fig. 2.1) have had recent surface rupturing earthquakes and anticlinal ranges are being uplifted relative to their basins. Long periods of quiescence on some faults and clusters of activity on others strongly point to episodicity across the Otago fault system (Beanland and Berryman 1989; Norris and Nicolls 2004). If the MFZ has been active as recently as the late Quaternary (traces mapped by Turnbull 2000), the lack of deformation of Wakatipu shorelines supports previous conclusions that the spatial distribution of elastic strain shifts over a relatively short timescale in Otago. Another possibility, if the MFZ is truly 'inactive', is that strain immediately adjacent to the plate boundary has been preferentially partitioned onto reverse faults west of the Alpine Fault in the long term (e.g. Beavan and Haines 2001, Plate 1).

2.6.4 Note on glacial modulation of fault slip rates

Multi-temporal records indicate that GIAs are associated with changes to stress distributions on faults during and following ice-sheet unloading (c.f. Stewart et al. 2000). These changes can be sufficient to modulate slip rates and associated seismicity on faults under and proximal to an evolving ice load (e.g. Mörner 1978; Thorson 1996; Tsuboi et al. 2000; Stewart et al. 2000; Sauber and Molnia 2004; Hetzel and Hampel 2005; Hampel et al. 2009; Hampel et al. 2010). Likewise, crustal deformation caused by the loss of small ice masses, such as the ice caps and valley glaciers involved in the glaciations of mountain ranges, has been documented (e.g. Hetzel and Hampel 2005; Ustaszewski et al. 2008; Sanchez et al. 2010) and local covariations in ice-mass with seismicity have been discovered along an active plate boundary (Sauber and Molnia 2004). Episodicity of earthquakes on a fault may therefore be influenced by ice mass variations and have consequences for estimating seismic hazard.

Finite-element modelling by Hampel et al. (2010) indicates that slip rates accelerate during deglaciation over reverse and thrust faults, provided that the lower crust is less viscous than the lithospheric mantle. Hampel et al. (2009) also found that slip rates increase on faults outside the zone of the ice load *during* loading and decrease during and immediately following deglaciation. In central Otago, geodynamic modelling, interpretation of gravity anomalies and teleseismic data are indicative of a weak, ductile lower crust overlying stronger lithospheric mantle (Gerbault et al. 2002; Scherwath

et al. 2006), and ice thicknesses and extents were similar to that investigated by Hampel et al. (2007). Thus, one could expect local increases or decreases in fault slip rates and range uplift rates depending on the spatio-temporal distribution of ice in Otago.

The slip rate data for the eastern Otago faults and lack of post-glacial deformation presented in this study do not seem to follow the pattern observed in modelling and elsewhere in the world (Mörner 1978; Arvidsson 1996; Sauber and Molnia 2004; Hampel et al. 2007; Hampel et al. 2009). I consider the possibilities for this below:

(i) While the Lake Wakatipu shorelines do not show evidence of differential uplift over at least the Holocene, it is possible that there was an increase in fault slip rates on the MFZ prior to creation of the highest correlative shoreline in this study (351.5 m surface). I cannot rule this out, but consider it unlikely – the definition of the highest shoreline at most sites, including in bedrock, leads to the conclusion that the lake was stable at this level for a considerable period of time. The timing of its formation and abandonment are uncertain, but probably overlaps the 1.5 ka lag time interval between deglaciation (c. 17 ± 2 ka) and accelerated slip rates on reverse faults (Hampel et al. 2009). Surfaces above the 351.5 m shoreline are very discontinuous and seem to be mostly aggradational, so it is unlikely they reliably record rapid post-glacial offsets. There is also no clear pattern of an increase in activity on proximal faults during loading; for instance, there is no evidence for an event on the Pisa Fault since 23-35 ka, a time period which spans the majority of the LGM. Other faults in eastern Otago have been more recently active following long periods of quiescence (Litchfield and Norris 2000; Litchfield and Lian 2004), but their distances from the ice load may have been large enough that glacial effects were negligible.

(ii) The MFZ may have been active earlier than 17 ka, but over the time period considered (present day to c.12-17 ka) strain has been partitioned into the Australian Plate west of the Alpine Fault and in eastern Otago. If this is the case, and assuming that GIA does modulate fault activity as reported elsewhere, then fault proximity to ice loading does not appear to be the dominant control on slip rate modulation. In this case, the transient stresses observed on Otago faults (e.g. Beanland and Berryman 1989; Berryman and Beanland 1991; Norris and Nicolls 2004; Litchfield and Lian 2004) may overwhelm any glacially-induced increase in differential stress. Thus, the efficacy of glacially-modulated fault activity depends on the presence of faults whose activation is favourable in the prevailing tectonic stress-strain field. Decoupling a purely tectonic signal from a glacially-modulated one is therefore a particularly

challenging task on active faults with spatio-temporal slip rate variations; in these settings, background temporal variability should be discounted before deglaciation is deemed the cause of slip rate modulation.

(iii) The MFZ is 'inactive' and/or the differential stress changes due to kilometre scale glacial loading/unloading were not sufficient to induce failure. I consider the latter unlikely because models of c.1 km thick ice loads have been shown to modulate slip rates on faults (Stewart et al. 2000; Hampel et al. 2007). However, an over-thickened mantle and associated isostatic anomaly 'pulling' down the crust in the region (Bourguignon et al. 2007) may contribute to the disconnect between expected and actual stress changes. Thus, changes in lithosphere rheology along a plate boundary may play an important role in preventing or promoting glacially modulated slip rates (Stewart et al. 2000).

2.7 Conclusions

Since the formation of Lake Wakatipu, water levels have dropped by over 43 m, leaving behind a series of stranded shorelines that have been variously preserved along the length of the lake. Schmidt hammer exposure-age dating, calibrated with OSL and radiocarbon dates, indicate that the highest, best-preserved shoreline began forming by c. 17 ka, under assumed stable lake levels across the entire lake, and was abandoned at c. 13 ka. Measurements of shoreline elevations using dGPS, RTK GPS and LiDAR data indicate that there has been no differential uplift of the shorelines since their formation less than 17 ka. Numerical cross-correlation confirms that my field-based interpretations of zero or negligible offset are reliable. If the Moonlight Fault can be considered active, it has not currently accumulated any plate-normal interseismic strain across it and has not experienced coseismic faulting since at least c. 13 ka. These results agree well with previous conclusions that strain is heterogeneously distributed in space and time in this part of the Pacific-Australian plate boundary. This implies that earthquake hazard in Otago, outside that posed by the Alpine Fault, is still greatest from relatively small faults to the East where contemporary strain rates are higher (Beavan and Haines 2001). Additionally, this study highlights that the temporal variability of fault slip rates near formerly glaciated basins is not necessarily governed by the timing of GIAs.

2.8 Appendix 1: Survey Techniques

2.8.1 Real-Time Kinematic GPS (RTK)

A Trimble R8 GNSS base station and receiver with 15-30 mm vertical accuracy was used for manual surveying. High-order geodetic marks were used to calibrate the base/receiver data where available. For one location, where there were insufficient geodetic marks available, site calibration was achieved by differential correction of the base station to PositioNZ continuous GPS stations (Table 2.3). Positions were recorded in New Zealand Geodetic Datum 2000 (NZGD2000) with a New Zealand Transverse Mercator (NZTM) projection. Normal-orthometric heights were recorded in New Zealand Vertical Datum 2009 (NZVD09) which uses the New Zealand Geoid 2009 (NZG09).

Ten transects (between one and three at each site) oriented perpendicular to the shorelines, were surveyed from the oldest (highest) identifiable shoreline to the youngest (lowest) at each site. Points were recorded as frequently as necessary to define slope changes between terrace treads, risers, shoreline inner edges, and subtle topographic features such as beach ridges. At the Greenstone River fan (location shown on Fig. 2.1), three transects were conducted to cover all of the laterally discontinuous terraces and obtain a down-fan gradient (Fig. 2.5). Composite elevation profiles were constructed where preservation was variable between transects.

2.8.2 Differential GPS (dGPS)

At the Greenstone River fan, Jack's Point and Meiklejohns Bay, a Trimble GeoXH 2008 GPS hand-held receiver was used to map shorelines and collect continuous points along the terrace transect. At the former two sites, the GeoXH dGPS was used synchronously with the RTK in order to compare the instrument accuracy and ability to recognise terraces in the continuous lines (dGPS) versus point profiles (RTK). Data from the receiver were differentially corrected in Trimble Pathfinder against PositioNZ stations, with an estimated vertical accuracy of 200-1000 mm (Table 2.3).

Table 2.3: Survey methods and processing information.

Survey Method	(a) Vertical accuracy (mm)	(b) Calibration method	(c) Geodetic mark accuracy* (mm) (95% CI)	(d) Transformation	(e) Transformation standard deviation (mm)	(f) Estimated total instrumental error† (mm)
RTK (Greenstone River fan)	15-30	Differential correction	200	--	--	±215-230
RTK (Bible Tce and Blanket Bay)	15-30	Surveyed control point	400; 30	NZGD2000 ellipsoidal height to NZVD09	--	±415-430; 45-60
RTK (Jack's Point)	15-30	Geodetic mark-base station	350; 10	Dunedin 1958 to NZVD09	70	±435-460; 95-110
RTK (Glen Nevis)	15-30	Geodetic mark-base station	250; 10	Dunedin-Bluff 1960 to NZVD09	40	±305-320; 65-80
LiDAR (Bible Terrace)	26	Surveyed control points	--	Dunedin 1958 to NZVD09	70	±96
LiDAR (Queenstown)	32	Surveyed control points	--	Dunedin 1958 to NZVD09	70	±102
LiDAR (Kingston)	48	Surveyed control points	--	Dunedin 1958 to NZVD09	70	±118
dGPS§ (All sites)	200-1000	Differential correction	--	--	--	±200-1000

**Mark accuracy given as Tier (relative to datum); Class (relative to surrounding marks) confidence intervals (CI).*

† For simplicity, combined total (a), (c), and (e). Tier; Class designation as in (c), where indicated.

§ Estimated accuracy stated is 2x that of the horizontal accuracy following differential correction.

2.9 Appendix 2: Tests of quantitative identification of shorelines and cross-correlation method

Identification of correlative shorelines and quantification of their offset using cross-correlation is a three step process: (1) production of a PDF of elevations using a swath or profile of topographic data; (2) selection of a lower threshold of probability density for automatic identification of a terrace and production of a discrete step function; (3) cross-correlation of two step functions to determine offset. As (1) and (2) are discussed in the text, (3) is discussed in detail below. Illustrations of the process given two test scenarios (see below) are shown in Fig. 2.18 and 2.19.

The cross-correlation function is given in Eqn. 2.1. In its simple form, cross-correlation is calculated at several elevation shifts while sliding the entire function g across f. For the purposes of this study, there may be progressively greater offset of older lake shorelines which necessitates a test for elevation shifts within individual *parts* of the function. For example, a maximum cross-correlation between two flights of terraces (mathematically represented by two step functions) at an elevation shift of 5 m would indicate that *all* of the terraces have been offset by 5 m. If there are variable offsets between correlative terraces, this approach would yield misleading interpretations, and is only valid in the rare case that all of the tilting and/or offset occurred after the youngest terrace formed. Shifting individual parts of the function allows cross-correlation maxima at several terrace elevations and elevation shifts.

The cross-correlation of the two step function series was calculated using a sliding elevation-window approach (e.g. Boker et al. 2002). The result reports the cross-correlation 'score' between the two functions at each increment of elevation and over a user-defined window of elevation values. Cross-correlation was normalised for the maximum 'score' in the entire series and thus range from 0 to 1 in my plots.

Two trial scenarios were created to demonstrate the process above and assess the vertical accuracy of the cross-correlation technique (Fig. 2.18 and 2.19). LiDAR data for a flight of alluvial terraces were used to construct three elevation profiles (Lines 1, 2 and 3) at different distances down-valley but containing unequivocally correlative terraces. Line 1 and Line 2 (Scenario 1; Fig. 2.18a), are parallel to each other but with a constant +6.06 m vertical offset between correlative terraces (i.e. all terraces in Line 2 are an average of 6.06 m higher than correlative terraces in Line 1). In Scenario 2 (Fig. 2.19a), Line 3 contains progressive offsets and was compared to Line 1. Relative to Line 1, the lowest three terraces in Line 3 (T7-T5) were not offset; T4-T2 were offset +1.96 m; T1 was offset +4.8 m.

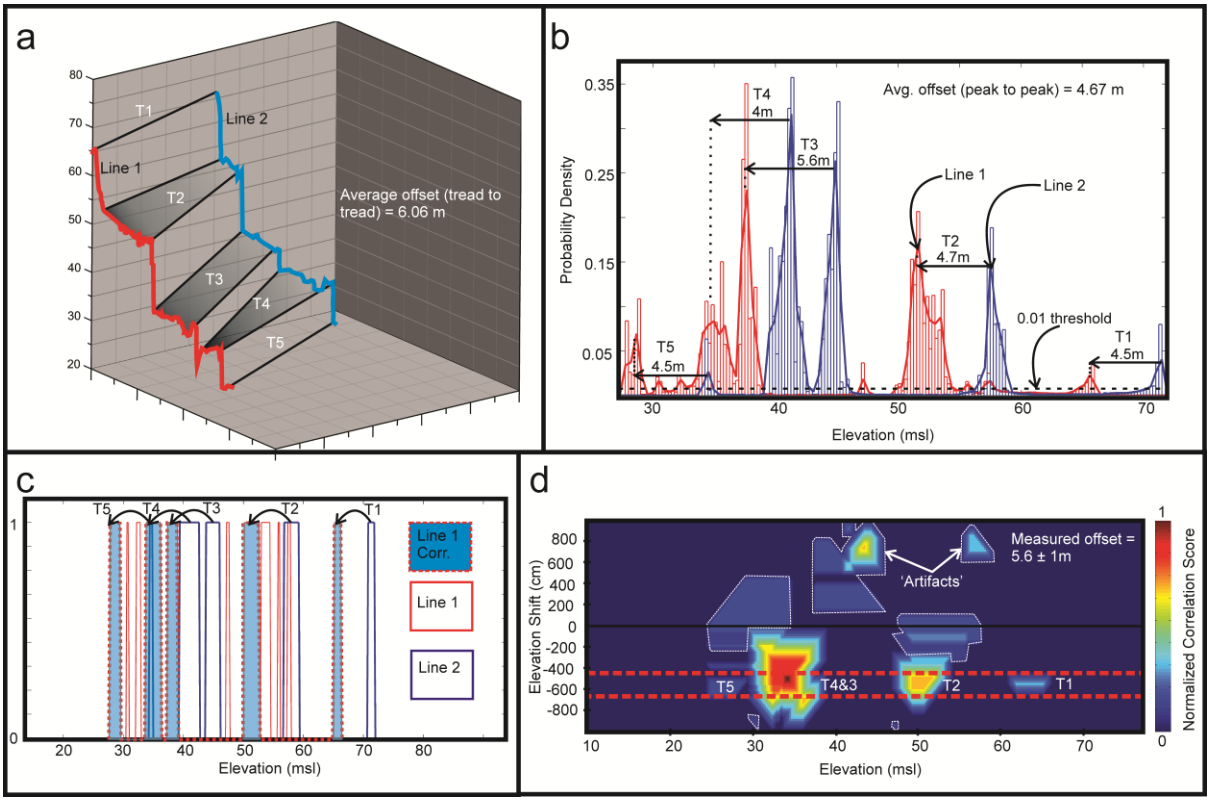

Figure 2.18: Cross-correlation technique applied to two surfaces containing correlated terraces with a uniform vertical offset. (a) Elevation profiles of two synthetically offset flights of terraces; (b) Elevation PDFs and apparent offset of terraces from two profiles shown in (a). Dashed line at a probability density of 0.01 is lower threshold for terrace identification; (c) Step function for elevation PDFs and threshold shown in (b); (d) Sliding-window cross-correlation of step functions in (c).

The elevation PDFs (Fig. 2.18b & 2.19b) illustrate offset(s) along the x-axis of otherwise similarly shaped distributions. Peak to peak offsets measured from the PDFs are variable – a better estimation of the true offset is gained by shifting the entire curve above the pre-set threshold (i.e. the terrace tread) over the reference curve. The step functions (Fig. 2.18c & 2.19c) allow such a comparison by filtering out the 'noise' below the probability density threshold and giving equal weight to all elevations above the threshold. The final output is a cross-correlation plot (Fig. 2.18d & 2.19d) displaying cross-correlation scores normalised for the highest value. At each increment along the x-axis (elevation) the cross-correlation (colour-coded) is computed for a range of possible elevation shifts (y-axis).

It should be noted that selection of the threshold value greatly influences the ultimate output and utility of the cross-correlation plots. Its selection depends on the resolution and accuracy of the topographic data and slope of terrace risers and treads. A value should be chosen so that elevations of the steps are in agreement with those of shorelines identified in the field (Fig. 2.11). While this may seem circular, the objective of quantitative identification is to run tests on their offset, and not test

terrace mapping accuracy. To obtain useful interpretations from the cross-correlation plots, terrace step function peaks must be spaced so that unrealistic shifts do not yield higher correlations than the actual shift. Thresholds should thus be set so that the best defined terraces in a profile are adequately spaced in the step function. Closely spaced terraces (<1-2 m apart) may become lumped together in the cross-correlation or yield high correlations at several elevation shifts (see below).

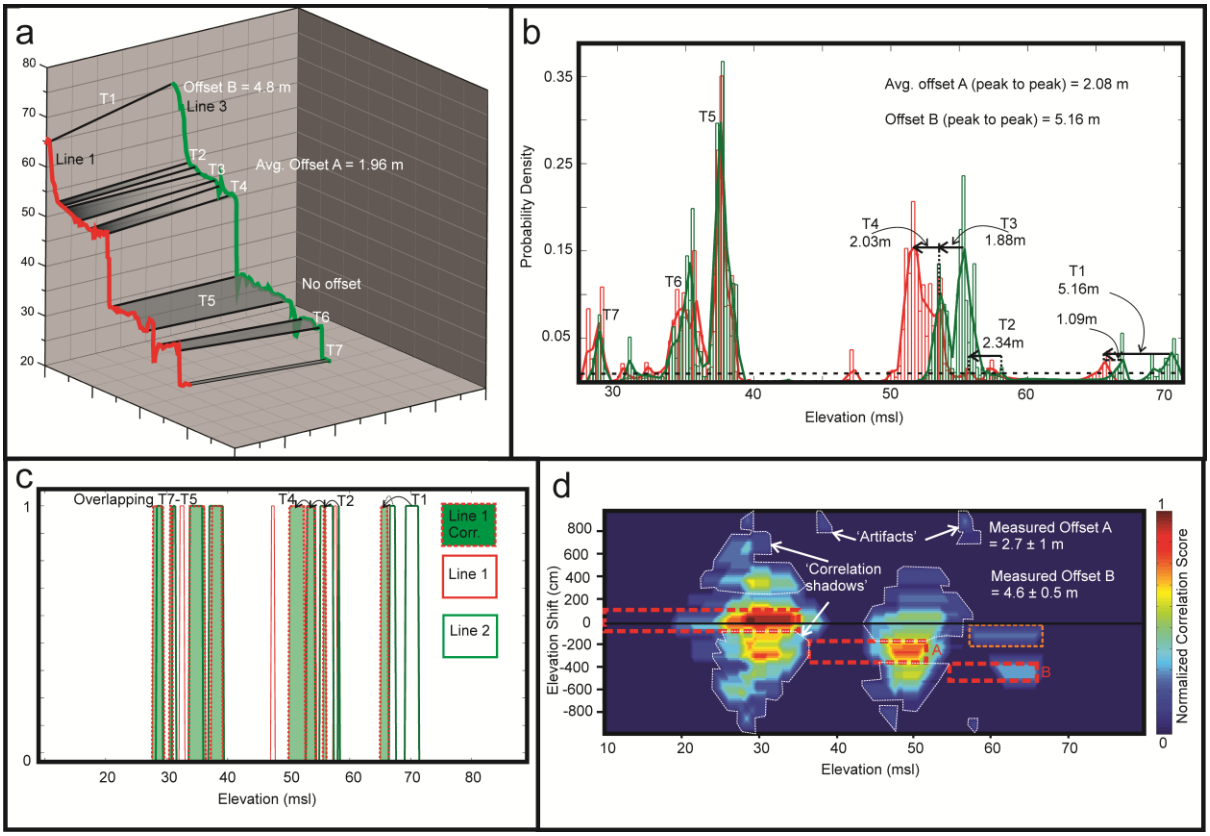

Figure 2.19: Cross-correlation technique applied to two flights of terraces with a progressively increasing vertical offset. See text for discussion.

Artefacts, or areas of cross-correlation unrelated to the actual offset, can occur if the step functions overlap at more than one elevation shift (Fig. 2.19d). Additionally, areas of lesser cross-correlation often surround areas of high cross-correlation due to the shape of the step function Fourier transform (correlation shadows in Fig. 2.19d). The highest cross-correlation values at a given elevation and shift should be interpreted as the 'real' signal, unless inconsistent with the overall trend of the data. Patterns in a terrace sequence and knowledge of the geomorphology are useful for distinguishing between artefacts or shadows and real offsets (e.g. lower terraces should not be offset more than higher terraces; adjacent terraces in one profile should not be offset in different directions relative to the other profile; there cannot be more than one 'real' offset at a given terrace elevation). Using these guidelines, offsets can be directly measured in the cross-correlation plots by identifying

clusters of high cross-correlation. Fig. 2.18d shows a constant offset of 5.6 ± 1 m; Fig. 2.19d shows no offset below 40 m elevation, but an offset of c. 2.7± 1 m for the next surfaces up, and an offset of c. 4.6± 0.5 m for the uppermost surface. These results are consistent with the known differences in terrace elevation.

The most easily interpreted scenario given any amount of offset is one in which lake shorelines at each site were created with similar wave action and in the same deposits (i.e. have similar terrace frequency, tread lengths and riser slopes). Absence of these criteria will result in more artefacts and larger correlation shadows that complicate interpretations. For this reason, the cross-correlation technique should be used as a test of field-based interpretations gained by high-resolution surveying and geomorphic mapping. Identification of offsets not ascertained by field-based correlations should rely on strong patterns of offset terraces to rule out the presence of correlation artefacts. The larger the range of the elevation distributions and wider elevation spacing of the terraces, the more likely it is that patterns of offset in the cross-correlation plots will yield useful interpretations.

CHAPTER 3. TECTONIC GEOMORPHOLOGY AND PALEOSEISMOLOGY OF THE FOX PEAK AND FOREST CREEK FAULTS: IMPLICATIONS FOR THE EARTHQUAKE HAZARD OF SEGMENTED REVERSE FAULTS

3.1 Abstract

The Two Thumb and Sherwood Ranges are situated in the eastern foreland of the Pacific-Australian plate boundary in the central Southern Alps of New Zealand. The ranges are bounded by moderately to steeply dipping reverse faults, the Forest Creek and Fox Peak Faults, which have been responsible for the uplift of the two ranges. The c. 36 km long Fox Peak Fault is comprised of three geometrically and structurally-defined segments: the Ribbonwood and Bray Segments at the base of the Sherwood Range, and the Cloudy Peaks Segment, which bounds the southern Two Thumb Range. The three Fox Peak segments have been mechanically linked by foreland propagation of the Forest Creek Fault at Cloudy Peaks and/or southward lengthening of the Ribbonwood Segment. Maximum fault slip rates range from c. 1-1.5 mm yr^{-1} on the Cloudy Peaks and Bray Segments. Slip rates vary along strike consistent with changes in range topography. Slip rates are significantly lower where there is distributed folding on the Ribbonwood Segment and at segment boundaries defined by NW-striking faults. The Forest Creek Fault is defined by a prominent up-hill facing scarp and southeast-dipping fault plane in the southern Two Thumb Range and by a recent surface traces to the North. Five paleoseismic trenches and events inferred from terrace ages were used to determine whether fault segment boundaries constitute barriers to earthquake rupture propagation. The results show that the MRE occurred less than c. 2.5 kya on the two end segments of the Fox Peak Fault as well as the Forest Creek Fault. There is evidence for a penultimate, full-length Fox Peak Fault rupture between 4-6 ka. Other events ages, long-term slip-rates and single event displacements on the fault are indicative of a 2-3 ka recurrence interval for both the Fox Peak and Forest Creek Faults. Segment boundaries defined by high-slip rate gradients near interesting NW-striking faults are not likely to limit earthquake rupture propagation. The results highlight the necessity of geologic, tectonic geomorphologic and paleoseismic studies in determining the earthquake hazard and magnitude potential of a fault system. Moment magnitudes (M_W) of 7.0-7.2 are expected for both the Forest Creek and Fox Peak Faults in isolation, but an earthquake sourced from coeval rupture could exceed M_W 7.4.

3.2 Introduction

Ruptures that cascade onto adjacent segments or faults have the potential to produce larger magnitude earthquakes than single-segment ruptures (e.g. King and Yielding 1984; Crone et al. 1992; Rubin 1996; Arrowsmith 2005; Wesnousky 2006; Wesnousky 2008; Xu et al. 2009; Oskin et al. 2012; Elliot et al. 2012). Fault segment boundaries can be identified by (a) changes in fault geometry or surface discontinuities (e.g. step-overs or cross-faults), (b) variations in structural or topographic relief, (c) slip rate or paleoearthquake age variations, and (d) historic rupture limits (Knuepfer 1989; dePolo 1991; McCalpin 2009). While mapping can address the long-term behaviour of faults and

segments (i.e. (a) and (b)), detailed paleoseismic studies are required to delineate (c) and determine the pattern of recent surface rupturing earthquakes. For most active faults, (d) is not available; seismic hazard evaluations rely on (a) through (c) for delineating likely barriers to earthquake propagation.

Most paleoseismic studies of fault segmentation have focused on continental strike-slip (Barka 1996; Langridge et al. 2005; Rockwell et al. 2009; Biasi and Weldon 2011; De Pascale et al. 2014) and normal faults (e.g. dePolo 1991; Machette 1991), and subduction zone thrusts (e.g. Goldfinger et al. 2012). Only a few paleoseismic studies have systematically examined the earthquake segmentation of continental reverse and thrust faults (Arrowsmith and Strecker 1999; Densmore et al. 2007, 2010; Amos et al. 2010, 2011; Hubbard et al. 2014), despite the propensity for reverse faults to jump multiple segments and faults in historic earthquakes (e.g. Officers of the Geological Survey 1983; Rubin 1996; Wesnousky 2008; Field et al. 2013). In New Zealand, reverse fault segmentation and growth has been analysed over 10^6 year timescales via the topographic and drainage evolution of anticlinal ranges (Jackson et al. 1996, 2002). The segmentation of faults and folds over 10^4-10^5 year timescales has also been studied in relation to displacement patterns along a listric reverse fault (Davis et al. 2005; Amos et al. 2007, 2010). In both cases, little is known on how these geometric, structural and rate-based segments control earthquake behaviour.

Here, I use high-resolution surveying, trenching, ground-penetrating radar (GPR), geomorphic mapping and Quaternary geochronology to investigate the temporal and along-strike evolution of the range-bounding, reverse Fox Peak and Forest Creek Faults in the central South Island, New Zealand. These faults display excellent surface expression of recent earthquakes and provide the opportunity to study fault segmentation over 10^2 to 10^6 year timescales, but have not been studied in detail. Segmentation (i.e. geometric, structural, rate-based and paleoseismic) is considered on timescales ranging from the most recent event (MRE) in five paleoseismic trenches to the structural and topographic evolution over millions of years. Slip rates are derived at over a hundred locations along-strike to define segment boundaries. The results highlight the utility of detailed field studies in delineating segment boundaries on active reverse faults and offer insights into the future potential of large, multi-segment earthquakes.

3.3 Geologic setting and previous work

New Zealand is situated at the margin of the obliquely-convergent Pacific and Australian plates (e.g. Walcott 1998). Geodetically derived convergence rates at the plate boundary in New Zealand range from 30 mm yr^{-1} to 50 mm yr^{-1} (Wallace et al. 2007; DeMets et al. 2010). Approximately 75% of this oblique convergence in the South Island is taken up on the Alpine Fault, a 400 km-long, right-lateral, reverse fault. In the central South Island, the remaining c. 25% is distributed primarily onto structures east of the Alpine Fault in the Pacific plate.

A zone of N-NE striking, predominantly west-dipping reverse faults c. 70 km from the plate boundary (referred to here as the South Canterbury Fault system, SCFS), including the Lake Heron, Forest Creek, Fox Peak, Irishman Creek, and Ostler faults corresponds with a secondary maximum in convergence and strain rates (e.g. Beavan and Haines 2001; Wallace et al. 2007). Seismic and magneto-telluric surveys indicate that the SCFS may be a semi-continuous zone of backthrusts off the Alpine Fault (Wannamaker et al. 2002) and have surface traces that indicate on-going activity through at least the latest Pleistocene (Beanland 1987; Berryman et al. 2002). Faults are moderately to steeply dipping at the surface and sole into a decollement at 10-20 km depths. Historical seismicity in this region is low, but focal mechanisms from micro-seismicity indicate predominantly thrust motion, with some sinistral strike-slip (Fox 1987; Leitner 2001).

Geologically-derived slip rates of c. 1-2 mm yr^{-1} are well-established on the Ostler and Irishman Creek faults (Amos et al. 2007; Amos et al. 2010). Other faults in the SCFS like the Lake Heron, Forest Creek, and Fox Peak faults have not yet had slip rates established by field studies. Geodetic slip rates are 2-3 times higher for this zone of faults than those measured in the field (Beavan et al. 2007; Amos et al. 2007; Wallace et al. 2007; Amos et al. 2010). Significant strike-slip (2-5 mm yr^{-1}) is predicted by the geodetic models (Wallace et al. 2007), but not observed in the field (e.g. Amos et al. 2007). If some of this deformation is taken up by episodically occurring earthquakes localised on the major, identifiable faults in the region, current estimates to the regional seismic hazard could underestimate the contribution of the SCFS (Stirling et al. 2012).

The Fox Peak Fault (FPF) is a 30-40 km long range-front structure that bounds the Sherwood and Two Thumb Ranges to the west and the Fairlie Basin to the East (Fig. 3.1 & 3.2). The ranges are comprised primarily of Permo-Triassic Torlesse greywacke and Textural Zone IIa semi-schist (Fig. 3.1) (Cox and Barrell 2007). Strike ridges and synclines of Tertiary sandstones, limestones, and siltstones, which have been progressively uplifted from regression in the Miocene, mark the fringes of the Fairlie Basin (James 1998; Cox and Barrell 2007) (Fig. 3.1). The FPF and related structures have thus been active since at least the late Miocene-Pliocene (e.g. Upton et al. 2004; Ghisetti et al. 2007; 2012). The FPF is likely to be an inverted normal fault from a period of Miocene extension as has been proposed for the nearby Ostler Fault (Ghisetti et al. 2007); field studies and geophysical surveys show that the fault is listric at shallow depths (Long et al. 2003; this study).

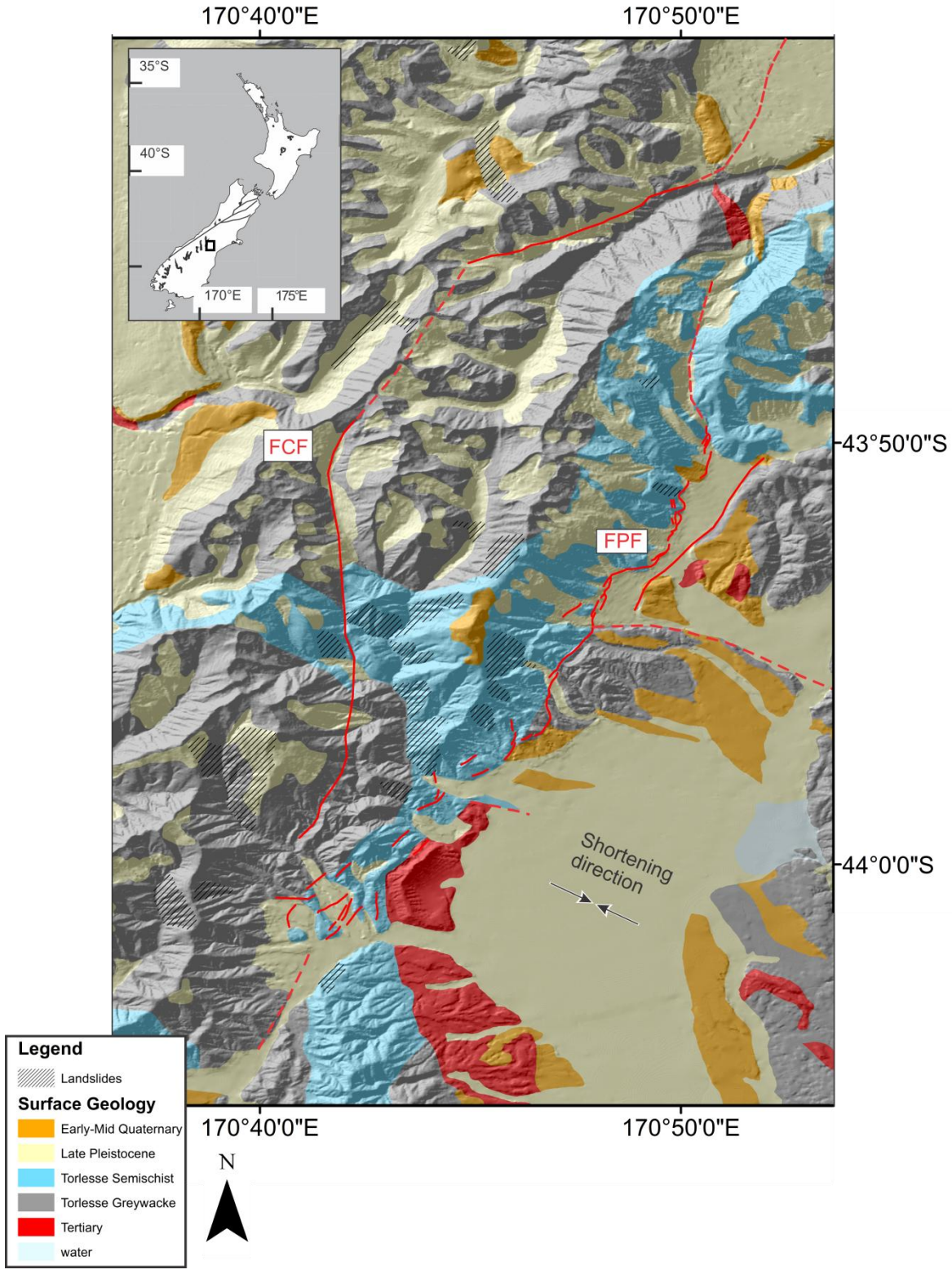

Figure 3.1: Location and geology of the study site. (A) Simplified geology and fault traces overlain on hillshade model (modified after Cox and Barrell 2007), which are updated in this study. Surface traces of the Fox Peak Fault (FPF), Forest Creek Fault (FCF) and intersecting structures identified later in the text. Traces are solid where known and dashed where inferred.

Peaks in the Sherwood and Two Thumb Ranges can reach well over 2000 m, and contain the highest topography east of the main ranges in South Canterbury and Otago (Fig. 3.2). Tarns and lateral moraines indicate widespread mountain glaciers in the high catchments during the Last Glacial Maximum (LGM). Post-LGM alluvial fans and landslides dominate the geomorphology along the northern Sherwood Range front, although older fan surfaces are preserved further to the South (Fig. 3.1). Cut-in-fill and degradational strath terraces of variable age are present where major streams emerge from the Two Thumb and Sherwood Ranges.

Previous studies on the Fox Peak Fault (FPF) have focused on structural mapping and reconnaissance of active faulting (e.g. Beanland 1987; Cutten 1990; James 1998; Upton et al. 2004). Uplift rates of c. 1 mm yr^{-1} have been assigned based on estimations of faulted terrace ages and offsets (e.g. Beanland 1987; James 1998; Upton et al. 2004; Berryman et al. 2002). Evidence of strike-slip motion is limited to a proposed offset of an abandoned channel on in the northern portion of the fault that could indicate up to 2.5 mm yr^{-1} of strike-slip (Cutten 1990; James 1998; Berryman et al. 2002). Therefore, the net geologic slip rate of the FPF alone could accommodate a significant portion of the geodetically derived slip rates (2.5-7 mm yr^{-1}) for the eastern Southern Alps (Wallace et al. 2007).

The Forest Creek Fault (FCF) is present as a c. 40 km long, 2-4 m up-hill facing scarp bounding the Two Thumb Range (Fig. 3.1). Northeast of the field area, the on-fault deformation becomes more diffuse and branches into oppositely-verging folds underlying glacial moraines and river terraces in the Rangitata River (Cox and Barrell 2007). Upton et al. (2009) continue the FCF northward into the Lake Heron Fault, with a total possible length of c. 80 km (Upton et al. 2004; Upton and Osterberg 2007). In this study, I focus on the recent surface traces bounding the Two Thumb Range (Fig. 3.1).

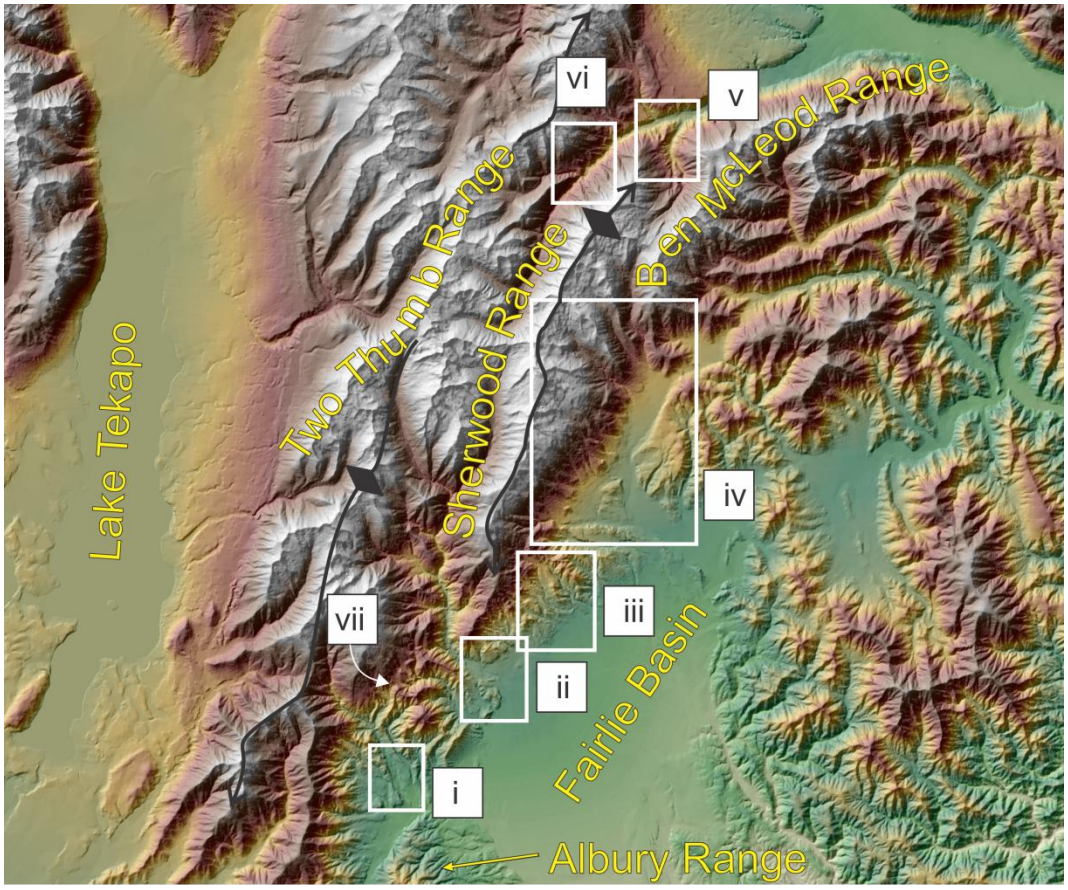

Figure 3.2: Topography from 15 m DEM and locations of detailed field mapping. (i) Cloudy Peaks, (ii) South Opuha River area, (iii) Ribbonwood Station, (iv) Fox Peak and Lilydale Stations, (v) Butlers Creek, (vi) Forest Creek Fault at Forest Creek, (vii) Forest Creek Fault at Dobson ski field road.

3.4 Tectonic geomorphology of the Fox Peak Fault

3.4.1 Cloudy Peaks Station

At Cloudy Peaks Station (Fig. 3.3, Appendix 1), four imbricate reverse traces of the FPF are present across a 2 km wide zone. The traces vertically offset primarily degradational river terraces at c. 2 to 90 m above Firewood Stream. The terraces have previously been mapped as late LGM (c. 16-18 kya) to recent outwash terraces and cut-in-fill terraces (Beanland 1987; Cutten 1990; James 1998; Upton 2004). The terraces are comprised of bedrock straths with thin (2-5 m) veneers of fluvial gravel and are not associated with glacial outwash. The development of the terrace sequence represents ongoing incision due to a combination of tectonic-controlled uplift and local sediment fluxes (e.g. landslides), as well as climatically-controlled sediment supply (Bull 1990; Merrits et al. 1994; Amos et al. 2007). Therefore, the ages of the river terraces may be unrelated to regional glacial cycles or marine isotope stage (MIS) correlations. For instance, the abandonment of discontinuous terraces immediately up and downstream of faults (e.g. T7, T6 in Fig. 3.3) could be related to tectonic uplift

over a single earthquake cycle or landslide-controlled sediment supply in the catchment (Fig. 3.3). The development of more extensive terraces (e.g. T5, T4, T2, T1), with wide straths (terrace treads) and long lateral continuity, are likely to be more strongly influenced by sustained climate-controlled sediment abrasion and supply (e.g. Bull 1990; Quigley et al. 2007).

The river terraces show progressive vertical offset on the four fault traces in the field area. In the southeast, a frontal fault (Fault 1, Fig. 3.3) splays at the surface across T5 into a NW-dipping master fault and an antithetic fault to form a pop-up structure, and may indicate complex, flexural-slip faulting at the front of the imbricate wedge. The next fault to the NW (Fault 2, Fig. 3.3) offsets every terrace in the field area with exception of T1, and displaces the youngest mapped terrace (T7). The persistence of this trace through the development of the terrace sequence implies that this has been the dominant fault (i.e. principal slip surface) since the abandonment of T2, and further supports the flexural-slip origin of Fault 1. A possible structure cutting T2-T4 is present c. 80 m NW of Fault 2, though any apparent offset is likely to be enhanced or perhaps produced entirely by local erosion (see GPR section below). Northwest of Fault 2, a backthrust (Fault 3, Fig. 3.3) displaces T2 and T4f (fill terrace) on the east side of Firewood Stream, and T5, T4a, T4, and a late Quaternary terrace remnant on the west side. Because of the magnitude of displacement on Fault 3 and location on the 'backlimb' of the Fault 2 anticline, it is likely that it is kinematically linked and slips sympathetically with Fault 2. A c. 150 m wide crestal graben with 12 normal fault traces occupies the hinge zone of the anticline produced by Fault 2. Local extension is enhanced by antithetic faulting on Fault 3. Fault 4, a NW-dipping reverse fault, is located a kilometre to the North of Fault 3, and displaces T1, T2 and T4 by variable amounts (Fig. 3.3). There is no clear indication of strike-slip offset anywhere in the field site.

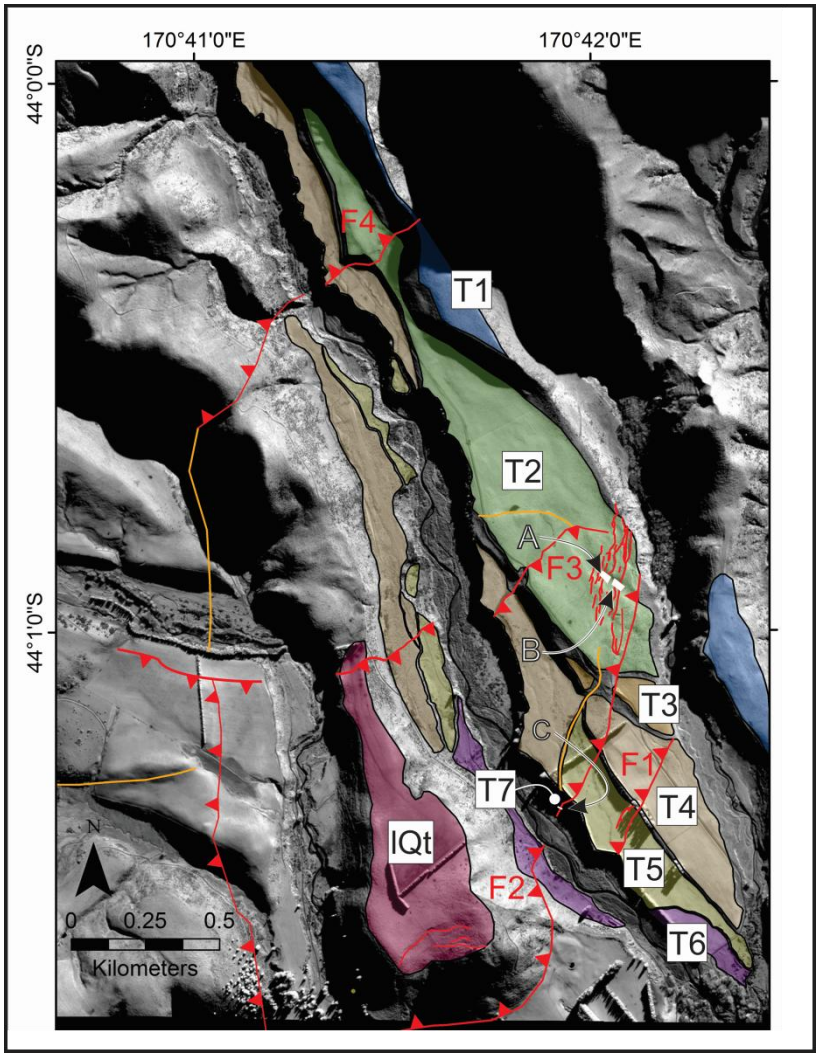

Figure 3.3: Tectonic and Quaternary geomorphic map of the Fox Peak Fault at Cloudy Peaks. A, B and C are the locations of paleoseismic trenches discussed later in the chapter (Section 3.7.1). Orange lines are the traces of possible faults. Red lines without teeth are normal faults, which are limited to the crestal graben between Fault 2 and Fault 3, near A and B. Firewood Stream runs NNW to SSE through the terrace sequence. See Appendix 1 (Section 3.11) for detailed geomorphic map.

All faults exposed in outcrops are moderately to steeply dipping at the surface, with the major structures dipping to the NW. Outcrop data (e.g. Fig. 3.4 & 3.5) indicate that the faults are listric and dips decrease at very shallow depths. This manifests in the landscape as steep fault scarps (or anticline forelimbs) with gentle backlimbs and is similar to the morphology of the folded outwash plains crossing the listric Ostler Fault to the South (Fig. 3.4 & 3.5)

Figure 3.4: A listric fault in Firewood Stream. (A) Over a distance and depth of c. 20 m, the fault dip changes from c. 45 to 0°. (B) Normal displacement of a quartz vein and a lack of a modern surface trace suggest that this fault has been inherited from past extension, and is not a bending-moment fault related to the modern deformation. Hammer for scale.

Immediately SW of Cloudy Peaks, fault traces become less pronounced and deformation is accommodated by broad-wavelength folding of terrace surfaces. Structural contours of Barrell and Strong (2012) show that the FPF does not continue South into the Albury Range (Fig. 3.1). Rather, it is inferred that the FPF becomes blind beneath the SW extent of the Two Thumb Range, where topographic and structural relief decrease with accrued slip (and surface expression) of the fault (Fig. 3.1). Northeast of Cloudy Peaks, the principal fault traces are indistinct and recognised only by topographic lineaments (Appendix 1). Deformation is transferred onto a homocline of Tertiary sedimentary rocks (Fig 3.1). Flexural-slip faulting of a fan surface inferred to be of MIS4 age (c. 70 ka) suggests that the folding is ongoing, though younger river terraces show no evidence of folding. Steep, bedrock fault traces observed in outcrop closer to the Two Thumb rangefront are likely to be the principal fault planes of the FPF (Fig. 3.7 & 3.8), but do not show any evidence for late Quaternary displacement beyond producing a topographic/erosional lineament.

The Tertiary homocline ends abruptly near the South Opuha River at a NW-striking fault mapped by James (1998) and Barrell and Strong (2012) (Fig. 3.1). The fault separates Torlesse greywacke in the NE from Tertiary units to the SW. While there is no topographic expression of this fault, the depth to basement increases to the North of the South Opuha River (Barrell and Strong 2012), indicating that it may represent an uplift-rate delineated segment boundary (rather than a purely structurally or geometrically-defined segment) along the FPF.

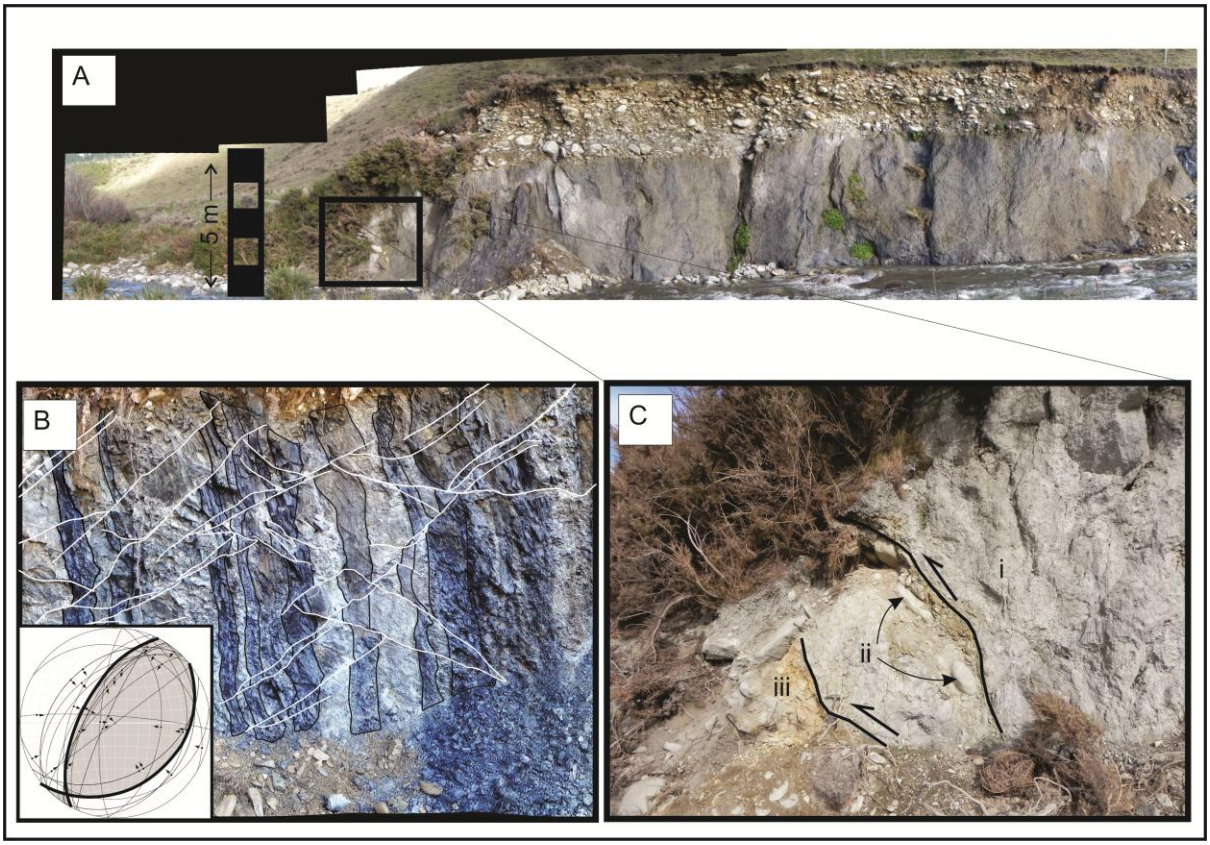

Figure 3.5: Stream exposures of faults at Cloudy Peaks. (A) T6 displaced by c. 5 m across Fault 2. Inset shows location fault in (C). (B) Outcrop scale 'triangle zone' with facing thrusts and backthrusts (white) offsetting vertically-bedded Torlesse greywacke sandstone and argillite (black). The inset fault plane solution is for the entire Cloudy Peaks area and agrees with measurements taken from this outcrop alone. The small component of right-lateral strike slip is not apparent at the surface, and may be related to tear-faulting or transfer structures near this end of the FPF. (C) Reverse fault splays dug out from the steam exposure in (A). (i) Torlesse greywacke, (ii) terrace gravels entrained in fault zone between splays, (iii) terrace gravels.

3.4.2 South Opuha River and Ribbonwood Station

3.4.2.1 South Opuha River terraces

The South Opuha terraces have formed by incision into fan sediments (Fig. 3.6 & 3.7). The age of the fan deposit is unknown, but the thickness of the deposit and position at the rangefront indicates that it is probably derived from a late to post-LGM sediment flux (c. 18-14 ka) as is observed elsewhere in Canterbury (Knuepfer 1988; Bull 1990; Alloway et al. 2007). Thus, the degradational river terraces are younger than 18-14 ka. Other fan surfaces above the degradational terraces on the north side of the South Opuha River were mapped according to MIS stages (after Cox and Barrell 2007) to produce rough age estimates.

On the south side of the river, there is a single, c. 1-2 m high scarp of the FPF that crosses the South Opuha river terraces. The throw is the same (c. 1 m) on T1, T1a and T2. On the upper fan

surface, throw apparently doubles to c. 2 m, though the scarp height has likely been modified by erosion. Some fault planes were mapped further into the rangefront, but do not lie along strike of the scarp (Fig. 3.8). On the NE side of the river, antithetic faults c. 2 km downstream of the main FPF trace offset T1 and fan surfaces of two different ages. These traces coincide with a narrow bedrock gorge of the South Opuha River and the along-strike projection of the Tertiary homocline (Fig. 3.6). They are therefore likely to be flexural-slip faults representing the emerging surface manifestation of the well-established homoclinal folding to the South. Progressive basinward tilting of older (MIS4-6) fan surfaces at Ribbonwood Station to the North is suggestive of a similar style of folding; however, the lack of Tertiary units at the surface at both locations implies a decrease in net uplift across the South Opuha River (Fig. 3.9).

North of the South Opuha River at Ribbonwood Station, active fault traces are discontinuous and cross-cut older fan surfaces and river terraces within a diffuse zone of uplift expanding out from the main range (Fig. 3.9). A possible basinward splay may be an out-of-syncline bending-moment fault, however, clear indications of active faulting are sparse at the rangefront.

Another W-NW striking structure at the northern end of Ribbonwood Station, here named the Stony Creek Anticline (SCA), separates two geometrically distinct segments of the FPF (Fig 3.1, 3.10). Wind gaps with late Quaternary gravels abandoned along the length of the SCA, along with a fault trace running into the Clayton Ranges (Cox and Barrell 2007) indicate that it has been active in the recent past (Fig. 3.9). This L-shaped pattern of interfering faults and folds is common elsewhere in Canterbury (Campbell et al. 2012) and produces characteristic secondary folds and faulting (Nicol 1993) which are also present to the North. The-re-emergence of Tertiary units in a syncline to the NE of the SCA and FPF (Fig. 3.1) may indicate an uplift-rate delineated boundary across the SCA, rather than simple geometric complexity or surface expression variability on the FPF.

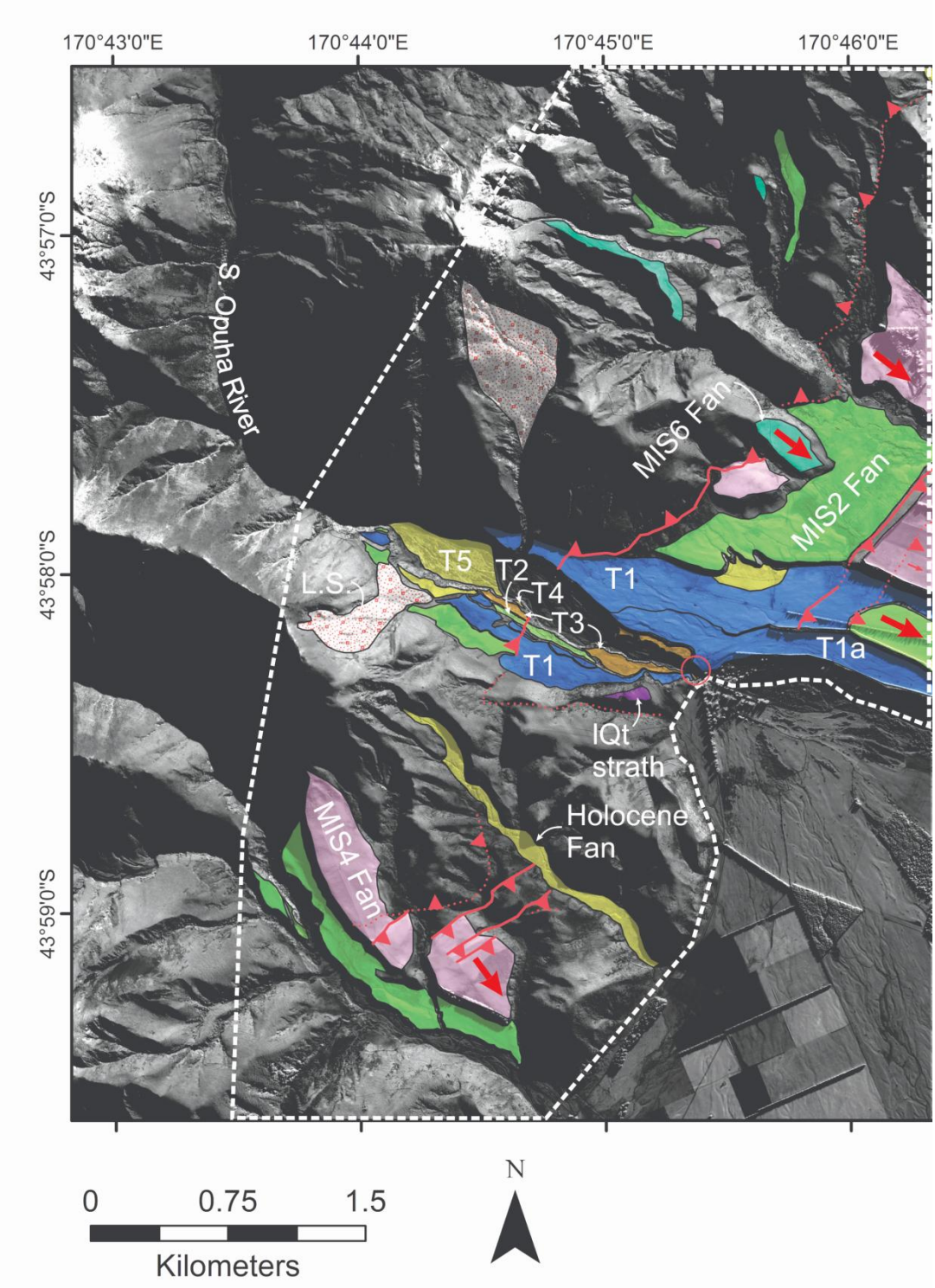

Figure 3.6: Tectonic and Quaternary geomorphic map of the Fox Peak Fault at the South Opuha River area. South of the river, surface expression of faulting is dominated by flexural-slip faults within the Tertiary homocline. At the river, faulting is confined to a single, NW-dipping trace with a small displacement (c. 1-2 m throw) (compare with Cloudy Peaks, to the South). Terraces have formed by incision into a late-glacial fan, though higher terraces and fans are also preserved near the river. To the North, flexural-slip faulting is again evident and coincides with a narrow gorge in the South Opuha River (red circle). The main, range-bounding fault continues to the North but has only intermittent surface expression north of the river. Red arrows denote the direction of tilting of late Quaternary fan surfaces.

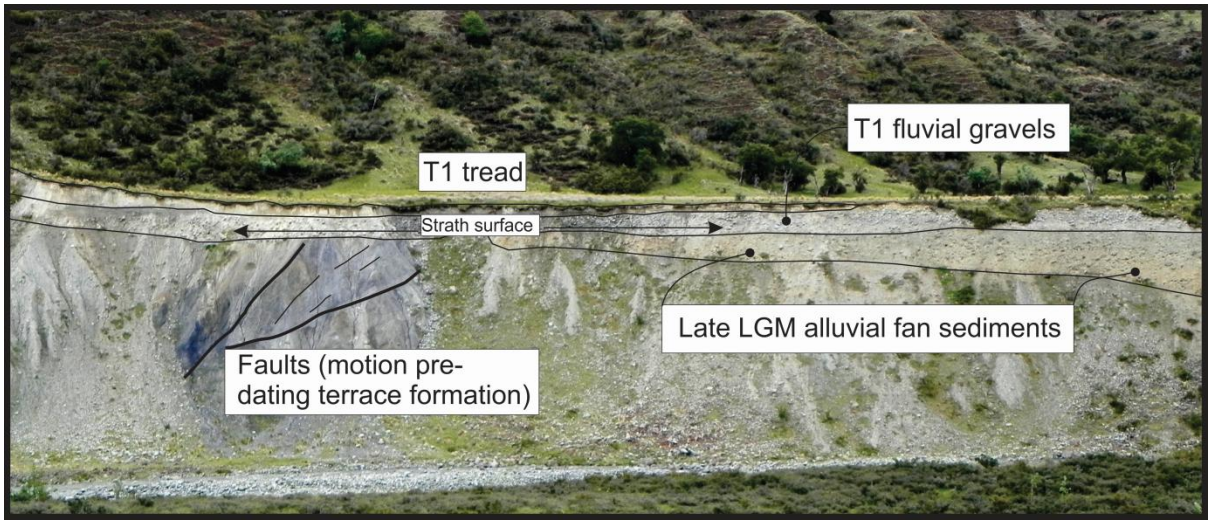

Figure 3.7: Outcrop of fan gravels underlying fluvial boulder lag at the South Opuha River. The fan gravels are assumed to be of late to post-LGM age, though further dating may be required to constrain this estimate. The strath surface cuts evenly across brecciated Torlesse greywacke and the fan gravels. Faults exposed in the Torlesse have no surface expression and do not offset the fluvial gravels, indicating they have not slipped since deposition of the fluvial gravels.

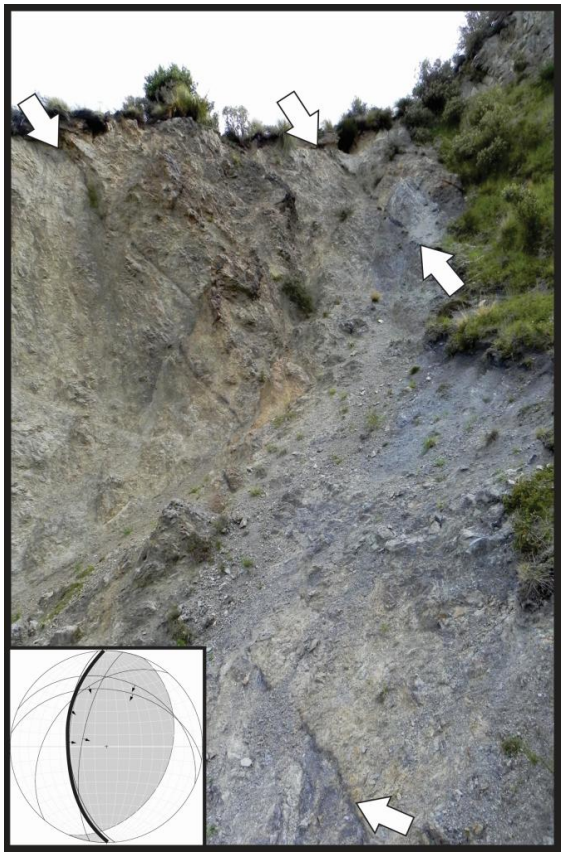

Figure 3.8: Outcrop of bedrock faults near the South Opuha River and fault plane solution for the area. Gently-dipping, East-West striking faults are located the river outcrop shown in Fig. 3.7 (above).

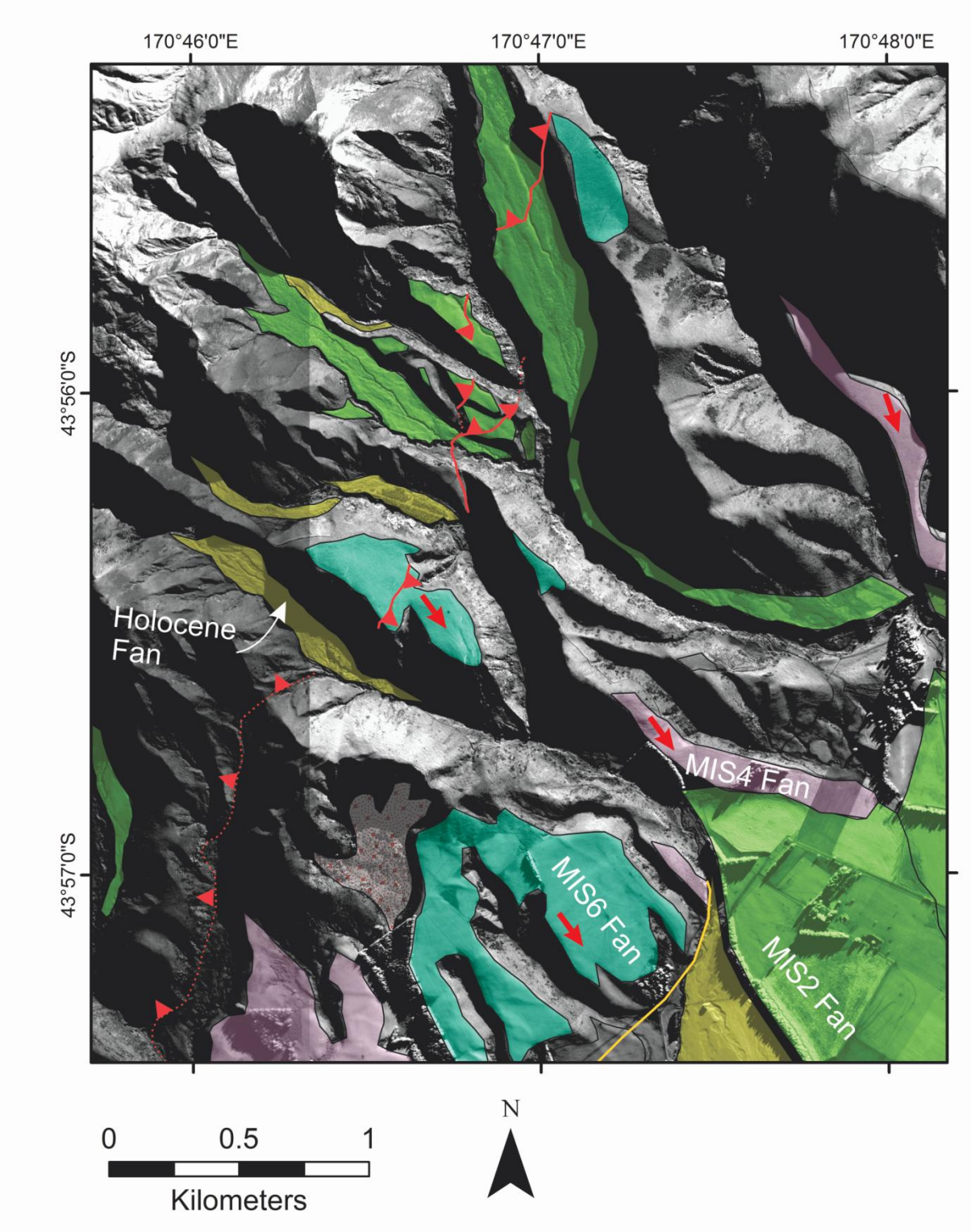

Figure 3.9:Tectonic and Quaternary geomorphic map of the Fox Peak Fault at Ribbonwood Station. Fan surfaces are given inferred MIS correlations based on modified mapping of Cox and Barrell (2007), observations of gravel in outcrop and elevation/tilt differences between surfaces. An unknown/possible fault (orange) bounds the rangefront in the Southeast. Late Quaternary fan surfaces are progressively steepened basinward (red arrows indicate direction of tilt), indicating either decreasing stream power or progressive folding through time. There is little evidence for Holocene surface faulting.

3.4.3 Fox Peak and Lilydale Stations

Northeast of the SCA, the main trace of the FPF becomes more continuous and localises near the rangefront (Fig. 3.10). The fault is generally confined to a single trace but splays into two or more sinuous traces near stream valleys. The fault dip in outcrop and as inferred by mapping is c. 55° (Fig. 3.11A), though it flattens where the fault crosses valleys in the SW (Fig. 3.11B, and as evidenced by scarp morphology).

Just north of the SCA, the western edge of a NE-trending syncline has uplifted fluvial terraces in the field area, enhances local drainage incision and coincides with a reentrant on the main FPF (Fig. 3.10). The terrace sequence just north of the SCA has likely formed in response to periodic uplift of the syncline and/or the SCA (i.e. in a W-E directed water gap). The North Opuha River channel narrows when crossing the fold, also suggesting ongoing uplift (e.g. Amos and Burbank 2007).

A prominent normal fault trace is present at an elevation of c. 1300 m (Fig. 3.10). It is unclear if this trace is an old, range-bounding reverse fault that has had its fault zone eroded (interpretation of James 1998), a part of an active range-front thrust-wedge, or sackung. Disruption and possible displacement of active gullies across the trace indicates normal motion that post-dates glaciation and is therefore likely to be kinematically or dynamically (ground shaking) linked to motion on the main FPF trace (Fig. 3.10). As this upper feature cannot be traced for more than 3 km with a variable scarp height and remains at an elevation of c. 1300 m, I consider it more likely to be sackung (e.g. McCalpin 2009), but is mapped as a possible (unknown) fault here.

Alluvial fans, debris-mantled slopes and landslides that grade to the same, prominent base level (a stream cut riser) above the North Opuha River are the most prevalent Quaternary formations in the area (Fig. 3.10). For mapping purposes, I tentatively assigned the surfaces an age correlation of late to post-LGM, similar to the assumed age of the fan at the South Opuha River. Younger landslides and river terraces that grade to below this prominent riser are offset by less across the FPF. Older surfaces were mapped based on MIS age correlations of Cox and Barrell (2007) and position in the landscape relative to age-dated deposits in the area (see below).

In the northern part of the field area, the throw across the fault rapidly diminishes into a subtle topographic step across a bedrock slope. Clear surface expression of faulting ends where indicated in Fig. 3.10); however, to evaluate the possibility of a longer active fault extending to the North (e.g. Berryman et al. 2002; Upton et al. 2004), I conducted further surveying and mapping in Butlers Creek.

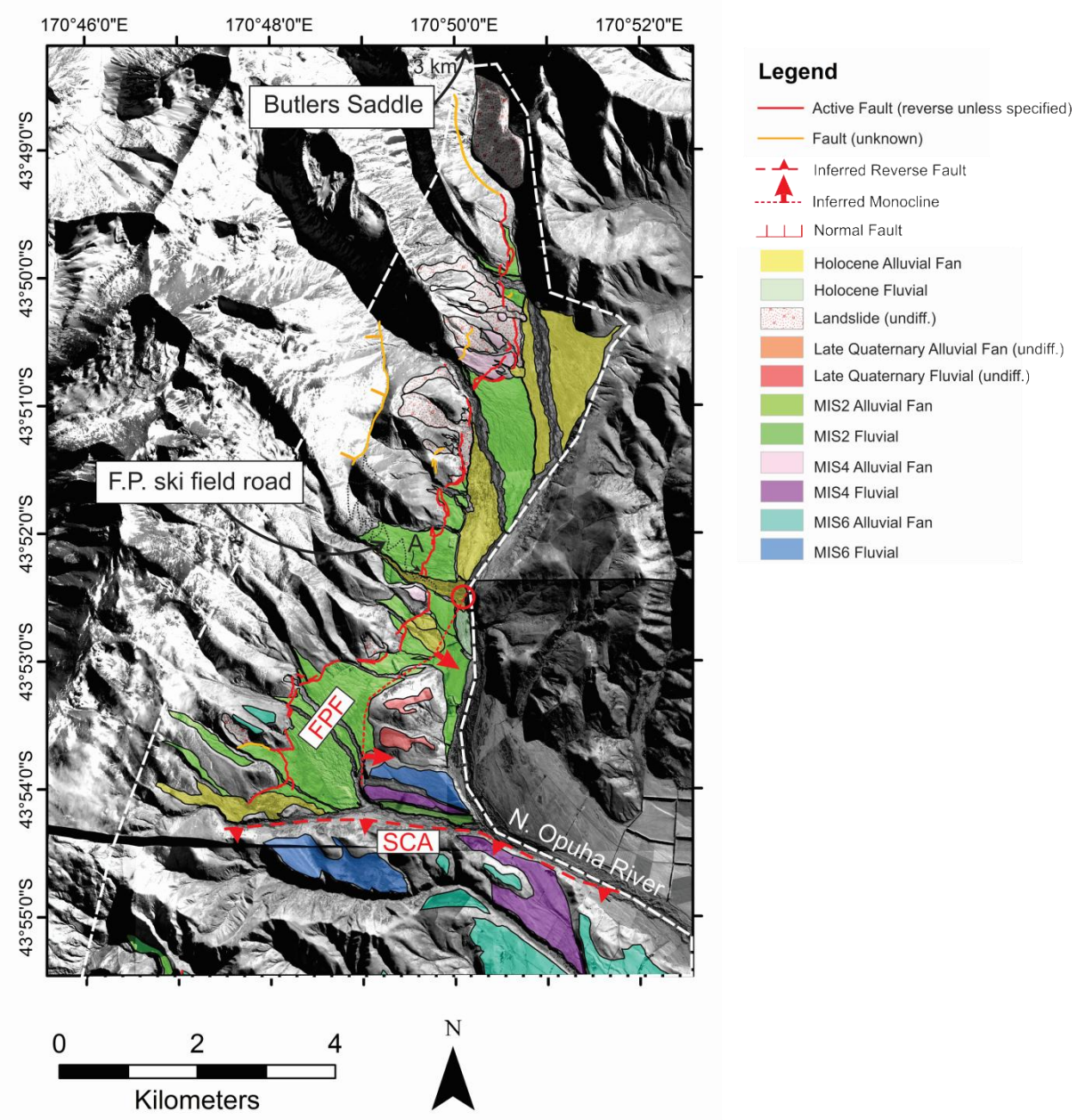

Figure 3.10: Tectonic and Quaternary geomorphic map of the Fox Peak Fault at Fox Peak and Lilydale Stations. Age control and MIS correlations are discussed in text. Debris mantled slopes and alluvial fans are not differentiated in my mapping as the former are rare (only present at Fox Peak ski field road) and closely resemble the latter. A NE-SW striking monocline (western edge of a syncline not in the map area) has been active in the late Quaternary. Fault traces of the FPF are often sinuous and splay into two or more traces around valleys. (A) is the location of Trench 4 (Section 3.7.3). Red circle is the location of the North Opuha River at its narrowest – an effect of the uplift of the frontal monocline.

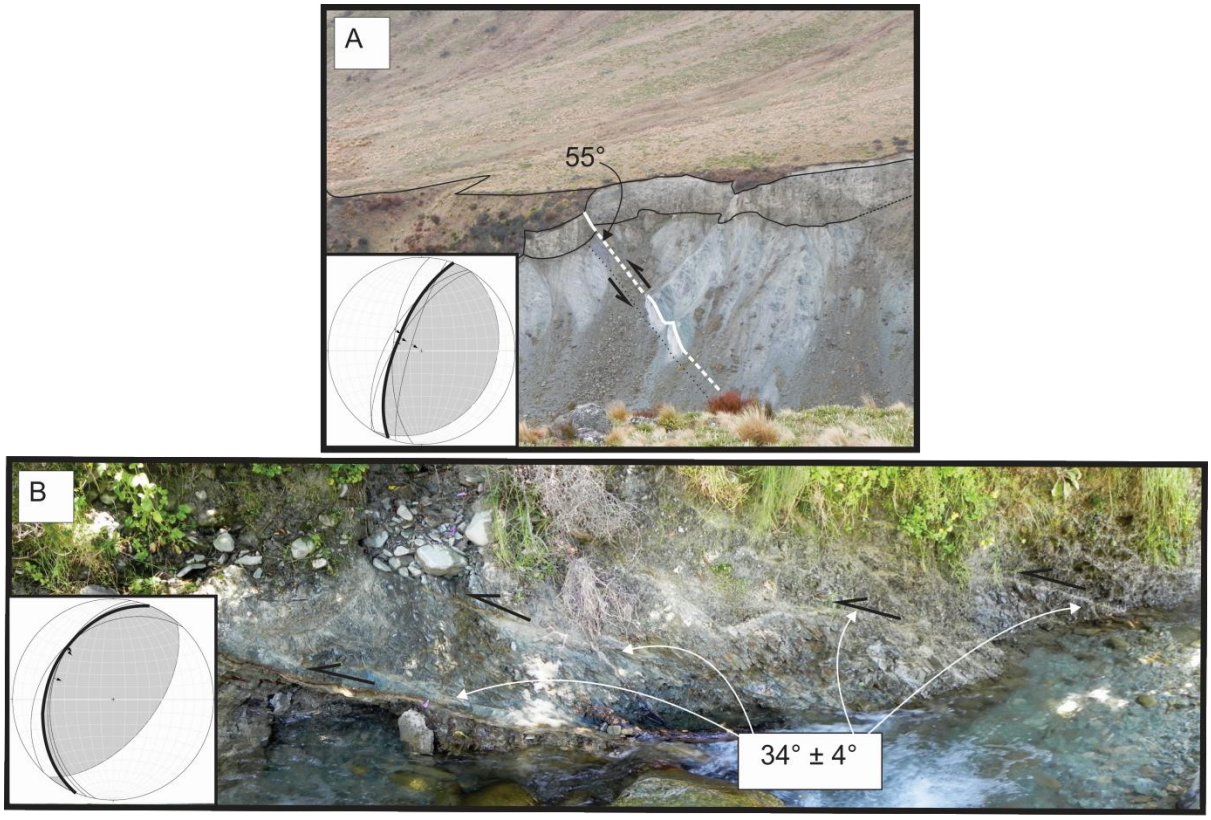

Figure 3.11: Fault outcrops and dip variability on Fox Peak and Lilydale Stations. (A) Moderately to steeply dipping faults are the most common geometries seen in outcrops (though there is no clear surface expression of this fault trace); (B) A stream exposure of gently-dipping fault splays (with fault dips indicated) coinciding with sinuous fault splays at the surface.

3.4.4 Butlers Creek

Butlers Creek flows North from Butlers Saddle – at the junction of the Sherwood and Ben McLeod Ranges (Fig. 3.2). Near the divide, lateral moraines and tarns indicate previous glaciation, probably dating to the LGM (Mabin 1980; Cox and Barrell 2007) (Fig. 3.1). The geomorphology in the lower reaches (i.e. within c. 5 km of Forest Creek) is dominated by landslides. Pliocene gravels, silts and clays (Kowai Formation) outcrop near Forest Creek, but are probably reworked in other locations where mapped by Upton et al. (2004) (Fig. 3.12) (Cox and Barrell 2007; this study).

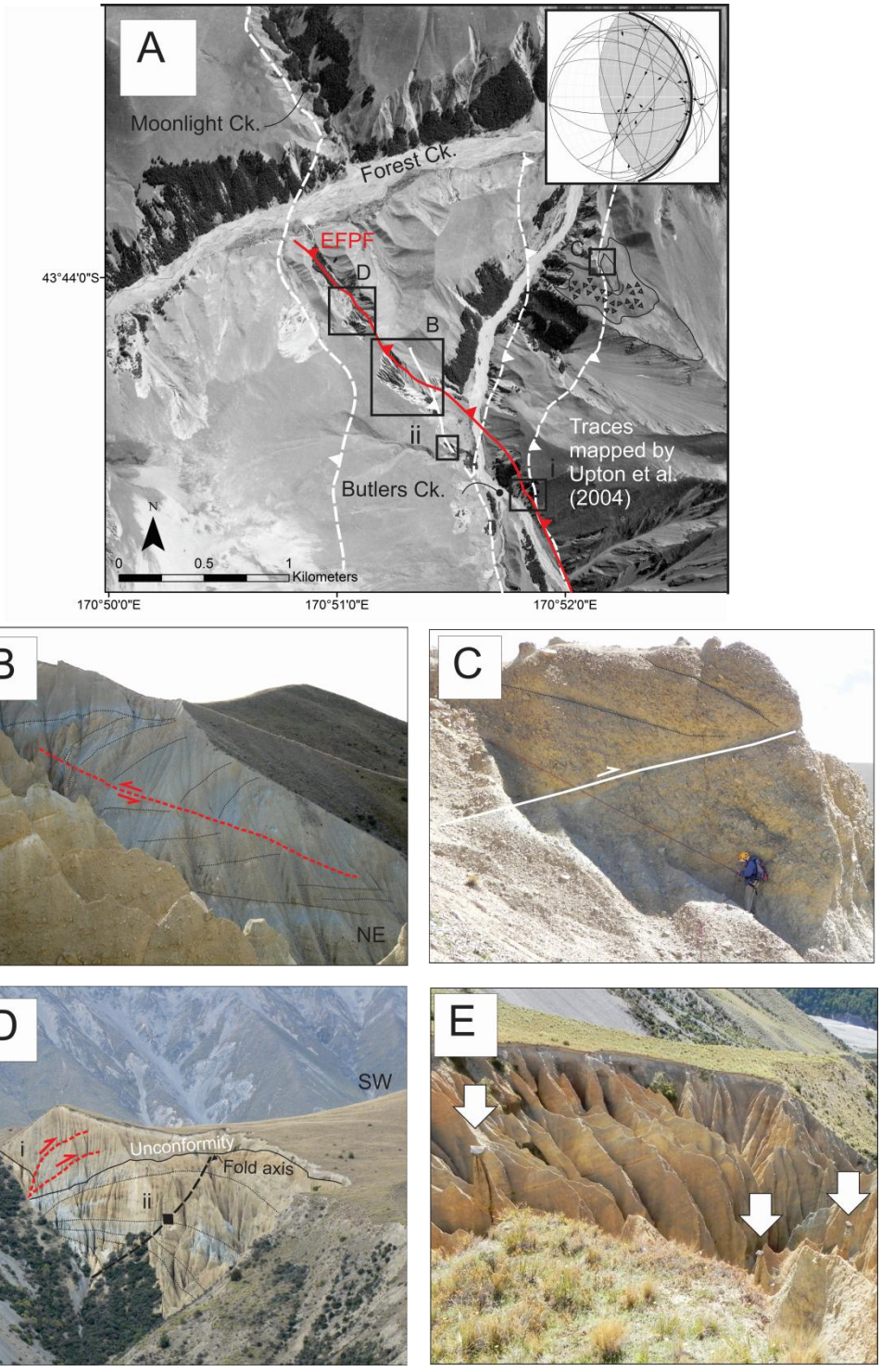

Figure 3.12: Overview of Butlers Creek faulting. (A) Previous mapping of fault traces by Upton et al. (2004) in white; the location of the 'western' FPF (in red, becomes the main fault to the South) is uncertain, as there is little evidence of active faulting; 'eastern' FPF (E. FPF) in black (mapping of this study). (i) Fig. 3.13 and 3.14; (ii) Fig. 3.15. Fault plane solution for all faults in Butler Creek provided in inset; the eastern FPF and related faults are the dominant plane. (B) Outcrop of the eastern FPF folding the Pliocene Kowai Formation, but not breaking the surface. (C) Outcrop of a non-tectonic landslide 'fault' along a tectonic trace mapped by Upton et al. (2004). (D) Looking South across Forest Creek where an outcrop of the eastern FPF in reworked Kowai gravels (i) coincides with a possible fold scarp. An antiform is developed in Kowai gravels (ii). (E) Precariously balanced rocks perched on hoodoos in outcrop seen in (D).

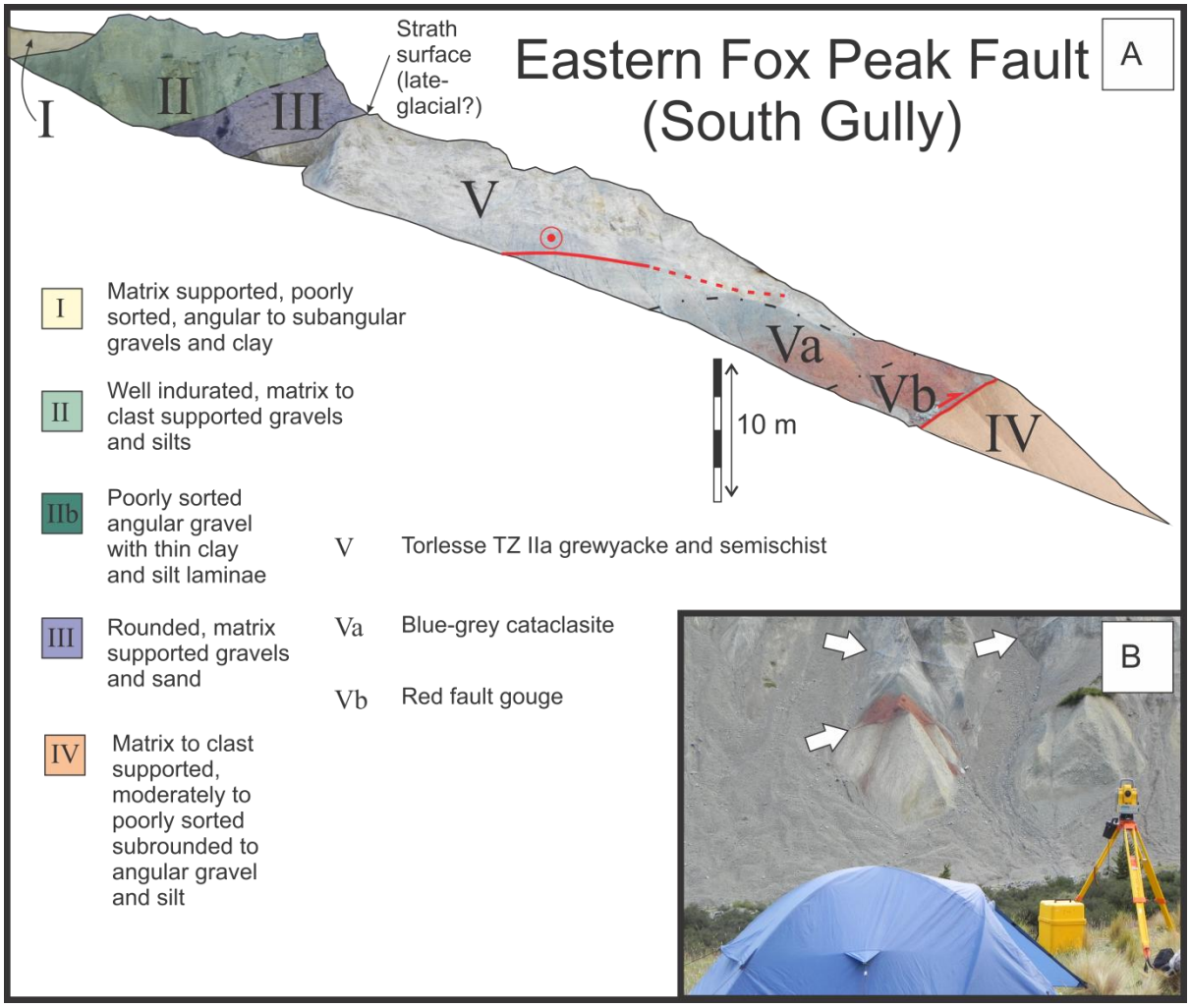

Figure 3.13: Exposure of the EFPF at Butlers Creek. (A) Interpreted panorama of the outcrop. The top part of the section shows late Pleistocene colluvium (I) and fan/debris flow deposits (II, IIb) overlying and grading into river gravels (III). The river gravels are deposited on a bedrock (Torlesse greywacke/semi-schist, V) strath, and are at a similar height above river level across the valley (i.e. on the footwall of the faults shown in the diagram). Torlesse greywacke becomes progressively disturbed in zones of cataclasite (Va) and gouge (Vb) nearer to the principal slip surface of the lower fault. The bedrock is thrust over gravels that resemble reworked Kowai Formation gravels elsewhere in the field area. Key applies to this figure and Fig. 3.14. (B) View of lower outcrop from across Butlers Creek, with arrows pointing to the locations of faults.

Despite the many fault outcrops in Butlers Creek, there is little evidence of active surface faulting. Faults in bedrock and Pliocene-Pleistocene gravels are predominantly NW-striking reverse and thrust faults collectively called the eastern FPF (EFPF) (Upton et al. 2004). This fault has been involved in the uplift of the Ben McLeod range to the East and forms one side of a narrow, fault-bounded basin at Butlers Creek. Most outcrops were inaccessible or did not show any evidence of late Quaternary deformation on seismogenic faults (Fig. 3.12B-E). A possible fold scarp is located immediately above gently-dipping fault traces over-thrusting a Kowai Formation antiform (Fig.

3.12D) and could indicate Pleistocene or younger uplift; however, the initial form of the offset hillslope cannot be reliably reconstructed to measure a displacement. The presence of precariously balanced rocks in the same outcrop suggests a paucity of recent strong ground shaking in the area, though the time required to erode the hoodoos on which the rocks are perched may be short compared with similar rock formations (Appendix 2).

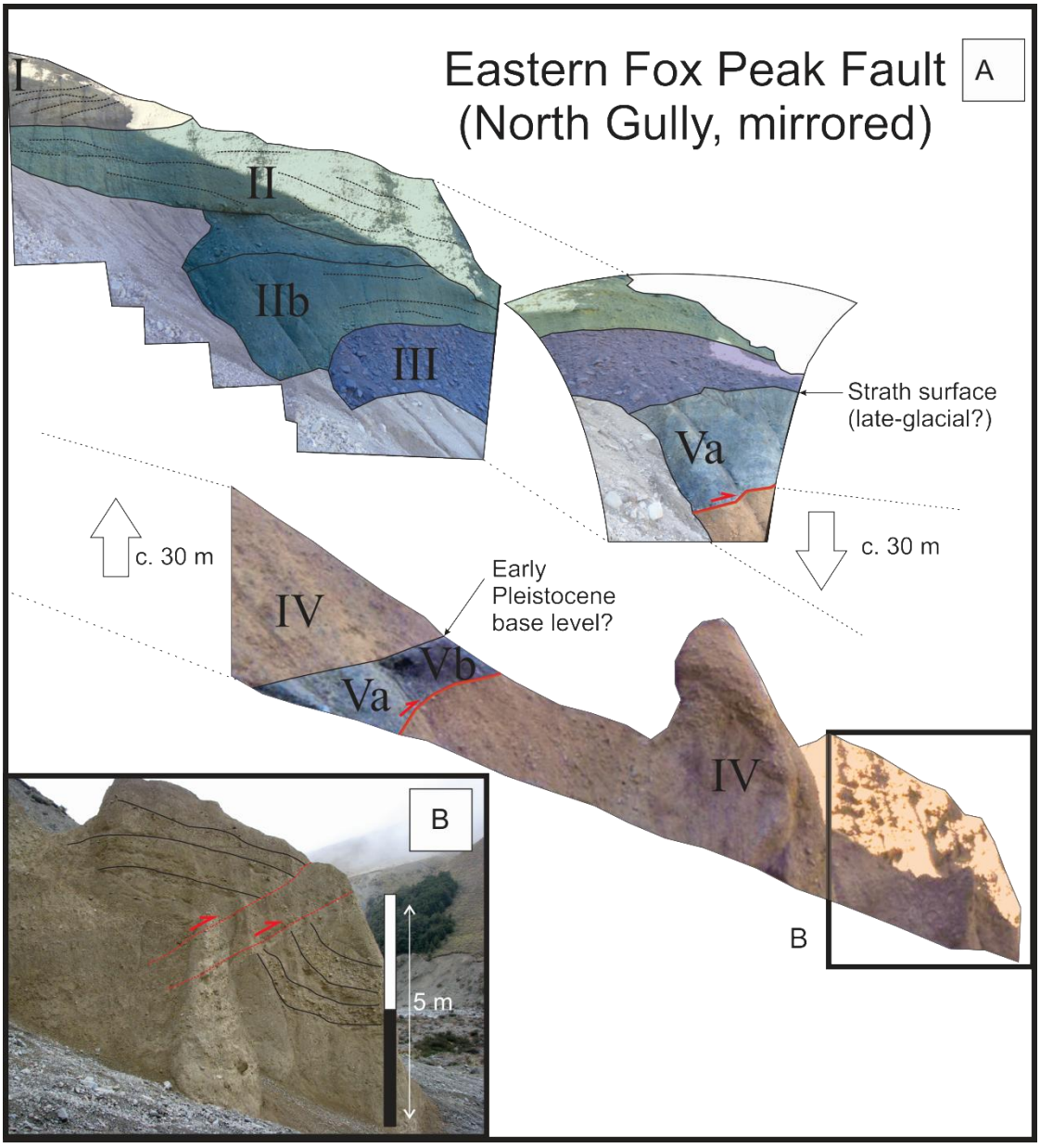

Figure 3.14: Outcrop of the EFPF just north of that shown in Fig. 3.13. Key is presented in Fig. 3.13. Top succession of colluvium (I), fan gravels (II and IIb), river gravels (III) and faulted bedrock (Va, Vb) is the same as in Fig. 3.13. Layers of fines dipping back into the hill slope in (I) may represent localised thrusting associated with the collapsing slope above the outcrop. A distinct hydrologic boundary separates (I) and (II), and is suggestive of the induration and relative ages of the two units. The upper fault at this location thrusts bedrock (V) over gravels of assumed early Pleistocene age (IV), which may be due to the variable preservation of the gravels between the sites in Fig. 3.13 and here. (B) At the base of the outcrop, gravels are drag folded along planes which are likely to be frontal splay faults of the main fault zone.

A strongly-oxidised outcrop of the EFPF in Butlers Creek (Fig. 3.13 & 3.14) reveals some indication of late Quaternary faulting. Here, Torlesse TZ IIa greywacke and semischist, often cataclastic and with a 1-2 m red to grey gouge zone at the principal slip surface, is thrust over gravels that resemble reworked Kowai Formation (i.e. a tentative age of early Pleistocene) elsewhere in the field area. Throw is greater than c. 40 m (Fig. 3.13). A strath surface is developed in the Torlesse bedrock above the two main faults, on which river gravels and fan/debris flow deposits are deposited. These same gravels form a prominent terrace across Butlers Creek (i.e. on the footwall of the faults) and are at the same elevation above the stream, suggesting no throw post-dating their deposition. The preservation of the terrace as a landform indicates that the gravels are likely to post-date the LGM (< 18 ka). The EFPF is unlikely to have slipped in at least the last 18 ka. Thus, while there is evidence for late Quaternary activity on the EFPF at two locations, there is a lack of compelling evidence to suggest it has been active over the Holocene and mid to late Pleistocene.

The trace of the 'western' FPF (Upton et al. 2004; 'WFPF') becomes poorly defined in Butlers Creek (Fig. 3.12). Upton et al. (2004) map an inferred trace along the steep hillside of the Butlers Creek basin and in a cataclasite outcrop near Forest Creek. At the time of this study, no definitive West-dipping fault planes could be observed in this outcrop. Faults observed across Forest Creek to the North are dominated by fault orientations that are inconsistent with the orientation of the FPF. A landslide that was observed to have possible cross-cutting, 'West-up' traces, and is at an elevation of Upton et al.'s (2004) WFPF trace, was surveyed using a continuous RTK rover attached to a backpack (Fig. 3.15A, B). The points (n = 1900) were gridded and smoothed to produce a digital elevation model of the landslide. No surface offset could be detected from this data (Fig. 3.15B).

A vertical fault outcrops 0.5 km north of the landslide site. Mid to late Pleistocene fan and river gravels overlie cataclastic Torlesse greywacke/semi-schist on the upthrown side (Fig. 3.15C). Here, the relative age of the Pleistocene gravels are distinguished from others by a gradational, West to East transition from fan gravels to river gravels. Measurements of imbrication directions in the lower, rounded gravels indicate that they were deposited by Butlers Creek in an orientation similar to that of the modern stream (Fig. 3.15C) (i.e. not Kowai Formation). The gravels are higher above the stream and more weathered than unit (III) in Fig. 3.13 and 3.14, and so must be older than the latest Pleistocene. On the downthrown side of the fault, there is a small amount of drag folding of interbedded fines, gravels and dark organic horizons, which may have accumulated behind the fault scarp when the gravels on the upthrown side were located near stream level. The fault has been active in the Pleistocene, but based on the landslide survey in Fig. 3.15B, displacement has been small, absent or pre-dates the landslide. The fault sense is opposite of what would be expected for the FPF, so the fault is either associated with the EFPF and uplift of the Ben McLeod Range, or is an antithetic

splay of the FPF. For the purposes of measuring surface rupture length in recent earthquakes, it is not considered to be an active trace of the FPF, which ends near Butlers Saddle to the South (Fig. 3.1, 3.10).

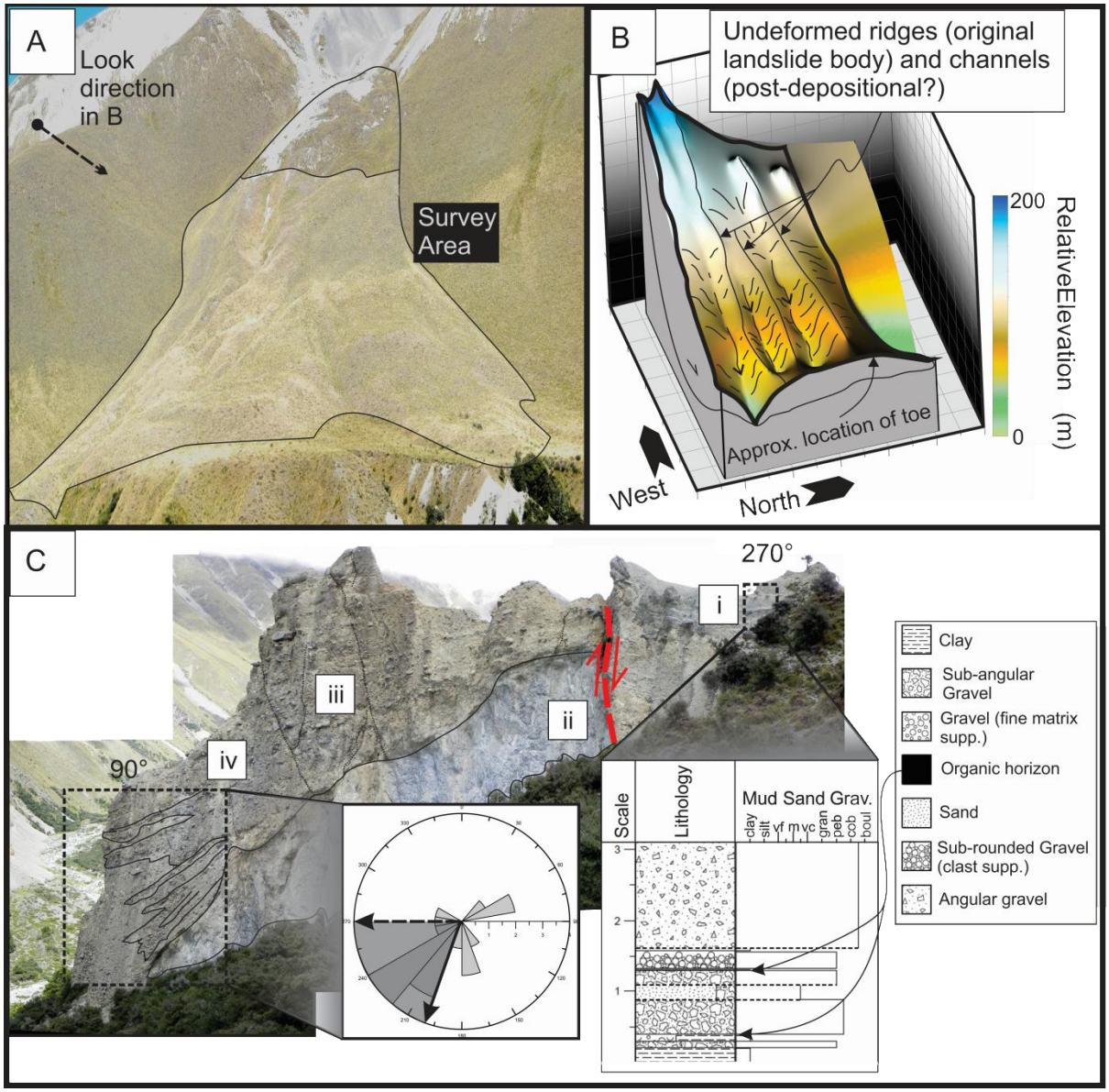

Figure 3.15: Investigation of possible FPF traces in Butlers Creek. (A) A landslide with some internal deformation resembling that of fault scarps. (B) An RTK survey revealed no clear evidence for faulting (elevation scale in metres). (C) Outcrop of a fault on the true left of Butlers Creek (looking due South). (i) Location of stratigraphic column (scale in metres); (ii) Cataclastic Torlesse grewywacke/semischist; (iii) Fan gravels with cross-cutting vertical fractures (not associated with faulting); (iv) Transition into rounded river gravels near the base of the outcrop. In the rose diagram, imbrication directions of rounded gravels parallel the modern stream (solid line, upstream direction) and are influenced by hillslope sedimentation (dashed line, direction of slope sedimentation. This pattern indicates that the gravels are younger than the Pliocene Kowai Formation, likely to be younger than unit (IV) in Fig.3.12 & 3.13 based on the presence of rounded clasts, and older than unit (III) based on weathering and elevation.

Although the Butlers Creek area contains reverse faulting associated with the modern plate convergence, there is little evidence of faulting like the pronounced activity on the main FPF to the South. From the surface expression of faulting, I calculate a surface rupture length of c. 36.5 km for the FPF, with three geometrically distinct segments delineated by structural boundaries. From South to North, these segments are hereafter referred to as the Cloudy Peaks, Ribbonwood and Bray (i.e. Fox Peak to Lilydale station) segments. The Cloudy Peaks and Ribbonwood segments have their northeastern terminations at intersecting NW-striking faults. The fault tips are located 2.5 km NE of Burke's Pass in the South and 1.5 km north of Butlers Saddle (Fig. 3.1).

3.5 Tectonic geomorphology of the Forest Creek Fault

3.5.1 Forest Creek

A c. 4 km long, uphill-facing scarp bounds the Two Thumb Range at Forest and Neutral Creeks (Fig. 3.16). The trace cuts across contours, corresponds to folds near the Rangitata River mapped by Cox and Barrell (2007), and has been imaged dipping deep into the crust (e.g. Wannamaker et al. 2002). The scarp has variable height and cuts across young hill slopes and channels with no indication of lateral offset. Upton et al. (2004) measured West-dipping, high-angle reverse fault planes and striae along strike of this trace, indicating that the normal fault trace seen at the surface is probably a result of the principal slip plane splaying near the surface in response to the topographic load (e.g. Khajavi et al. 2014).

Approximately 2 km SW of the Neutral Creek-Forest Creek confluence, the trace disappears into the Two Thumb Range (Fig. 3.1, 3.16). I infer the FCF to follow the Two Thumb Range to the South, following bedrock faults of Cox and Barrell (2007) rather than traces inferred by Upton et al. (2004). Surface expression picks up again in the South Opuha catchment with a much larger and broader uphill-facing scarp than in Forest Creek.

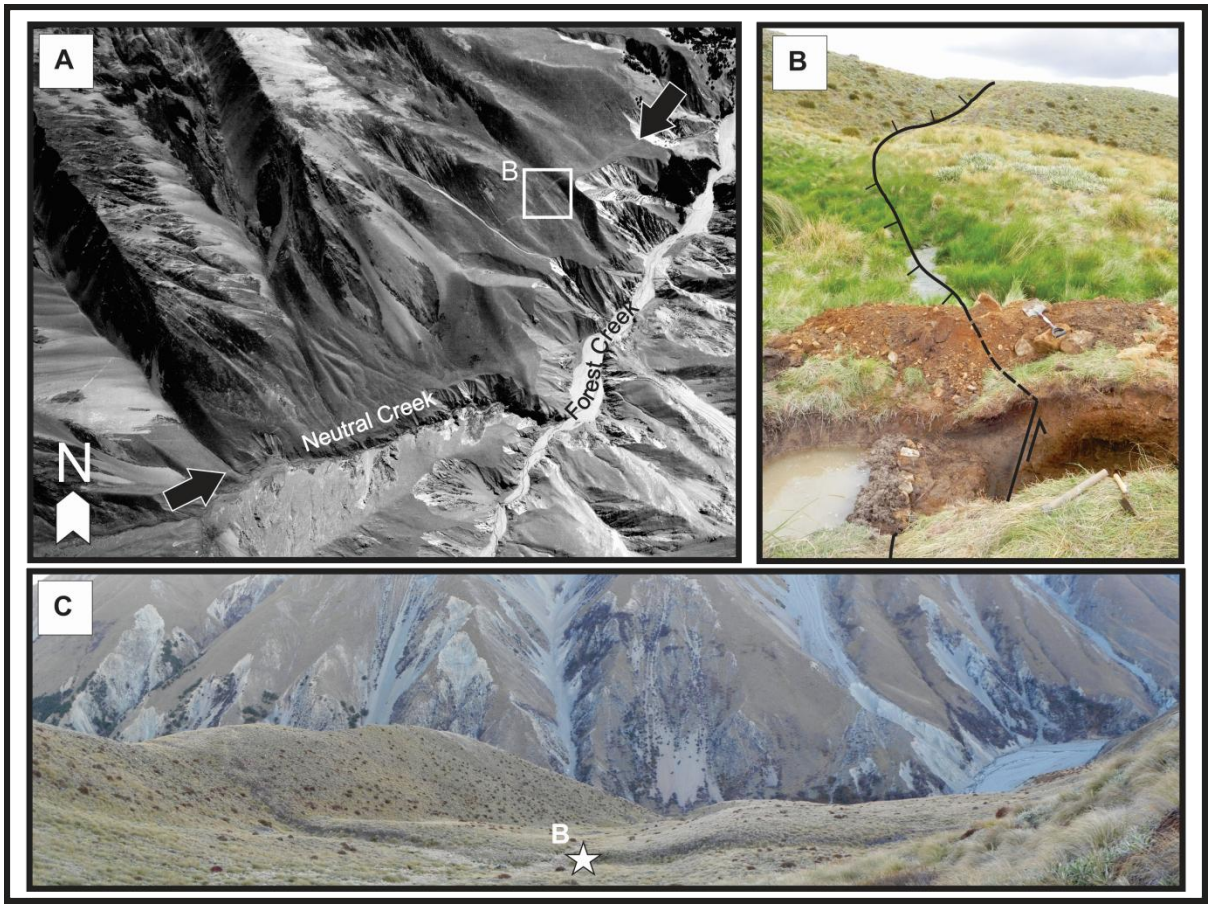

Figure 3.16: The FCF at Forest Creek. (A) Georeferenced aerial photograph of fault scarp, which runs for 4 km between the black arrows. Two Thumb Range is located to the NW of Forest Creek, the Sherwood Range to the SE. (B) Field photograph looking along strike and into a hand-dug exposure of the FCF. At the surface, relative motion is normal. (C) Field photograph looking down onto the FCF scarp and into Forest Creek.

3.5.2 South Opuha River to Mt. Dobson

A c. 50 m high 'ridge-rent' scarp begins 7 km south of the Forest Creek-South Opuha catchment divide and continues until reaching the lower slopes of Mt. Dobson (Fig. 3.17 & 3.18). Here, the scarp trends NE-SW and coincides with a fault outcrop on Mt. Dobson ski field road (Fig. 3.17). Interestingly, the fault does not dip into the slope, as would be expected for a continuation of the FCF from the North. The fault is reverse and dips to the southeast. This could be part of a larger fault zone, of which the exposed plane is only an antithetic splay. However, the juxtaposition of two textural zones of Torlesse greywacke/semischist, coincidence of the scarp at the surface, and a zone of cataclasite, implies that this is not the case. The fault could have been rotated to its current orientation, but this is also unlikely.

In their investigation of the Dunstan Fault in Otago, Beanland et al. (1986) also found that uphill facing scarps can be produced by reverse faults dipping out of the slope. They may form as pop-up or positive flower structures linked to rangefront faults in the foreland that dip into the slope. In this case, the rangefront fault is the imbricate wedge of the FPF at Cloudy Peaks Station, c. 3 km to the South (Fig. 3.18).

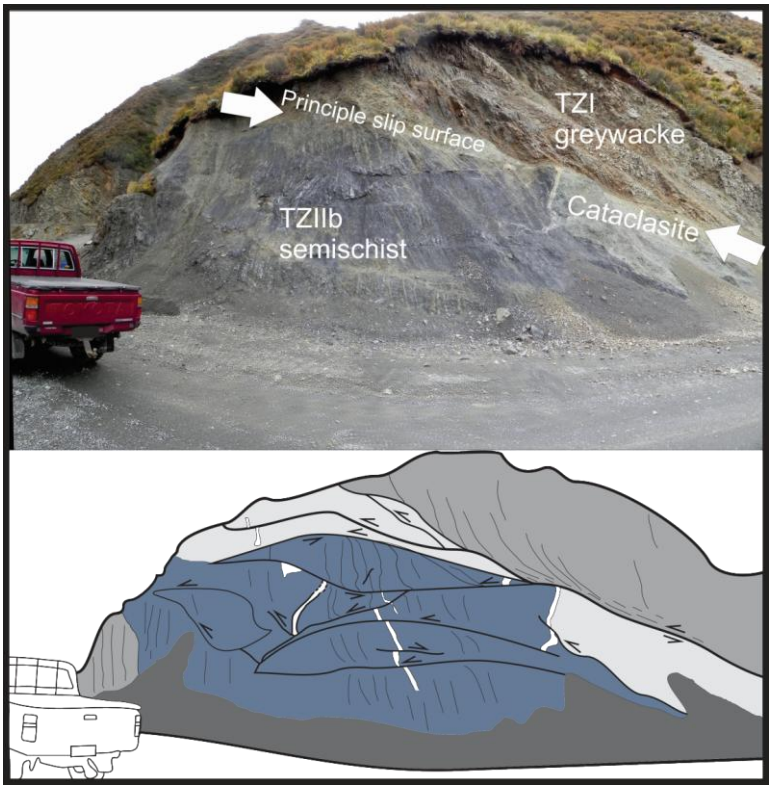

Figure 3.17: Fault outcrop at Mt. Dobson ski field road. Offset quartz veins and cataclasite indicate predominantly SE-dipping reverse motion in a zone of complex faulting.

There is no clear evidence of this scarp cutting recent surface deposits in the South Opuha River catchment. It is uncertain whether the fault becomes blind in this zone of steep topography (as clearly and abruptly occurs with the northern FCF trace) or has not ruptured following the abandonment of these terraces. However, the prominence of the scarp in quickly eroding, steep terrain points to towards recent activity and active uplift (Fig. 3.2 & 3.18). Its proximity to known, active fault traces, both along strike of the northern FCF trace and the FPF at its down-dip extent further suggests it is an active structure.

A combined northern and southern FCF surface rupture length could be as large as c 40 km. There is no evidence of segmentation though the geomorphic expression of the fault is poor compared to the FPF. A shorter surface rupture length of 15-21.5 km derived from the length of the scarp in Forest Creek and folds near the Rangitata River is possible (Fig. 3.1). However, given the displacement observed on the Forest Creek scarp, a 15-21.5 km length of fault would be unlikely to rupture in isolation.

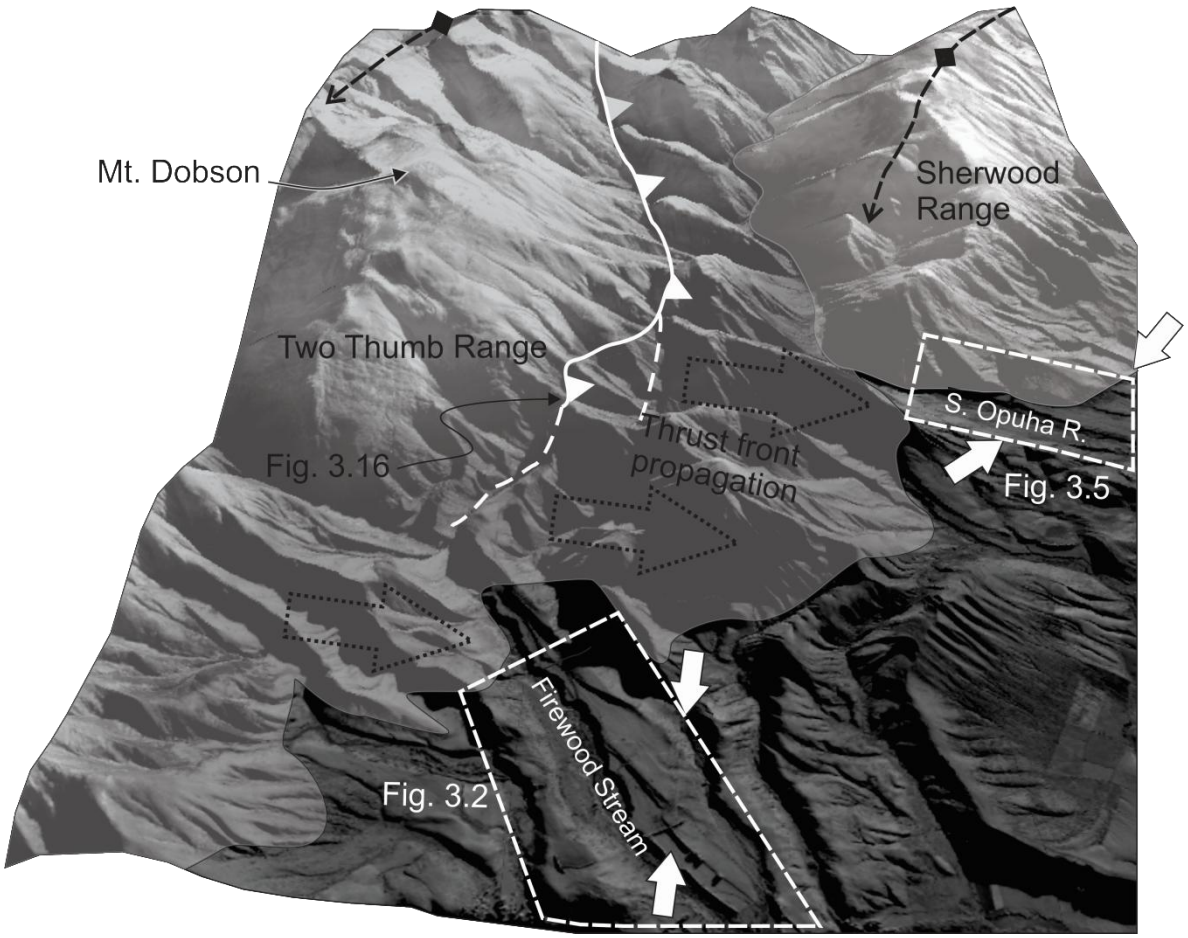

Figure 3.18: Northward view of the southern FCF from Cloudy Peaks Station. The surface is a near-infrared band satellite image overlain on a 15 m DEM with no vertical exaggeration. The location of Fig. 3.17 is shown just below Mt. Dobson. White arrows show principal fault traces of the FPF at Cloudy Peaks Station and the South Opuha River. The Cloudy Peaks traces of the FPF, which bound the Two Thumb Range, are inferred to be intermediary structures between the foreland propagating FCF to the West and FPF segments bounding the Sherwood Range, to the North.

3.6 Surface ages, net slips, and slip rates

The surface expression of the FPF is suggestive of geometric and structural segmentation. To determine if these segments slip at different rates, surface slip rates were obtained using high-resolution topographic surveying of fault scarps and dating of deformed geomorphic surfaces. Fault geometry and kinematics measured in natural exposures, trenches and GPR were used to define slip

vectors and fault position along the scarp. Below, I outline the methodology behind each component that was used to calculate net slip and slip rate calculations.

3.6.1 Survey data

Scarp profiles were measured using a combination of real-time kinematic (RTK) GPS, a differential GPS (dGPS), and a Trimble 5600 DR200 Total station. RTK data was collected with a Trimble R8 receiver fixed to a stadial rod and has an internal vertical accuracy of 15 to 30 mm. Its usage was the preferred method to collect point profiles in the field, where practical. A handheld Trimble GeoXH dGPS was used in difficult terrain, to check RTK data, to collect dense point assemblages (continuous recordings taken every 1 s) for critical sites, and fix RTK and Total station base stations. It has an estimated internal vertical accuracy of 10-50 mm. Total station use was restricted to Cloudy Peaks, where it was used in conjunction with other techniques to accurately survey scarps and create a micro-topographic map of a paleoseismic trench site. The internal accuracy of the Total Station is less than 2 mm.

A total of 140 fault scarp profiles (inclusive of repeat profiles using different survey techniques) were collected along the length of the FPF (Fig. 3.19, Digital Supplementary Information). Examples of survey data are shown in Fig. 3.20-3.22. At Cloudy Peaks (Fig. 3.20), the listric geometry of the faults seen in outcrop is clearly shown in backtilting of T1 and T2 (folding shown with stream gradient removed). While no efforts are made here to calculate fault slip based on this folding (e.g. Amos et al. 2007), it is clear that the radius of curvature is relatively small- the folding dies out over < 0.5 km at which point the normal terrace gradient is resumed. This is also in accordance with the outcrop pattern (Fig. 3.4).

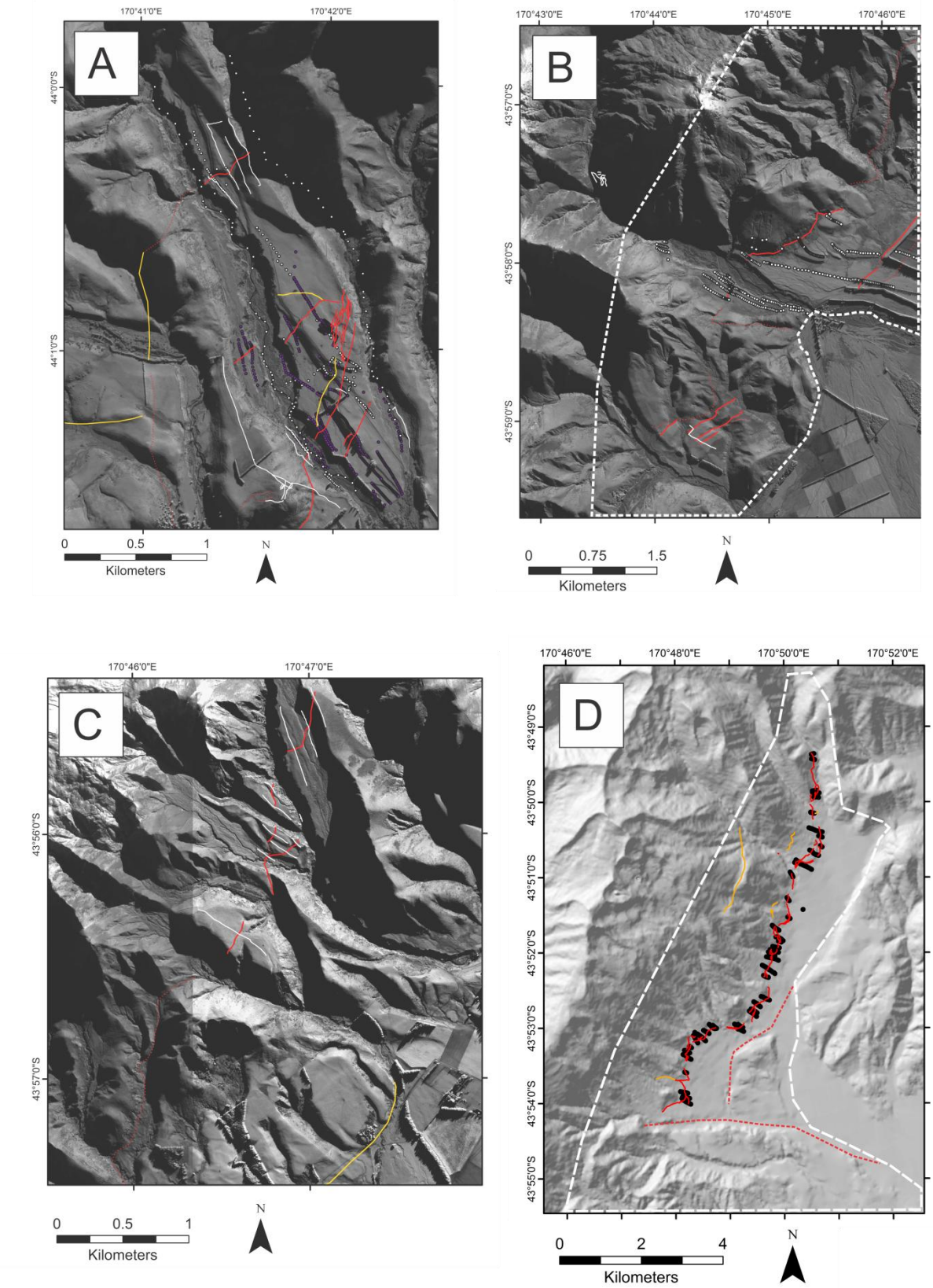

Figure 3.19: Overview and extent of survey lines across the FPF. (A) Cloudy Peaks Station: GPS (RTK and dGPS) data in white; Total Station points in purple; (B) South Opuha River: RTK points in white; dGPS lines in white; (C) Ribbonwood Station: dGPS lines in white; (D) Bray Segment, RTK profiles in black.

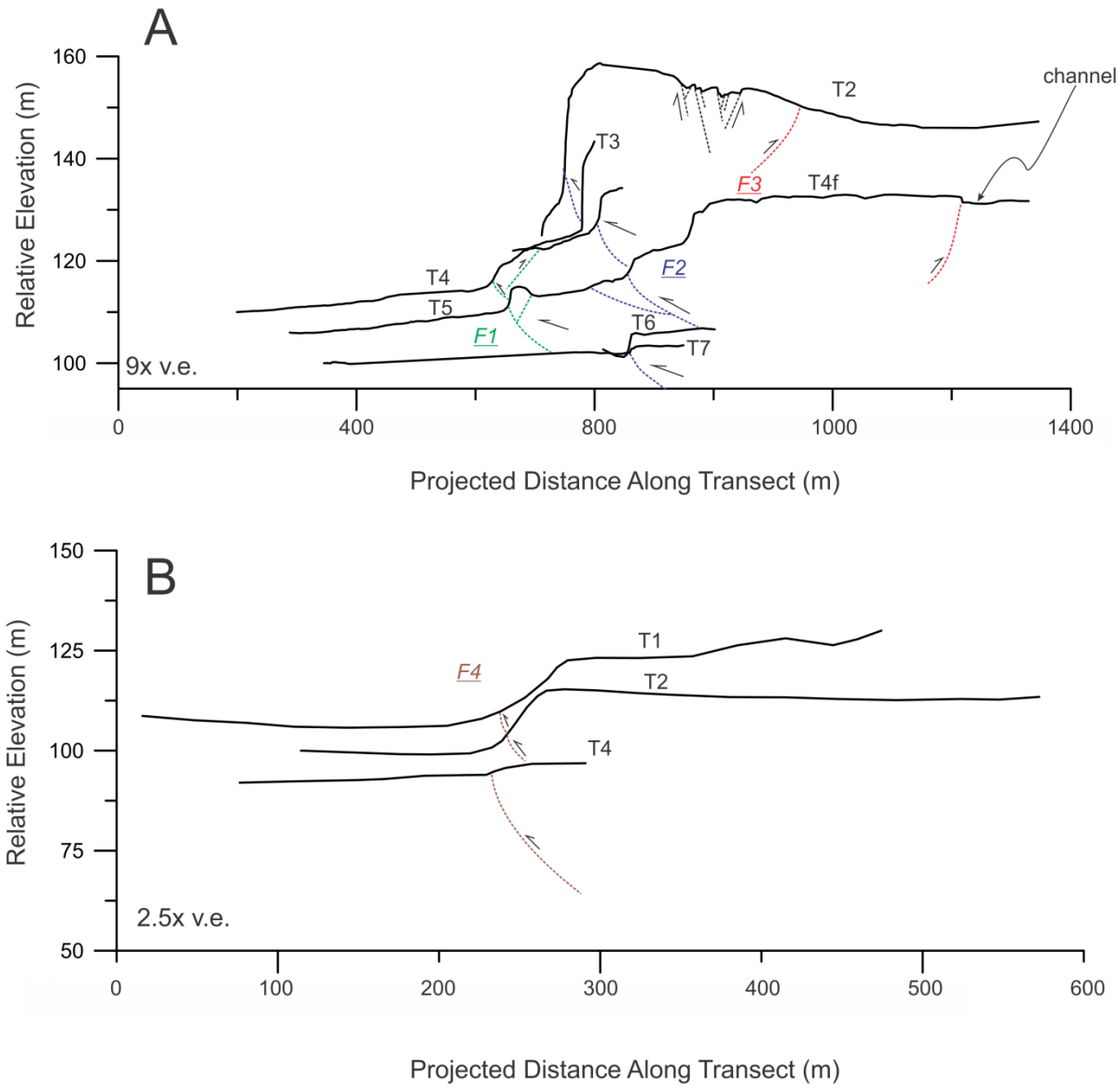

Figure 3.20: Example of fault scarp/terrace long profile survey data at Cloudy Peaks Station. The modern stream gradient has been removed to show the extent of listric folding. (A) The frontal 3 faults (dips and geometry not drawn to scale) cutting across all terraces except T4a and T1; (B) Fault 4 at T1, T2, and T4. Only T4 crosses all of the faults

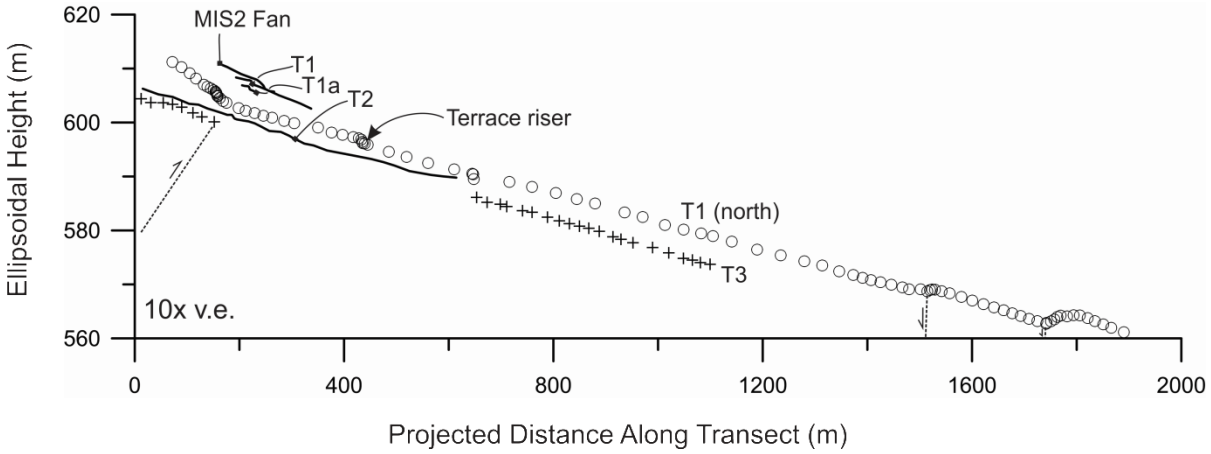

Figure 3.21: Fault scarp/terrace long profiles from the South Opuha River terraces.

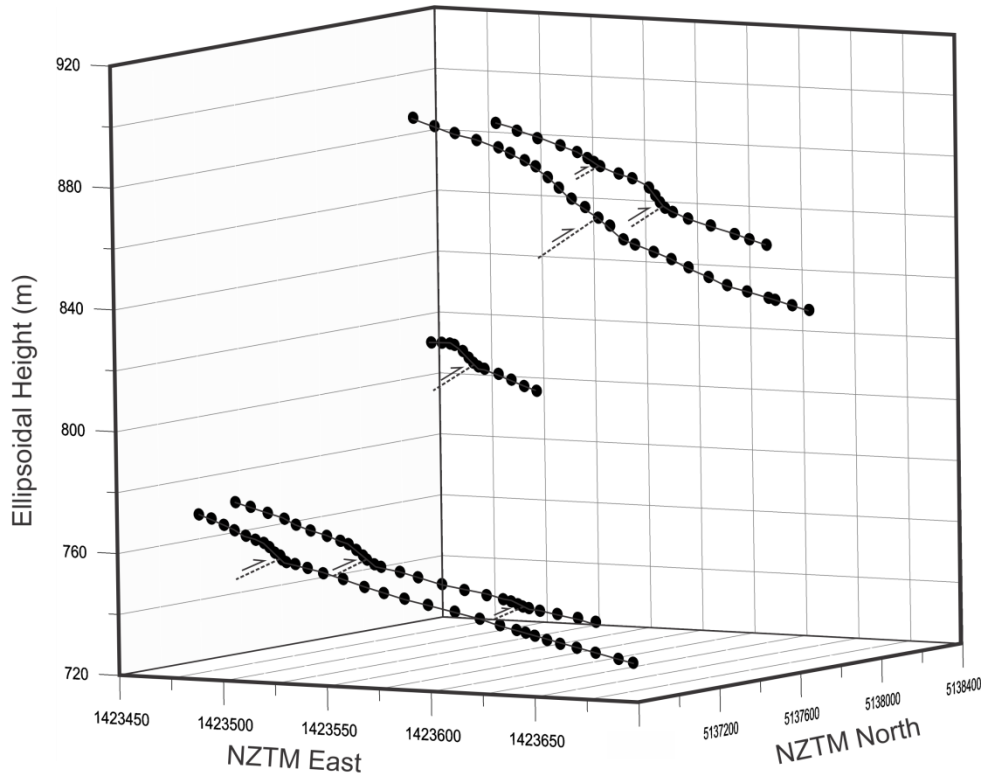

Figure 3.22: Examples of fault scarp profiles from the Bray Segment. Transverse Mercator projection: Northing and Easting units are in metres.

3.6.2 Fault dip and position along scarp

Fault dips were determined in the field by direct measurement in outcrop, trench exposures (e.g. Fig. 3.23C, see below) or via projection across landforms (e.g. terrace risers and treads). Where these data were not available, the fault plane solution for a given area and surface expression of the fault were used to infer a range of fault dips. Where a single fault trace splayed into 2 or more, closely

spaced traces at topographic lows (e.g. Fig. 3.10 & 3.11B), trench data and 'anastomosing' fault traces indicate a flattening of the fault plane at the surface. A range of gentler fault dips were used for net slip calculations at these locations (Digital Supplementary Information).

The position of the fault along the scarp was likewise determined from a combination of natural exposures and trenches. At Cloudy Peaks, ground penetrating radar (GPR) was used to further investigate fault dips and the positions of fault plane-scarp intersections. GPR imaging was conducted using a Sensors & Software pulsEKKO system, with both 100 and 50 MHz antennas. The antennae were manually stepped in 0.1 to 0.5 m increments along the surface. The profiles were migrated using a velocity of 75 m μs^{-1} which was obtained using a central midpoint analysis. Faults were inferred based on disruption and/or offset of reflectors and were 'ground-truthed' at one location (Fig. 3.23A, C).

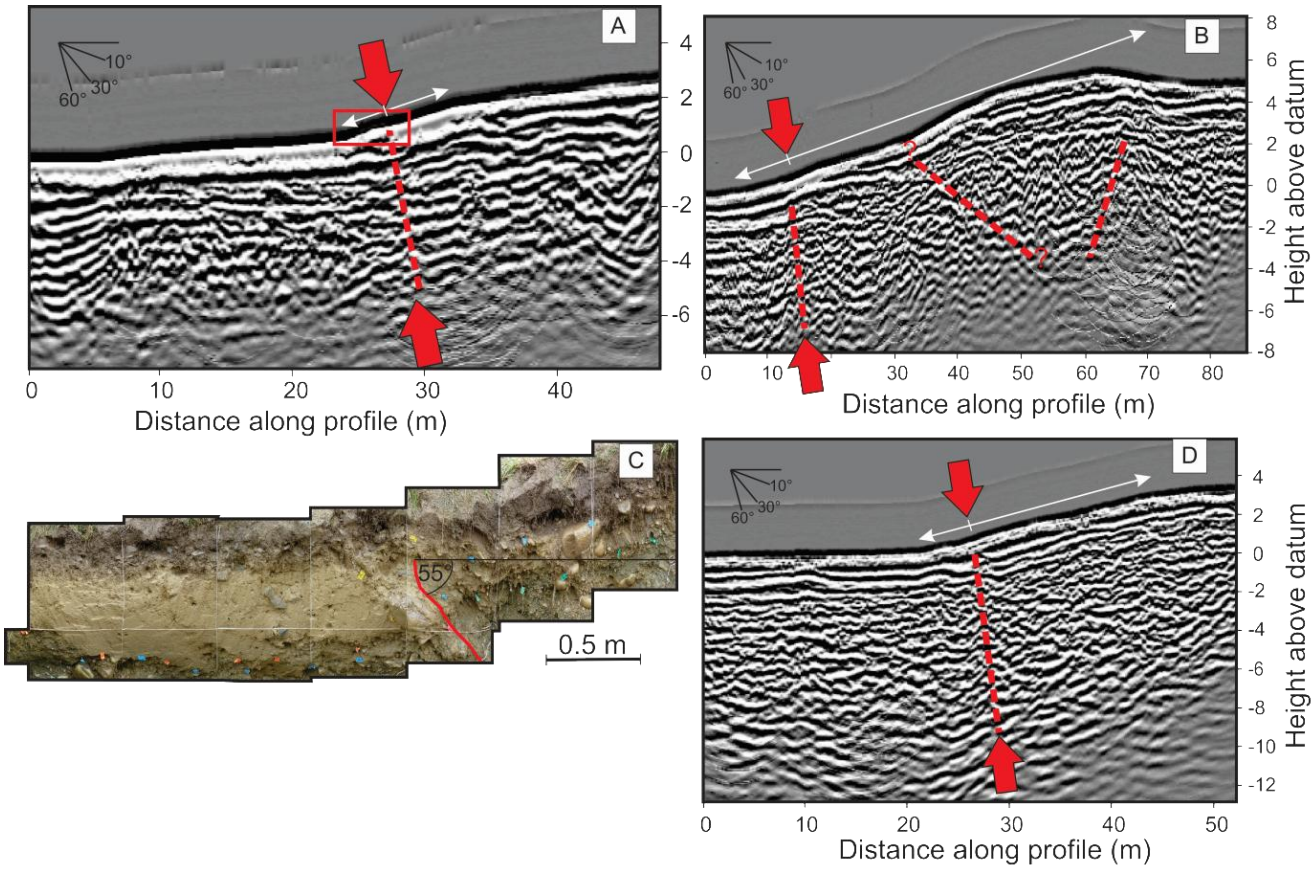

Figure 3.23: GPR of three Cloudy Peaks station fault scarps. (A) The youngest scarp across T7. Red square is location of (C); (B) A pop-up structure on T5 with three possible fault traces in the subsurface; (C) Photomosaic of trench across young scarp on T7. The similar dips of the fault in the trench match those of the interpreted GPR; (D) Fault 4 across T4 (see Fig. 3.20B).

3.6.3 Net slip

I used the method of Thompson et al. (2002) for fitting linear regressions to surfaces across fault scarps and calculating fault slip. The slope and intercepts of lines projected perpendicular to fault strike and fit to the hanging wall, scarp, and footwall were determined along with their standard deviations. The net slip then is a function of these lines, fault dip (Section 3.4), and the point of intersection of the fault with the scarp face.

Where profiles traversed two or more faults (e.g. widely spaced backthrusts or subsidiary synthetic faults), the survey line was broken into components with the aim of calculating slip on each fault. Where fault geometry was uncertain due to closely spaced backthrust 'pop-up' structures, line-length shortening was resolved onto the dominant fault mechanism at the site to calculate net slip (e.g. Fig. 3.20, Fault 2). Net slips were calculated from vertical separations on terraces that were discontinuous across a fault by assuming fault and scarp geometries from adjacent terraces. Hanging wall gradients of backtilted terraces were taken near the scarp-hanging wall interface. I do not consider interseismic strain accumulation as a contribution to the observed offset (e.g. Amos et al. 2007).

3.6.4 Surface ages

Where possible, I used OSL to date silts and sands in exposed alluvial deposits (Table 3.1). Trench exposures with detrital charcoal provided age constraints on terrace formation, but ages typically pre or post-date depositional processes that created the original surface (Section 3.7) and are excluded here. Ages of some regionally extensive fan surfaces were inferred where mapping and correlation with surfaces and deposits of known age allowed me to have some confidence in their approximation (after Cox and Barrell 2007; Quigley et al. 2007) (Section 3.4). For river terraces with embedded surface clasts of Torlesse greywacke, I used Schmidt hammer exposure-age dating (SHD) to derive calibrated ages (see below). These ages were processed following the methodologies set out in Chapters 1 and 2 (Stahl et al. 2013).

3.6.4.1 Absolute ages

OSL samples were taken at two locations. At the Fox's Peak ski field road, a sample was taken from channel deposit silts embedded within an alluvial fan/debris mantled slope (Fig. 3.24A). At Cloudy Peaks, an OSL sample was taken from fluvial sands in a hand-dug pit on T4 (Fig. 3.24B, location in Chapter 1, Fig. 1.1B, G). Both are representative of surface ages as their locations near the top of the depositional sequences are maximum ages for the timing of surface abandonment.

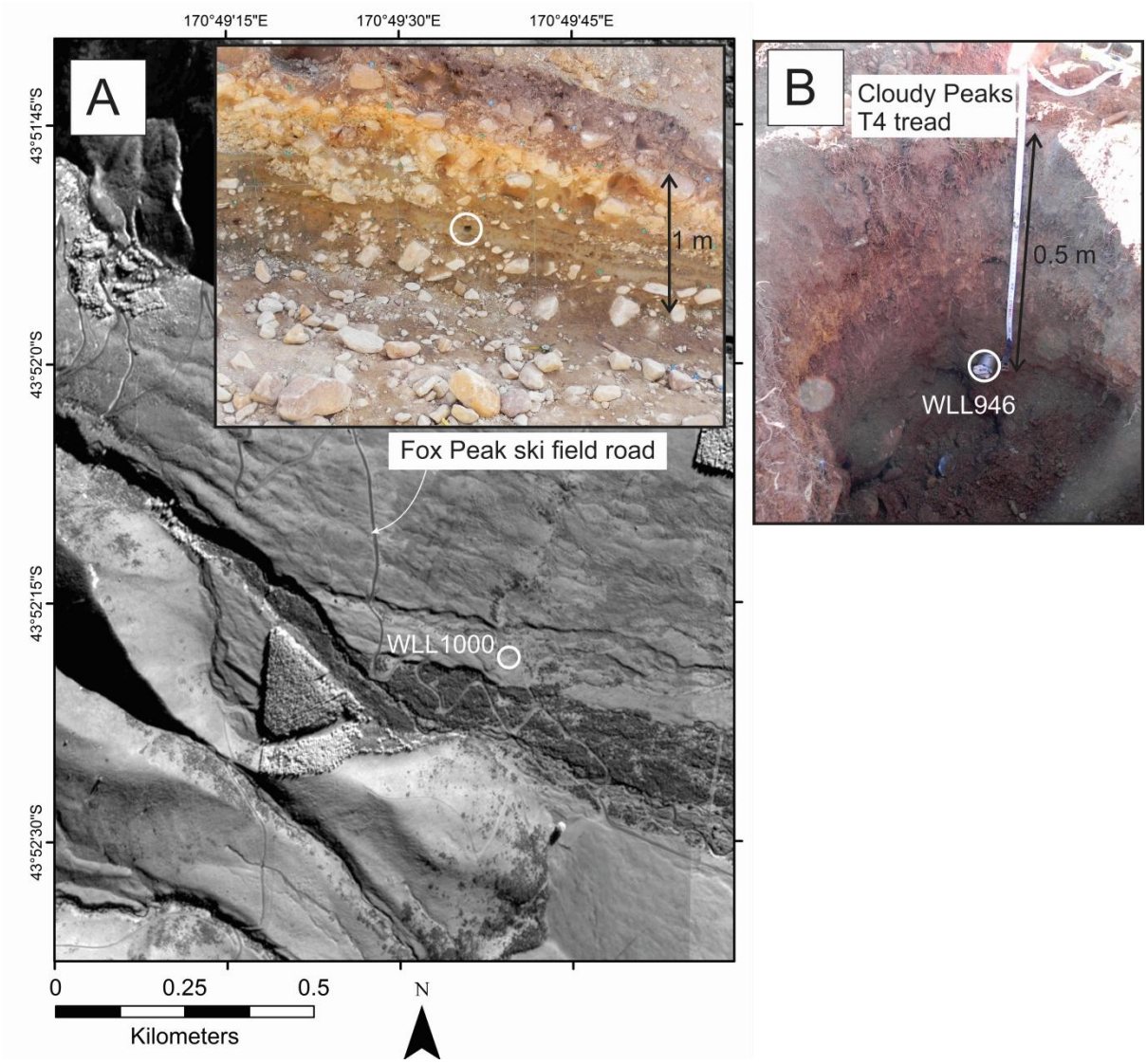

Figure 3.24: Locations of OSL samples for determination of surface ages. (A) At Fox's Peak ski field road (Bray Segment of the FPF). (B) At Cloudy Peaks Station, T4.

Table 3.1: OSL sample ages and measurements

Sample Number*	**Deposit**	**Depth**	**Lat/Long**	**dD_e/dt (Gy/ka)** [§]	**Water Content (%)**	**K (%)**	**U (ppm) from ^{234}Th**	**U (ppm) from ^{226}Ra, ^{214}Pb, ^{214}Bi**	**U (ppm) from ^{210}Pb**	**Th (ppm) from ^{208}Tl, ^{212}Pb, ^{228}Ac**	***a* value**	**D_e[†] (Gy)**	**dD/dt[§] (Gy/ka)**	**OSL Age**
WLL946	Fluvial sand (T4 at Cloudy Peaks)	0.5 m	-44.017, 170.693	0.2162 ± 0.0108	17.3	1.97 ± 0.04	2.69 ± 0.21	2.49 ± 0.12	2.08 ± 0.16	10.53 ± 0.12	0.05 ± 0.01	88.74 ± 8.70	3.57 ± 0.17	**24.8 ± 2.7 ka**
WLL1000	Alluvial channel silt (Alluvial fan / debris-mantled slope on Fox's Peak ski field road	1.0 m	-43.872, 170.827	0.1978 ± 0.0099	23.5	2.15 ± 0.04	**3.39** ± 0.26	3.29 ± 0.16	3.43 ± 0.22	13.35 ± 0.15	0.06 ± 0.02	67.57 ± 6.50	4.13 ± 0.32	**16.4 ± 2.0 ka**

*Sample preparation and measurements performed at School of Earth Sciences, Victoria University of Wellington, Wellington, NZ

[†]Equivalent dose

[§]Doserate.

*Sample preparation and measurements performed at School of Earth Sciences, Victoria University of Wellington, Wellington, NZ

[§]Contribution of cosmic radiation to the total doserate.

3.6.4.2 Schmidt hammer exposure-age dating (SHD) of fluvial terraces

At Cloudy Peaks and the South Opuha River, SHD was used to date Torlesse greywacke surface clasts. Semi-schist (TZIIa or b) clasts were avoided during sampling; however, the possibility that they were inadvertently sampled increases the error in age calculations. The age of the oldest terrace at Cloudy Peaks (T1) was assumed to be younger 100 ka to confine other terrace age estimates to realistic bounds. Given previous age estimates of all of the terraces being c. 18 ka and younger, I consider this assumption to be reasonable. The *a*-value (Eqn. 1.1) for South Opuha was calculated from the same climate and petrographic data for Cloudy Peaks (Chapter 1, Table 1.3) adjusting for temperature lapse rate (*a=269)* (Stahl et al. 2013). The topmost degradational terrace was assumed to be younger than 18 ka as per field observations (Section 3.4.2), but this assumption did not significantly affect the results. Input parameters, age constraints for rejection sampling, and age outputs are summarised in Tables 3.2 and 3.3.

Table 3.2: SHD data from river terraces at Cloudy Peaks

Terrace	Age control	Bootstrapped SH_R	SH Exposure Age (ka) (5^{th} and 95^{th} Percentiles)
1	<100 ka	31.8	72^{+25}_{-32}
2	<T1	34.4	48^{+32}_{-20}
3	<T2	36.5	35^{+25}_{-10}
4	= 24.8 ± 2.7 ka	39	24.8 ± 2.7
4a	<T4	41.6	$17.6^{+6.2}_{-8.4}$
5	<T4a	44.9	$11.7^{+6.8}_{-5.5}$
6	<T6	48.6	$7.7^{+6.2}_{-4.1}$
7	<T6	55.8	$3.7^{+3.5}_{-2}$

Table 3.3: SHD data from the South Opuha River terraces.

Terrace	Age control	Bootstrapped SH_R	SH Exposure Age (ka) (5^{th} and 95^{th} Percentiles)
1	<18 ka	44.8	$13^{+3.6}_{-3.8}$
2	< T1	48	$9.1^{+2.1}_{-2.6}$
3	<T2	51.1	$6.5.^{+2.2}_{-1.8}$
5	<T3	55.6	$4.2.^{+1.7}_{-1.3}$

3.6.5 Slip Rates

A Monte Carlo simulation was used to calculate uncertainty in fault slip rates (e.g. Thompson et al. 2002). Random samples derived from input probability distribution functions (PDFs) of scarp profile regression statistics (Section 3.6.3), fault geometry (Section 3.6.2), and surface ages (Section 3.6.4) were used to calculate output histograms of net slips and slip rates. The shape of the input distribution depends on the accuracy to which the input parameter was measured or estimated in the field, or calculated from SHD ages. Scarp profile intercepts and slopes were modelled as normal PDFs (Thompson et al. 2002). For fault dips, normal PDFs (i.e. defined by a mean and standard deviation) were used where measurements could be taken from outcrops, trenches, or GPR and matched well with surface scarp morphology. Where dip measurements were taken from outcrops not correlating with surface scarps, or were inferred based on scarp morphology, a trapezoidal distribution was used for fault dip. Trapezoidal distributions of fault position along scarp were derived from measurements in outcrop and subsurface data and vary from site to site. I used discrete distributions of the SHD ages derived in Section 3.6.4 rather than pre-specifying a distribution. Ages constrained by OSL and mapping were modelled as normal PDFs. Where minimum and/or maximum ages were designated based on mapping and climate correlation, uniform distributions were used to model the inferred ages.

In this study, the form of output slip rate distributions range from approximately normal to long-tailed, highly skewed (e.g. log normal). For consistency, I report medians and associated 5^{th} and 95^{th} percentiles as the best representative values for both types of distributions (Digital Supplementary Information). Reported slip rates are subdivided into minimum (e.g. surfaces with younger deposits in the footwall than on the hanging wall, the surface is not offset by all faults in area, or only the maximum age is known), maximum, inferred (surface age inferred), good (based on a high degree of confidence that the mapped surface correlates to a dated one), or best (based on the age of a dated surface) rates.

3.6.6 Segmentation of the Fox Peak Fault

Slip rates were plotted against distance along the FPF (Fig. 3.25). The 'best-fitting' line was drawn through the highest quality and/or average slip rate data points and further constrained by slip rate minima and maxima. The fault tips, which are slightly extended to 40 km in the graph, are assumed to have slip rates equal to zero. The shape of the slip rate profile shows covariation with the topographic profiles of the Sherwood and Two Thumb Ranges, which were constructed by drawing elevation profiles along the ridge crest of each in a 15 m DEM and projecting onto distance along the FPF. A detailed fault trace map is provided below the diagram (Fig. 3.25)

Slip rates are integrated over varying timescales reflecting the distribution of offset features of different ages. Thus, temporal slip rate variations are not accounted for, though they are apparent on at least the Cloudy Peaks segment. Here, the best slip rate is calculated from the displacement of T4 (red square), which is offset across all identified faults (Fig. 3.25). Most slip rate minima for other terraces fall below this data point; however, two minima are actually higher rates than that for T4. For instance, the highest rate was calculated for T2, despite not taking into account possible displacement on the frontal fault (i.e. Fault 1 in Fig. 3.20A) which does not cross T2. This fault may have started accommodating some of the fault zone's displacement only after the abandonment of T2. If the T2 rate truly is a minimum, then there is evidence for temporal variations in slip rate. The uncertainty in the data does not permit further investigation of this phenomenon.

The decrease in slip rates near geometrically-defined segment boundaries and the semi-parabolic form of the distributions on each segment lends further evidence towards long-term segmentation of the FPF. Covariation of hanging wall topography in the Sherwood Range with slip rates on the Bray segment suggests that modern topography reflects variations in fault slip over 10^6 year timescales (e.g. Jackson et al. 1996). James (1998) and Upton et al. (2004) suggested that this may have taken as little as c. 2 Myr. The topographic expressions of the ranges are proxies for the accumulated net slip on the FPF segments.

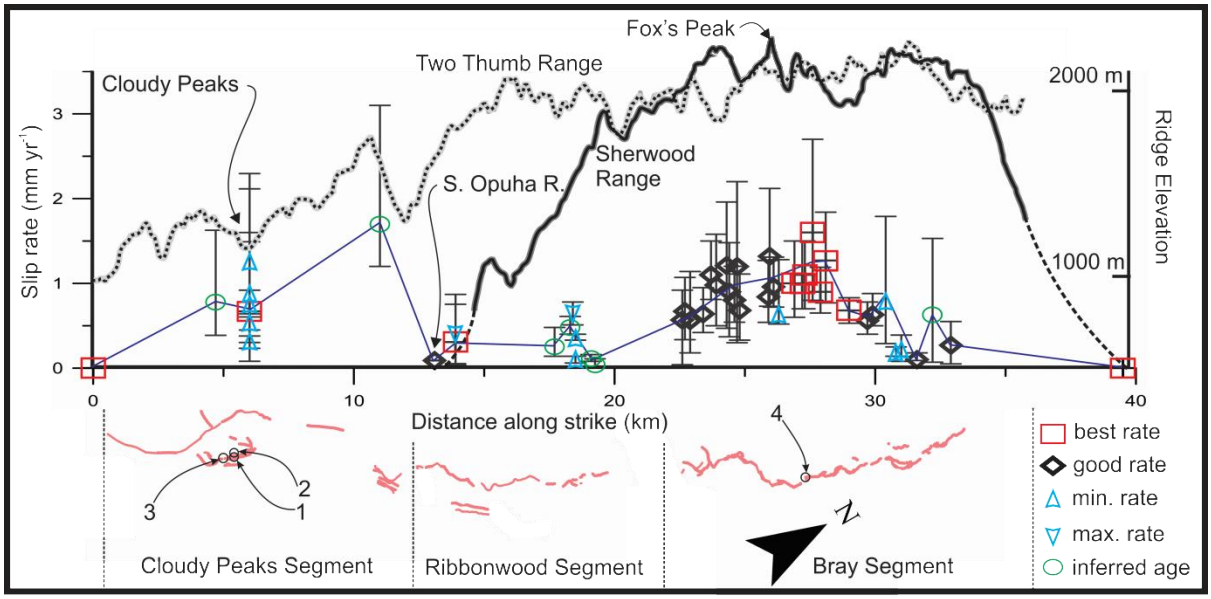

Figure 3.25: Along-strike distribution of slip rates on the FPF and covariance with topography. 'Best' rates are from dated surfaces; 'good' rates are from surfaces correlated to dated features; 'min' and 'max' rates are from calculations using minimum/maximum slip and/or age; 'inferred age' are rates derived from surface of inferred age (lowest confidence). Locations of trenches (#1-4) are shown on fault trace map below. See text for discussion

This result indicates that the Bray and Ribbonwood Segments have been responsible for the uplift of the Sherwood Range. The Cloudy Peaks Segment, at the base of the Two Thumb Range, may have formed as an intermediary structure between the FPF to the North and the foreland propagating FCF to the West (e.g. Fig. 3.1, 3.18). The intermediate (10^3-10^5 year) to long term (10^6 year) geomorphology is thus suggestive of both fault to fault and fault segment interactions.

3.7 Paleoseismology of the Fox Peak Fault

Four trenches, three on the Cloudy Peaks traces and one on the Bray Segment, were excavated to determine the ages of past earthquakes, aid in determining single event displacements, and to compare time-averaged vs. paleoseismic slip rates (Fig. 3.25).

Trenches 1 and 2 (Fig. 3.25) were positioned across a crestal graben in the hinge zone of Fault 2 at Cloudy Peaks (Fig. 3.3A and B, respectively). This location was chosen so as to maximise the probability of finding dateable material and several earthquake 'event' horizons. Reconnaissance augering revealed fine-grained graben–fill sediments, some containing charcoal, in four locations. Additionally, satellite images and a Total Station micro-topographic survey (Appendix 3) showed that local lows abut the bending-moment fault scarps nested in a paleochannel (e.g. Fig 3.3), increasing the likelihood that ongoing slope-wash processes would lead to small residence times of detrital wood/charcoal at the surface (i.e. ensuring that samples collected for radiocarbon dating within units

are not vastly older than the deposits themselves). Trenches were oriented perpendicular to fault traces as no strike-slip displacement could be detected from GPS mapping and surveying. The trenches were located in two separate graben (defined by oppositely dipping, bounding faults and separated by a horst) to account for the migration of the axial trace and bending-moment stresses through time (e.g. Fig. 3.20A).

Trench 3 (Fig. 3.25) was dug by hand across the youngest scarp of Fault 2 at Cloudy Peaks (i.e. on T7, Fig. 3.3C). This location was chosen to obtain a single event displacement and age of most recent event (MRE) on the main fault trace, ground truth GPR profiles across the Cloudy Peaks terraces (Section 3.6.2) and check consistency of events with the bending-moment faults of the crestal graben (e.g. McCalpin 2009; Heddar et al. 2013).

Trench 4 (Fig. 3.24A & 3.25) was located across a fault trace adjacent to the Fox's Peak ski field road on the Bray segment. At this location, a single trace NE of the trench site splays into two to three separate traces as it crosses a paleochannel. Surveying of the paleochannel and the surface to either side revealed that (i) changes in elevation are ± 1 m and attributable to natural undulations in the till sheet surface or the radially sloping surface and (ii) the paleochannel is offset the same amount as the surface to the South (summed across the traces). Therefore, I determined that there is no resolvable difference between the surface either side of the paleochannel, and any difference in net slip is likely due to a change in fault dip, expressed as splaying of surface traces, as the fault approaches the 'free face' of the stream. Similar patterns of changing fault scarp morphology and dip, are observed further along the FPF (e.g. Fig. 3.11B).

In all instances, please refer to Appendix 4 for full size, colour versions of the trench logs and photomosaics.

3.7.1 Cloudy Peaks Segment

3.7.1.1 Trench 1

Excavation revealed five faults in Trench 1 with vertical displacements ranging from 1.42 ± 0.10 m to c. 0.02 m (Fig. 3.26). Trench stratigraphy consisted of a Torlesse greywacke bedrock strath (Unit 1) underlying a c. 1 m thick bed of imbricated fluvial gravels (Unit 2). Imbrication is consistent with the paleochannel direction and a flow direction similar to that of the modern drainage. A buried soil (Units 4-6) is developed in loess on top of a matrix-supported debris flow deposit (Unit 3) which consists of elongate, flat-lying clasts in a silt matrix. Units 1-6 are offset and down-dropped into fissures across the graben. Unit 7 is comprised entirely of collapsed Unit 6. A cumulic B-horizon, comprised of slope wash derived silt (Unit 8), drapes minor fault scarps and further in-fills voids left

by fissuring, indicating that it was deposited soon after faulting. The sequence of deposition/faulting is as follows:

(i) Bevelling of bedrock strath (Unit 1) and subsequent fluvial incision in Firewood Stream causing abandonment of fluvial gravels (Unit 2)
(ii) Deposition of debris flow (Unit 3) during abandonment or from flooding event in nearby drainage (Cowan Stream)
(iii) Accumulation of loess (Units 4 & 5), presumably sometime during LGM or earlier
(iv) Soil development within loess with top of Unit 6 (AEb-horizon) as paleo-surface
(v) Faulting: Simultaneous offset of Units 1-6 on Faults 1-5 ; discrete blocks of previously developed soil down-dropped into major fissure; fluvial gravels form 'collapse-fabric' on fissure margins
(vi) Slope-wash (Unit 8) from surrounding topography (scarps and channel margins) in-fills remaining voids formed by faulting and drapes scarps within graben
(vii) Further soil development with formation of modern A and E horizons, translocation of fines to Unit 8 and partial welding of the buried soil (Units 4-6)

A radiocarbon and two OSL samples were taken to constrain the age of faulting. As the timing of faulting lies between the ages of the stable surface formed by Unit 6 and that of post-faulting deposition of Unit 8, one OSL sample was taken from each unit. Unit 6 has a luminescence age of 15.9 ± 1.1 ka (Fig. 3.26, sample *c*), which is consistent with the timing of late LGM loess deposition elsewhere in the South Island (e.g. Alloway et al. 2007). This represents a maximum age for Unit 6, which is a buried AE horizon developed in the loess. A calibrated calendar age of 8496 ± 80 cal. years BP (2σ) was obtained for detrital charcoal at the top of Unit 6 (Fig. 3.26, sample *b*). The position of the charcoal at the top of the unit corresponds to the stratigraphic location of root traces extending down from the Unit 6/8 contact near the western end of Trench 1. This age represents one of the latest periods of time that Unit 6 occupied the surface before faulting. A luminescence age of 10.6 ± 1.2 ka was obtained for Unit 8 (Fig. 3.26, sample *a*). As this is incompatible with the underlying age for Unit 6, the small difference may be due to incomplete bleaching of the source material during relatively short transport within the local basin (e.g. Appendix 3). The extent to which the prior luminescence signal influences that of Unit 8 is unknown; however, the 10.6 ± 1.2 ka is not likely to be a vast overestimate due to Unit 8's thickness and partial welding to the underlying soil which may take several thousand years (Tonkin and Basher 1990). The best constraint on the timing of faulting is limited to a maximum age of the detrital charcoal 8496 ± 80 years BP.

Table 3.4: Trench 1 unit descriptions.

Unit Name	Deposit/Horizon	Colour	Texture	Notes
1	Torlesse Greywacke	--	--	--
2	River gravels	--	--	Imbricated
3	Debris flow	5Y 6/2	Silty clay loam; Grav. < 25%	Flat-lying, broken clasts
4	Cb (Buried C-horizon)	5Y 6/2	Silty clay loam	Limited extent; interface between 3 and 5
5	Bbts	2.5Y 6/4; 5Y 6/2	Clayey silt	(Buried clayey, iron-stained B-horizon)
6	AEb	2.5Y 6/4	Fine sandy silt	(Buried AE horizon)
7	Unit 6 Fissure Fill	2.5Y 6/4	--	More massive structure than Unit 6
8	Bcm	2.5Y 5/4; 2.5Y 6/6	Clayey silt	(Cumulic B-horizon)
9E	E	2.5Y 6/6	Fine sandy silt	--
9A	A	7.5YR 3/1	Silt	--

3.7.1.2 Trench 2

Excavation revealed three faults with vertical MRE displacements ranging from 1.3 ± .20 m to 0.38 ± 0.10 m (Fig. 3.26). The style of faulting and sedimentation is markedly different than Trench 1 which is located 40 m to the NW on the same terrace. A strongly indurated breccia-conglomerate with clasts of Torlesse greywacke-sandstone (Unit 1a) forms the strath in this location, which is again overlain by fluvial gravels (Units 2a & 2b). Unit 1a is backtilted on the footwall of the principal fault,

but not immediately apparent elsewhere in either Trench 1 or 2. A small sliver of indistinct bedrock (either Torlesse greywacke or Unit 1a) is present on the hanging wall. Trench flooding and a limited depth of excavation prevented identification of the basal unit on the hanging wall. It is likely that Unit 1a is a highly localised deposit either from an earlier phase of faulting or from landsliding at the old river margin. Unit 1b, fault breccia, is only evident along the main fault zone. It is likely to have been in-faulted along Unit 1a prior to the initiation of normal faulting in the crestal graben, further evidenced by a small gouge zone smeared along the modern fault plane. Unit 3, overlying the fluvial gravels, is a silt-loam that has been subject to pedogenesis- manganese nodules and iron-staining indicate sustained saturation during a period of prolonged soil development, probably in a pre-existing topographic low. Liquefaction dykes, sourced from fluvial silts of Unit 2b, cross-cut Unit 3 and have created a silt deposit of limited lateral continuity that drapes the top of 3 (Unit 4). Some liquefaction dikes cross-cut and re-intrude Unit 4. A debris-flow unit with flat-lying, irregular clasts at its base (Unit 5) overlies Unit 4. Unit 6, a clayey silt and sand, thins toward the SE and is overlain by a second debris-flow unit (Unit 7). A colluvial wedge (Unit 8) overlies Unit 7 and has the modern A-horizon (Unit 11) developed directly on to it on the hanging-wall. On the footwall, the A-horizon overlies a B (Unit 10) and C (Unit 9) horizon. At the scarp interface, the A-horizon is developed directly on the C-horizon.

The hanging wall stratigraphy shows evidence of progressive faulting via up-section flattening of dips and thickening of deposits towards the principal fault. The sequence of deposition/faulting is as follows:

(i) Deposition and induration of Unit 1a in an alluvial environment prior to incision down to base level of paleochannel
(ii) Faulting creates 1b
(iii) Fluvial incision and deposition of Unit 2a and 2b (Unit 2) prior to abandonment of terrace
(iv) Earthquake (EQ1) on principal fault offsets existing stratigraphy and tilts Unit 2a and 2b (Unit 2) on hanging and footwalls
(v) Fine sediment (Unit 3) in-fills fault-bounded low created by EQ1. Deposit thickens towards scarp
(vi) Rudimentary soil development in Unit 3
(vii) Earthquake shaking (EQ2) induces liquefaction and deposition of Unit 4. Dikes remain as conduits for liquefaction silt during future events/aftershocks (Quigley et al. 2013). Further hanging/footwall tilting of Unit 1a and Unit 2 (a & b); hanging wall tilting of Unit 3.
(viii) Deposition of Unit 5 debris (‘hyperconcentrated’) flow, in-filling new fault-bounded basin and thickening towards principal fault scarp
(ix) Slope-wash sedimentation (Unit 6) thickens towards the axis of graben
(x) Possible earthquake (EQ3): minor initial tilting of Units 5 & 6 and deposition of debris flow (Unit 7)

(xi) Earthquake (EQ3a), tilting of Units 5-7, further tilting of underlying strata. Offset of units across two secondary faults at the northwestern end of the trench
(xii) Deposition of colluvial wedge (Unit 8), thickening toward principal fault scarp and in-filling fissure between secondary faults (where it is present as collapsed Unit 7)
(xiii) Modern soil development (Units 9-11)

A radiocarbon and two OSL samples were taken to constrain the timing of the MRE (EQ3a) and older events. The timing of the MRE was constrained by charcoal detritus found within the colluvial wedge deposit (Unit 8, Fig. 3.26, sample *f*). The charcoal returned an age of 8483 ± 70 cal. years BP that overlaps in age with the radiocarbon sample taken from Trench 1. It represents a maximum age of MRE faulting. There is no younger, constraining age; however, assuming that the principal faults in both trenches slipped in the MRE (which seems reasonable given the ages of youngest faulted deposits and the mechanics of bending moment faults in an expanding crestal deformation zone, Gonzalez et al. 2008), the calibrated age of 8483 ± 70 ka is probably close to that of the MRE. I note that this age also roughly corresponds to the 7700 ka exposure age of T6 at Cloudy Peaks, which may have been abandoned during the same uplift that caused faulting observed in both trenches' MRE.

A luminescence age of 19.1 ± 1.7 ka for the underlying debris flow deposit (Unit 7, Fig. 3.26, sample *d*) is consistent with the expected chronologic and stratigraphic ordering. The increased compaction of Unit 7 relative to 8 is also indicative of an extended period of time between deposition of the two units. It is peculiar that there is no evidence of a soil having developed on Unit 7 given the minimum 10 ka interval between its deposition and that of Unit 8. Periodic renewal and deposition of fines from aeolian and wash deposition in the pre-existing low may have overwhelmed and outpaced pedogenesis, in which case the age of 19.1 ± 1.7 ka may represent an average for Unit 7 (a maximum age for its top, and a minimum for its base). This model of deposition would also explain the apparent lack of late LGM loess in Trench 2 that was observed in Trench 1, as it would have been incorporated into Unit 7.

A luminescence age of 23.0 ± 2.0 ka was obtained for Unit 5 (Fig. 3.26, sample *e*). This represents a minimum age for the remainder of the units and faulting in observed in Trench 2. Unfortunately, an OSL sample of the terrace gravels (Unit 2) was deemed inadmissible for dating purposes due to mobility within the sample tube. However, evidence of a long period of graben in-filling and pedogenesis (Unit 3) between a minimum of 23.0 ± 2.0 ka and earlier deposition of the terrace gravels matches well with T2 (c. 48 ka, SHD) being significantly older than T4 (24.8 ± 2.7 ka, OSL) in the SHD results. A possible earthquake (EQ3), apparent only in a slight dip increase (i.e. rollover) from Unit 7 to Unit 6 has an age between 19.1 ± 1.7 ka and 23.0 ± 2.0 ka.

Table 3.5: OSL results from Trench 1 and 2.

Sample Number*	**Deposit**	**dD_c/dt (Gy/ka)** [§]	**Water Content (%)**	**K (%)**	**U (ppm) from ^{234}Th**	**U (ppm) from ^{226}Ra, ^{214}Pb, ^{214}Bi**	**U (ppm) from ^{210}Pb**	**Th (ppm) from ^{208}Tl, ^{212}Pb, ^{228}Ac**	***a* value**	**D_e** [†] **(Gy)**	**dD/dt** [§] **(Gy/ka)**	**OSL Age**
WLL944	Trench 1 Unit 8	0.2153 ± 0.0108	30.88	1.97 ± 0.04	3.46 ± 0.28	3.37 ± 0.17	2.95 ± 0.22	10.23 ± 0.14	0.08 ± 0.03	34.33 ± 1.33	3.25 ± 0.35	**10.6 ± 1.2 ka**
WLL945	Trench 2, Unit 7	0.1948 ± 0.0097	26.98	1.97 ± 0.04	1.85 ± 0.04	3.16 ± 0.16	3.11 ± 0.21	12.09 ± 0.14	0.07 ± 0.01	70.09 ± 4.20	3.66 ± 0.25	**19.1 ± 1.7 ka**
WLL947	Trench 1, Unit 6	0.2153 ± 0.0108	21.85	1.67 ± 0.04	3.32 ± 0.34	2.81 ± 0.20	3.20 ± 0.27	11.74 ± 0.16	0.07 ± 0.01	58.77 ± 2.04	3.69 ± 0.22	**15.9 ± 1.1 ka**
WLL948	Trench 2, Unit 5	0.2059 ± 0.0103	31.13	1.75 ± 0.04	3.33 ± 0.29	3.39 ± 0.18	3.99 ± 0.25	13.01 ± 0.16	0.07 ± 0.003	83.46 ± 4.46	3.63 ± 0.24	**23.0 ± 2.0 ka**

Table 3.6: Trench 2 Unit descriptions.

Unit Name	Deposit/Horizon	Colour	Texture	Notes
1a	Indurated debris flow	--	--	Random clast orientation, poor sorting
1b	Fault breccia	--	--	--
2a	Clast supported river gravels	--	--	Imbricated
2b	Matrix supported river gravels	--	--	Poor imbrication
3	Low energy graben-fill / paleosol?	2.5Y 6/3; Gley 1 6/10Y (lower facies)	Clay to Clayey silt	Iron-manganese concretions and water/iron banding
4	Liquefaction silt	2.5Y 6/4	Silt	Sharp top contact
5	Debris flow	5Y 6/4	Loam	Boulder 'lag' at base
6	Graben-fill wash element	5Y 7/1	Clayey silt and sand	--
7	Debris flow	5Y 5/4	Silt loam	Near-random clast orientation
8	Colluvial wedge	2.5Y 6/4	Silt loam	Iron band at base
9	AC/C	5Y 5/4		--
10	B	5YR 5/8	Silty clay	--
11	A	7.5YR 3/1	Silt	--

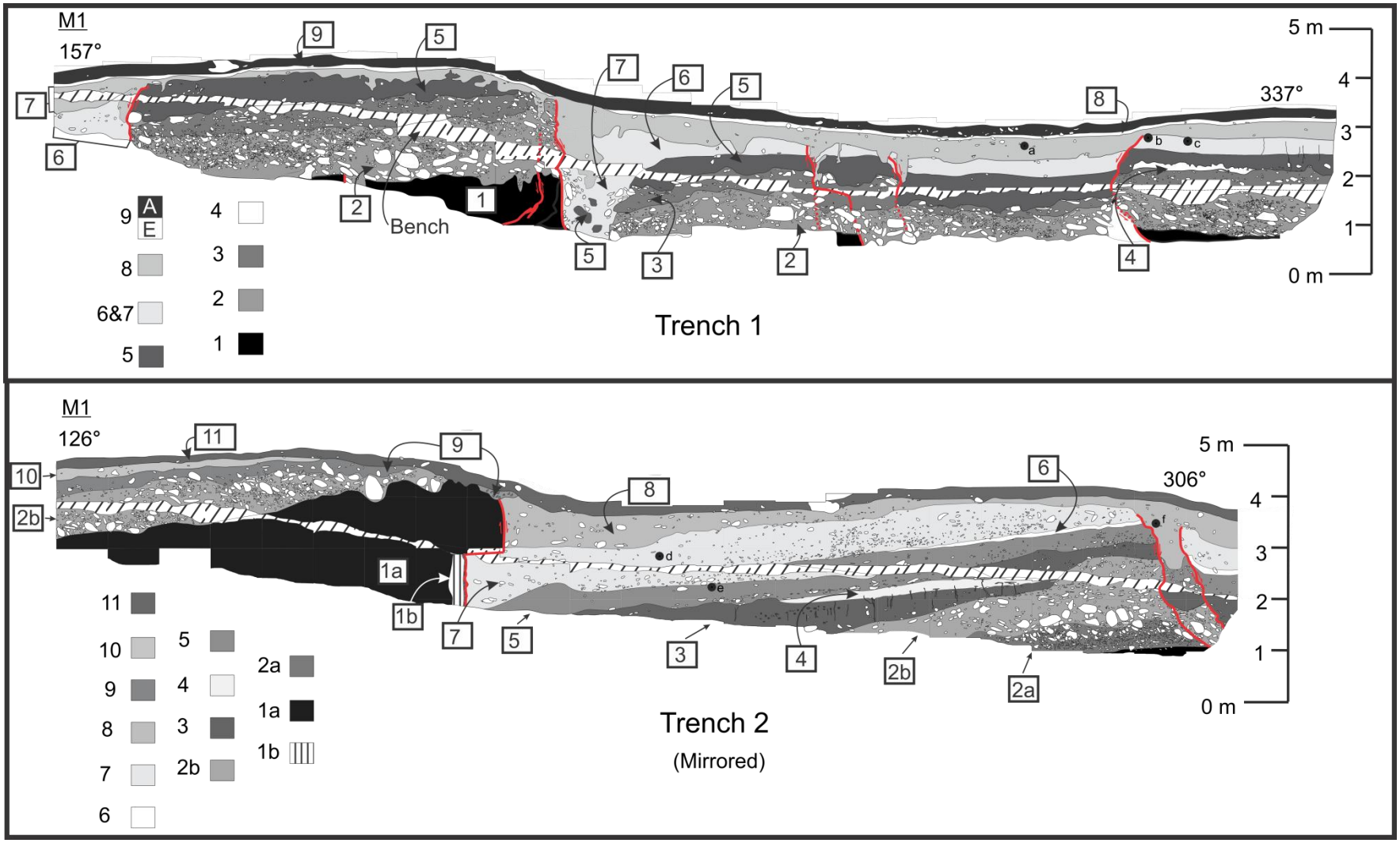

Figure 3.26:Trenches 1 and 2. See text and Appendix 4.

3.7.1.3 Trench 3

Excavation across the youngest scarp at Cloudy Peaks revealed evidence for 1.25 ±0.2 m of total offset across a 7 m zone of distributed fault-related folding (Fig. 3.27). Vertical displacement at the fault is less than 0.5 m; a large portion of the deformation is accommodated by coseismic folding accompanying faulting (e.g. Gold et al. 2006; Amos et al. 2011). Fluvial gravels, silt, and sand (Units 1 and 2) have had a rudimentary B-horizon form in overbank silts (Unit 3). Unit 3 is thickest in a small depression on the hanging wall, suggesting that faulting may have occurred while the terrace was active, trapping additional fines, or that flooding (and overbank silt deposition) occurred soon after faulting. The paucity of gravels within the unit indicates that this sedimentation did not come from the nearby terrace riser. On the footwall of the fault, a thickened B-horizon (Unit 4) is differentiated from Unit 3 to highlight significant cumulic input from slope-wash that has outpaced soil development since faulting. An AC horizon is adjacent (i.e. grades laterally into) Unit 4 and overlies the fault. The AC horizon formed synchronously with cumulic thickening of the B-horizon on the footwall and does not postdate the top of Unit 5. The modern A-horizon (Unit 6) is noticeably stonier at its base on the footwall and grades laterally into Unit 5 near the fault. The sequence of deposition/faulting is as follows:

(i) Aggradation of fluvial gravel, silt and sand (Units 1 and 2). Possible initial deposition of overbank silts (Unit 3)
(ii) Terrace abandonment
(iii) Faulting and folding of Units 1-3. Further input of fines into hanging wall syncline via flooding
(iv) Scarp erosion and pedogenesis forms thickened B-horizon, AC horizon and rough stone line at base of modern A-horizon

Charcoal at the base of Unit 3 on the hanging-wall has a calibrated age of 2513 ± 167 cal. years BP (Fig. 3.27, sample *a*). This represents a minimum age for the abandonment of the terrace and a maximum age for the earthquake that produced the fault scarp. SHD of the terrace tread (T7, Table 3.3) yielded an age of c. 3.7 ka, which is consistent with radiocarbon dating and the interpretation that at least some of Unit 3 was deposited after terrace abandonment in a hanging wall syncline produced by faulting. There is no lower age constraint on the timing of faulting; however, the degree of soil development in the footwall (i.e. thickened B-horizon and crude AC horizon) probably requires at least c. 1 ka to develop. This skews the preferred age for the age of the MRE at Cloudy Peaks towards that of a maximum 2513 ± 167 years BP, with a decreasing likelihood of a younger age towards c. 1 ka. Upton and Osterberg (2007) attributed mass movement deposits in Lake Tekapo dated to 1720 ± 344 and 2810 ± 562 years BP to earthquakes on nearby faults. These ages are generally consistent with the MRE at Cloudy Peaks, but assumptions in determining the ages of the mass-movement

deposits (i.e. based on sedimentation rates) and a wide range of seismic sources makes their correlation with a FPF earthquake difficult.

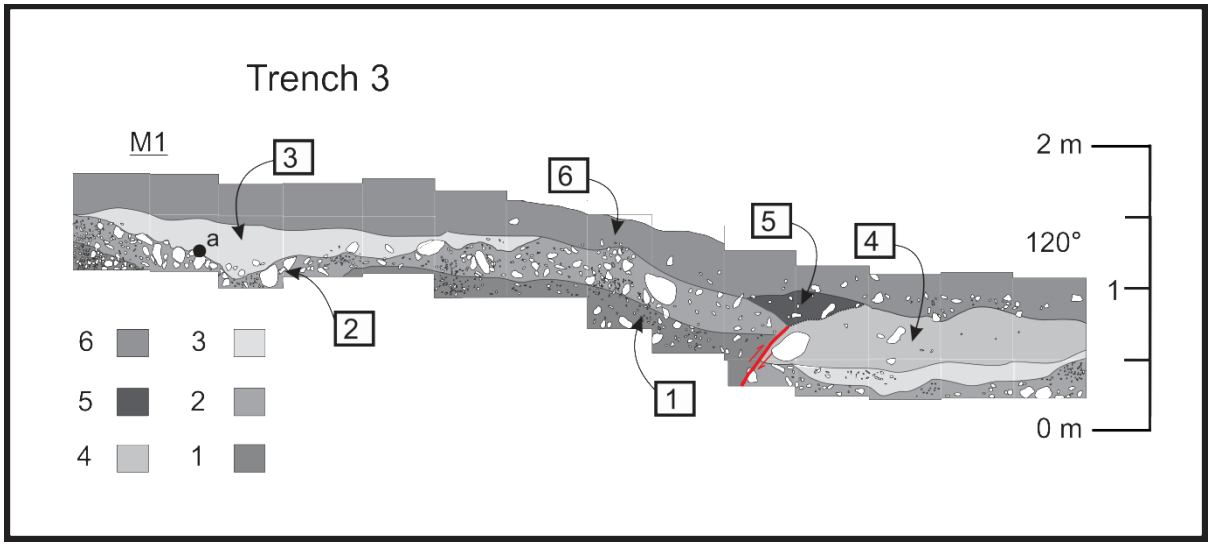

Figure 3.27: Trench 3

Table 3.7: Trench 3 unit descriptions

Unit Name	Deposit/Horizon	Colour	Texture
1	River gravel	--	--
2	Sandy gravel, C	--	--
3	Overbank silts, B	2.5Y 6/4	Silt loam
4	Bcm	2.5Y 6/4	Silt loam
5	AC	2.5Y 5/3	Sandy gravel and silt loam
6	A	10YR 4/2	Silt loam

3.7.1.4 Events inferred from terrace ages

Terrace SHD exposure ages and data gained from the three trenches provide additional constraints the timing of earthquakes at Cloudy Peaks. As stated in Section 3.7.1.2, the mean SHD age of 7.7 ka roughly corresponds to the preferred age of MRE faulting in Trenches 1 and 2. Since slip on

the normal faults exposed in Trenches 1 and 2 is controlled by the same fault that governs the offset observed in Trench 3 and across T6, some basic conclusions on the timing of events can be drawn.

Given a single event displacement (SED) of c. 1.9 m on the main fault trace (Fault 2, from net slip calculations), and neglecting significant displacement variability at a point, the total offset of T6 (c. 5.6 m) can be interpreted as repeated slip in 3 earthquakes. The minimum age for the penultimate event is the maximum age of the MRE (c. 2.5 ka). Using a recurrence interval for this fault trace of 3300 years, derived by dividing the SED by the average surface slip rate on the trace (0.45 mm yr^1), the penultimate earthquake occurred at a maximum age of c. 5.8 ka. The first earthquake (antepenultimate earthquake occurred at or around 8.4 ka, contemporaneous with the event found in Trenches 1 and 2.

3.7.2 Ribbonwood Segment

There is evidence of only one event in the terrace ages at the South Opuha River (Fig. 3.6, Table 3.3). T1, T2 and T3 are all offset by the same amount, within error (avg. 0.72 m). There is no evidence that T4 is offset at the fault. This constrains the timing of the earthquake to lie between the abandonment of T3 and T4. Since no suitable surface clasts for SHD were found on T4, the age of T5 is used as a lower bounds. Thus, the best estimate for the age of this earthquake is between 4.2 and 6.5 ka (Table 3.3). I note that the MRE at Cloudy Peaks is not evident at the South Opuha River, which may either indicate a segmented rupture spanning only the length of the Cloudy Peaks Segment or a lack of surface expression of the MRE on the terraces on the south side of the South Opuha River. While the former is possible, the latter interpretation is preferred given the evidence for flexural slip folding on the north side of the river and the large SED to length ratio for Cloudy Peaks Segment (Wells and Coppermsith 1994; Wesnousky 2008).

3.7.3 Bray Segment

3.7.3.1 Trench 4

The North and South walls of Trench 4 exposed different faulting and depositional histories Fig. 3.28). Accordingly, both walls were logged. The oldest unit in both cases is a sub-rounded to angular, clast-supported gravel with sand lenses and sandy matrix (Unit 1). This unit forms the base of the debris-mantled slope, which likely formed periglacially from the catchment near Fox Peak. Alternations between debris-flow and small channel deposition occurred before abandonment of the surface.

3.7.3.2 North Wall and Depositional History

Four moderately to steeply dipping fault splays with a cumulative vertical displacement much less than the scarp height were observed on the North Wall (Fig. 3.28). On the footwall of these faults,

matrix-supported, sub-rounded gravel (Unit 2) underlies channel deposits consisting of silts, sands, and gravel lenses (Unit 3). A chaotically-bedded, sub-rounded to angular debris flow (Unit 4) overlies these deposits and is cut-off by colluvial wedge deposits towards the fault scarp. Units 1-4 are consistent with periglacial-alluvial deposition of the debris-mantled slope and predate all evidence of faulting. The slope of the surface, height of the fault scarp and the lack of cohesion in the gravels limited the extent to which these units could be exposed on the hanging wall. However, Units 1-4 appear in a small exposure at the top of the trench (Appendix 4, North Wall of Trench 4, b and c).

Deposition after abandonment of the surface is dominated by fault-derived colluvium. An inferred D-shaped colluvial wedge (Unit 5) is marked at its base by a line of large boulders and at its edges by discontinuity across adjacent units. Unit 5 overlies Units 2 and 3, but abuts Unit 4 at a similar stratigraphic level. Together with the lack of apparent soil development and fine material in the wedge, this implies that deposition of this unit occurred soon after or during abandonment of the surface. A second colluvial wedge (Unit 6) is again marked at its base by a layer of coarse boulders, here entrained in an orange, silty clay matrix. Units 7 and 8 constitute different facies of MRE fissure-fill. Unit 7 is a free-face collapse deposit (reworked Unit 1). Unit 8 is a matrix-supported gravel deposit that in-fills a c. 0.5 m wide fissure between Unit 1 and Unit 6. Unit 8 also forms a down-slope thinning unit, which consists of remobilised Unit 4 and is thickest immediately down-slope of the fault scarp. The scarp and all units are overlain by a rocky AC horizon (Unit 9). The sequence of deposition/faulting is as follows:

(i) Periglacial deposition of debris flow/alluvial fan gravels, sand and silt (Units 1-4)
(ii) Abandonment of surface
(iii) Faulting (EQ1) soon after surface abandonment and deposition of colluvial wedge 1 (Unit 5)
(iv) Stabilisation of slope as fines accumulate at surface (soil formation or loess?)
(v) Faulting (EQ2) and incorporation of fines of (iv) into colluvial wedge 2 (Unit 6).
(vi) Stablisation of slope and soil formation
(vii) Faulting (EQ3) - in-filling of fissure on scarp (Units 8a and 8b) and down-slope mobilisation of Unit 4 (Unit 8b). It is likely that the small offsets and folding observed in the trench on all four faults occurred during this MRE
(viii) Formation of AC-Horizon over sedimentary package

Table 3.8: Trench 4 unit descriptions

Unit Name	Deposit/Horizon	Colour	Texture	Notes
1	Clast-supported gravel with sand beds	--	--	Variably imbricated
2	Sandy gravel	5Y 5/3	--	
3	Channel silts and sands	5Y 6/4	Silty sand	Gravel lenses
4	Debris flow	2.5Y 5/4; 7.5YR 7/8 (oxidised)	Medium sand to gravel	Some CaCO3 cementation, variably imbricated
5	Colluvial wedge 1	--	Gravel	--
6a (differentiated on South Wall only)	Colluvial wedge 2, free-face collapse element	10YR 5/6	Coarse sandy gravel	--
6 / 6b (North / South)	Colluvial wedge 2	7.5YR 5/8 (North); 10YR 5/6 (South)	Silty clay to Sandy silt	--
8a (differentiated on North Wall only)	Fissure-fill, free-face collapse element	5YR 5/6	Gravel	--
8b / 8 (North / South)	Fissure fill and remobilised Unit 4	10 YR 5/4	Clayey silt to fine sand	--
9	AC	10YR 4/3	Silt loam	Rocky

A radiocarbon and OSL sample were taken from the North Wall of Trench 4. Detrital charcoal was found within Unit 8b downslope of the 8b fissure fill facies (Fig. 3.28, sample *a*). This constrains a maximum age for the MRE and yielded a calibrated age of 3479 ± 79 cal. years BP. Given the degree of weathering of Unit 8 and the AC horizon developed on top of it, the preferred age is skewed towards this upper bounds.

A luminescence age of 16.4 ± 2.0 ka was obtained for Unit 3, as discussed in Section 3.6.4. Unfortunately, no datable material was found in the remainder of the trench. The age of Unit 3 constrains a maximum age for EQ1 and 2.

3.7.3.3 Trench 4 South Wall

Excavation revealed evidence for two gently to moderately dipping fault zones that offset Units 1-4 (Fig. 3.28). Unit 2 on the North Wall is not distinguishable here and the well-developed channels deposits of Unit 3 are not present. This may indicate that there was pre-existing topography on the south side of the trench site (e.g. a fault scarp) directing flow and channel deposits toward the current footwall of the North Wall. This topography would predate EQ1 on the North Wall. A thin colluvial wedge (Unit 6a and b) overlies the faulted strata, which is correlated with Unit 6 on the North Wall due to similar sedimentology and weathering. Unit 8, which post-dates the MRE, overlies the colluvial wedge Unit 6, and both are undeformed. Thus, the faults on the South Wall were only active during EQ2. No datable material was found to constrain the age of this event. A total SED of 2.2 ± 0.3 m was calculated across the two faults. This is likely to be a minimum estimate for the true SED at the site; displacement must have occurred on obscured faults under the North Wall in EQ2, and no SED was measured for the scarp just downslope of the trench site.

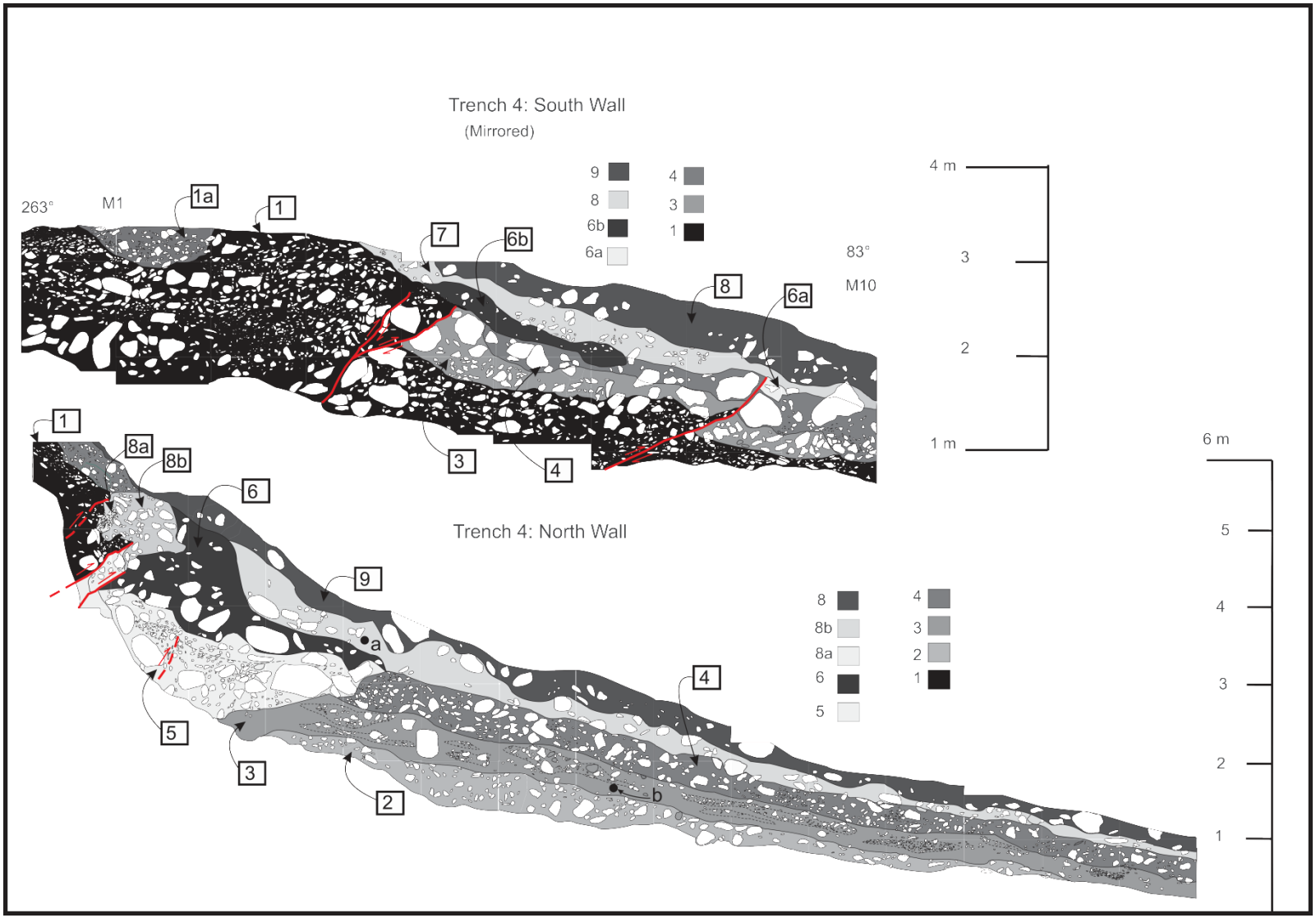
Trench 4: South Wall
(Mirrored)
263°
M1
83°
M10
1a
1
7
6b
8
6a
3
4
9
8
6b
6a
4
3
1
4 m
3
2
1 m
Trench 4: North Wall
1
8a
8b
6
9
a
4
5
3
2
b
8
8b
8a
6
5
4
3
2
1
6 m
5
4
3
2
1

Figure 3.28: Trench 4. See text and Appendix 4 for discussion.

3.7.4 Single event displacements and recurrence interval

Observations of SED from surface net slip calculations range from 1.2-1.8 m (c. 1.5 m) across the main trace at Cloudy Peaks to 0.7-4.0 m at the South Opuha River (4.0 m is inclusive of flexural-slip faulting which is likely to be multi-event), to 1.6-3.7 m on the Bray Segment (Digital Supplementary Information). On the Cloudy Peaks and Bray Segments, these figures agree with lower-limit constraints on SED from trenching. The displacements on the Bray Segment are taken roughly from the centre of the segment, and so may be more indicative of maximum displacements. At Cloudy Peaks, it is uncertain if displacement is accommodated across multiple strands or just one in any given earthquake (e.g. McCalpin 2009; Amos et al. 2011). I consider the c. 1.5 m SED here to be a minimum for the segment.

One approach to finding an average or maximum SED for a fault is to bin all net displacements and examine the spacing of 'peaks' in the dataset (McGill and Sieh 1991). For the FPF, a bin width was chosen to show small variations in the dataset, and closely-spaced multi-modal peaks are interpreted as being the combined result of variable along-strike displacement and bin width (Fig. 3.29). Using this method, the last three earthquakes produced an average of 3.0 m displacement. These are interpreted as being SED maxima for the FPF, as smaller displacements are unlikely to be detected due to poorer preservation (e.g. McCalpin 2009). Using the empirical equations of Moss and Ross (2011) to convert maximum displacement to average displacement for reverse faults, an average SED of 1.3 ± 0.5 m is obtained. Based on the lower limits observed in trenching, the best estimate of average SED is c. 2 m. This estimate agrees with the application of Wesnousky's (2008) average displacement-fault rupture length scaling to the FPF (calculated 33 km rupture length vs. 37 km mapped) and the 2-4 m SED for the nearby Ostler Fault (Van Dissen et al. 1994).

A surface-derived recurrence interval (RI, equal to SED divided by slip rate) depends on the location along the fault the slip rate is chosen. Taking a slip rate of 1 mm yr^{-1} and SED of 2-3 m, which are near the values taken from Cloudy Peaks and the central Bray Segment, the average RI would be 2000 to 3000 years for the FPF. This value is consistent with RI of related faults in the eastern Southern Alps and SCFS (Van Dissen et al. 1994; Berryman et al. 2002; Amos et al. 2011).

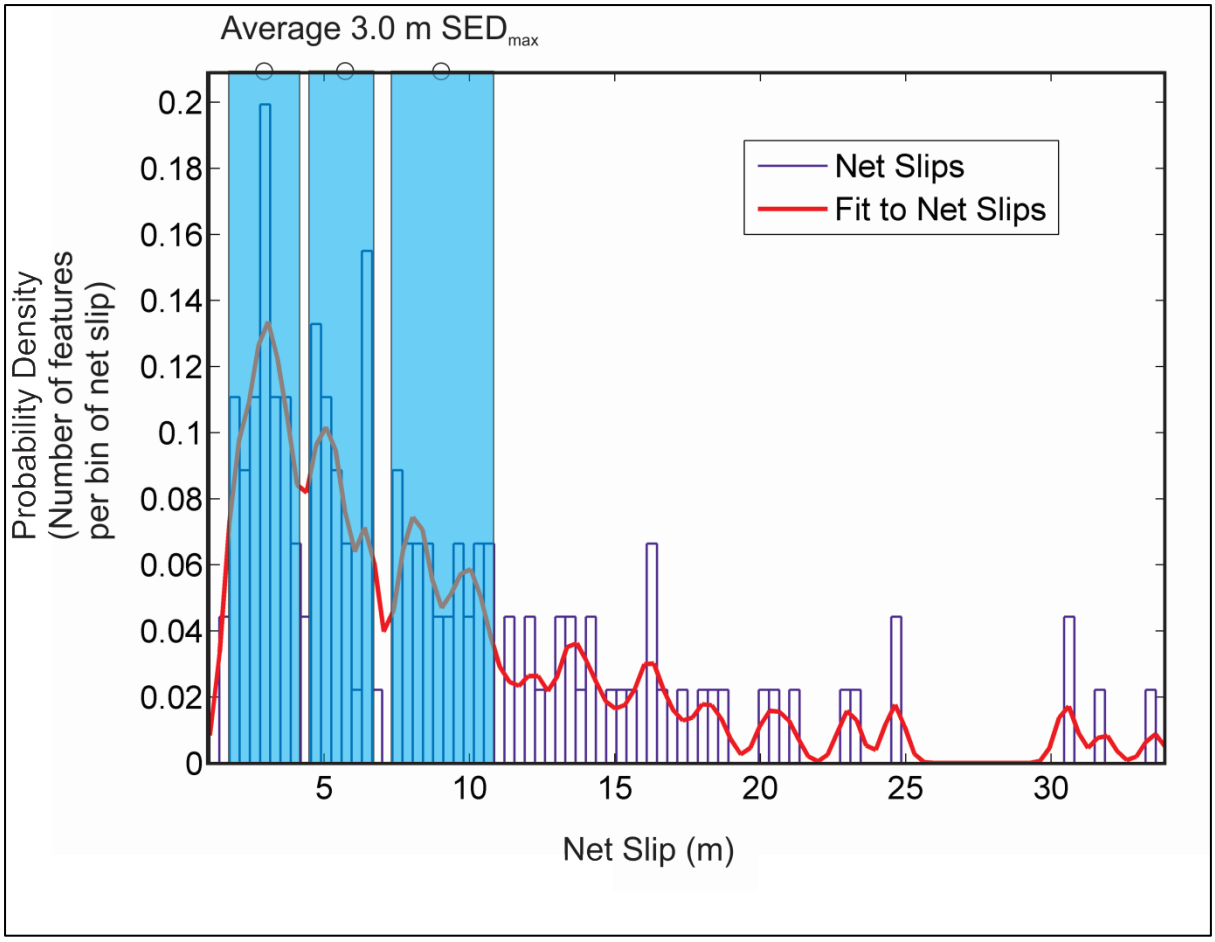

Figure 3.29: Determination of single event displacement from pooled net slips.

The paleoseismic, or actual RI, is more difficult to determine. The RI of events on the bending moment faults is much longer than the surface-derived RI, indicating that these faults do not capture every event on the underlying reverse fault. The RI derived from offset of T7 and T6 on the reverse fault is estimated at 2600 to 3300 years (Section 3.7.1.4), which is consistent with the surface-derived RI. The North Wall of Trench 4 provides evidence for 3-4 events over c. 16 ka, suggesting an average RI of 4000-5300 years. This relatively long period provides an upper bounds for the RI, given that some events may have ruptured only through the frontal scarp that was not trenched at this location.

3.8 Paleoseismology of the Forest Creek Fault

3.8.1 Forest Creek scarp: Trench 5

A hand-dug trench was excavated across the scarp shown in Fig. 3.16. The location was chosen to coincide with the edge of a scarp-impounded pond that currently drains out through the scarp. It was hypothesised that during interseismic periods, a sequence of graben fill silts and sands would accumulate behind the scarp, followed by organic or A-horizons as the edge of the pond emerged

from the running water. Excavation revealed two faults separating primarily graben-fill sediments on the hanging wall from slope colluvium on the footwall (Unit 1) (Fig. 3.30). On the footwall, Unit 1 is overlain by an A and E horizon (Units 9 and 10). The A-horizon thickens, becomes more clay-rich and is 'interbedded' with peaty O-horizons on the hanging wall. Units 2-5 are dragged along the principal fault plane and offset by a more gently-dipping intersecting fault. Unit 3 is composed of dark clay and contains charcoal fragments, which suggests it is a buried A or O-horizon. Units 2, 4 and 5 are clayey silts and silty clays which are interpreted to be old graben-fill sediments. On-lapping the vertical Units 2-5 are horizontally-bedded, modern graben-fill sediments which are drag-folded at the gently-dipping fault. A matrix-supported gravel (Unit 8) derived from Unit 1 and the footwall soil horizons is perched between Unit 1 and Units 6 & 7. This is interpreted to be a colluvial wedge/fissure-fill deposit (Unit 8) that formed following the MRE. The sequence of deposition and faulting is as follows:

(i) Deposition of colluvium (Unit 1) on steep slope

(ii) Faulting (EQ1) and offset of Unit 1

(iii) Post-seismic accumulation of fines (Unit 2 and underlying strata) against scarp

(iv) Organic A or O-horizon (Unit 3) develops at pond edge as slope stabilises

(v) Second accumulation of fines (Units 4 and 5) and burial of Unit 3, possibly in a flood behind EQ1 scarp

(vi) Faulting (EQ2) and drag-folding of Units 2-5 into vertical

(vii) Accumulation of fines behind scarp (Units 6 and 7) and near total filling of graben

(viii) Faulting (EQ3)- minor offset of Units 2-5 and drag-folding of Units 6 and 7. Fissure/colluvial wedge develops above fault tip in region of extension.

(ix) Scarp is defeated by modern drainage and pond level lowers, leaving modern A and peaty O-horizons (Unit 10) to develop in trench area, thickest on hanging wall.

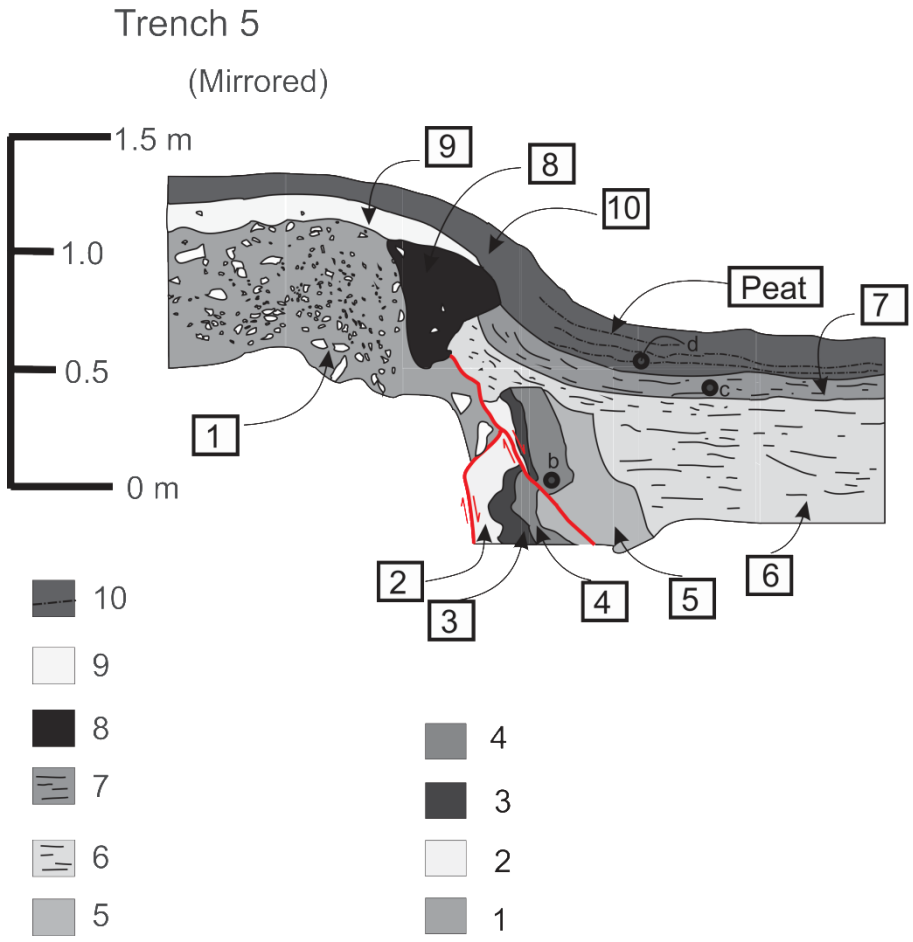

Figure 3.30: Trench 5 across the Forest Creek Fault. See text and Appendix 4 for details.

Four radiocarbon samples were taken from Trench 5 (Fig. 3.30 & Appendix 4, samples *a-d*). Charcoal in Unit 3 (sample *a* location located on trench floor, Appendix 4) returned an age of 6066 ± 115 cal. years BP and constrains a maximum age for Unit 3. Detrital charcoal in Unit 4 (sample *b*) returned an age of 5075 ± 200 cal. years BP and constrains a minimum age of Unit 3. Therefore, the antepenultimate earthquake (EQ1) occurred before 5570 ± 611 cal. years BP. Charcoal in Unit 7 (sample *c*)returned a calibrated age of 3514 ± 68 years BP, which is a minimum age for Unit 6. Since EQ2 occurred between deposition of Units 5 and 6, EQ2 occurred between c. 5.5 and 3.5 ka, probably closer to 5.5 ka. EQ3 occurred between deposition of Unit 7 and modern soil formation. Peat in the lower portion of the modern A/O –horizon (sample *d*) returned an age of 539 ± 16 cal. years BP. Thus, EQ3 (MRE) occurred between 3.5 ka and 0.5 ka, probably closest to 0.5 ka given the preservation of discrete peat bands within the A/O-horizon.

Table 3.9: Trench 5 unit descriptions

Unit Name	Deposit/Horizon	Colour	Texture	Notes
1	Colluvium		Clast-supported gravel	--
2	Scarp-impounded graben-fill	5Y 6/2	Silty clay	Very light- paleo E or B-horizon?
3	A/Ob	10YR 2/1	Clay	Abundant charcoal
4	Flood / graben-fill	2.5Y 5/3	Clayey silt	--
5	Flood /graben fill	2.5Y 5/1	Silty clay	--
6	Scarp-impounded graben-fill	2.5Y 5/1	Clayey silt	--
7	Scarp-impounded graben-fill	5Y 6/1	Silty clay	--
8	Fissure-fill; colluvial wedge	2.5Y 7/1	Matrix supported gravel	Less gravel and induration than Unit 1
9	E			--
10	A/O	10YR 3/1	Clay (hanging wall)	Peat stringers

3.8.2 Single event displacement and recurrence interval

An SED is difficult to calculate from the available information on the FCF. The MRE produced only a few centimetres of throw on discrete faults in Trench 5 (Fig. 3.30). However, if it is assumed that the accommodation space for Unit 8 fissure was created in EQ3, and some of the displacement was distributed onto the steeply-dipping fault at depth, then throw was on the order of c. 0.6 m (separation of Unit 7 on the hanging wall from the top of Unit 1 on the footwall). In order to produce the drag-folding of Units 2-5 in two earthquakes, total displacement would have to be a minimum of

1.4 m (separation of base of trench to top of Unit 1). Units 2-5 are drag folded into the fault and dip vertically into the trench floor (Appendix 4), indicating that throw in the penultimate event (and an SED) would be greater than 0.8 m. I estimate an SED of 1.0 m for the FCF.

Without surface slip rate data, an RI can only be estimated from the constraining ages of earthquakes in the trench. The maximum time interval between EQ2 and EQ3 is 5000 years. A more realistic estimate of RI is likely to fall around 2000-3000 years (2-3 earthquakes in c. 6000 years).

3.9 Discussion

Over 10^6 year timescales (i.e. the period spanning the uplift of the Two Thumb and Sherwood Ranges), there is good evidence that the FPF has operated as a segmented reverse fault. This is apparent in the geometry and structural style of the fault, and its relationship to topography. The Ribbonwood and Bray Segments have been responsible for the uplift of the Sherwood Range. An intersecting fault, the SCA (Fig. 3.1 & 3.10), demarcates an additional boundary between these two segments, across which there is both a change in structural relief (presence of Tertiary units adjacent the Bray Segment, Fig 3.1) and surface expression of the fault. The FPF at Cloudy Peaks actually bounds the Two Thumb Range, but lies along the southern projection of the Sherwood Range and Ribbonwood Segment of the FPF. The Cloudy Peaks traces probably formed as an intermediary structure between the foreland-propagating FCF and lengthening FPF (Fig. 3.18). The Cloudy Peaks traces continue on towards the Ribbonwood Segment and Sherwood Range, rather than follow the Two Thumb Range (Fig. 3.1), indicating that their classification as part of the FPF is sound. This style of overlapping fault and fold (range) growth has been described from the pattern of long-term drainage development in Otago (Jackson et al. 1996, 2002).

The change in topographic and structural relief between the southern Two Thumb Range (Cloudy Peaks Segment) and southern Sherwood Range (Ribbonwood Segment) is reflected in the net slip of late Pleistocene surfaces and long-term slip rates (Fig. 3.25). The FPF slip rate profile (Fig. 3.25) shows a marked decrease at the South Opuha River (i.e. across the segment boundary), where offset terraces show evidence for 1-2 surface rupturing earthquakes in the last c. 13 ka (T1, South Opuha River) compared to at least 3-4 earthquakes over the same time period at Cloudy Peaks (from progressively offset terraces T7, T6 and T5). This begs the question of whether the apparent long-term geometric, structural and rate-based segment boundaries represent barriers to earthquake rupture propagation.

3.9.1 Earthquake rupture segmentation

Despite the large uncertainty associated with the timing of earthquakes in this study, some basic observations regarding the earthquake segmentation of the FPF and FCF are as follows:

(i) Both faults and all segments of the FPF have ruptured at least once during the Holocene

(ii) The timing of the MRE on the FCF, Cloudy Peaks and Bray FPF segments overlap (Fig. 3.31 & Appendix 5)

(iii) The MRE is not apparent on the Ribbonwood Segment, but could be due to the lack of constrained earthquake ages on flexural-slip faults north of the South Opuha River

(iv) The age of the penultimate events on the Cloudy Peaks and Ribbonwood FPF segments (and possibly all three segments) overlap within one RI of the penultimate event(s) on the FCF (Fig. 3.31 & Appendix 5)

(v) There is no clear evidence for activity on the EFPF or SCA over the late Pleistocene and Holocene (Section 3.4.4)

There is not enough data to determine if or how often the FPF segment boundaries present barriers to rupture in earthquakes. Based on the overlap of MRE ages on the Cloudy Peaks and Bray Segments, it seems likely that earthquakes on one segment affect the timing of the other. If these segments in fact rupture coevally, it is unlikely that rupture would 'skip' the central Ribbonwood Segment on a semi-continuous fault plane at depth. The analyses of Rubin (1996) and Wesnousky (2008) suggest these boundaries should be easily breached based on the limited historic reverse fault dataset.

The throw and timing of the single-event scarp at the South Opuha River indicates that a full-length FPF earthquake may have taken place at c. 4-6 ka. If the South Opuha River terraces were located at a barrier that rarely failed in otherwise regular earthquakes on the FPF, one would expect to see slip maxima at the barrier in less frequent events (Shen et al. 2009). If this was a location of consistently smaller displacements on a fully linked fault, one would expect to see evidence of progressively increasing displacements on older terraces, coeval with the ages of earthquakes on other segments. Instead, the data point towards a slip minimum on the FPF at this location in only 1 surface rupture since c. 13 ka. These observations are somewhat conflicting.

If some of the slip on the Ribbonwood Segment is accommodated by distributed folding in the Fairlie Basin, then the apparent decrease in on-fault slip rates at the South Opuha River and SCA underestimate the true slip rate. This is supported by the coincidence of tilted late Quaternary fan surfaces, flexural-slip faults and the main trace of the FPF on the Ribbonwood Segment. Earthquakes may always propagate through segment boundaries delineated by NW-striking faults but with net displacement variably taken up by the principal fault plane and basinward folding. That is, the NW-striking faults may only control slip gradients on the principal fault planes; the rest of the displacement may be preferentially distributed onto rangefront folds (e.g. Fig. 3.9). It has long been

recognised that distributed faulting and folding complicates the measurement of reverse fault slip (Rockwell 1988; Yeats 2000; Ishiyama et al. 2004; Gold et al. 2005; McCalpin 2009; Amos et al. 2011) and displacement transfer has been observed on slip rate profiles of en echelon fault traces of the Ostler Fault in the SCFS (Amos et al. 2010). On the FPF, this would explain the discrepant field observations, mismatch of Ribbonwood slip rates with Sherwood Range topography, and the large on-fault displacement-length ratios and scaling law-derived magnitudes observed in this study (the 'short, fat fault problem' of McCalpin 2009) (Fig. 3.32). Therefore, while the paleoseismic data allow for the possibility of rupture in short segments with large displacement-length ratios, the tectonic geomorphology is more suggestive of full-length fault ruptures.

The FCF may also rupture along with the FPF. Historic reverse faults earthquakes have certainly involved rupture on antithetic as well as synthetic segments, with some traces over 10 km away from the principal fault (c.f. Officers of the Geological Survey 1983; Rubin 1996; Field et al. 2013). Limited geophysical data also suggests that the FPF and FCF sole into the same listric fault at depth (e.g. Wannamaker et al. 2002; Long et al. 2003). As the 2008 Wenchuan earthquake showed, imbricate reverse faults can rupture in the same earthquake (e.g. Xu et al. 2009); Oglesby et al. (2003) and Fukuyama and Hao (2013) showed that stress interactions may actually favour this scenario. The paleoseismic data is consistent with, but not uniquely diagnostic of, coeval rupture of the FCF and FPF.

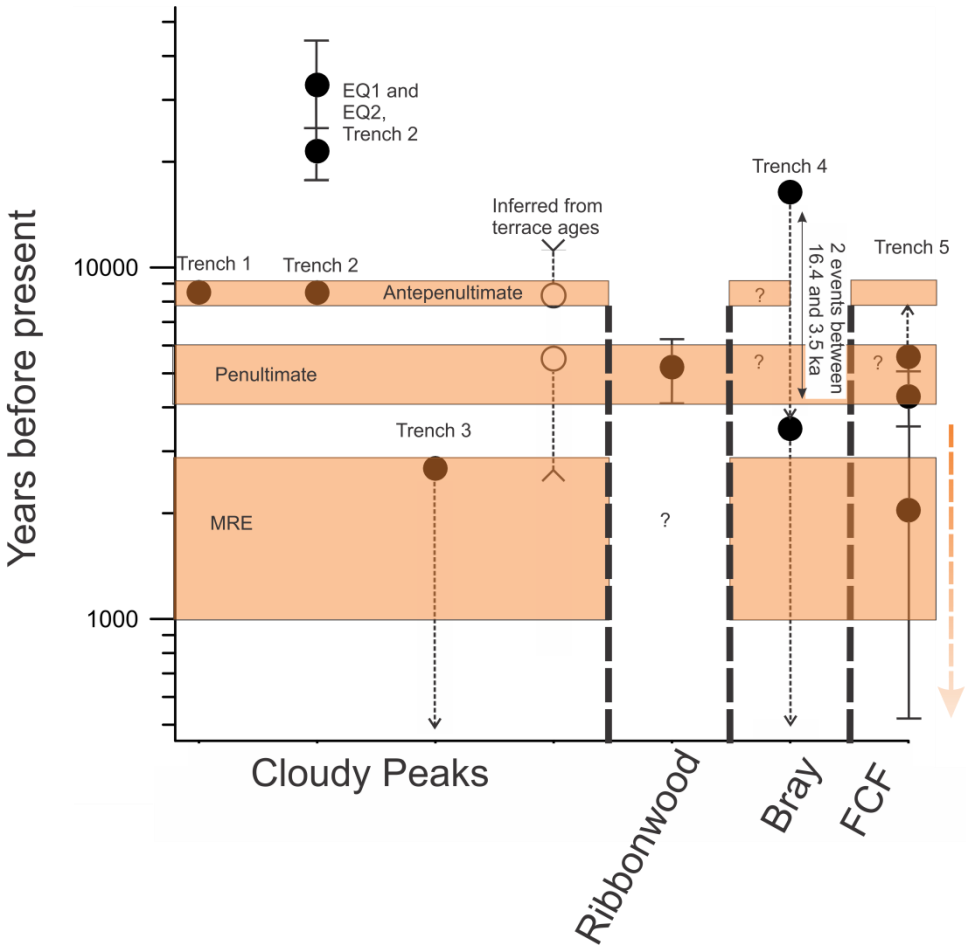

Figure 3.31: Event ages from paleoseismic trenching. Heavy dashed lines (vertical) separate segments of the FPF and the FCF, with distance along the x-axis being unrelated to trench location on either fault. A logarithmic y-axis is provided to view old events found in Trenches 1 and 2. Orange boxes are drawn around possible correlative earthquakes on separate segments of the FPF and FCF. Maximum and minimum ages given where appropriate.

3.9.2 Earthquake magnitudes

Earthquake magnitudes can be derived in a number of ways. The most recent and best regression is that of Moss and Ross (2011) for a global dataset of reverse fault maximum displacement scaling. For the FPF, a maximum displacement of 3.0 m equates to a M_W of 7.2 ± 0.3, which is the same as that calculated for the FPF by Berryman et al. (2002) and included in the national seismic hazard model (NSHM, Stirling et al. 2012) (Fig. 3.32). Using Wesnousky (2008) length scaling, I obtain M_W 7.03 ± 0.24. Both of these estimates only take into account full-length rupture of the FPF. The FCF is not currently included in the NSHM. The moment magnitude for full-length FCF rupture is 7.12 ± 0.24 (Wesnousky 2008), or M_W 6.6 and 6.5 on two separate segments (Fig. 3.32). Since these faults are structurally related and within close proximity of each other, characterisation of the maximum magnitude potential of the FPF and FCF system requires a

consideration of the probability that rupture on one fault jumps to the other (see Chapter 4 for a detailed analysis).

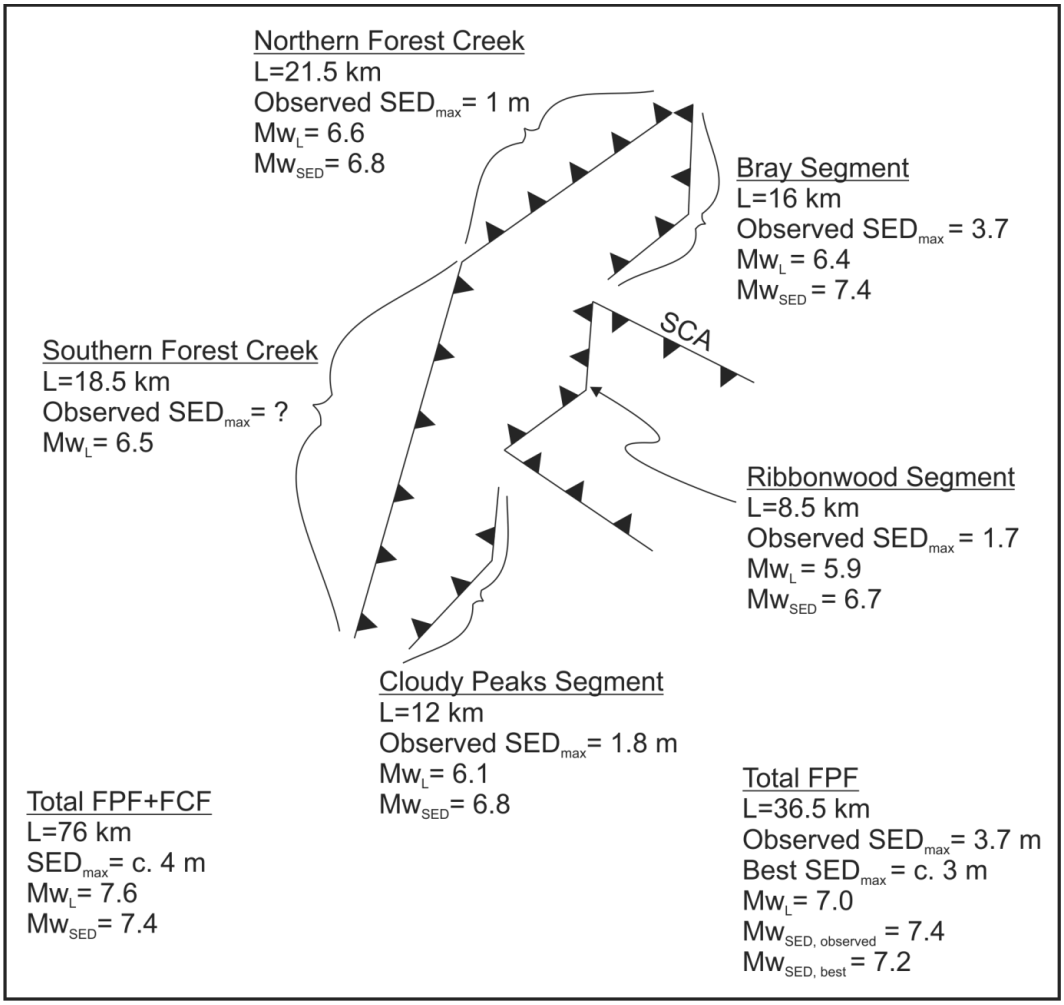

Figure 3.32: Expected magnitudes of segmented and full-length ruptures of the Fox Peak and Forest Creek Faults. Maximum SED scaling laws are from Moss and Ross (2011) and calculated by observed values on each segment (not via the slip-pooling method of Section 3.7.4). Length scaling is from Wesnousky (2008). The discrepant values illustrate the 'short, fat fault problem' of reverse faults (McCalpin 2009) and lend support towards full-length ruptures for the modern FPF.

3.9.3 Comparison of geodetic and geologic slip rates

As with many other central South Island reverse faults (e.g. SCFS), the geologic slip rates presented for faults in this study fall well below those predicted by geodetic modelling (Berryman et al. 2002; Wallace et al. 2007; Amos et al. 2007). Even discounting the predicted strike-slip component across the FPF and FCF, for which there is no evidence in the field, and accounting for conversion of surface slip to subsurface slip, geologically derived rates are 1-4 mm yr^{-1} slower than geodetic rates. Three possible reasons for this are the (i) the under-prediction of actual slip rates because the FPF and FCF are late in their seismic cycles, (ii) unmeasured distributed deformation on the hanging walls of the faults, or (iii) partitioning onto unrecognised faults in the eastern Southern Alps. Taking into

account paleoseismic data from both faults (i.e. over a hanging wall deformation zone of c. 5-10 km for the FPF) paleoseismically-determined slip rates are still significantly smaller than geodetic rates (Fig. 3.33).

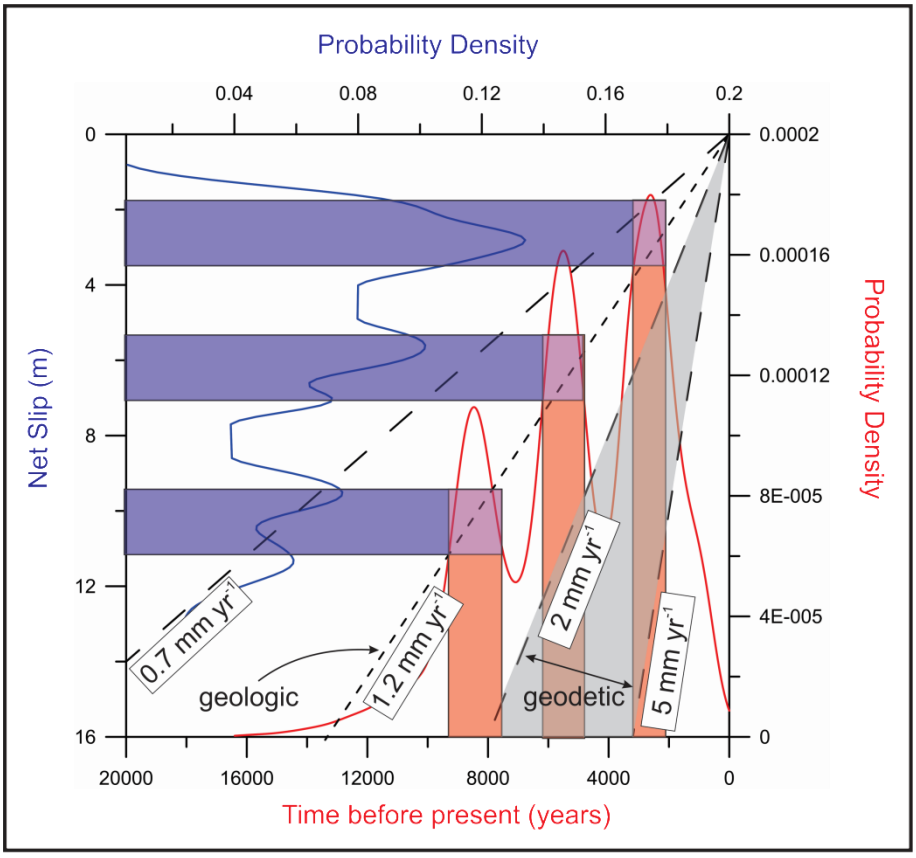

Figure 3.33: Best estimates of combined slip rates for the Fox Peak and Forest Creek Faults. Net slip PDF is derived by adding a FCF SED of 1 m to each event in Fig. 3.29. Age probability distributions are based off simplified and combined PDFs of event ages for the FPF and FCF (Appendix 5). The places where the two PDFs intersect form a line with a slope equal to the combined slip rate that is separate from the surface slip rates derived earlier for the FPF. The best-fitting line is for a slip rate of c. 1.2 mm yr^{-1}. Slip rates of 0.7, 2.0 and 5.0 mm yr^{-1} are shown for reference, with the latter two representing the limits of dip-slip rates from Wallace et al. (2007).

It is likely that the 'missing' dip-slip and strike-slip components are taken up on either unidentified faults in the Southern Alps (e.g. Cox et al. 2012) or many small faults and folds surrounding the geodetic block boundary defined by Wallace et al. (2007). Structures like the SCA and EFPF, while clearly not as active as the FPF and FCF, may accommodate some of the shortening over time. The contribution of NW-striking reverse and left-lateral oblique faults south of the FPF may also account for some of the 'missing' shortening.

3.10 Conclusions

Determining the rupture segmentation, and thus seismic hazard, of active reverse faults requires an examination of fault behaviour over many temporal scales. The cumulative net slip of reverse faults is reflected in the topographic expression of the hanging wall anticlines (mountain ranges) they produce. For the Fox Peak and Forest Creek Faults (FPF and FCF), this has resulted in the uplift of the Sherwood and Two Thumb Ranges, respectively. Modern surface expression of the faults and structural mapping were used to establish the endpoints of geometrically-defined segments along the rangefronts. The locations of spatially abrupt slip rate gradients on the FPF correlate well with the structure inferred from long-term topography (e.g. Fig 3.18), indicating that the segments accumulated displacement without significant lengthening (e.g. Amos et al. 2010). Despite large uncertainties in paleoseismic event ages, clustering of events and large single-event displacements suggest that geometrically and slip rate delineated segment boundaries are most likely breached by earthquakes, or that segment ruptures occur in close temporal succession.

The major findings of the present study are as follows:

(i) The Cloudy Peaks Segment of the FPF is an imbricate thrust wedge that has formed in response to the foreland propagating FCF; it has been assimilated into the FPF. This is reflected in the overlap of the Two Thumb and Sherwood Ranges.

(ii) The Eastern FPF (EFPF) and Stony Creek Anticline (SCA) are not as active as the FPF and FCF, and should be considered separate seismic sources.

(iii) The MRE on the FPF and FCF occurred less than c. 3 ka ago, and probably around 2.5 ky ago. The recurrence interval determined from surface slip rates and single event displacements, as well as through grouping of paleoseismic event ages, is 2-3 ka. The faults are thus likely to be late in their seismic cycles.

(iv) Trenches across bending moment faults provide important, but incomplete, archives of surface ruptures on the underlying principal fault.

(v) As the crestal graben and zone of hanging wall extension expands more normal faults will be created or activated. Therefore, multi-event scarps will lie closest to the thrust front and may fail simultaneously with young, single event scarps near the anticlinal axis.

(vi) The M_W derived from segment-specific SEDs are much larger than those derived from the segment length. This, along with the age overlap of paleoseismic events and likelihood of off-fault, distributed deformation on the Ribbonwood Segment, points towards full-length, multi-segment FPF earthquakes.

(vii) The best estimate M_W for full-length rupture of the FPF is 7.2 ± 0.3, though full characterisation of magnitude potential requires delineation of fault segments as well as consideration of fault-to-fault rupture probabilities.

(viii) Geologically-derived slip rates for the Fox Peak and Forest Creek Faults fall between 1-1.5 mm yr^{-1}, collectively.

(ix) Future studies of segmented reverse faults should focus on defining segment boundaries as barriers to earthquake propagation.

3.11 Appendix 1

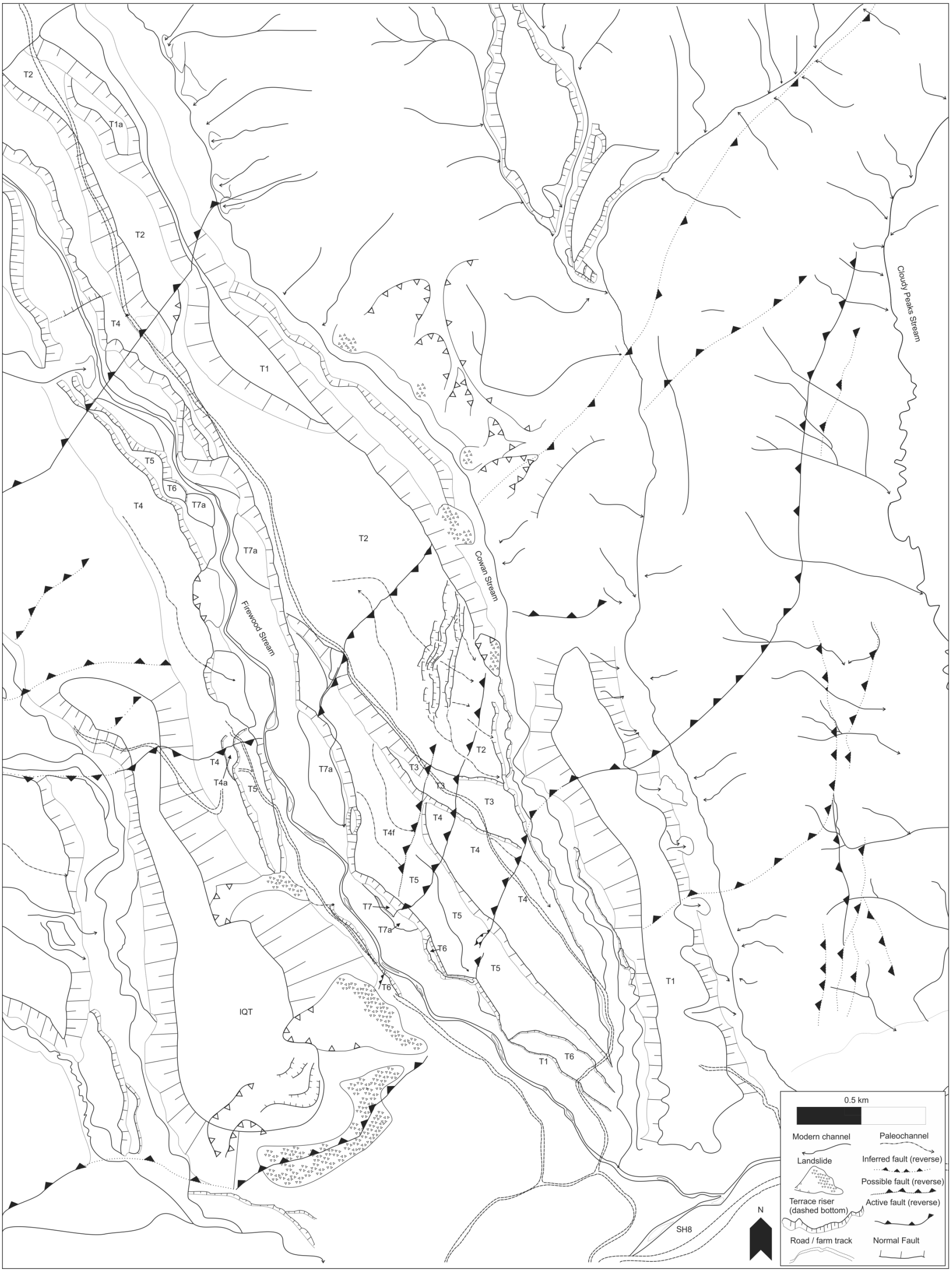

Figure 3.34: Geomorphic map of Cloudy Peaks

3.12 Appendix 2

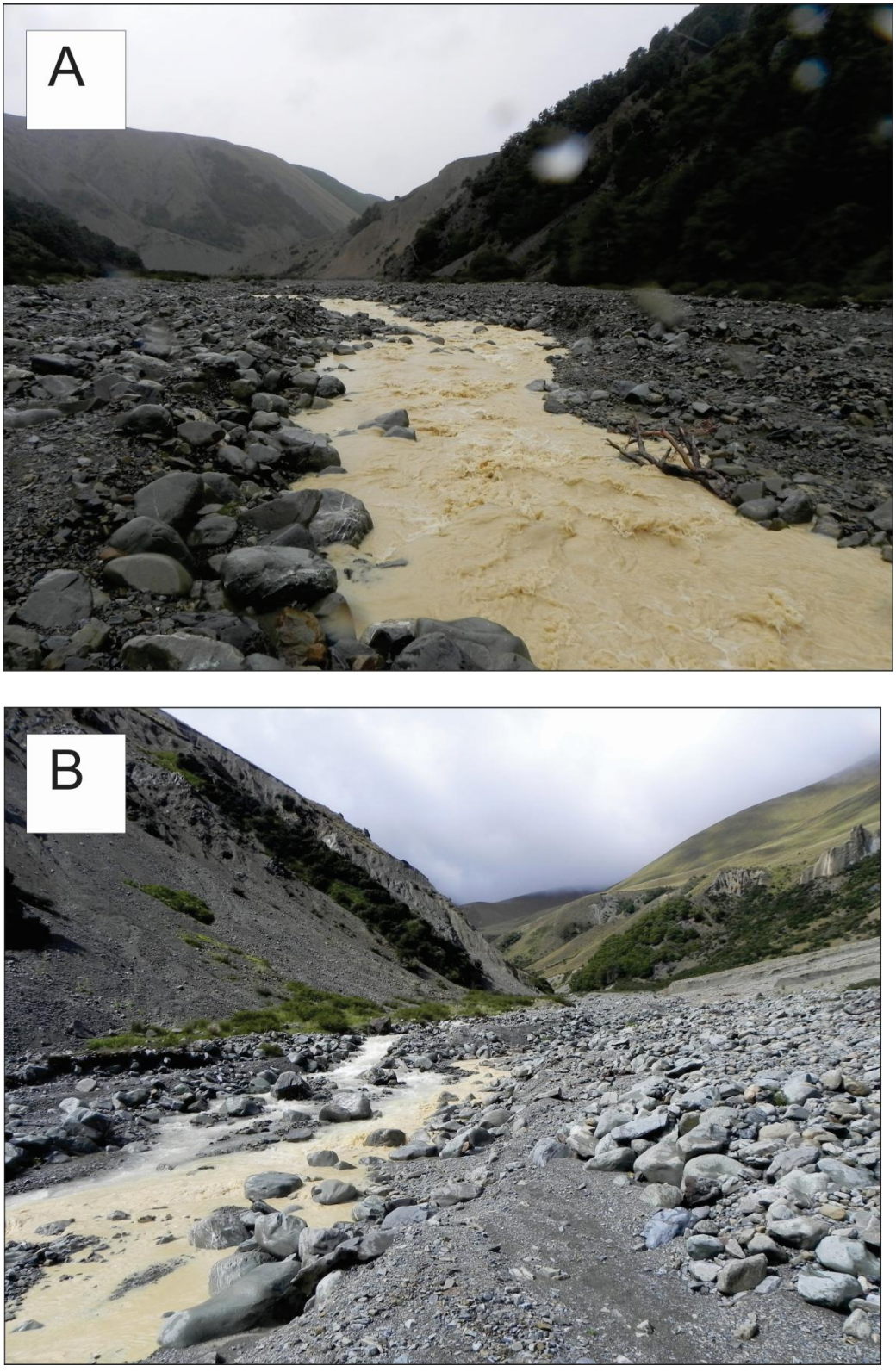

Figure 3.35: Rapidly eroding silts and clays from Pliocene Kowai Formation gravels in Butlers Creek. (A) Butlers Creek in flood; (B) The source of the suspended sediment is from the Kowai outcrop (right branch), and not upstream (left branch). Thus, the inferred age earthquake shaking, as deduced by the presence of prominent precariously balanced rocks in the Kowai outcrop, is not straightforward.

3.13 Appendix 3

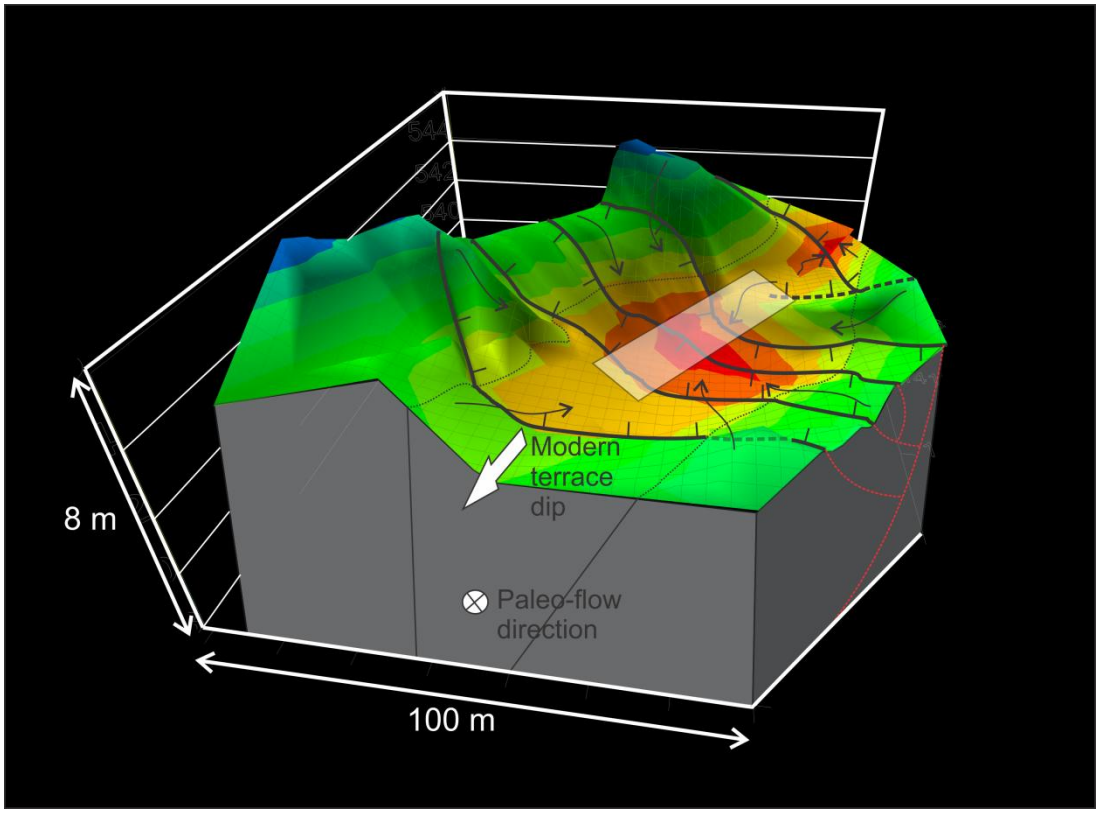

Figure 3.36: Microtopographic (Total Station) survey of Trench 1 site. White footprint is approximate location of the trench. The trench location is within a graben crossing a paleochannel. The local topographic low increases the likelihood of 'trapping' suitable sediments and charcoal for dating the stratigraphy. Trench 2 is located in the next graben over (to the top right, SE).

3.14 Appendix 4

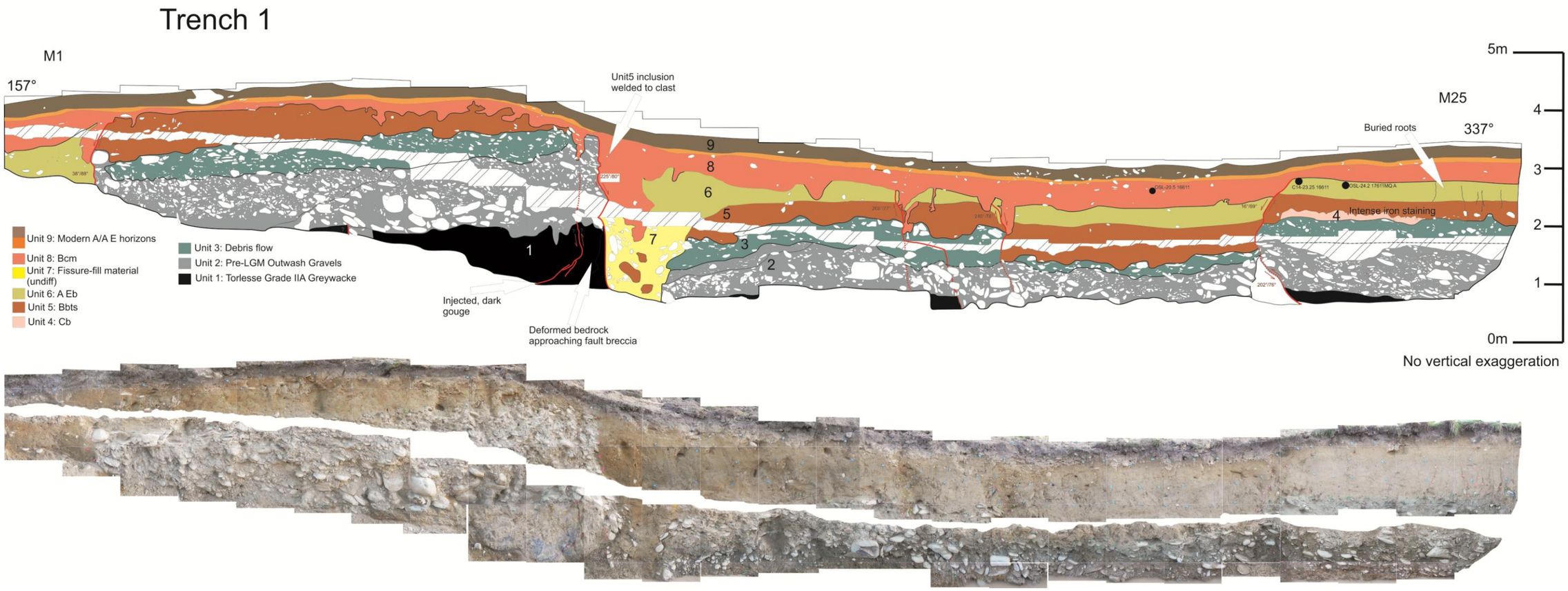

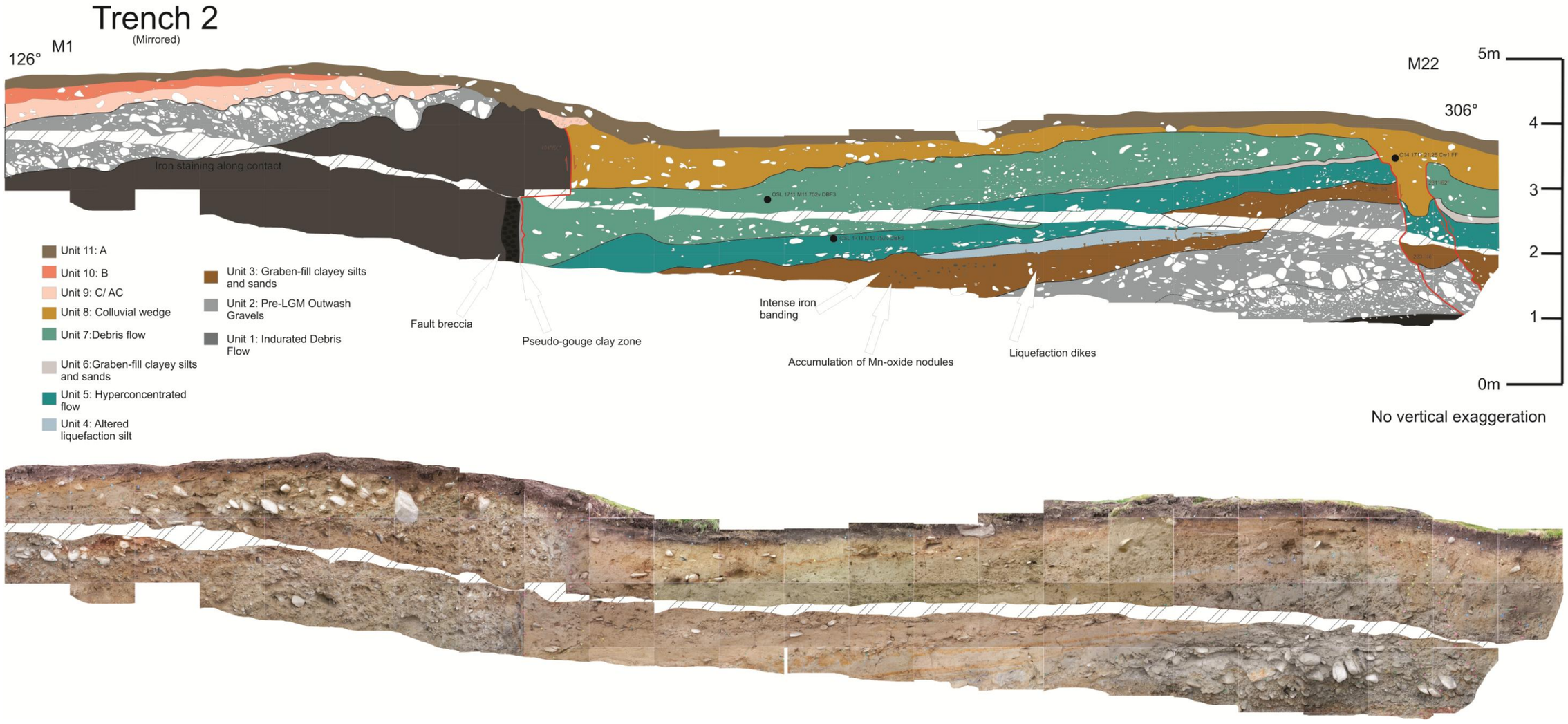
Trench 2
(Mirrored)
126°
M1
M22
306°
5m
4
3
2
1
0m
Iron staining along contact
Unit 11: A
Unit 10: B
Unit 9: C/ AC
Unit 8: Colluvial wedge
Unit 7:Debris flow
Unit 6:Graben-fill clayey silts and sands
Unit 5: Hyperconcentrated flow
Unit 4: Altered liquefaction silt
Unit 3: Graben-fill clayey silts and sands
Unit 2: Pre-LGM Outwash Gravels
Unit 1: Indurated Debris Flow
Fault breccia
Pseudo-gouge clay zone
Intense iron banding
Accumulation of Mn-oxide nodules
Liquefaction dikes
No vertical exaggeration

Trench 4: North Wall

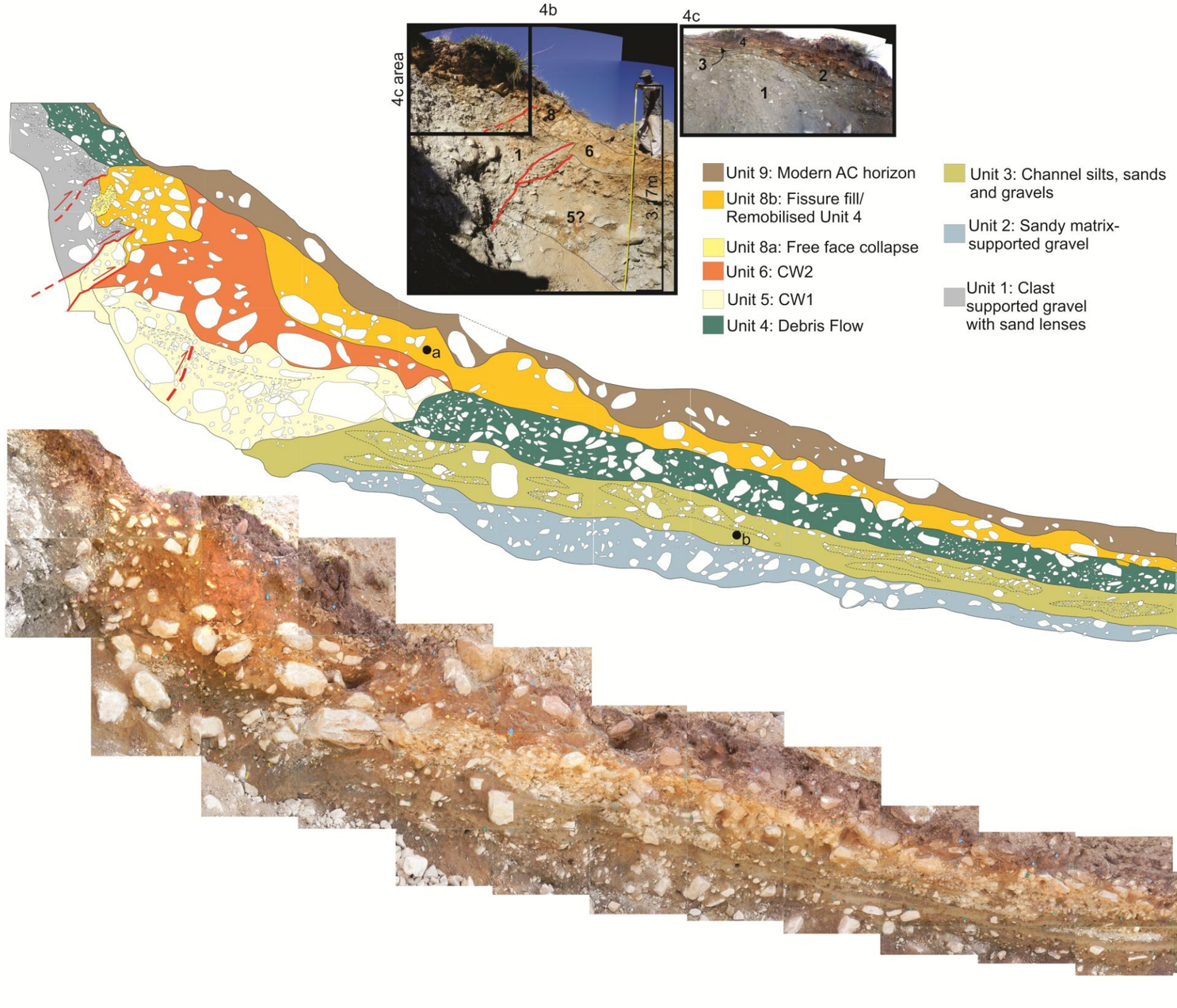

Trench 4: South Wall

(Mirrored)

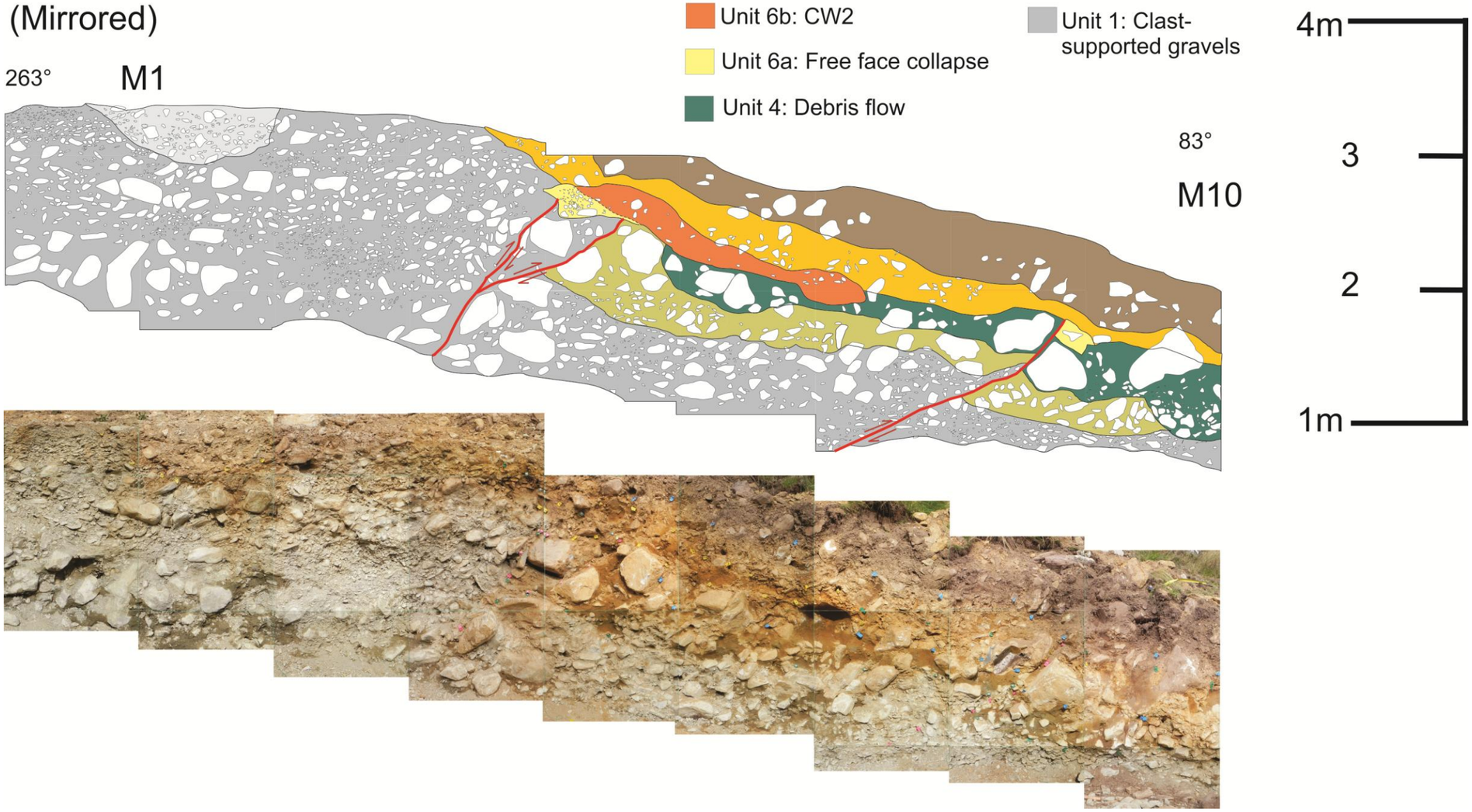

Trench 3

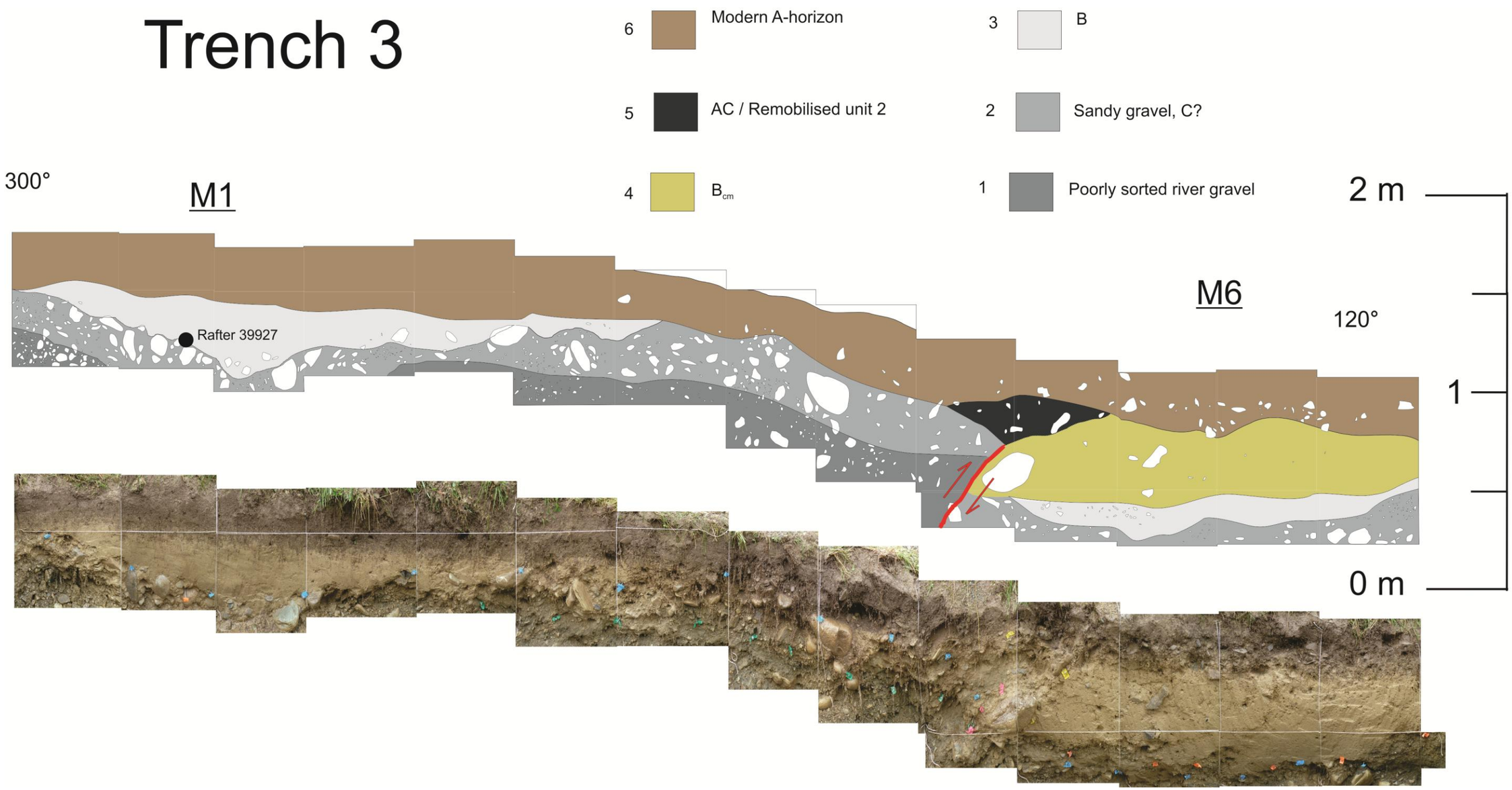
6 Modern A-horizon
5 AC / Remobilised unit 2
4 B_{cm}
3 B
2 Sandy gravel, C?
1 Poorly sorted river gravel
300°
M1
Rafter 39927
M6
120°
2 m
1
0 m

Trench 5

(Mirrored)

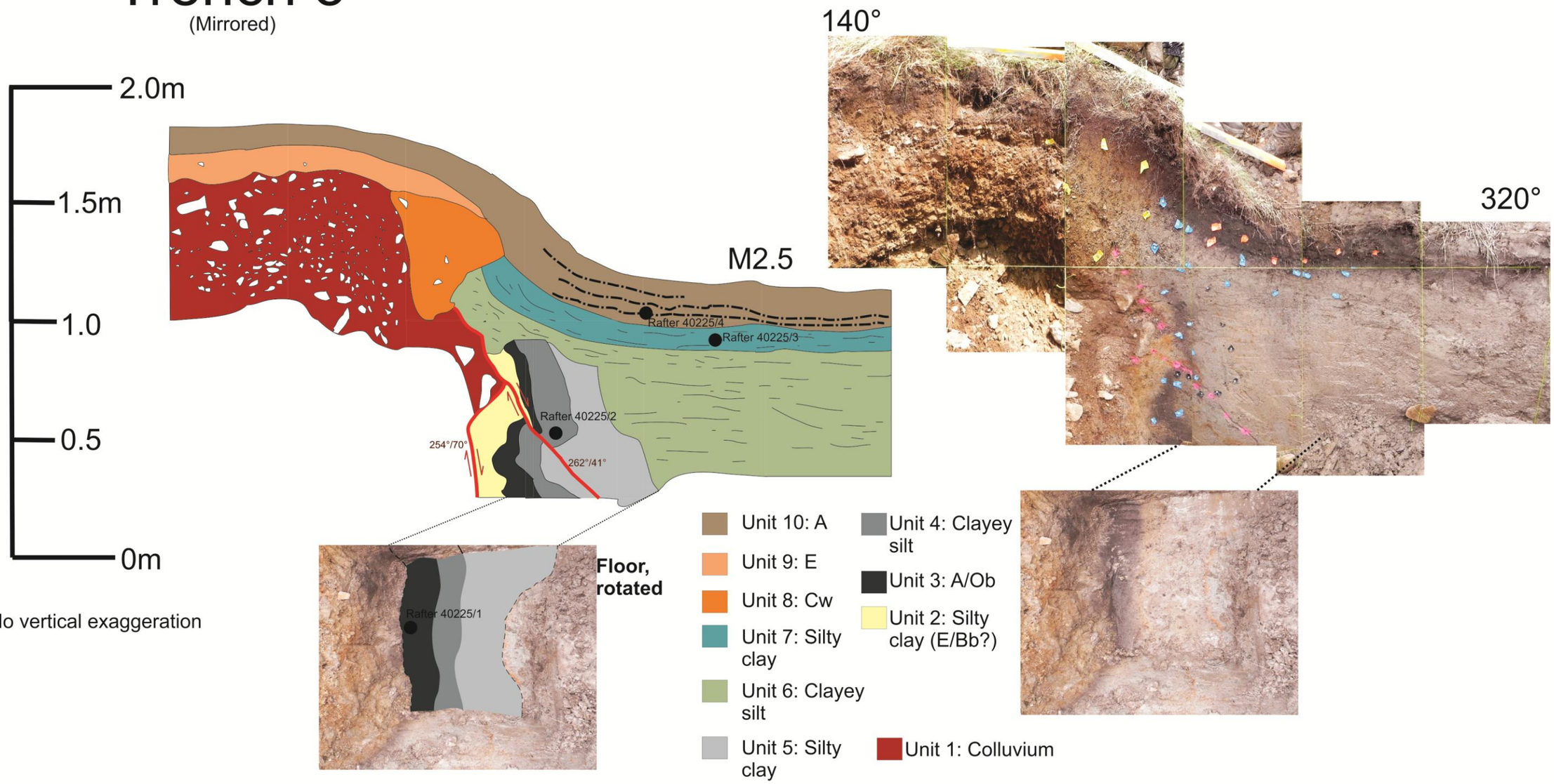

3.15 Appendix 5

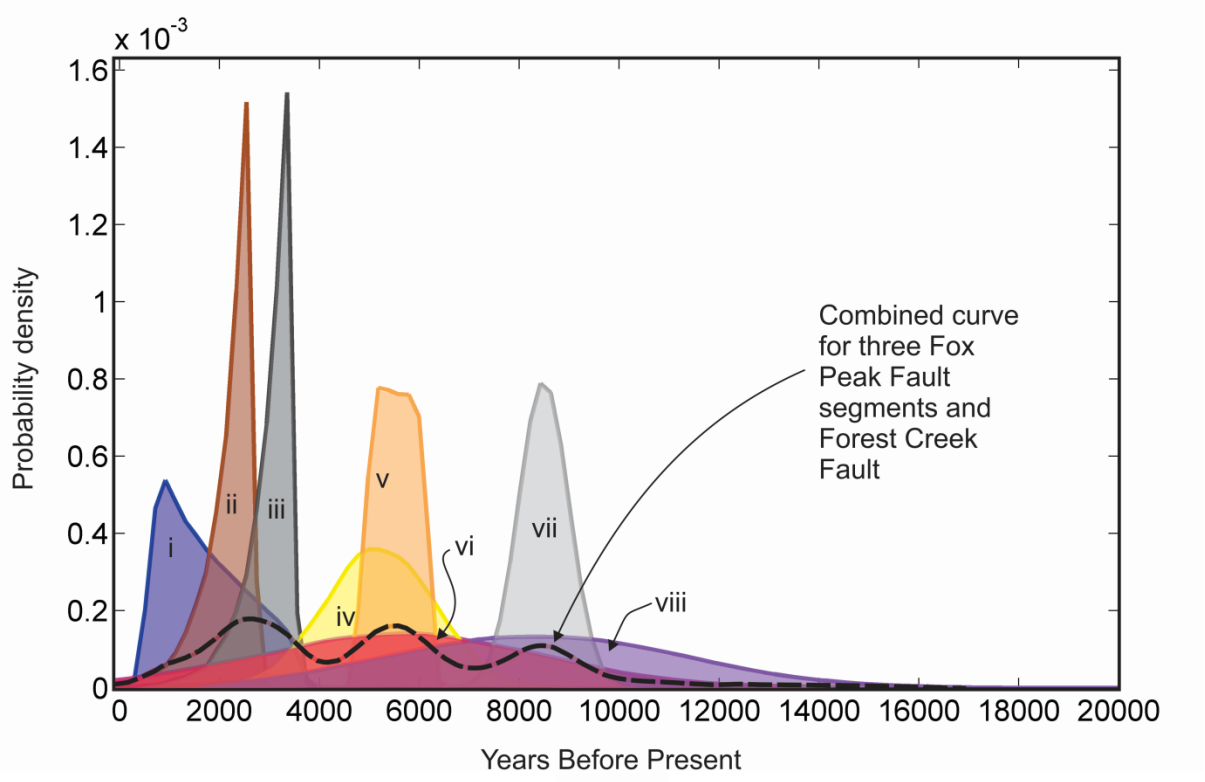

Figure 3.41: Probability density functions of event ages from paleoseismic trenching. The shape of some distributions were specified a priori based on geologic observations and constraining ages. (i) MRE in Trench 5 (Forest Creek Fault) as an exponential function decreasing from c. 500 years BP to a maximum value of 3500 years BP; (ii) MRE in Trench 3 (Fox Peak Fault at Cloudy Peaks) as an exponential function decreasing from a maximum value of 2500 years BP; (iii) MRE in Trench 4 (Fox Peak Fault at Fox Peak ski field road, Bray Segment) as an exponential function decreasing from a maximum age of 3500 years BP; (iv) Penultimate event at the South Opuha River terraces, inferred from terrace ages as a normal distribution with 2σ constrained by upper and lower 95th percentiles for bounding terrace ages; (v) Combined uniform distribution for the penultimate and antepenultimate events in Trench 5 – a simplification to remove large uncertainties in the age of the antepenultimate event; (vi) Inferred penultimate event age at Cloudy Peaks from on-fault recurrence interval and bounding ages of MRE/antepenultimate events; (vii) Preferred age of the antepenultimate event at Cloudy Peaks (Trenches 1 and 2); (viii) Age of antepenultimate event inferred from abandonment (SHD) age of T6. The combined curve was derived by concatenating the probability distributions for each event.

CHAPTER 4. MAXIMUM MAGNITUDES OF IMBRICATE REVERSE FAULTS: FAULT-TO-FAULT RUPTURE SCENARIOS

4.1 Abstract

Simultaneous rupture of imbricate reverse faults can increase seismic moment but is rarely considered in rupture scenarios for a fault system. In this chapter, I derive probability density functions of moment magnitudes for rupture scenarios on the Fox Peak and Forest Creek Faults. I use a Monte Carlo simulation to incorporate uncertainty in subsurface displacement, listric fault geometry and subsurface fault area. The exponential fault-to-fault jump probability depends on the distance between two faults, which is allowed to vary in the model. Coulomb stress modelling is used to analyse stresses induced on the receiver fault plane. The results indicate that maximum moment magnitudes of M_W 7.35 are likely for the fault system, which is a 0.15-0.2 point increase from other estimates and represents roughly 50-100% more moment release. Earthquake magnitudes will be even higher (c. M_W 7.4) if the fault is highly listric at seismogenic depths as is suggested by geophysical data and regional geologic data. This Monte Carlo approach is an improvement over simple empirical relationships for predicting M_W, provides realistic error estimates, and can be readily applied to other fault systems globally.

4.2 Introduction

Destructive earthquakes on reverse faults typically involve many complex surface traces (Rubin 1996). Where multiple fault segments rupture coevally the total seismic moment can be significantly larger than if the hypocentral fault ruptures in isolation (Dolan et al. 1995; Rubin 1996; Oskin et al. 2012; Elliot et al. 2012). Recent earthquakes have shown that multi-fault earthquakes are common and are accommodated by either static or dynamic stress changes on nearby faults and fault segments (e.g. Oglesby et al. 2003; Xu et al. 2009, Oskin et al. 2012; Elliot et al. 2012; Fukuyama and Hao 2013; Field et al. 2013). The incorporation of fault-to-fault triggering and segment jumping probabilities into seismic hazard models, however, has just recently begun to be implemented (Shaw and Dieterich 2007; Field and Page 2011; Carpenter et al. 2012; Parsons et al. 2012; Field et al. 2013).

Field data can help constrain fault parameters for modelling earthquake rupture scenario probabilities (e.g. Wesnousky 2006; Biasi and Weldon 2009; Parsons et al. 2012). Segment rakes, geometry, frictional strength, stress state and coseismic slip distributions determine whether rupture will propagate onto another segment (Oglesby et al. 2003; Lin and Stein 2004; Elliot et al. 2009; Schwartz et al. 2012). Faults that have no clear connection at the surface or that are blind are not typically involved in such analyses. In such cases, knowledge of whether the faults or segments are 'hard-linked' (intersect at the surface or at depth, or have transfer faults) or 'soft-linked' (have overlapping dimensions along-strike or down-dip) may play a critical role in whether rupture initiates on a secondary fault plane. For instance, the 2008 M_W 7.9 Wenchuan earthquake demonstrated that imbricate reverse faults soling into a single structure at depth can rupture in a single earthquake,

probably due to dynamic stresses and favourable fault strength/geometry (Oglesby et al. 2003; Xu et al. 2009; Densmore et al. 2010; Zhu and Zhang 2010; Fukuyama and Hao 2013). The 1911 c. M_W 7.8 Chon Kemin earthquake in the Tien Shan ruptured a wide zone of reverse and strike-slip fault segments of opposite vergence (Arrowsmith et al. 2005). Using Coulomb linking stresses, Parsons et al. (2012) showed that imbricate ruptures in California involving two or more faults may be more likely than continuous rupture on a single fault. Hubbard et al. (2014) showed the potential for large magnitude earthquakes on imbricate reverse faults in the Transverse Ranges. Fully dynamic fault models may increase the probability of multi-fault rupture (e.g. Oglesby et al. 2003), thus leaving simple physical and static Coulomb stress changes as proxies for the likelihood of coseismic fault triggering (Parsons et al. 2012).

In this study, I present a field and numerical approach to calculating maximum moment distributions of two imbricate reverse faults (the Fox Peak and Forest Creek faults) in the South Island of New Zealand. Coulomb failure stress (CFS) modelling is conducted to assess the feasibility of the specified rupture scenarios. Distributions of maximum moment magnitudes are calculated via Monte Carlo simulations that incorporate field data. Magnitudes and recurrence intervals of different rupture scenarios can be implemented into wider seismic hazard models, providing a route for the characterisation of reverse fault hazards in other areas.

4.3 Background

The Fox Peak and Forest Creek faults (FPF and FCF, respectively) are active back-thrusts of the Pacific-Australian plate boundary in the central South Island of New Zealand (Fig. 3.1 & 4.1). Geodetically-derived convergence rates at the plate boundary in New Zealand range from 30 to 50 mm yr^{-1} (Wallace et al. 2007; DeMets et al. 2010). Approximately 75% of this oblique convergence in the South Island is taken up on the Alpine Fault, a 400 km-long, right-lateral oblique fault. In the central South Island, the remaining c. 25% is distributed primarily onto structures like the FPF and FCF in the Pacific plate. Geodetically-derived slip rates across the FPF and FCF indicate dip slip rates of 2-5 mm yr^{-1} (Wallace et al. 2007).

Seismic and magneto-telluric surveys indicate that the FPF and FCF constitute a zone of major back-thrusting off the Alpine Fault (Long et al. 2003 Wannamaker et al. 2002), have surface traces that indicate on-going activity through at least the latest Pleistocene, and correspond to a secondary maximum in uplift and contraction rates in GPS transects (Beavan and Haines 2001). Both are 30-40 km long range-front structures that bound the Sherwood and Two Thumb Ranges (Fig. 4.1). Geophysical surveys (Long et al. 2003) and field mapping (Chapter 3) indicate that the two faults sole into a single structure at depth and that the FCF switches its vergence along strike to accommodate uplift of the merging ranges (e.g. Jackson et al. 1996) at their southern extent.

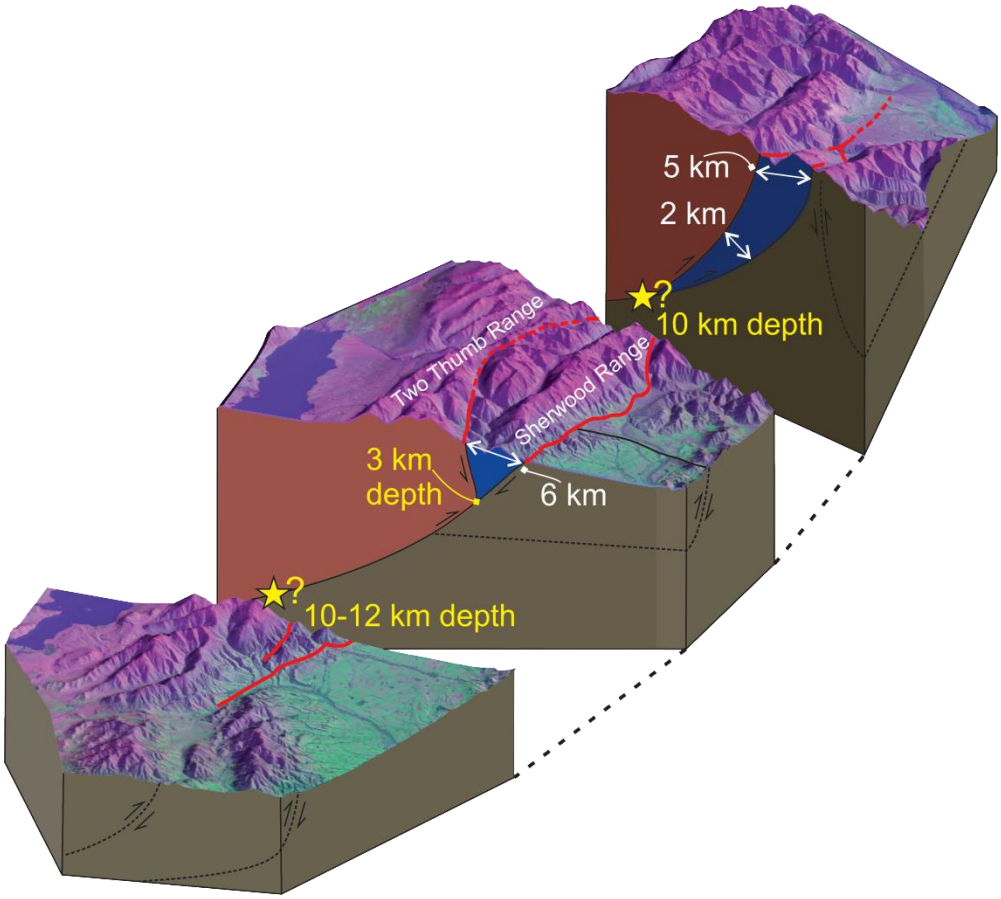

Figure 4.1: LANDSAT imagery and 15 m DEM block model of the field area. The FPF (bounding the Sherwood Range) and FCF (bounding the Two Thumb Range) are shown in red at the surface, with listric geometries predicted by regional geophysics studies, mapping and modelling. Other faults are included in cross-section that have been mapped, but do not have recent displacement and are not considered in this analysis. Derivation of the fault geometry is shown in Fig. 4.2. Yellow stars show the typical hypocentre depths in the field area (middle section, see Fig.4.4) and the branching depth of the listric FPF and FCF (northern section, top right).

The age distributions of paleoearthquakes observed in five trenches (Fig. 3.31 & 3.41) on active traces of the two faults have overlapping age errors. Due to the precision of the dating techniques, limited number of events, and uncertainty in timing of event horizons between bounding strata, it cannot be determined absolutely whether overlapping age distributions represent coincident FPF and FCF earthquakes. On a fast-slipping fault like the San Andreas, a 'stringing-pearls' analysis like that conducted by Biasi and Weldon (2009) may be warranted to find the most appropriate rupture scenarios based on observations in many trenches. In this analysis, I seek only to find the magnitudes of the largest earthquakes ('maximum credible events'), and so only need to assume that the FPF and FCF *can* rupture together (Chapter 3). Secondary/triggered faulting (e.g. Rubin 1996) and segment jumping distances observed in historical reverse earthquakes (Field et al. 2013) suggest that this assumption is warranted.

4.4 Methods

The moment magnitude distribution for rupture on the FPF and/or the FCF depends on (a) the fault geometry and structure, (b) the input seismic parameters (e.g. shear modulus and slip) and (c) the probability that rupture on one fault causes simultaneous rupture on the other. To address (a) and obtain the rupture area for (b) I combined field measurements of dip with constraints from regional studies (e.g. Wannamaker et al. 2002; Long et al. 2003; Upton et al. 2004; Beavan et al. 2007; Amos et al. 2007) to interpolate fault surfaces and their areas (Fig. 4.1 & 4.2, Table 4.1). The often conflicting structural models presented in these studies were analysed to construct two credible scenarios. The first scenario was constructed in Leapfrog Geo software by specifying a surface dip of 55° for a listric FPF that soles into a 15-20° dipping ramp at c. 4 km depth (after Long et al. 2003; Amos et al. 2007) near its southern tip. Surface measurements of dip and mapping further inform how the geometry of the FPF changes along strike. The FCF is inferred to sole into the FPF, which is a consequence of it being antithetic to the FPF in the South (Chapter 3, Long et al. 2003) and near vertical in the North (Chapter 3, Wannamaker et al. 2002, Beavan et al. 2007). The FCF is modelled as one continuous structure that changes its vergence along-strike for simplicity, though it may be comprised of two distinct fault segments in actuality. The second scenario includes a planar, high-angle FPF (55° dip) down to 5 km depth, flattening into a 30°-dipping planar fault, and a 55°-dipping FCF down to 12 ± 2 km depth. In both scenarios, the fault width is cut-off at 12 (± 2 for the planar scenario) km depth, as defined by the base of the seismogenic zone for the region (e.g. Berryman et al. 2002; Reyners et al. 2011). A normal distribution is used for seismogenic thickness to allow for the small possibility of an earthquake initiating on a shallow fault plane (e.g. Elliot et al. 2011).

Single event displacements for the faults were measured from surveyed scarp profiles and fault exposures in trenches (Chapter 3). Average surface displacement was then calculated based on the scaling relationships of Moss and Ross (2011) and converted into an average subsurface displacement (ASD) (Table 4.1). Shear modulus was fixed at 2.7×10^{-11} dyn cm^{-2} (Berryman et al. 2002).

I use the exponential, distance-based jumping probability of Shaw and Dieterich (2007) to model (c). This is considered reasonable for use in reverse faulting because reverse faults are more

likely than strike-slip faults to jump segments (Field et al. 2013), and this procedure allows specification of a jump distance based on constraints on subsurface geometry. Additionally, this model is easy to implement, agrees well with empirical datasets (e.g. Field et al. 2013), and does not rely on interpretation of the mode of fault triggering (e.g. rupture branching, or static or dynamic triggering). For short distances (<10 km) the relationship is

$$p(r) = e^{\frac{-r}{r_0}} \qquad \textit{(Eqn. 4.1)}$$

where r is the jump distance, r_0 is a constant inversely proportional to the fall-off of probability with distance, and $p(r)$ is the jump probability (Shaw and Dieterich 2007). I use a value of r_0=3, as this is yields conservative probabilities at $r \geq 5$ km that are consistent with the limited data for reverse fault earthquakes (cf. Rubin 1996; Wesnousky 2008; Field et al. 2013)

A Monte Carlo simulation was used in which input parameters were allowed to vary based on uncertainty in the fault geometry, location on the FPF where jumping occurs and ASD. In each iteration (i.e. earthquake), rupture on the FPF jumps onto a pre-specified length of the FCF depending on the randomly sampled r and exponential jump probability density function. M_W is then calculated from the cumulative rupture area, ASD, shear modulus, and relationship with seismic moment (Hanks and Kanamori 1979).

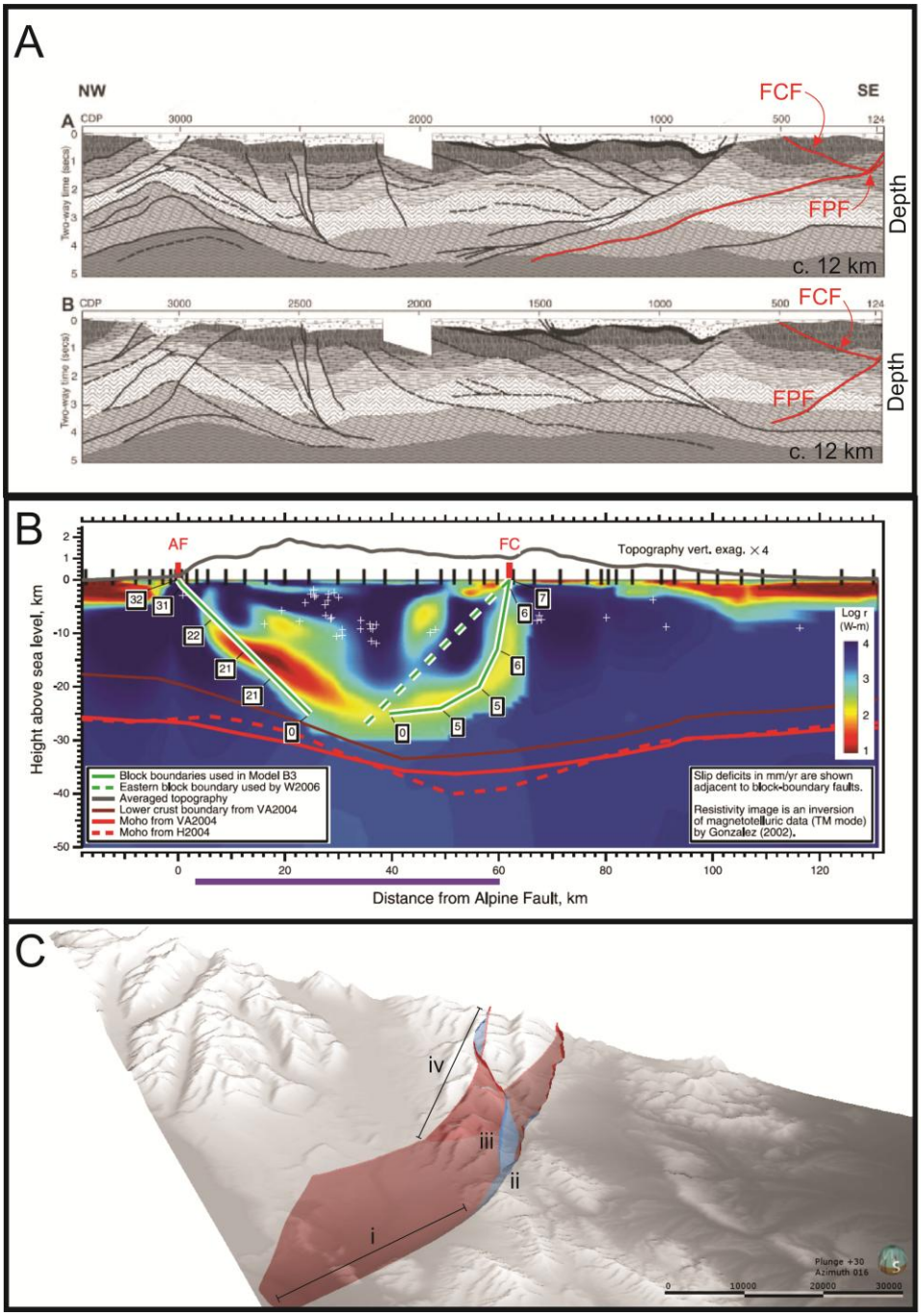

Figure 4.2: Determination of fault geometry for the listric rupture model.(A) Seismic survey of Long et al. (2003) which crosses the subsurface FPF and FCF at their southern end (ii in C). (B) Interpretation of Alpine Fault and FCF geometries based on magneto-telluric survey that crosses the northern FCF at the Rangitata River (Beavan et al. 2007). Faults (green) are drawn along anomalies in resistivity. Green dashed line is FCF geometry used by Wallace et al. (2007); solid green line is used in Beavan et al. (2007). Both infer a steeply dipping structure at the surface that is planar to the base of the seismogenic crust, which is inconsistent with other subsurface studies. (C) The geometry used in this study, controlled by (A), (B) and field mapping. (i) 15-20° dipping ramp from 12 to 4 km depth; (ii) Listric from 4 km depth to a surface dip of 55°; (iii) Antithetic FCF in the South; (iv) Steeply dipping, synthetic FCF soling into the FPF at c. 10 km depth.

4.1: Input parameters for Monte Carlo simulation of M_W.

Input parameter	Shear modulus[a]	Average Surface Displacement[cd]	Subsurface:Surface Displacement Ratio[a,b,c,d]	FPF Area (listric)[d,h,i,k]	FCF Area (listric)[d,h]	Jump Distance[g,h,i,j]	R_0[gl]	FPF Surface Length	FCF Surface Length	Subsurface: Surface Length Ratio	Fault dip	Seismogenic thickness (ST)[a,d]
Model PDF	Fixed	Fixed, Calculated from field mapping	Trapezoidal	Fixed from model	Fixed from model	Normal	Fixed	Fixed	Fixed	Trapezoidal	Fixed from field mapping, geophysics	Normal
PDF constraints*	2.7E11	2 m	1-1-4/3-5/3	2046 km^2	585 km^2	2.5 (± 2.5) km	3	35.7	0, 15, 40	1-1-4/3-5/3	FPF: 55° @ 0-5 km; 30° @ 5-ST km; FCF: 55° @ 0-ST km	12 (± 2) km

*[a]Berryman et al. (2002); [b]Wesnousky (2008); [c]Moss and Ross (2011) ; [d]This study (Chapter 3); [e]Upton et al. (2004); [f]Cox and Barrell (2007); [g]Shaw and Dieterich (2007); [h]Long et al. (2003); [i]Beavan et al. (2007); [j]Wannamaker et al. (2002); [k]Amos et al. (2007); [l]Field et al. (2013); *Single value is given where a constant is used; Mean and (2σ) given for normal distributions; Lower bound - Maximum 1 - Maximum 2 - Upper bound given for trapezoidal distributions. Shaded area is for planar fault model only.*

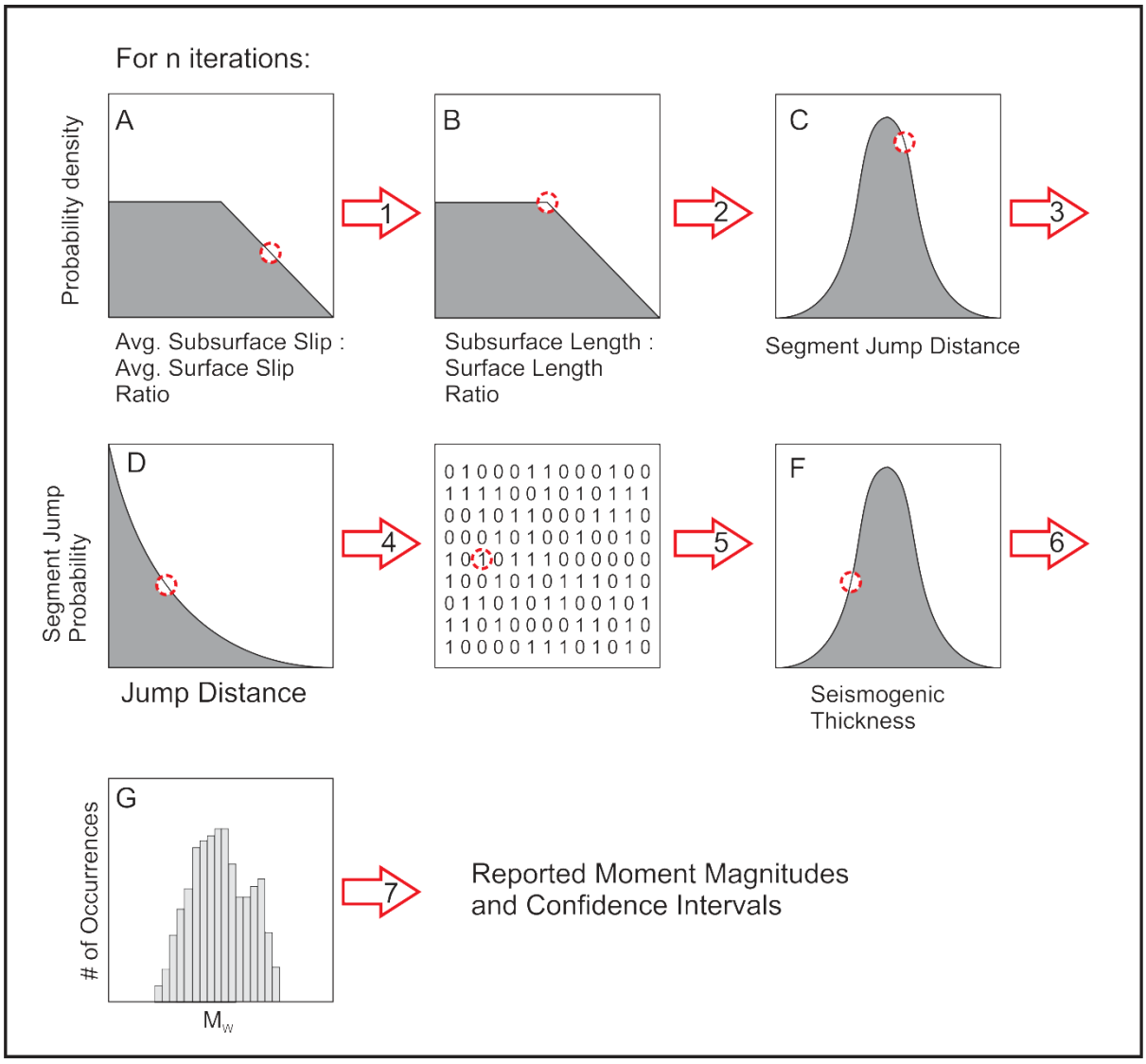

Figure 4.3: Algorithm for calculating M_W in the planar fault model. For each probability distribution, the values used can be found in Table 4.1. Red circles are examples of random samples from the allocated distribution. (A) Convert average surface displacement to a subsurface displacement by randomly sampling a trapezoidal distribution. (B) Perform the same sampling technique for converting surface length to subsurface length. (C) Sample from a normal distribution of 'step-over' distances, which depends on how and where on the fault planes rupture initiates and propagates. Distance is not allowed to be negative. (D) Using the distance in (C), calculate the probability that rupture initiates on the FCF. (E) Generate an array of ones and zeroes, where 1=FCF ruptures and 0=FCF does not rupture, and the number of each in the matrix depends on value in (D). (F) Sample from the seismogenic thickness distribution. Step 6 uses the information from A-F to calculate the fault width, area, seismic moment, and finally M_W using equation of Hanks and Kanamori (1979) (see Table 4.1 for parameters). The process is repeated to produce (G). For the listric fault model M_W, the fault geometry is pre-specified, and so only relies on (A), (C), (D) and (E).

Coulomb stress modelling was conducted using Coulomb 3.3 (e.g. Lin and Stein 2004). I consider three simple scenarios, each involving stress transfer from a rupturing FPF onto the FCF. The alternative was considered – FCF triggering the FPF – however, the FPF is clearly the more active of the two structures over the late Quaternary and preliminary modelling suggests that the stress

change on the FPF is negligible in this scenario (Chapter 3). Therefore, the stress changes are only considered in one direction (FPF to *both* segments of the FCF). The effect of one FCF segment on the other has not been investigated.

Ruptures on other intersecting faults (e.g. those shown in Fig. 4.1 and discussed in Chapter 3) were likewise ruled unlikely and not shown in the Coulomb models. Listric geometries for the FPF and FCF were constructed via connecting planar segments of different dips. The first considers 3 m of slip on the central down-dip segment of the FPF (40° dip, 4-6 km depth), where slip might be expected to concentrate in an earthquake (e.g. Kaneko and Fialko 2011). The second considers 3 m of slip only on a 20° dipping ramp at 8-12 km depth, where hypocentres cluster in the field area (Fig. 4.4). The third considers only 60° dipping planar faults with 3 m of slip on the FPF tapering from the centre of the fault. In each scenario, the receiver fault (FCF) is subdivided into 3-4 km long and wide divisions. Coulomb stress was calculated for dip-slip motion on the FCF and FPF. I used a coefficient of friction of 0.8 (after Lin and Stein 2004), though varying this parameter did not heavily influence preliminary tests. Default values of 8×10^5 Bars and 0.25 were used for Young's modulus and Poisson's ratio, respectively.

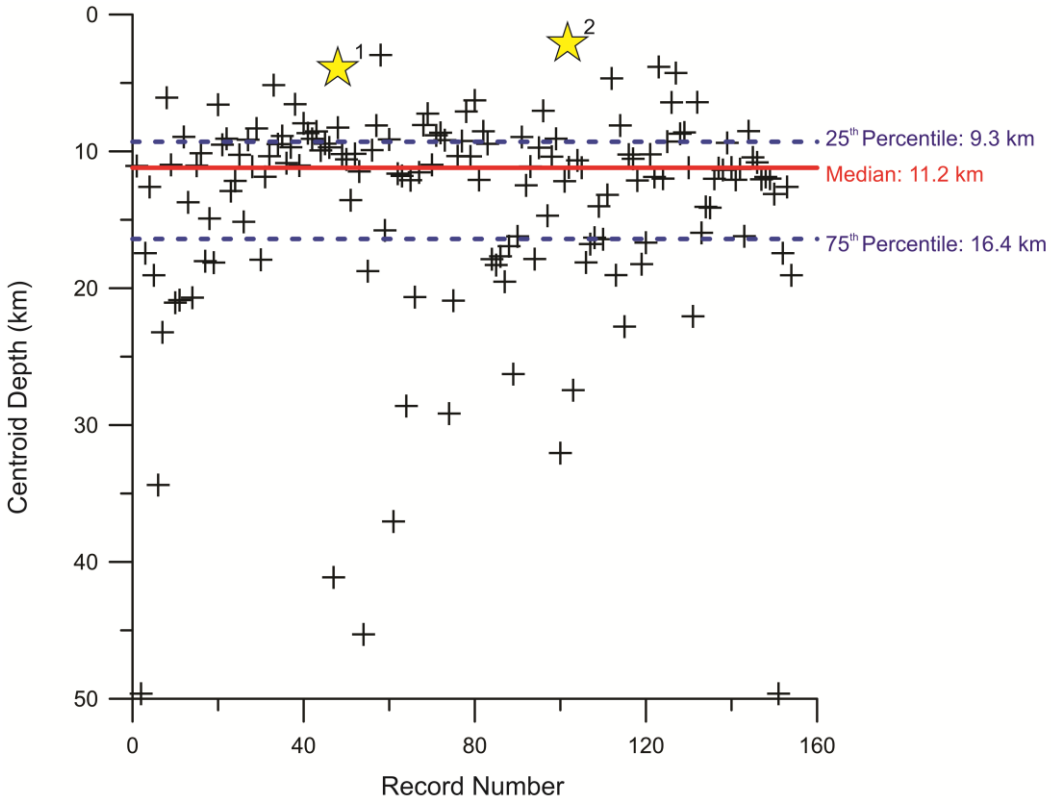

Figure 4.4: Relocated hypocentres for the central South Island (after Reyners et al. 2011). Yellow stars are for known, high-angle reverse mechanism earthquakes: [1]2011 M_W 4.2 earthquake near the Ostler Fault (data available from USGS) at 4 km depth; [2]2004 M_W 4.5 earthquake near the Fox Peak Fault (data available from GeoNet) auto-located at 2 km depth.

4.5 Results

Five rupture scenarios are considered in the fault-triggering model (Fig. 4.5). In each scenario, moment magnitude distributions change form to account for different allowable lengths and widths of the rupture on the faults. Variability about a peak is due to uncertainty in the input parameters and consequent variability in each iteration of the model (n=10000 iterations). The shape of the output distribution is determined by the input distributions and how often an earthquake is triggered on a given length of FCF.

The M_W of an earthquake involving only the FPF depends heavily on whether the fault is listric. The planar fault model produces an average of M_W 7.15 ± 0.12 (5^{th} and 95^{th} percentiles), which is consistent with the estimate in the national seismic hazard model (Stirling et al. 2012, M_W 7.2) and estimations from the scaling laws in Chapter 3 (M_W 7.03 ± 0.24 and 7.2 ± 0.3) (Fig. 4.5A). Including a 15 km FCF in the planar model increases the mean and skews the distribution to the left (M_W 7.18 ± 0.14), but there is no distinguishable second mode in the data due to FCF rupture (Fig. 4.5B).

Inclusion of a 40 km FCF results in a distribution with two modes, though the summed effect of the uncertainty surrounding each 'peak' results in a flat, almost trapezoidal distribution. The average for this scenario is M_W 7.22 ± 0.20, with 'peaks' at M_W 7.15 and 7.32 (Fig. 4.5C).The listric model distribution for the FPF alone (Fig. 4.5D) is more asymmetric and produces an average of M_W 7.39 ± .06. The listric model produces an average of M_W 7.42 ± 0.08 with primary peaks at M_W 7.35 and 7.4 for the 40 km FCF rupture scenario (Fig. 4.5E)

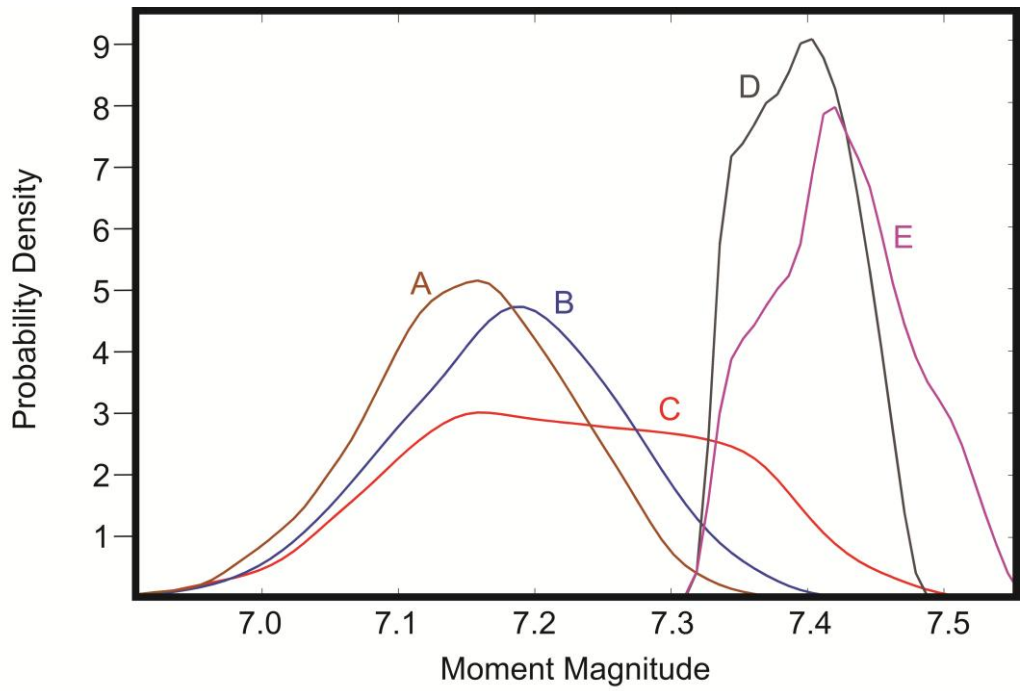

Figure 4.5: Probability density functions of maximum M_W for five rupture scenarios. Planar fault models: (A) FPF in isolation; (B) FPF allowing for 15 km surface length of FCF; (C) FPF allowing for 40 km surface length of FCF; Listric fault models: (D) FPF in isolation; (E) FPF allowing for 40 km surface length of FCF. See text for discussion. Output histograms were fit with nonparametric distributions using a normal kernel and bin width of 0.01.

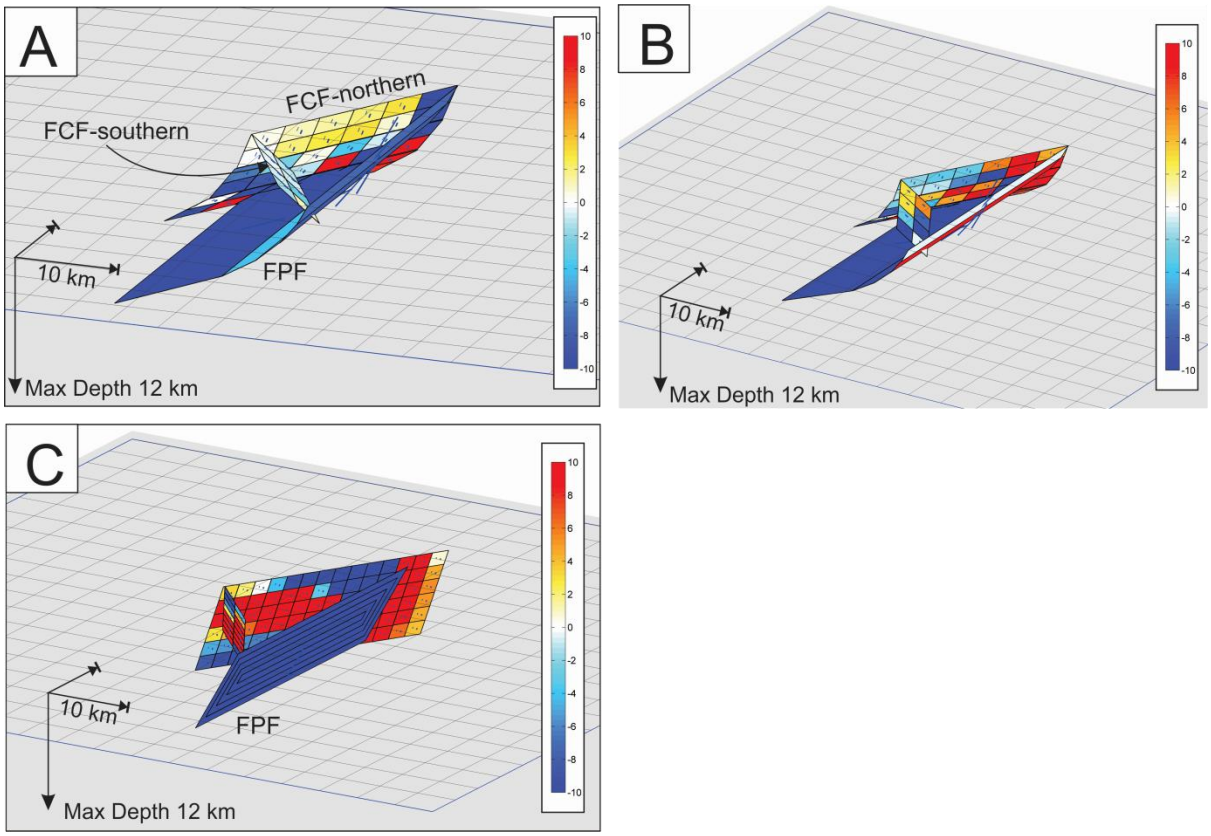

Figure 4.6: Induced Coulomb stresses on the FCF from rupture on the FPF. (A) 3 m slip on a 40° dipping segment of the FPF causes small decreases on the southern (antithetic) FCF (c. -1 Bar), small increases on the central FCF (c. 2 Bar) and large increases (10> Bar) on the northern FCF at depth. (B) 3 m slip on a 20° dipping segment of the FPF causes equal negative and positive changes on the southern FCF, negative changes on the central FCF (c. -3 Bar) and large increases on the northern FCF (5+ Bar). (C) 3 m tapered slip on the entirety of a steep (60° dipping FPF) causes large increases on the southern FCF (10> Bar), large increases on most of the central and northern FCF (10> Bar), and a patch of large negative changes (< -10 Bar) in the North.

The Coulomb stresses caused by slip on the FPF depend on the fault geometry used and the displacement pattern. For rupture on a moderately dipping reverse fault plane (Fig. 4.6A), large positive changes (>10 Bar) are only induced on the lowest portion of the FCF (10-12 km depth). While this area is small compared to the total area of the fault, it is coincides with the depth of hypocentres on the region (Fig. 4.4) and with the most recent surface trace of the FCF (Chapter 3). Large stress shadows are located at the edges of the fault, and stress decreases on the southern, antithetic FCF are negligible. For rupture on the gently-dipping ramp of the FPF (Fig. 4.6B), Coulomb stresses show large (>10 Bar) increases on the 50°-dipping portion of the FPF, the northern FCF, and part of the southern FCF. Again, increases on the northern FCF coincide with the recent surface trace. Decreases in the middle section coincide with a lack of any FCF trace at the surface. The steeply-dipping planar fault model (Fig. 4.6C) shows large increases on the FCF except in the section that

roughly coincides with the recent surface trace. Tapering of fault slip produces the same pattern of increases and decreases as non-tapered slip (not shown).

4.6 Discussion

4.6.1 Evaluation of Monte Carlo method

To date, most seismic hazard evaluations of segmented or fault-to-fault ruptures and resulting M_W have relied on informed opinion to create weighted logic tree branches. For instance, if a panel of geologists determines that the probability of a certain fault-to-fault rupture is 0.5, with all other inputs being equal, the two possible M_W outcomes are equally weighted in the hazard evaluation. The Monte Carlo approach in this study is different in that the most likely jump distances and the equation governing the jump probability is pre-specified (Eqn 4.1), but not the probability itself. This is a preferred methodology because it reduces subjectivity in defining rupture scenarios and produces a range of possible rupture scenarios over many model iterations. Because the jump equation used in this study is dependent on distance, many fault-to-fault rupture scenarios could be possible, though at large distances they become increasingly improbable (e.g. Parsons et al. 2012). Furthermore, because fault kinematics and geometry are constrained in the present study, Coulomb stress models can be used to test the feasibility of triggered slip. In future models, distributions of induced Coulomb and dynamic stresses on a receiver fault plane may be used to inform the jump probability directly, similar to cellular automata or synthetic seismicity models (e.g. Bebbington and Harte 2003; Robinson 2004).

4.6.2 Determination of appropriate M_W distribution for the Fox Peak and Forest Creek Faults

Distributions A and D in Fig. 4.5 represent baseline (i.e. no FCF rupture) calculations of M_W on the FPF. While (A) agrees well with previous calculations, (D) is c. 1.5-2 times larger in terms of moment release. Because there is uncertainty in the depth and to which angle the FPF flattens, it is difficult to favour one model over another. The inclusion of variable FCF rupture lengths in (B) and (C) brings the M_W closer to (D) and (E). Thus, maximum M_W values for the FPF and FCF are larger than indicated by a planar FPF rupturing in isolation.

The results of the Coulomb stress modelling can inform which rupture length of FCF is feasible. This is not to imply that large patches of fault elements that see a stress increase will initiate rupture, or that stress shadows on the fault planes represent barriers to rupture propagation. The length of the FCF rupture, if any, depends strongly on the distribution of stress on the plane prior to the initiating earthquake (e.g. Steacy and McCloskey 1998; Schwartz et al. 2012) and dynamic rupture stresses (Oglesby et al. 2003). Additionally, triggering may take days to years, even if the faults have been partially ‘synchronised’ over several earthquake cycles (Scholz 2010). Since this is an

investigation of the maximum M_W potential of the system, it is assumed that the FCF is capable of being triggered at any point in its own earthquake cycle. The minimum stress increases on parts of the FCF in all Coulomb models (>10 Bar) are within the lower bounds of historical earthquake stress drops and imply that this assumption is not unfounded (e.g. Baltay et al. 2011).

Caskey and Wesnousky (1997) found that sites of Coulomb stress increases on one fault rupture coincided with the locations of surface rupture on another during the Fairview Peak and Dixie Valley earthquakes. Oglesby et al. (2003) found that Coulomb stresses are good predictors of, or underpredict, the ability of ruptures to jump onto overlapping thrust faults. If this is true for the FPF-FCF, then the stress increases observed on the northern FCF underlying the recent surface trace at seismogenic depths may indicate that only this c. 15 km stretch of fault consistently ruptures with the FPF (and preference should be given to distribution (B) in Fig. 4.5). The overlap in the last two event ages on the faults (Chapter 3) is in agreement with this interpretation, though no paleoseismic data is available on the southern FCF. The southern FCF has variable stress increases/decreases, depending on the fault geometry used and location of slip on the FPF (consistent with the observations of Kato [2011] for a similar fault geometry). Thus, the rupture length of the FCF may also change based on the slip distribution on the FPF in any given earthquake. For the purposes of seismic hazard, distribution (C) may be the most appropriate, as it accounts for the full-length FCF rupture and has a primary mode around that of (B).

Not surprisingly, the listric models have significantly larger fault widths and therefore M_W. If the listric geometry predicted by regional seismic surveys and fold models (Long et al. 2003; Amos et al. 2007) is correct, then the resultant increase in seismic moment outweighs the consideration of fault triggering in this study. Given that at least one historical earthquake has occurred on a listric reverse fault with no surface manifestation of a low-angle ramp (i.e. 2008 M_W 7.9 Wenchuan earthquake: Yu et al. 2010; Zhang et al. 2010) this requires serious attention in considering maximum M_W. Given my modelling results, a maximum M_W of at least 7.35 (Fig. 4.5C, D) should be considered for the FPF and FCF.

4.7 Conclusions

Multi-segment and imbricate reverse fault rupture pose devastating societal consequences and a challenge to earthquake hazard models. Inability to quantitatively predict the relative frequency and location of multi-fault/multi-segment earthquakes can lead to large underestimates of moment magnitudes for a fault system. Using field and geophysical data, I have provided a methodology for calculating moment magnitude distributions for the largest earthquakes expected from a system of interacting faults. Studies that do not take into account fault triggering or listric geometries could significantly under-predict the moment magnitude of an earthquake.

CHAPTER 5. COSEISMIC LANDSLIDING DURING THE 2010 M_W 7.1 DARFIELD (CANTERBURY) EARTHQUAKE: IMPLICATIONS FOR PALEOSEISMIC STUDIES OF LANDSLIDES

5.1 Abstract

The head scarp of the Harper Hills landslide consists of extensional ground cracks with vertical displacement that opened during the 2010 Darfield (Canterbury) M_W 7.1 earthquake. The geomorphology of the cracks, regional geology and ground penetrating radar indicate that the landslide formed by bedding-controlled translation and joint-controlled toppling, and suggest incipient deep-seated movement. Crack depth and displacement along the head scarp vary along the ridge; maximum values are located where the head scarp is closest to the local ridge-line. Increased seismic shaking due to topographic and geometric amplification of seismic waves is suggested as an explanation for this relationship. An excavation across the head scarp revealed no evidence of prior slip events over a time period that is likely to exceed the return period (1000–2500 years) of peak ground accelerations experienced at this location in the Darfield earthquake. I suggest that specific seismologic attributes of the Darfield earthquake may have influenced the location of landsliding in this instance. Studies of paleo-landslides must consider crack preservation potential as well as complex source/site effects that may complicate estimates of acceleration return periods from the subsurface investigation of individual landslide head scarps.

5.2 Introduction

Earthquake-induced landslides are a major hazard in tectonically active regions. Characterising the seismic conditions under which landslides are triggered is assisted by empirical data from past landslides. Characteristics of strong ground motion may be ascertained by combining geological and geomorphologic studies with back-analysis models of slope stability (Jibson and Keefer 1993; Jibson 1996, 2011). These studies are of interest to paleoseismologists because landslides have the ability to provide a history of earthquake-induced strong ground motion at a site independent of fault studies.

Where deep-seated landslides have been preserved in the landscape, geomorphic mapping and trenching can yield information on ground failure (e.g. Nikonov 1988; Nolan and Weber 1992, 1998; McCalpin and Irvine 1995; Onida et al. 2001; McCalpin and Hart 2002; Gutiérrez et al. 2010a; Hart et al. 2012; Moro et al. 2012; Carbonel et al. 2013). Trench studies allow determinations of landslide kinematics and movement rates that can help distinguish whether motion is episodic or progressive (Agliardi et al. 2001; Johnson and Cotton 2005; Gutiérrez et al. 2008, 2010b). Without a detailed inventory of mechanical rock properties, ground water conditions, and a range of possible seismic inputs and site-response characteristics, unambiguous evidence of a seismic origin is often difficult to obtain. In areas of active faulting, the determination of a seismic or aseismic origin, and the causative fault source, has a significant impact on determining seismic hazard.

In this chapter, I present a geomorphic and subsurface study of ground cracks that opened coseismically during the 2010 Darfield earthquake in New Zealand. Trenching and ground penetrating radar (GPR) are used to investigate the kinematics, morphology and failure mechanism of the landslide. I conclude with suggestions for incorporating subsurface records of strong ground motion from landslides into paleoseismic analyses.

5.3 Geologic and tectonic setting

5.3.1 Darfield earthquake

The M_W 7.1 Darfield (Canterbury) earthquake (henceforth the Darfield earthquake) in New Zealand was caused by rupture on a series of previously unrecognised faults underlying the low relief Canterbury Plains (Fig. 5.1; Quigley et al. 2010, 2012; Beavan et al. 2010, 2012; Gledhill et al. 2011; Elliott et al. 2012). The earthquake initiated on the steeply dipping, reverse Charing Cross fault which triggered predominantly strike-slip motion on three to four E–W to NW–SE striking Greendale Fault segments. Two other strike-slip faults intersecting the main Greendale Fault traces and a second high-angle, blind reverse fault to the West (the Hororata Anticline Fault, HAF) also ruptured (Beavan et al. 2012; Elliott et al. 2012; Jongens et al. 2012). Differential interferometric synthetic aperture radar (DInSAR) (Fig. 5.1) highlights the relative motions of the major fault planes towards (lighter) and away from (darker) the line of sight of the recording satellite (Beavan et al. 2010). GPS measurements and other survey techniques indicate a maximum of 1.4–1.6 m vertical, normal displacement on the western segment of the Greendale Fault at the surface and 0.4 m uplift on the intersecting HAF, both NW-side up (Beavan et al. 2010, 2012; Duffy et al. 2013).

Peak ground accelerations (PGAs) on the Canterbury Plains reached a maximum of c. 1.3 times that of gravity (g) near the Greendale Fault (Gledhill et al. 2011; Bradley 2012). Finite-element modelling of un-instrumented ridge-tops in the Port Hills (east of the Greendale Fault) where boulders were displaced in the Darfield earthquake indicates frequency-dependent amplification of PGAs of up to 80% greater than at the base of the hills (Khajavi et al. 2012). The multiple-fault rupture contributed to complex and varying waveforms at recording stations, though in general accelerations recorded within 25 km of the Greendale Fault all exceeded 0.1 g (horizontal and vertical over 0.01–10.0 s period) with 5–95% significant durations of 20–30 seconds (Bradley 2012).

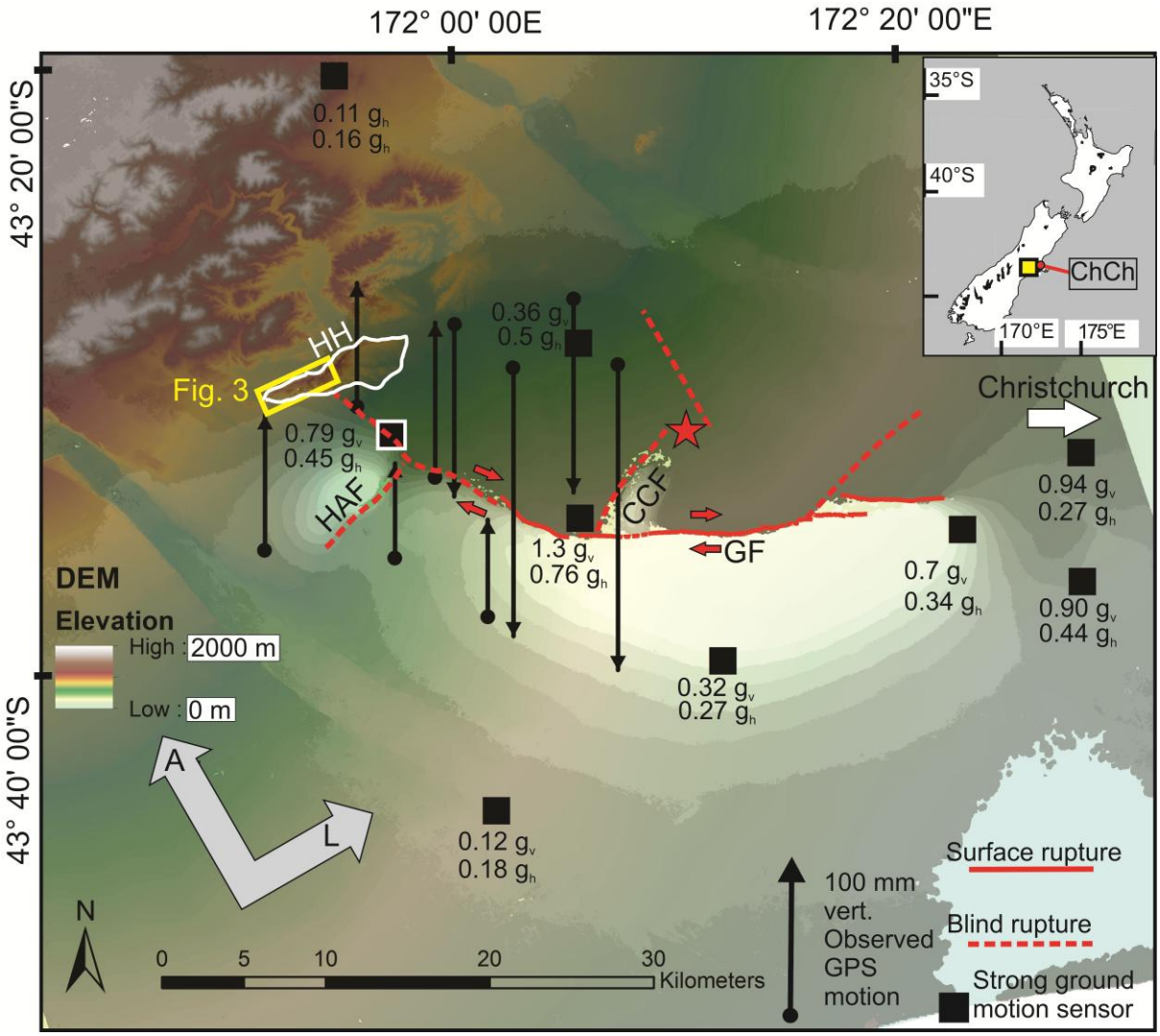

Figure 5.1: Map and study site location. 15 m Digital Elevation Model (DEM) showing location of i) faults involved in the 2010 Darfield earthquake: Greendale fault (GF), Hororata anticline fault (HAF), Charing Cross Fault (CCF) and other unlabelled structures from Beavan et al. (2012); ii) DInSAR interferogram showing relative motion of faults with respect to the satellite heading direction (A) and satellite look direction (L). Lighter areas moved toward the satellite in the direction of L, and darker away; iii) Selected GPS stations with absolute motions; iv) Selected strong ground motion sites with vertical and horizontal PGAs reported from Bradley (2012). White outlined station is HORC (see text for discussion); v) Location of the Harper Hills (white outline on the DEM) and the field area (Fig. 3=Fig. 5.3).

5.3.2 Harper Hills

The Harper Hills are located 20 km west of the epicentre of the Darfield earthquake and 9 km NW of the up-dip surface projection of the HAF (Fig. 5.1). The south-western 5 km of the E–NE trending strike-ridge is located on the hanging wall of both the HAF and the subsurface extension of the Greendale Fault (see Fig. 5.1). The nearest strong motion seismometer ('HORC', Hororata School, Fig. 5.1) recorded a peak vertical acceleration of 0.79 g and a peak horizontal acceleration of

0.45 to 0.51 g (using methods of Bradley 2012 and GeoNet for horizontal accelerations, respectively). The 5–95% significant duration was markedly shorter for HORC (8.7 seconds) compared with stations further away from the causative faults (Bradley 2012). Horizontal accelerations were strongest in W–NW/E–SE directions with the highest vertical accelerations recorded in the NW and SE quadrants (Fig. 5.2; 0.1 Hz high-pass filtered data currently held by GeoNet).

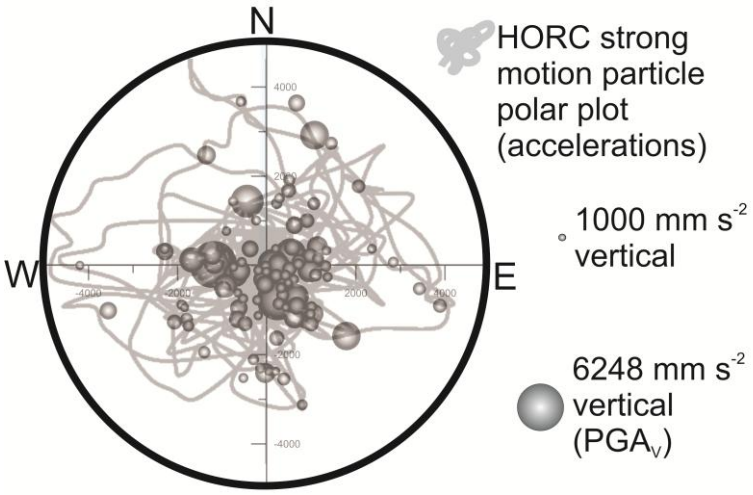

Figure 5.2: Local strong ground motion characteristics. Strong motion polar plot at Hororata School (HORC) with i) two-component horizontal accelerations and ii) largest vertical accelerations scaled to magnitude and located according to its two horizontal components (data from GeoNet).

The Harper Hills strike-ridge is asymmetric with a steep scarp slope (40–70°) and gentle dip slope (20–40°) defined by joint and bedding planes, respectively (Fig. 5.3 & 5.4). It is one of the easternmost topographic highs in the foothills of the Southern Alps despite the relatively subdued 210 m of relief. The regional geology consists of SE-dipping Cretaceous-Tertiary sandstones, volcanics, and locally-mined beidellite-montmorillonite-bentonite units of the Burnt Hill Group (Carlson et al. 1980; Browne 1983). On the scarp slope, jointed blocks of the Upper Miocene Harper Hills Basalt can be observed conformably overlying well-bedded Sandpit Tuff. Pliocene gravels overlie the Burnt Hill Group on the dip slope of the field area. North-east of the field area, Forsyth et al. (2008) mapped undifferentiated Quaternary landslide deposits along the dip-slope below the Harper Hills Basalt (Fig. 5.3). The Hororata Fault (a different structure than the HAF, which ruptured in the Darfield earthquake, Fig. 5.1) bounds the NE section of the Harper Hills (Fig. 5.3).

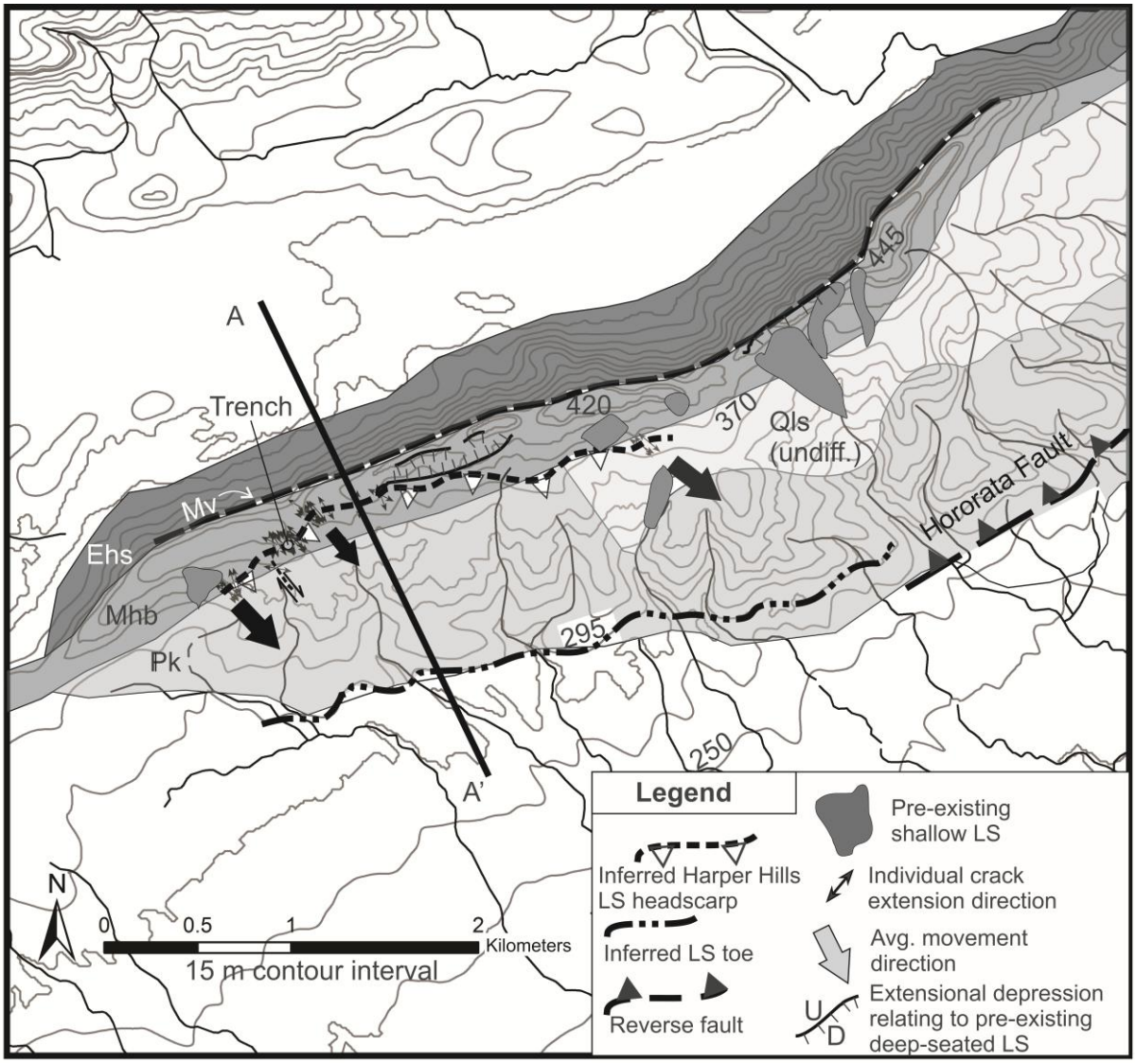

Figure 5.3: Geologic and geomorphic map of the field area. LS (in the legend): Landslide; Ehs: Homebush Sandstone; Mv: Undifferentiated volcanics (Sandpit Tuff & Chalk Hill Clay) with minor limestone; Mhb: Harper Hills Basalt; Pk: Kowai Gravels; Qls: Undifferentiated Quaternary landslide deposits. Based on Forsyth et al. (2008). Cross-section A–A' shown in Fig. 5.9.

The Harper Hills Basalt is identifiable as a prominent scarp along the length of the Harper Hills. Rolling hills with c. 10 m scale local relief, slope-parallel drainages and numerous swales dissected by small streams characterise the dip-slope of the Harper Hills. Arcuate to curvilinear breaks in slope, hummocky terrain and several shallow slope failures are indicative of ongoing landsliding. Muirson (2003) identified a bedding-controlled, deep-seated landslide north of the field area in this study. The Chalk Hill Clay, a bentonitic unit, and the overlying Sandpit Tuff were identified as possible failure planes. The former has a residual internal friction angle (21°) less than the regional slope (c. 30°) (Muirson 2003). Historical photos show that the landslide is older than 50 years, but could be much older.

5.3.3 Harper Hills coseismic landslide

Curvilinear ground cracks parallel to the ridge-line of the Harper Hills were documented two days after the Darfield earthquake (Fig. 5.3 & 5.4). Landowners stated that the cracks had opened during or within 2–3 hours of the main shock (4:35 am NZST) as the features were first observed at dawn. A small stock pond (seen in Fig. 5.4B) was reported to have drained in an aftershock within two days of the main shock, perhaps implying a second phase of displacement on the cracks. The ground cracks displaced farm tracks in a few locations and tension from surface extension caused fence wire to snap in at least one location and tighten at several others. Damage to infrastructure was otherwise minor.

Cracks were mapped on the ground using differential GPS (dGPS) aided by aerial reconnaissance (Fig. 5.4A–F). The cracks occur intermittently along the southern Harper Hills for 2.5 km, with the south-western-most 1 km containing over 75% of the features. Cracks occur at 340-380 m elevation, but most commonly at 370-380 m. The longest continuous features are approximately 120 m long and occur at the south-western and north-eastern extremities (Fig. 5.4C and 5.4E, respectively). In places, the cracks traverse the local slope but remain parallel to the average strike of the Harper Hills ridge-line (i.e. cut across topography; Fig. 5.4A). On the top of interfluves in the central region of the landslide, displacement is relatively small and often expressed as fissures that straddle surface cobbles (Fig. 5.4F). There was no surface break at the foot of the Harper Hills, though a 27 m long crack was observed 460 m SE (down-slope) of the head scarp. The best expression of this crack was on a road which was re-graded soon after the earthquake, but displacement was observed to be small in comparison to the head scarp region.

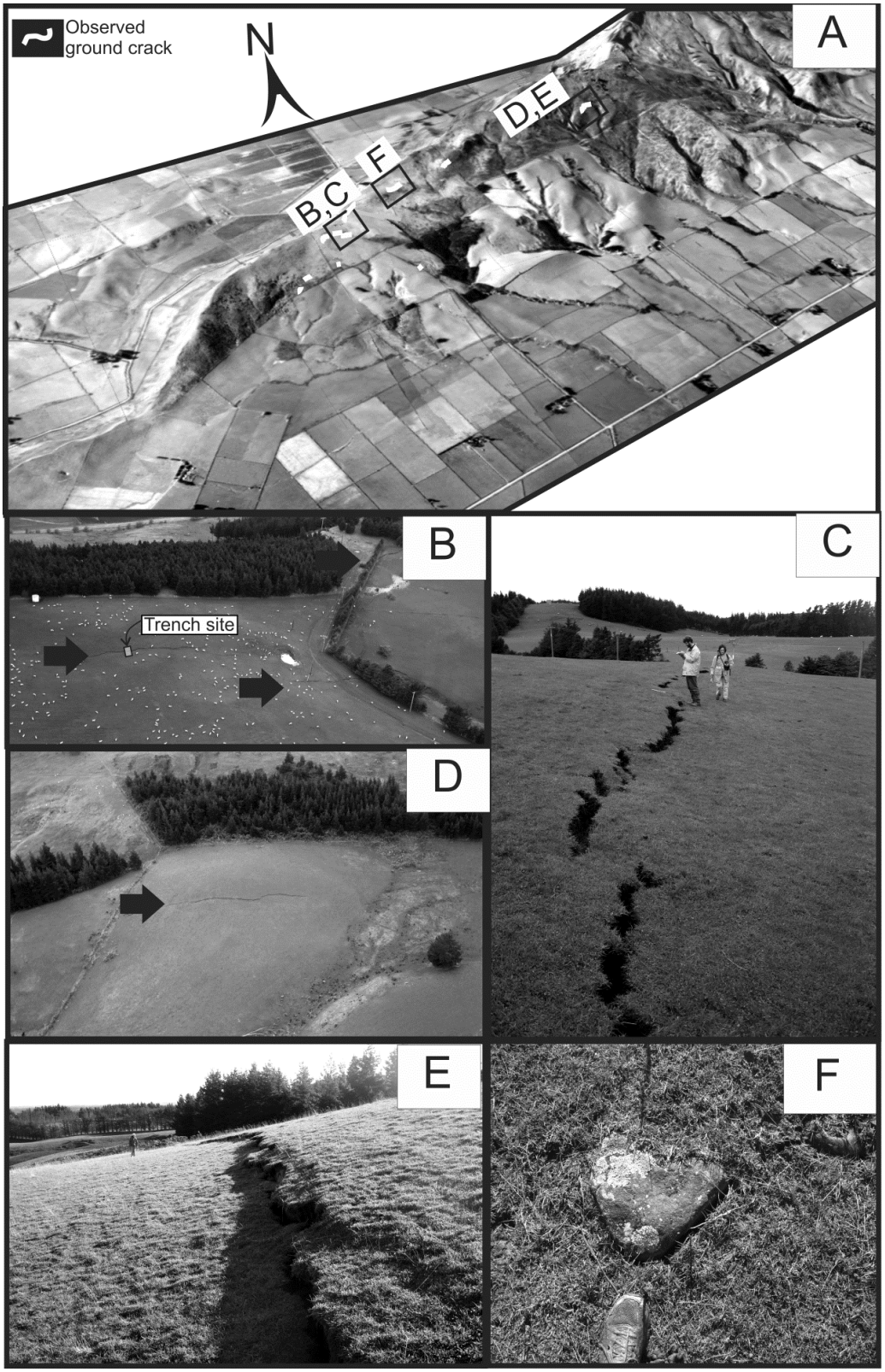

Figure 5.4: Ground crack map and field photos of the Harper Hills landslide. A) Aerial photography overlain on a 15 m DEM showing hill geometry and location of mapped ground cracks shown as short white lines. B–F) Field photos of ground cracks (See text for discussion).

Measurements of crack depth, extension, vertical displacement and movement direction were taken at 41 points along the length of the cracks. The most pronounced cracks are located in a 400 m stretch on the south-western end of the landslide where 73% of the cumulative net displacement is recorded over 16% of the along-strike distance. The largest net displacements were measured on the cracks with the greatest fissure depth, and these are typically situated closest to the Harper Hills ridge-line (Fig. 5.5). Monitoring arrays consisting of two to three wooden pegs were placed across the features at seven locations. Over the course of two years, the pegs were re-measured five times using a tape measure, and no further relative displacement across the cracks was observed.

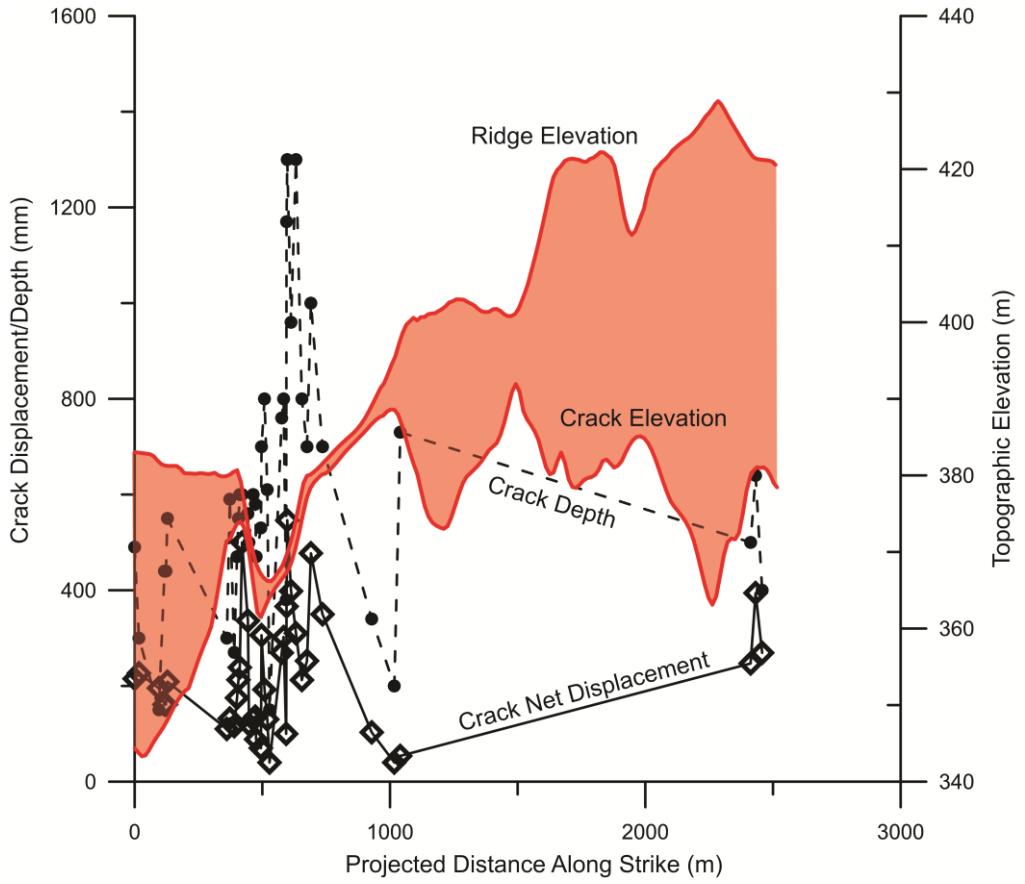

Figure 5.5: Measurements of ground deformation in the Harper Hills landslide. Crack net displacement (open diamonds, solid line) and depth (filled circles, dotted line) in millimetres plotted against projected distance along the landslide. Ridge to crack relief envelope (red) shows that cracks with the most displacement/depth generally occur nearest the ridge-top (i.e. where the envelope is thinnest). Where cracks were discontinuous across the slope, the lower boundary of the relief envelope was determined by connecting straight elevation profiles (in map view) to the next feature.

Crack extension directions were weighted by net displacement and compared to the regional structural geology trends and slope (Fig. 5.6). Bedding and joint measurements were taken NW of the head scarp from outcrops of the Harper Hills Basalt overlying the Sandpit Tuff. Bedding

measurements NE of the field site reveal a consistent strike and dip along the length of the Harper Hills (Carlson et al. 1980; Muirson 2003). Poles to the dominant joint set (steeply NW-dipping, $n = 9$) and bedding planes (SE-dipping, $n = 4$) match the average orientation of the crack extension direction and DEM-derived aspect of the dip-slope. Crack extension direction best coincides with dip-direction of bedding (135° and 144°, respectively), though the 95% confidence interval of poles to joints and the dip-slope aspect both overlap the crack extension directions.

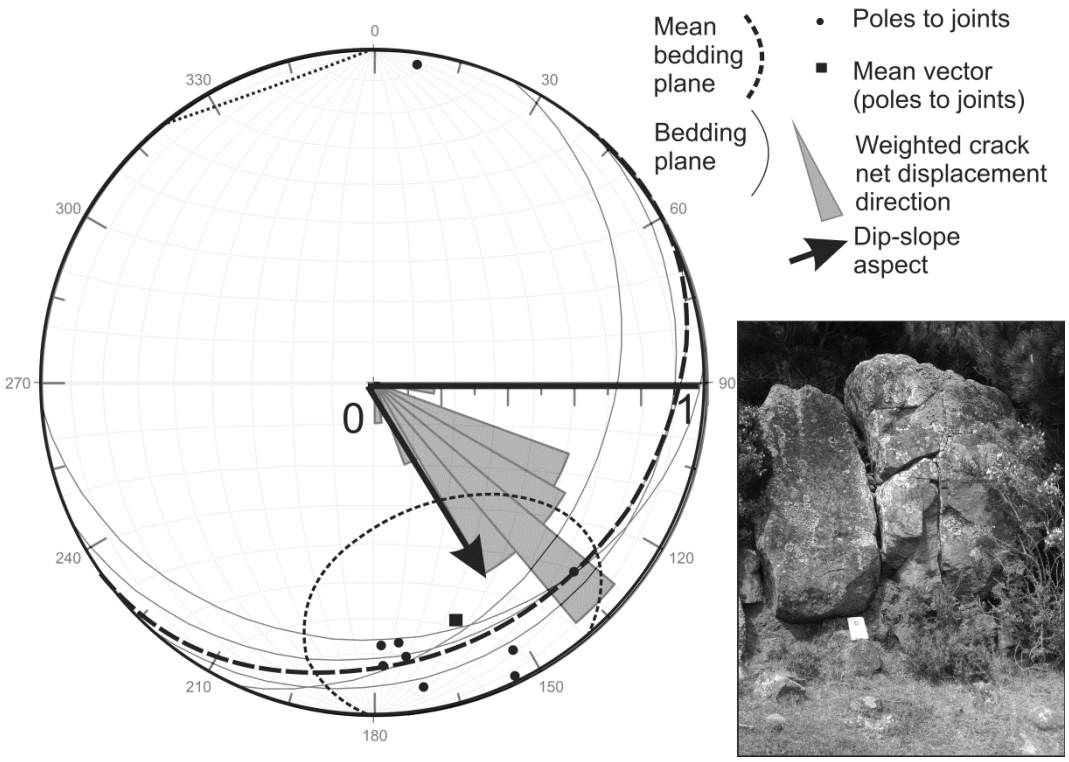

Figure 5.6: Structural and kinematic measurements in the Harper Hills. Combined rose diagram and lower-hemisphere equal area projection showing i) Crack displacement direction weighted for net displacement; ii) dip-slope aspect (down-slope direction); iii) orientations of bedding derived from an outcrop in the lower right corner (thin lines) and average bedding plane orientation (thick dashed line); iv) poles to the dominant set of joints (filled circles) with the mean vector (square) and 95% confidence cone (dashed). Outcrop at bottom right shows the Harper Hills Basalt overlying the Sandpit Tuff. Bottom of the field notebook is situated on a bedding plane contact, dipping gently into the page, and the cover is parallel to the dominant joint set, dipping steeply out of the page.

Some small, shallow landslides showed signs of reactivation in the Darfield earthquake. Landowners north of the field area reported tension cracks in the weeks after the main shock, but these were predominantly found around pre-existing features, typically in shallow, scalloped soil slides, and finite displacement could not be attributed solely to the Darfield earthquake. Aerial photographs of 'fresh' cracks days after the quake indicate that motion was recent. Ground reconnaissance of c. 20 m long, ridge-parallel cracks in this area showed that they occurred at the

head scarps of pre-existing landslides. There was no vertical component observed in these cracks, and extension was small (5–10 cm) compared to the other ridge-parallel cracks described in this study. The features were mapped and logged but not considered as continuations of the features on the southern end of the Harper Hills. Shallow landslides within the field area (Fig. 5.3) were not reactivated.

Pre-existing deep-seated landslides were mapped using aerial photography and a 15 m DEM. The prominent ridge-line scarp to the NE of the modern cracks was mapped by Muirson (2003) and an extensional depression in the central portion of the field area was identified in this study (Fig. 5.3).

5.4 Subsurface investigation of the Harper Hills landslide

5.4.1 Trench investigation

A 2.5 m deep by 4 m long trench was excavated across a prominent ground crack in the zone of highest crack displacements and fissure depths (Fig. 5.4B & 5.7). Following excavation, the walls and a section of floor were scraped clean of excess material left by the backhoe. Due to the rapid desiccation of the excavated material and resultant change in observable soil properties, one of the walls (North Wall, Fig. 5.7) was chosen for detailed cleaning and the other was allowed to weather for three days. Both walls and a section of floor were gridded at 1 m horizontal and 0.5 m vertical intervals (0.5 m NE and 1 m SE for the floor). Photographs of each grid section were taken and corrected for any distortion from the camera angle. Logging was then conducted directly onto the corrected orthophotos.

The North Wall of the trench reveals the modern slip plane that propagates to the surface and vertically displaces the soil profile. On the up-thrown block of this structure, subsidiary shears with normal displacement are oriented at c. 60° to the main trace. These features were observed at the surface immediately after the rupture (fissure orientation in Fig. 5.4C) but have subsequently degraded and become subdued. There is a forward rotation of 9° within 75 cm up-slope of the slip plane. At the base of the scarp free face, small amounts of mineralised A-horizon and sandy material from the exposed E-horizon have accumulated. A fissure on the up-dip extension of the slip plane has been in-filled with this material, though it is unclear if this fissure is coseismic or related to the shrink-swell (and subsequent in-fill) nature of the soil, for which there is pedogenic evidence in the veins of the underlying fragipan.

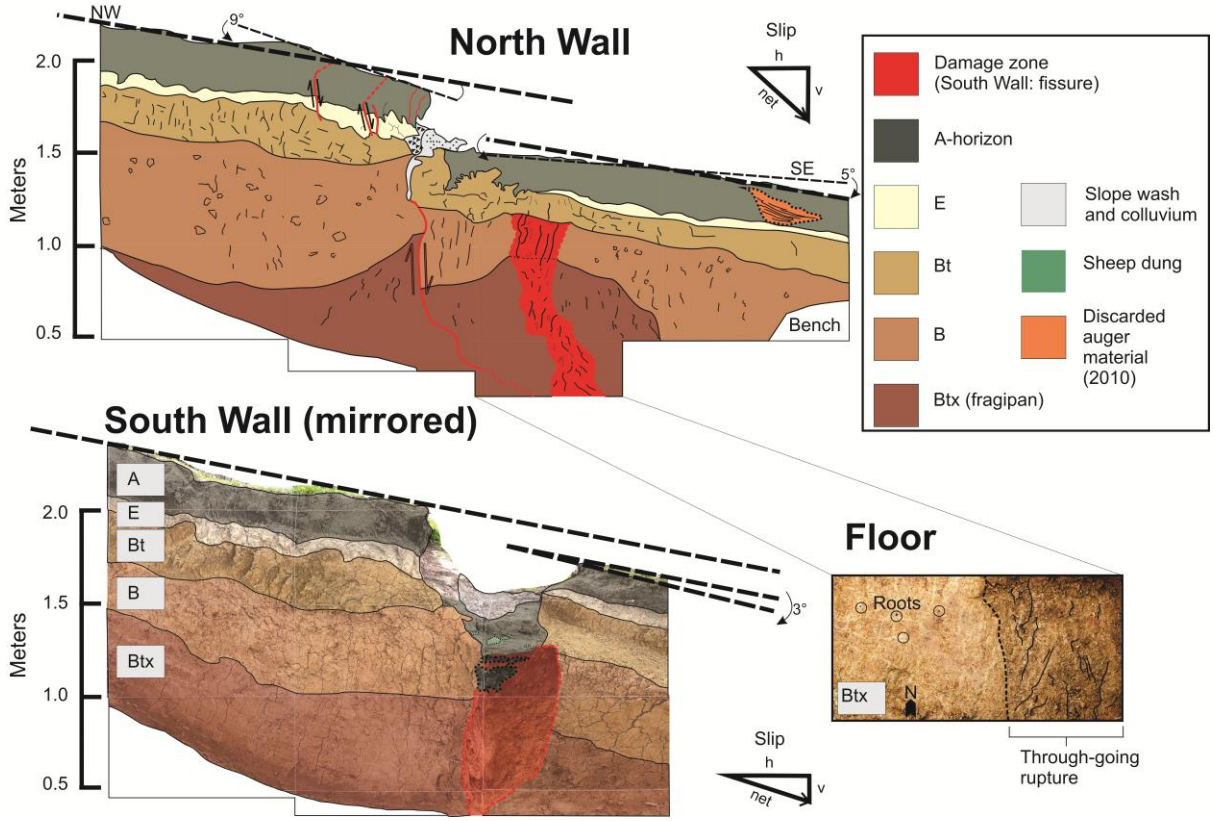

Figure 5.7: Trench across the head scarp of the Harper Hills landslide. The South Wall is shown with transparent units to show the soil structure of the weathered face. Rotations are indicated by dashed lines on the ground surface and arrows. Slip triangles are derived from the vertical displacement (v) and extension (h) across the deformation zones. The width of the damage zone on the North Wall is considered as the amount of extension, though not expressed at the surface. See Table 5.1 and text for discussion.

The downthrown block contains a broader zone of deformation (c. 1 m) than the up-thrown block, which is commonly observed in trenches across normal faults (McCalpin 1987). There is a small component of backtilt (5°) upslope due to the SE-dipping, listric geometry of the slip plane in the shallow subsurface. This plane cannot be traced into the floor, which implies that its geometry is controlled by the soil stratigraphy at the surface (i.e. does not rupture through harder material, see below). The rotation is therefore superficial at the ground surface and not related to overall landslide kinematics. Measurements of vertical surface displacement using the far-field slope match those observed in the soil profile at depth.

Down-slope of the slip plane, deformation is marked by an A-horizon that has washed down into vertical fissures. Beneath 18 cm (down from the surface), leached A-horizon material can be found coating narrow, closely spaced cracks. These cracks form naturally in the Bt, Bt2, and Btx horizons (South Wall, see below), but are particularly dense and wider in the 1 m zone downslope of the scarp. A 30 cm-wide zone of loose B-horizons and leached A-horizon occurs on the down-slope extremity of the deformed zone. While this ‘damage’ zone does not break the base of the A-horizon, it

is developed in the basal fragipan and joins the main slip zone on the South Wall (annotated photo of trench floor in Fig. 5.7). It is interpreted to represent an along-strike die out of the extension on the South Wall (below), as there is no evidence to suggest it is a previously filled fissure. The scarp-forming slip plane cannot be traced down-dip to the bottom of the trench.

The South Wall, which was allowed to dry and weather, displays the soil stratigraphy more clearly (transparent units, Fig. 5.7). A strong, basal fragipan is the most defined horizon and limited the depth to which the trench could be excavated. It is impermeable at its base where water can be seen accumulating. Floor exposures show that it consists of heavily oxidised polygons of loamy fine sand, with clay content increasing downward, rare basalt pebbles (<5%) and grey silt veins (yellow-grey soils of Raeside 1964; Gradwell 1974). Woody roots (c. 2 cm diameter) penetrate the softer, permeable silt veins on the trench floor, and are likely remnants of a pre-human, low land to montane, conifer-broadleaf forest that spanned the Canterbury plains (Molloy et al. 1963; McGlone 1989). Deforestation in this region took place primarily from about 750–500 years BP due to anthropogenic burning, although climate-induced forest reductions occurred from about 3000 years BP (McGlone 1989; McGlone and Wilmshurst 1999). By the time of European surveys c. 1840 CE, most, if not all, of the Canterbury plains was deforested (McGlone 1989). The silt veins in the fragipan developed before the roots exploited them as zones of weakness. The minimum age of the fragipan is thus very likely to be older than 500–750 years BP, and probably older than about 3000 years BP (see below for discussion).

The scarp morphology on the South Wall is markedly different. Greenish-blue pockets of sheep dung beneath what appears to be down-dropped A-horizon indicates that not all of the fissure sedimentation is natural. Below the ovinogenic layer (34 cm below the surface), however, a block of modern A-horizon has been preserved within the Bt-horizon. This block was exposed when a c. 35–50 cm-wide, unconsolidated area in the fracture zone collapsed from the trench wall, a width which generally agrees with crack measurements in this location immediately post-quake (30 cm extension). There is a small component of forward (down-slope) rotation on the down-thrown block of 3°.

The net slip vectors for each wall were drawn using several measurements of extension and vertical displacement (Fig. 5.7). Variations in the soil thickness and gradational contacts contribute to error which I estimate as ± 10 cm. While the individual components on each wall vary significantly, the net slip vector lengths (0.46 and 0.54 m for the North and South Walls, respectively, assuming the damage zone width on the North Wall is analogous to extension on the South Wall) are comparable and match measurements taken at the surface after the event (0.50 m).

Table 5.1: Trench unit descriptions

Unit/Horizon	Colour (moist)	Texture	Structure	Notes
A	7.5YR 2.5/1	Silt loam		Transitional into E-horizon
E	7.5YR 7/2	Silt loam	Granular	Mottled, bioturbated lower boundary
Bt	2.5Y 4/3	Clay with some silt; silt and sand content increasing toward base	Massive to blocky	Dessication cracks abundant: dipping subvertically to steeply up-hill
B	2.5Y 5/3	Sandy clay loam w/ dark vesicular basalt lithics	Blocky to prismatic	Basalt sapprolite pebbles present (c. 5%)
Btx	2.5Y 5/4; 5Y 6/2 (veins)	Loamy fine sand to silt Fine silt (veins)	Gammate	Dessication cracks narrowing into basal, dense fragipan marked by increase of clay coating sand grains; Rare basalt pebbles
Damage zone	2.5Y 5/3-4	---	Massive, indistinct	Soil boundaries obscured across zone; Low cohesion; Modern roots grow preferentially in zone; Leached A-horizon infilling and coating cracks

5.4.2 Ground Penetrating Radar (GPR)

A 90 m GPR survey was conducted across the major set of cracks in an attempt to map the subsurface geometry of identified surface fractures and to identify any unrecognised subsidiary features. The imaging was done using a Sensors & Software pulsEKKO system, with both 100 and 50 MHz antennas. The antennae were mounted on a sled and towed from the lower GPS reference point to a point over the crest of the hill, and the profile was repeated by towing the sled back down to the reference point. This was done to test repeatability and to yield a number of profiles from which I could choose the one with the least amount of noise. Noisy traces can cause anomalous features in the processed data, in particular in migrating the profiles.

Markers were placed on the ground at regular intervals and as each marker was passed, a marker was placed on the file. These *fiducial markers* were then used to interpolate the continuously

acquired traces to yield profiles with equally spaced traces. The sled was towed slowly so that the number of traces acquired far exceeded the number of traces needed for optimum resolution of subsurface features. The average trace spacing was less than 10 cm for the 100 MHz antennas and less than 50 cm for the 50 MHz antennas. The interpolated trace spacing used for the 100 MHz profiles was set to 10 cm, or 10 traces per metre, and the spacing used for the 80 MHz profiles was set to 50 cm, or 2 traces per metre.

Diffractions in the unprocessed dataset are the result of scattering from features such as rocks, roots, and truncations of bedding. The curvature of the diffraction hyperbolae are inversely related to the square of the subsurface radar velocity. The 'best fit' velocity was determined to be 80 m μs^{-1} (0.08 m ns^{-1}). This is typical for a moist but not saturated fine-grained soil. The depths estimated by converting the travel times to depth were checked against the depths of the soil layers in the trench, in particular the fragipan that appears to have been the deepest reflective boundary at this site. The 'best fit' velocity in this case appears to be about 100 m μs^{-1} (0.10 m ns^{-1}). This discrepancy may be due to the fact that the diffractions are originating from shallower subsurface features and the deeper velocity is faster.

The 80 m μs^{-1} velocity was used to migrate the profiles. The process of migration collapses the diffractions to points and places dipping features into their correct geometric positions. If too high a velocity is used, then the diffractions are turned inside out and become 'smiles' (noise spikes also become smiles regardless of the migration velocity used). The resultant migrated profiles, with topography added, are shown in Fig. 5.8. The profiles have been converted to elevation using the 100 m μs^{-1} velocity so that the depth to the fragipan is more realistic. The fragipan is demarcated by dashed lines at 2–2.5 m depth in both profiles.

The modern deformation zone occurs at 50–60 m distance in both profiles (Fig. 5.8). In the 100 MHz profile (Fig. 5.8A), there is clear offset of two blocks on three structures, one of which at 55 m was observed in the trench and reaches the surface. The vertical offset of the reflectors on this structure is 27–30 cm, which is comparable to vertical offset measured on the North Wall of the trench (29 cm). The other two structures are inferred from offset or folded reflectors but do not reach the surface. The structures are sub-vertical and appear to dip more gently into the slope beneath the fragipan, but the penetration of the 100 MHz antennae drops off near this depth making interpretation difficult. Directly down-slope of the three structures, the reflectors appear to be drag folded, consistent with normal motion at the head scarp. From 30–45 m in the 100 MHz profile, there is expression of a possible graben or rotational wedge in the subsurface. While it is uncertain what the kinematics of the two bounding structures are, they are clearly oppositely dipping and occur at slope inflection points at the ground surface.

The 50 MHz profile (Fig. 5.8B) has less resolution but a greater depth of penetration, allowing for alternative and/or supplementary interpretations of the near-surface kinematics. The head scarp geometry is less clear than the 100 MHz profile but similarly suggests offset on vertical to near-vertical structures. The deformation zone at 30–45 m along the profile is better imaged by the 50 MHz antennae and concave reflectors suggest it is more likely to be a graben. At 3–4 m depth, a discontinuous, 'noisy' reflector is likely to be the top of the Harper Hills Basalt. Displacement and rotation on structures dipping into the slope between 0–30 m imply that joints in the Harper Hills Basalt accommodate some of the slope failure. It is unknown whether this deformation was pre-existing or occurred simultaneously with head scarp motion in the Darfield earthquake.

5.5 Discussion

5.5.1 Landslide kinematics

The consistent crack extension direction and horizontal extension indicate primarily translational kinematics. Near the south-western extent of the cracks, tension oriented c. 45° to the predominant direction of motion is the inferred surface manifestation of incipient strike-slip shear on the flank of a coherent spread or translational slide (Technical Advisory Group 1991; Muller and Martel 2000). The remediated crack 460 m down-slope of the head scarp and the features observed in the GPR are also indicative of internal deformation of a coherent, translational landslide.

The landslide is considered to be deep-seated (>3 m depth, well below rooting depth), as a subsurface 'damage' zone was observed to rupture a dense fragipan in the trench at c. 2.5 m depth and the GPR profiles show structures penetrating to at least 3–4 m depth. At the surface, cracks can be traced cutting across topography (Fig. 5.4A) while running parallel to strike of the Harper Hills bedrock geology, which lends itself to down-dip, rather than simple down-slope motion. Fig. 5.6 shows that crack extension direction is most coincident with bedding dip-direction. Pre-existing shallow landslides showed only minor motion compared to displacement on the main cracks, also pointing towards failure driven by bedding plane weaknesses. It is possible that slip on the Chalk Hill Clay could have facilitated down-dip translation as has been inferred for more discrete ridge-line failures NE along the Harper Hills. The 21° residual internal friction angle of the unit is significantly less than the slopes where the failures occurred (Muirson 2003).

Down-dip projection of bedding from a contact between Harper Hills Basalt and Sandpit Tuff observed in Fig. 5.6 coincides with a bulge at the base of the Harper Hills which could be a toe of a pre-existing failure (Fig. 5.9A). The intense brecciation of the Sandpit Tuff (Browne 1983), and its variable thickness overlying the Chalk Hill Clay, make both units possible slip surfaces for the Harper

Hills landslide. If it is the basal failure plane, the volume involved in total failure of the slope is a maximum of 6.9×10^7 m^3.

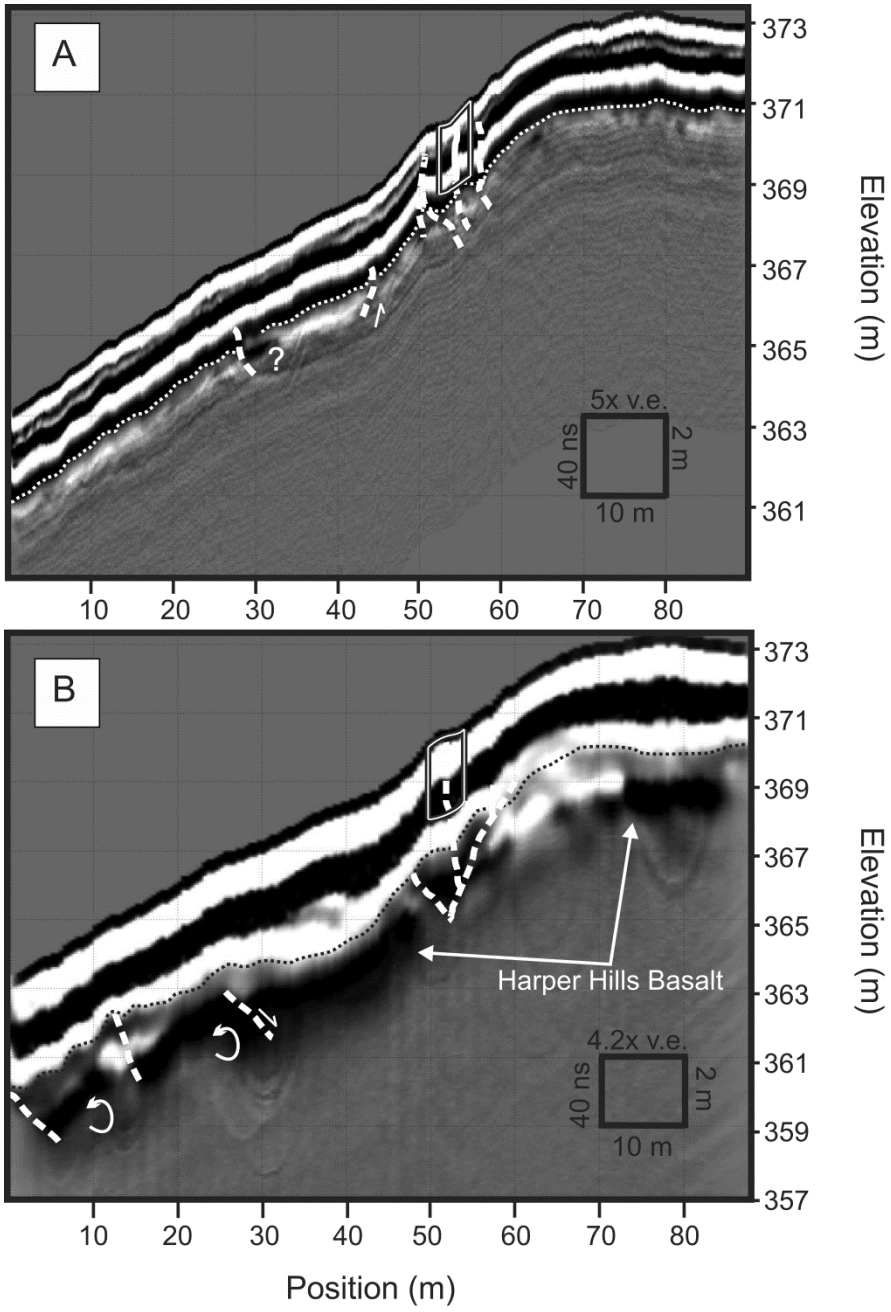

Figure 5.8: GPR Profiles from the 100 MHz (A) and 50 MHz (B) ground penetrating radar (GPR) surveys across the trench site. Utilizing two frequencies allows for alternative and/or supplementary interpretations of landslide geometries. The fragipan is a strong reflector and its base is demarcated by a thin dashed white (100 MHz) or black (50 MHz) line. Trench locations are outlined in solid white lines outlined black. Slip surfaces are dashed where inferred and solid where definite. Trench stratigraphy and displacement match well with observations from the 100 MHz profile, and both profiles show evidence for deformation down-slope of the head scarp.

Where observed, rotation appears to be caused by slumping from scarp degradation and secondary (i.e. superficial) fracturing. The down-dip tapering, listric slip plane on the North Wall of the trench accounts for a small component of up-slope back-tilting, though this back-tilt was not observed elsewhere. Down-slope rotation of the down-thrown block at places, as implied by fissures that narrow with depth and observed in the 50 MHz GPR profile, may be due to translation accompanied by toppling on joint-bounded basalt blocks (Fig. 5.8 & 5.9B). The mode of failure illustrated in Fig. 5.9C fits well with my observations of crack morphology and structural geology, and matches observations of earthquake-induced ridge spreading and fissuring elsewhere (Agliardi et al. 2001; McCalpin and Hart 2002; Sleep 2011; Gutierrez et al. 2012). The features observed in this study probably fall on a continuum between coherent landslide and ridge-top spreading, as proposed by McCalpin and Hart (2002).

Both crack displacement and depth increase with decreasing ridge-to-crack relief (Fig. 5.5). This could be an effect of topographic and geometric amplification, which allows for maximum ground displacement at ridge crests and decreases quickly away from these areas (Meunier et al. 2008; Buech et al. 2010). If indeed due to topographic amplification, this observation also lends itself to a component of joint-controlled toppling at the head scarp: deeper cracks with more extension occurred nearest the top of the ridge. There is no clear reason for bedding-controlled translation to respond to amplification by producing the crack depth/displacement gradient observed. However, without further controls on variations in soil properties along the ridge, I cannot state conclusively that this pattern is solely a result of topographic or geometric amplification.

In contrast to the deep-seated landslide studied by Muirson (2003), which had surface movement rates of 24 cm yr^{-1} during 2002–2003, no detectable motion was observed on the Harper Hills landslide in 2 years of surface monitoring. Post-quake measurements and subsurface crack widths in the trench confirm this observation. Without further constraints on stratigraphic and water table differences between the current study area and that of Muirson (2003), I am unable to speculate on future, creeping motion of the Harper Hills landslide. However, there is some evidence that progressive displacement has not occurred in the last one thousand years. Trenching and GPR did not reveal conclusive evidence for previous head scarp displacement, though features in the GPR could have formed in past events. Roots post-dating fragipan development at the base of the trench are probably a minimum of 500–3000 years old, but have not been dated (McGlone 1989; McGlone and Wilmshurst 1999; McWethy et al. 2009). In the Eastern USA, Ciolkosz et al. (1992) postulated a period of 6–18 ka for fragipans to develop, and 'proto-fragipans' have developed within 4500 years in Pennsylvania (Cremeens 1998; Ciolkosz and Waltman 2000). Age constraints on fragipan genesis elsewhere are tenuous, but there are indications that the formation process takes several thousand

years (Bockheim and Hartemink 2013). If age ranges from the USA are adopted in this study, the age of the soil could be as old as 6.75–21 ka. A progressively deforming slide moving at 24 cm year^{-1}, or even a tenth of this rate, would have moved up to several kilometres in that time. There is no evidence for this amount of material being transported in the field area, though a pre-earthquake toe bulge near the base of the slope (Fig. 5.3 & 5.9) that is present in pre-quake digital elevation models could indicate at least some down-slope creep. Mountjoy and Pettinga (2006) note that deep-seated landslides in Tertiary soft-rock terrain of New Zealand are predominantly controlled by periodic earthquake shaking, though catastrophic failure can occur well after initial motion (e.g. Pettinga 1987).

5.5.2 Paleoseismology

New Zealand's national seismic hazard model predicts a 1–2.5 ka return period for peak horizontal accelerations (0.45–0.51 g) that the Harper Hills experienced in the Darfield earthquake (for Class C shallow soils) (Stirling et al. 2008, 2012; Cousins and McVerry 2010). A critical acceleration for landslide initiation is difficult to constrain as subsequent aftershocks that did not generate any clear surface manifestations of landslide movement only generated PGAs of <0.1 g at the study site (Table 5.2). Rigid-block, coupled and decoupled Newmark analyses using SLAMMER software (Jibson 2011; Jibson et al. 2013) indicate that the net displacements I measured of 22 and 55 cm (average and maximum, respectively) and acceleration-time history are consistent with critical accelerations of 0.1–0.16 g for the Harper Hills landslide (Table 5.3). If Newmark displacements are indicative of field displacements (e.g. Pradel et al. 2005), then smaller episodic displacements should be expected at return periods of less than 150 years (Stirling et al. 2001). However, the likelihood of internal deformation within the Harper Hills landslide and the inability of Newmark analyses to suitably model dynamic sliding conditions make interpretations of predicted return periods at the site difficult. Rather, if PGAs in the main event are indicative of the required shaking for failure, episodic displacement would be expected on 1–2.5 ka timescales at the Harper Hills.

Although there are no absolute age data on the soil in the current study, it is probable that the fragipan (Btx) developed over thousands of years (see above). Since trenching did not reveal any prior events over a time period greater than the predicted return period of strong ground motions at the site, one or a combination of the following must be true: a) past events of similar PGAs were not preserved or did not induce cracking at the trench site, b) PGAs are not the only seismologic factor in determining landslide initiation, and/or c) PGAs equal to or above the landslide-triggering threshold have not occurred at the study site over the time interval captured within the trench record. While (c), the underestimation of return periods for a given ground motion in probabilistic seismic hazard

models (PSHAs), has been studied in some detail by Brune (1999) and Brune et al. (2006), I focus my discussion on (a) and (b) below.

Table 5.2: Strong ground motions recorded at HORC for main shock and aftershocks.

Date (UTC)	Time	M_W	PGA_h (g)	PGA_v	Epicentral distance to HORC (km)
3 Sep. 2010	16:35:46	7.1	0.45	0.79	20
4 Sep. 2010	4:55:56	4.7	0.05	0.04	1.9
4 Sep. 2010	8:54:27	4.1	0.03	0.02	6.3
5 Sep. 2010	16:06:26	4.5	0.02	0.01	9
6 Sep. 2010	11:40:50	4.8	0.07	0.08	8.3
6 Sep 2010	15:24:44	5.4	0.01	0.009	26

Table 5.3: Newmark analysis parameters and output. [1] HORC N00E component (PGA direction) input acceleration-time history; [2] Landslide thickness of 30 m, Shear wave velocities of units above and below failure plane derived from Bienawski (1989), Carlson et al. (1980), Kowallis et al. (1984), and Muirson (2003) (Harper Hills Basalt=3900 m/s; Homebush Sandstone=1500 m/s, Damping ratio of 5% and reference strain of 0.05% (Jibson et al. 2013). Critical accelerations were calculated iteratively by optimizing to the range of Newmark displacements to match field displacements

Model	Input Parameters	Newmark $Displacement_{avg}$ (cm)	Field $Disp._{avg}$ (cm)	Ac_{avg} (cm)	Newmark $Displacement_{max}$ (cm)	Field $Disp._{max}$ (cm)	Ac_{max} (cm)
Rigid-block	[1]	21.81	22.2	0.16	53.16	54.6	0.1
Decoupled	[1],[2]	21.37			51.54		
Coupled	[1],[2]	24.45			55.29		

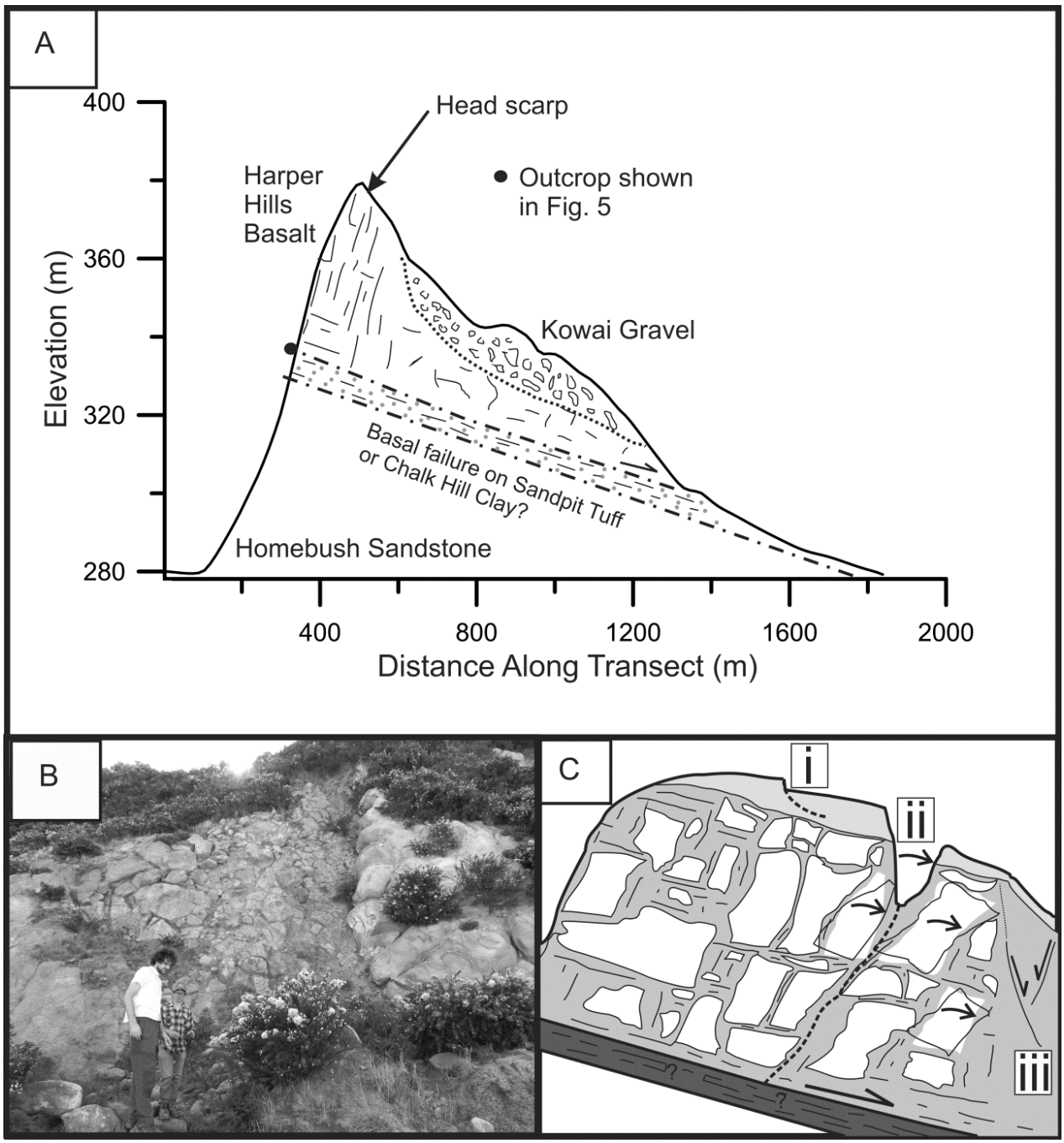

Figure 5.9: Cross-section and failure mechanism of the Harper Hills landslide. A) Schematic cross section of the Harper Hills landslide with bedding-plane failure in the Sandpit Tuff/Chalk Hill Clay. B) Heavily jointed and brecciated basalt along the Harper Hills ridgeline NE of the field area. C) Proposed failure mechanism of combined bedding-plane translation and joint-controlled toppling leading to extension and vertical displacement: (i) Shallow (i.e. superficial) listric slip in soil due to broad extension at head scarp and mechanical differences of soil horizons (as in trench); (ii) Ground cracking and fissuring with both vertical displacement and horizontal extension; and (iii) Internal deformation of coherent slide, not always rupturing the surface (as in trench and GPR).

5.5.3 Head scarp and subsurface preservation

The ability to recognise evidence for prior slope failure depends on the preservation of head scarp features in the subsurface as well as trench location. Whether or not the modern head scarp has been repeatedly reactivated in the past may be difficult to constrain. Vegetation may have stabilised the shallow subsurface in previous events and thereby reduced the susceptibility of the ground surface to the type of discrete cracking observed within the contemporary agricultural landscape. GPR did not show conclusive evidence for pre-existing deformation within 45 m up and down-slope of the modern cracks, though further trenching and dating would have to be conducted to further investigate this. Deformation need not pierce the surface as has been observed in the trench (North Wall 'damage' zone, Fig. 5.7). Thus, offsets observed in the GPR profiles are small enough (i.e. comparable to direct measurements made in the trench) to be considered to have occurred only in the most recent event.

Increasing crack displacement and depth with proximity to the ridge suggests that the trench location chosen was ideal for identification of older features, although it is unclear if this pattern would have been repeated by past events. Evidence from trenches in ridge-top spreads and sackungen elsewhere in the world suggest that it is more common for episodic displacement to occur at the same location on a scarp or ground crack than elsewhere if the displacement is greater than 3–5 cm horizontal and 1–3 cm vertical (Technical Advisory Group 1991; Nolan and Weber 1992, 1998; McCalpin and Hart 2002). The displacement at the trench site well exceeded these values, but this relationship may change due to spatial and temporal changes in the soil mechanical properties.

The preservation and recognition of prior events in a trench depends on the scarp morphology, soil stratigraphy and offset. In this study, scarp morphology and the amount of offset determine the accommodation space, and thus volume of material available for syn- and post-event deposition. Graben or fissures (Fig. 5.10A–C) create the most space and have the highest preservation potential, whereas cracks with primarily vertical displacement have less space and rely on the erosion of a free face.

Secondary slumping and shearing of the A and E horizons observed on the North Wall of the trench would go unnoticed without a surrounding B horizon for contrast (lower A-horizon block on the South Wall). With further soil development, the only remnant of vertical cracks will be a slightly thickened A-horizon on the down-thrown block. Even with sufficient burial, preservation of a discrete, organic soil block over >1000 ka is tenuous and evidence for past events would 'anneal'. A-horizon film coating cracks on both walls is not likely to persist over hundreds of years and could form by desiccation just as easily as by down-slope extension.

The best opportunity for preservation and recognition of older features is via fissure-fill style deposition. Observations of crack degradation from two months to two years after the Darfield earthquake, though subject to human and sheep modification, shows that this deposition takes place on features with the greatest component of extension (Fig. 5.10A–C). Interpretations of smaller fissure-like features in this study are complicated by the shrink-swell nature of the B-horizons.

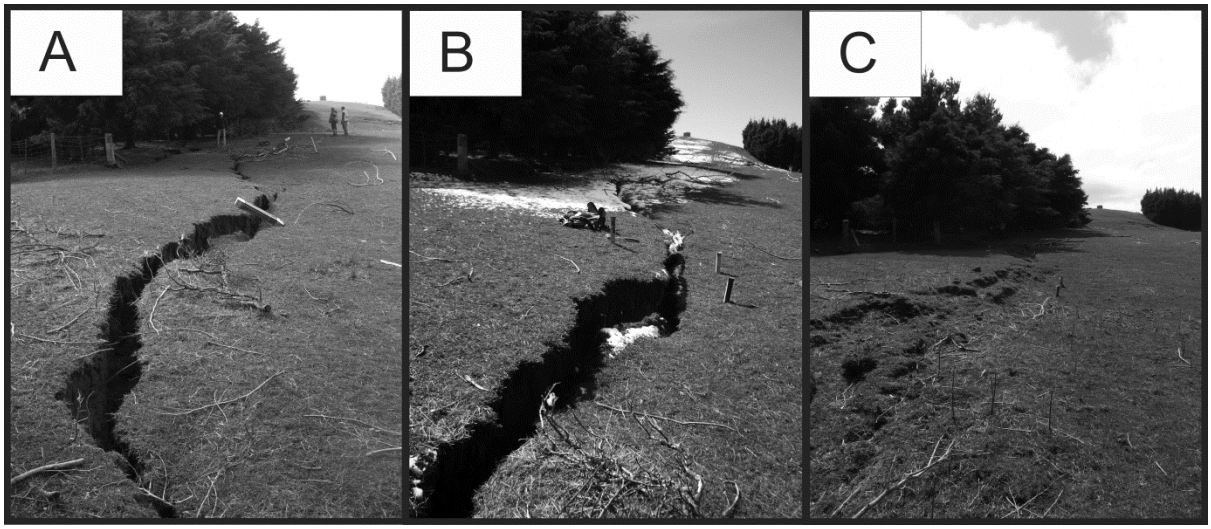

Figure 5.10: Preservation potential of the head scarp. Harper Hills scarp degradation and fissure-fill through time. A) Two days after the quake. B) Two months after the quake. C) Two years after the quake, probably altered by anthropogenesis and ovinogenesis, but showing the style of deposition likely to occur if left over longer time periods.

Observations of ground cracks following the Loma Prieta earthquake and this study show that cracks and fissures are vertically discontinuous up and down-dip (Technical Advisory Group 1991). For example, the subsurface, extensional 'damage' zone (Table 5.1, North Wall in Fig. 5.7) coincides with surface rupture on only one of the two walls, and the primary slip plane on the North Wall cannot be traced onto the floor exposure. This implies that over a 2 m scale, the characteristics of fissuring and displacement on discrete structures can change drastically. In the 50 MHz GPR profile, deformation in the underlying Harper Hills Basalt does not always have a surface expression. Up-dip propagation to the surface of structures within the slide body may occur over several episodes, or not at all. Extension from older events may not have ruptured the surface, and, depending on stratigraphy, may not show identifiable offset in the subsurface. It is advisable to log all faces of the trench, when possible, to decrease the possibility of false negatives and develop a full model of kinematics at the surface.

5.5.4 Peak ground acceleration and other factors

Slope response during an earthquake relies on a number of factors. Peak horizontal acceleration and shaking duration, widely used in Newmark displacement analyses, are only two seismic parameters that will influence landslide-triggering (Jibson and Keefer 1993; Jibson 1996). The effect of vertical accelerations could play a major role in reducing shear strength in detachment horizons, particularly for near-source, deep-seated landslides (Huang et al. 2001; Ingles et al. 2006). Slope orientation and topography can increase susceptibility by redistributing wave energy into slope-normal components (Del Gaudio and Wasowski 2007) and rupture-sourced forward directivity affects the occurrence of landslides (Jibson et al. 2004; Sleep 2011).

Darfield earthquake ground motions recorded near the Harper Hills principally reflect rupture of the HAF and the western Greendale Fault (Fig. 5.1). The main ground cracks observed in this study are discontinuous north-eastward across the sub-surface Greendale Fault. High accelerations starting at c. 20 seconds into the earthquake sequence at HORC and spanning the 5–95% significant duration of 8.7 s correlate with rupture of the HAF (Holden et al. 2011; Bradley 2012). Vertical PGAs at HORC were more than double those of the nearest station on the NE side of the Greendale Fault, probably due to near-source effects that enhanced ground motion (Abrahamson and Somerville 1996; McVerry et al. 2006; Meunier et al. 2007; Bradley 2012) and close proximity to the HAF. Velocity pulses in both the E–W and N–S components at HORC are indicative of forward directivity of the bilaterally rupturing Greendale Fault and HAF (Bradley 2012).

While no attempt is made here to model the complicating effect of these ground motion characteristics on slope failures in the Harper Hills, it is suggested that they offer insights into the lack of prior fissures observed in the trench. Hanging-wall amplification and forward directivity are linked to the specific rupture kinematics in any given earthquake, and can thus be expected to have longer return periods than modelled horizontal PGAs. A lack of evidence for prior events in the trench could indicate that ridge failure on the Harper Hills landslide is associated with a site response resulting from Darfield earthquake-type fault kinematics and source characteristics (Fig. 5.11). For ground cracks generated in the Loma Prieta earthquake, Nolan and Weber (1998) concluded that cracks may only form in specific, multi-segment ruptures on the San Andreas Fault based on a longer return period of crack displacement than faulting. Preliminary analyses indicate the penultimate earthquake on the Greendale Fault occurred between ca. 22 and 28 ka (Hornblow et al. submitted); if the specific seismologic character of earthquakes resulting from this fault rupture have a first order control on the location of the landslide head scarp documented in this study, then a similarly long return time of landslide reactivation at the trench site might be expected.

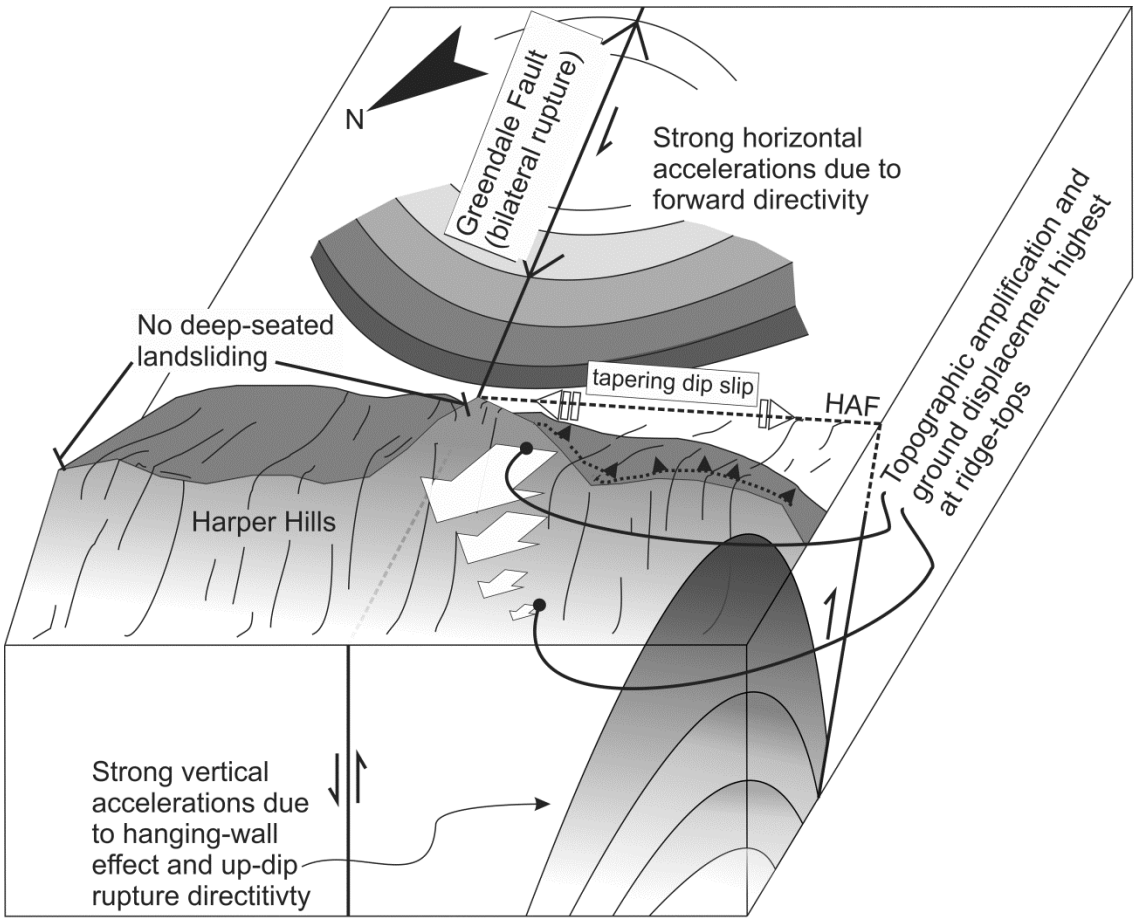

Figure 5.11: Influences on landslide failure and location. Block model of the Harper Hills, with topographic and seismic-source effects on the occurrence of deep-seated landsliding. Ground cracks were only observed on the hanging wall of the Hororata Anticline Fault (HAF) and Greendale Fault, the former being truncated by the subsurface Greendale Fault. It is proposed that rupture directivity affects the location of cracks, and that crack location and displacement (e.g. Fig. 5.5) may be related to topographic amplification of incoming seismic waves.

5.6 Implications for future studies

Ridge-top ground cracks**,** sackung, and large translational slides have been reported in several historical earthquakes (c.f. Technical Advisory Group 1991; McCalpin and Hart 2002; Gutiérrez et al. 2008). There have been comparatively few trenching studies of documented coseismic landslide scarps and/or fissures, though most trenches have revealed evidence for prior events (Technical Advisory Group 1991; Nolan and Weber 1992, 1998; McCalpin 1999). The key questions in paleoseismic investigations of these scarps are a) Is motion episodic or progressive? b) If prior episodic displacement is observed in the trench, can a seismic origin be deduced? c) Is rupture of a specific fault or set of faults responsible for the observed displacement? Having constrained parts of these in the present study, I consider contributions to these questions below.

5.6.1 Episodic vs. progressive deformation

Trench location may assist in determining how a landslide fails. While the ground cracks in this study were undoubtedly formed in the Darfield earthquake, there are indications of on-going deep-seated landsliding down-slope of the modern cracks and along the Harper Hills ridge. I cannot, therefore, rule out an on-going interaction between progressive failure and episodic displacement caused by earthquake shaking. While it is clear that both triggering mechanisms occur in nature, paleoseismic trenches typically produce evidence of only one mechanism. When both are observed, colluvial deposition on the down-thrown block will either produce cumulic soil horizons (progressive deformation) or buried soils (episodic) (Technical Advisory Group 1991). Patterns of folding and offset in well stratified material can also reveal a history of motion (e.g. McCalpin et al. 2011). In the current study, it is unlikely a distinction could be made between the two soil types for scarps without a component of extension because the soil stratigraphy is relatively homogeneous. Fissures with large amounts of extension are more likely to form episodically and fissure stratigraphy will indicate more clearly if opening occurred abruptly or over time (Fig. 5.10). Therefore, if the geomorphology is suggestive of graben or fissure development, these areas should be targeted for trenching studies over scarps with vertical displacement alone.

5.6.2 Seismic vs. aseismic origin

Deep-seated translational landslides can be caused by earthquake shaking, raised water tables (Johnson and Cotton 2005), glacial debuttressing, and/or fluvial undercutting (Gutierrez et al. 2008). Determining a seismic origin of episodic displacement can be difficult and relies on independent age control of primary tectonic features and corroborative age control on other landslide features (McCalpin and Hart 2002; Gutiérrez et al. 2008). From my observations, a seismic origin can be considered likely if head scarp displacement and depth covary with site effects that amplify incoming waves (Fig. 5.5). For example, if several trenches reveal a pattern whereby age-correlated fissures closer to the ridge or overlying weaker soil have the greatest displacement, it is possible that they formed coseismically. This conclusion matches the results, but more field studies and numerical modelling should be carried out to test this hypothesis, as similar displacement profiles might be created from other triggers.

5.6.3 Relationship to specific (paleoseismic) faulting events

Establishing a relationship of landslide displacement with specific or recurrent earthquakes requires a long record of sympathetic, tightly age-bracketed events (McCalpin 1999; McCalpin and Hart 2002). Slope stability modelling that includes different rupture scenarios, pore pressures, topographic amplification, forward directivity and vertical accelerations should be conducted to determine that the proposed fault system can induce failure. In regions where faulting is blind, or

obscured by geomorphic processes, these parameters may be impossible to determine. Difficulties in determining a history of multi-fault ruptures and longer term, static-stress triggered seismicity, as well as in event recognition and preservation, further complicate the use of landslides as secondary paleoseismic evidence. This is not to say that seismic origins of landslides cannot be deduced, or that landslides in regions with historical seismicity and limited seismic sources cannot be linked to earthquakes on a given fault system using Newmark analyses (e.g. Jibson and Keefer 1993). However, in high seismicity regions like New Zealand, interpreting the seismic source from field data and without actual acceleration-time data is challenging. The Darfield earthquake sequence may have led to 'characteristic ground-motions' (Brune 1999; Brune et al. 2006) at the Harper Hills presenting the unique conditions for failure, even though the Darfield earthquake was allowed for in the New Zealand PSHA via a distributed source model (Stirling et al. 2008). Unless there is an identifiable kinematic link between permanent deformation caused by faulting and ground failure, landslides in high seismicity regions may not yield information pertaining to the specific fault sources.

5.7 Conclusions

Detailed geomorphic mapping, trenching and GPR provide insights into the kinematics and failure mechanism of the Harper Hills landslide with implications for regional paleoseismicity. The geomorphology and geology suggest predominantly bedding-controlled translation accompanied by inferred joint-controlled toppling at the head scarp. Measurements of crack displacement, depth and position along slope indicate that shaking variability, possibly due to topographic amplification, is a factor in determining crack displacement. Trenching studies on similar features should concentrate on ridge-top graben or fissures for the best record of episodic displacements, and include several trenches to determine if there are indications of seismic triggering. Connecting evidence of strong ground motion in a trench to any one fault system requires considerations of complex fault rupture scenarios and resultant waveforms, site response characteristics, and preservation potential of the event in the stratigraphy. These factors present a difficult, but worth-while, challenge for paleoseismologists seeking to derive a history of earthquakes at a site from landslide studies.

CHAPTER 6. CONCLUSIONS

6.1 Introduction

This thesis investigates several aspects of reverse fault paleoseismology in the central South Island of New Zealand. Topographic surveying, paleoseismic trenching, geomorphic and structural mapping, ground penetrating radar, and surface exposure-age dating were employed to collect paleoseismic data on key faults. These faults – the Moonlight, Fox Peak, and Forest Creek – are just three of several faults located in this zone of plate boundary backthrusting. The field and numerical tools I have developed to measure offsets and ages of landscape features, and to predict the maximum magnitudes of earthquakes on a fault system, can be applied elsewhere to improve existing paleoseismic datasets. Below, I summarise the key findings of this thesis and make recommendations for locations in the central South Island to further investigate reverse fault geohazards.

6.2 Key findings

The key findings are summarised below.

Table 6.1: Analysis of the aims and outcomes of this thesis (after Table P.1)

Goal/Scientific Contribution	Research Questions	Relevant Chapter(s)
Obtain slip rates to identify segments and recent fault activity on the **Fox Peak Fault** ✓	How can the required age control be obtained for sequences of offset geomorphic markers?	Chapter 1
	How are discontinuous geomorphic markers correlated and their offset measured across a fault?	Chapter 2
	Is the paleoseismicity of a group of fault segments related to long-term range growth, and what are the implications for future seismic hazard?	Chapter 3
	Are geologically derived slip rates consistent with current geodetic models of fault slip rates in the central South Island?	Chapters 2 & 3
Obtain ages and single-event displacements of earthquakes on fault segments to identify the recurrence interval and magnitude potential of reverse fault systems ✓	How can estimates of seismic hazard be improved by integrating field data into fault segmentation and fault-to-fault rupture scenarios?	Chapter 3
	How reliable are secondary (fault-induced) and indirect (off-fault, shaking-induced) records for determining the paleoseismicity of the **Fox Peak Fault** and **Darfield earthquake source?**	Chapters 3 & 5
Investigate earthquake interaction and secular modulation of slip rates on reverse faults ✓	Is the **Moonlight Fault** active? What is the nature of strain heterogeneity and fault episodicity in Otago, and is it influenced by glaciations?	Chapters 2 & 5
	Does activity on the **Fox Peak Fault** influence the timing of earthquakes on the **Forest Creek Fault?**	Chapter 3 & 4

6.2.1 How can the required age control be obtained for sequences of offset geomorphic markers?

River terraces in high energy environments can be difficult to date. For the purposes of this thesis (i.e. acquiring a dense network of fault slip rate measurements along a fault and within sequences of terraces), many terrace ages were required. I have shown that Schmidt hammer exposure-age dating (SHD) is a simple, repeatable, and relatively rapid method to determine the exposure-ages of terrace treads containing clasts of Torlesse greywacke sandstone. Although SHD uncertainties are large compared with radiometric and luminescence techniques, they can be reduced using the stratified sampling method presented in Chapter 2. Calibration with absolute-dating techniques is advisable, but the chronofunction parameters can be constrained via site-specific temperature, precipitation and petrographic information (i.e. modified chemical weathering rates, Chapter 1). Using SHD, I have constrained the lake level lowering rates of Lake Wakatipu over the Holocene and identified slip rate-delineated segment boundaries of the Fox Peak Fault.

SHD has previously been applied to many other types of landforms (c.f. Goudie 2006). I consider river terraces to be the 'ideal' landforms for SHD – the initial rounding and weathering profile of the surface clasts are homogeneous compared to moraines, for instance, and known ordering of terraces allows numerical reduction of variance. However, to reduce uncertainty, calibrated exposure-age dating could be improved by calibrating to the exposure-ages of individual clasts, or by using multiple techniques in tandem to produce an exposure-age 'index'. The former has become possible with the widespread usage of terrestrial cosmogenic nuclide dating on late Quaternary landforms. The latter has not been attempted, but similar indices (e.g. the soil profile development index of Harden 1982) have improved margins of error in age calculations by integrating many metrics of how a feature weathers at or near the surface.

6.2.2 How are discontinuous geomorphic markers correlated and their offset measured across a fault?

Geomorphic mapping is the best and most straightforward way to correlate landforms. However, where the geomorphology is not indicative of the maturity of the features, or uplift has made elevation-based correlations not possible, many dates may be required to make useful correlations. If clasts are of a suitable size, relative ages and correlations can easily be calculated using SHD and a Kruskal-Wallis ANOVA test. For lake shorelines that contain platy, disk-shaped clasts, SHD is not advisable due to the small thickness of rock being sampled (Demirdag et al. 2009).

I developed a cross-correlation technique to quantitatively check the elevation-based correlations of lake shorelines (or any flat landscape features controlled by the same base level). While this does not supplant the need for geomorphic mapping and subjective correlation, it does

provide an objective means of finding the most likely correlations and calculating vertical offsets. The technique may prove particularly useful where high-resolution photogrammetric or LiDAR DEMs are available for remote lake basins with discontinuous shorelines. In this case, cross-correlation can provide a preliminary analysis of tilting and offset, and identify faults or axes of uplift that require further field investigation. This, like SHD, is not limited in its application to reverse faulting regimes, but has proven useful in the central South Island where reverse faulting has created high-relief, high-erosion landscapes.

6.2.3 Is the paleoseismicity of a group of fault segments related to long-term range growth, and what are the implications for future seismic hazard?

As Jackson (1996) showed, the modern and future configuration of an orogenic mountain range is controlled by coalescing folds and fault segments. Linkage can occur via fault segment tip propagation over several earthquake cycles (e.g. Davis et al. 2005). Since the magnitude of an earthquake depends on the area of the fault plane ruptured, the inclusion of newly-linked fault segments in subsequent earthquakes will result in a magnitude increase. The 'stage' to which a fault system has developed will influence the seismic hazard. The long-term topographic growth of anticlinal ranges provides insights into the history of fault development.

For the FPF, along-strike changes in topography, surface expression and structure correspond to changes in slip rates. This is similar to the trend observed on the Ostler Fault (Amos et al. 2010). Unlike the Ostler Fault, FPF segments do not display significant step-overs at the surface and thus do not show evidence for displacement transfer among overlapping segments. That is, the summed slip rate profiles are parabolic over individual segments and not over the entire FPF length. This pattern covaries with the topography of the Sherwood and Two Thumb Ranges, implying either that (i) the three segments of the FPF operate independently over long timescales (small fault-length earthquakes, large D:L ratio), (ii) that surface displacements are consistently smaller at certain locations along the FPF (long fault-length earthquakes, D:L ratio depends upon distance from segment boundary), or (iii) displacement is distributed off the fault plane near segment boundaries.

There is good evidence that (iii) best explains the behaviour of the FPF. Paleoseismic trenches show coincident age ranges of earthquakes on the Cloudy Peaks and Bray Segments. At the boundary of the Cloudy Peaks and Ribbonwood Segments (i.e. where the Two Thumb and Sherwood Ranges coalesce), a c. 1 m high single-event scarp on late Pleistocene and Holocene terraces implies through-going rupture in an earthquake 4-6 ka. Surface rupture has not been produced at this location repeatedly. If this site was a semi-persistent barrier to rupture on an otherwise through-going fault, than the single-event displacement should be *larger* than elsewhere on the fault over the several earthquake cycles observed in the Bray and Cloudy Peaks segment trenches (e.g. Shen et al. 2009).

Likewise, if this site was a location of systematically smaller displacements than elsewhere on the fault, there should be evidence for progressive faulting over the time range of the faulted terraces. This is not the case. The best interpretation is that the high, on-fault slip rate gradients observed at segment boundaries are controlled by intersecting NW-striking faults, across which deformation is distributed in fundamentally different ways (expressed by the structural relief and topographic expression of folds).

6.2.4 Are geologically derived slip rates consistent with current geodetic models of fault slip rates in the central South Island?

The results of this study and others (c.f. Berryman et al. 2002; Amos et al. 2007 and 2010) show that temporally averaged geologic slip rates are systematically lower than their GPS-derived counterparts in this area. This could be due to broadly distributed strain in the hanging wall blocks of the faults or unrecognised faults in a wide zone roughly coinciding with Wallace et al.'s (2007) block boundaries.

In the case of the Fox Peak and Forest Creek Faults, combined, maximum slip rates do not approach even the minimum of 2.5 mm yr^{-1} net slip rate estimate of the geodetic model. Because the geologic slip rates encompass a broad, boundary-normal distance of c. 10 km, I consider it more likely that the excess geodetic strain is being accommodated by distributed faults in the Southern Alps (as in an alternative model proposed by Wallace et al. 2007 used to explain excess strain on the Alpine Fault). This is likely given the numerous seismic sources identified by Cox et al. (2012) in the Southern Alps, and the recognition of subsidiary structures like the Hororata Anticline Fault, Stony Creek Anticline, Eastern Fox Peak Fault, and others in this study. Geologic rates on identified central South Island reverse faults are the best estimates and should be used in the NSHM. In the case of the Moonlight Fault, the discrepancy between geodesy and geology is rather easily resolved: Wallace et al. (2007) state explicitly that the choice of allowing 1 mm yr^{-1} on the Moonlight Fault is in a sense arbitrary, and my results show that there is no evidence to indicate broadly distributed strain on a dip-slip Moonlight Fault.

6.2.5 Is the Moonlight Fault active: what is the nature of strain heterogeneity and fault episodicity in Otago, and is it influenced by glaciations?

The Moonlight Fault Zone (MFZ) has not been active over at least the Holocene, and probably since the LGM. The strain map of Beavan and Haines (2001), while lacking a dense coverage of continuous GPS stations around Lake Wakatipu, shows that modern shortening rates are negligible and thus agrees with my findings. The national seismic hazard model's (NSHM) assignment of a M_W 7.6 earthquake every c. 6 ka on two traces of the MFZ is inconsistent with my observations of activity of the MFZ over the last c. 12-17 ka.

The presence of Tertiary inliers along the MFZ, the local topographic relief and depth of rock exhumation in this part of Otago imply that the MFZ has not always been inactive. Beanland and Berryman (1989) were the first to posit that fault activity in Otago may be episodic, citing a lack of deformation on the Pisa Fault. Litchfield and Norris (2000) and Litchfield and Lian (2004) provided further evidence for this hypothesis in the aperiodic activity and quiescence of the Akatore Fault in eastern Otago. A better fundamental understanding of how strain is accommodated across an entire fault system, and at any particular time, is required to adequately characterise earthquake hazards here.

Studies in formerly glaciated regions have suggested that GIAs influence the recurrence of earthquakes over the time period considered in Chapter 2. My research implies that this is not necessarily the case for a fault situated in lithospheric conditions that favour such behaviour (Gerbault et al. 2002; Scherwath et al. 2006; Hampel et al. 2010). Glacial modulation of slip rates requires background tectonic loading – if, as in the case of the Otago fault system, the *tectonic* loading rate is not constant, slip rate variations cannot be attributed to *glacial* loading cycles. Tectonic loading exerts the primary control. Places where slip rate variations on single faults have been attributed to glacial cycles should be reevaluated in the context of the entire region to discount purely tectonic variations, which are known to exist in many settings (e.g. Oskin et al. 2008).

6.2.6 How can estimates of seismic hazard be improved by integrating field data into fault segmentation and fault-to-fault rupture scenarios?

The identification of faults, fault segments, and the ability of ruptures to jump segments or to other faults are major objectives of paleoseismic studies. Segment boundaries on reverse faults should be delineated on the basis of slip rates (e.g. Amos et al. 2010; Chapter 3), not based on geometry or surface manifestation. Even then, paleoseismic data is required to test the feasibility (or perhaps probability, with enough data) that these segments represent rupture barriers in earthquakes. To this end, field data is essential.

Establishing a chronology of correlative earthquakes on different fault segments and faults is more difficult. Even with many trenches on all segments and faults, dating resolution is rarely sufficient to correlate events from site to site. Numerical models that produce probabilistic rupture scenarios are currently the best way to handle this problem. Paleoseismic event ages can be explicit inputs into these models (e.g. Biasi and Weldon 2009) but this approach requires a relatively large catalogue of events to be meaningful. I have produced a model that uses fault-specific data collected in the field and empirical/model-based data from other fault systems to explain the apparent coincidence of event age distributions on the Fox Peak and Forest Creek Faults (FPF and FCF). This approach yields realistic M_W estimates that are consistent with previous studies, but makes the

important distinction that larger, multi-fault earthquakes may occur as regularly as single-fault earthquakes. It is also in line with recent studies exploring the role of static Coulomb stresses in earthquake triggering.

6.2.7 Does activity on the Fox Peak Fault influence the timing of earthquakes on the Forest Creek Fault?

It is likely that rupture on the FPF influences the timing of, if not triggers, earthquakes on the FCF:

(i) The timing of earthquakes interpreted from my paleoseismic excavations overlap over the last two FCF earthquake cycles.

(ii) The step-over distances at the surface are within the range reported for historical reverse fault earthquakes and in numerical models of fault ruptures (Shaw and Dieterich 2007; Wesnousky 2008; Field et al. 2013). At depth, FPF to FCF distances are smaller, and perhaps sole into the same fault plane (Wannamaker et al. 2002; Long et al. 2003; this study).

(iii) Coulomb stress modelling shows that displacement on the FPF increases the stress on large areas of the FCF. The areas of high stress at depth roughly coincide with identifiable surface traces of the FCF.

6.2.8 How reliable are secondary tectonic (fault-induced) and indirect (off-fault, shaking-induced) earthquake records for paleoseismic catalogues?

In this thesis, I have examined two separate kinds of secondary evidence for earthquakes in the subsurface:

(i) Bending moment faults are faults produced by folding in the hanging and foot walls of a reverse fault during an earthquake. These are most commonly normal faults caused by extension at the crest of a fault-cored anticline, though they can also be 'out-of-syncline' thrusts in the foot wall. Because these are created and slip concomitantly with the principal slip plane, they can provide useful supplementary information on the timing of earthquakes. Normal faults in a crestal graben, in particular, are useful because they create accommodation space and events are typically more clearly represented in the stratigraphy than on reverse/thrust faults (McCalpin 2009; Heddar et al. 2013). However, it is apparent from this study and others around the world that the normal faults do not slip in every earthquake (McCalpin 2009). Additionally, as the fold axis migrates with progressive faulting, the crestal graben will expand and create

new faults, complicating the reliability of the record preserved across any one normal fault.

It is not known what causes slip on these faults in some earthquakes and not in others. One possibility is that the magnitude or direction of slip at a point varies from earthquake to earthquake, so that the extensional strains required for failure are only produced in certain earthquakes. The amount of slip at a point may vary, especially in an imbricate wedge like that observed at Cloudy Peaks on the FPF. Liquefaction features found in one trench and the closed drainage system of the crestal graben at Cloudy Peaks may point towards a dual mechanism for failure. That is, perhaps slip occurs if the detachments are saturated at the time of the earthquake, facilitating spreading in a direction perpendicular to the uplift. Determining what causes failure in some earthquakes and not others is an important area of research and will increase the utility of these features (e.g. McCalpin 2009, see section 6.4.2).

(ii) Deep-seated landslides probably have comparable detachment depths to bending moment faults, but are produced by shaking rather than tectonics (e.g. Dramis and Blumetti 2005). Thus, a deep-seated landslide can give useful information on the return period shaking required to induce failure at a site, provided that the critical acceleration is known. Relating landslide failure to an earthquake on a specific fault requires a demonstration that failure can only occur with the source characteristics of that fault.

In Chapter 5, I argue that the Harper Hills landslide may be related to a Darfield-type earthquake, caused by directivity effects specific to the Greendale and Hororata Anticline Faults. This type of study may be useful in settings similar to the Canterbury Plains with fault sources not conducive to direct trenching. That is, if the kinematics of the fault of interest is known and the critical acceleration of a nearby deep-seated landslide is only reached as a direct consequence of those kinematics, then trenching of the landslide may yield evidence for earthquakes on the fault (e.g. McCalpin et al. 2011).

6.3 Research summary

The seismogenic faults and secondary tectonic features examined in this thesis have provided new insights into earthquake hazards in New Zealand and elsewhere. On-fault evidence and modelling from the Moonlight, Fox Peak and Forest Creek Faults indicate that predicting the recurrence intervals of large magnitude earthquakes is not straightforward in this region. In the Otago fold and thrust belt, large earthquakes on surface rupturing faults seem to occur periodically, but show

no evidence for being influenced by glacial unloading. The recurrence intervals of faults in this structurally-defined block may be influenced by a combination of plate boundary and intermediate-field stresses that would likely require a full visco-elastic relaxation stress model to understand. Even where recent surface rupturing earthquakes on a fault system are evident, the expected magnitudes, and recurrence interval of expected magnitudes, can change based on the potential faults and segments involved in a rupture. Variability in recurrence intervals and maximum magnitudes of individual faults are not currently accounted for in hazard models, though averaging over large regions and periods of time may eliminate the need to specifically address this problem.

Since off-fault records of paleoseismicity take many sources into account, they are attractive targets for testing and improving the seismic hazard models. Despite offering ideal trench locations and event stratigraphy, secondary tectonic features like bending-moment faults may not record all of the events on the master fault. In lieu of other records, events found in trenches across bending moment faults can be confidently related to earthquakes on the master fault and can be an important supplement to other trenches.

Based on the research presented in this thesis, I propose four recommendations for improving seismic hazard models:

(i) Fault-to-fault and fault segmentation models should use objective, quantitative criteria for identifying earthquake scenarios (e.g. Shaw and Dieterich 2006; Field and Page 2011; Parsons et al. 2012; Field et al. 2013; this study). Once an acceptable model is chosen, geologic data can be integrated with Monte Carlo simulations to obtain maximum moment magnitudes on a system of faults. Expected ground motions and the return periods thereof will change accordingly.

(ii) Measures should be taken to phase out the characteristic earthquake model on faults that clearly display aperiodicity. Probabilistic models of variation in recurrence interval and single event slip based on geologic investigations and modelling should be implemented (e.g. Nicol et al. 2012).

(iii) In regions where geologic investigations identify irregular fault recurrence intervals, off-fault evidence should be sought to determine spatio-temporally averaged return periods of strong ground motions.

(iv) When evaluating the return periods inferred from evidence of strong ground-shaking, analyses need to take into account near-source effects (e.g. rupture directivity, topographic amplification, the ‘hanging wall effect’) or ensure that modelling these results in negligible effects (e.g. Joshi and Bradley 2014). Paleoseismic evidence from

nearby faults should be used to supplement off-fault records to determine if the two are coupled.

6.4 Future avenues and potential locations of research

6.4.1 Lake Heron Fault

The Lake Heron Fault (LHF) is an active reverse fault NE of the FPF-FCF system. Upton et al. (2000, 2003) consider the LHF as a northern extension of the FCF. This interpretation is not universal, but if true would make for a total FCF-LHF length of c. 80 and allow the possibility of a M_W 7.6-7.7 earthquake (using reverse faulting length scaling of Wesnousky 2008). The LHF is also the northernmost, major reverse fault in the central South Island. To the North, faulting becomes oblique and dominated by strike-slip. It is therefore important to map, obtain slip rates and determine paleoseismic event ages on the LHF.

As a preliminary study, I mapped, surveyed and performed SHD on offset river terraces at the Paddle Hill Creek fan area (Fig. 6.1). SHD *a*-value was controlled by data from the closest climate station, which is not located in the basin. Survey and offset data were processed in the same way as in Chapter 3. Fault dip was inferred to be c. 60° which matches the steep projection of the fault across terrace risers and matches fault plane solutions derived from nearby outcrops. Other Monte Carlo simulation parameters were chosen based on those in Chapter 3. Only the most reliable survey/offset data were included in the analysis.

While there is significant error and no absolute age-control for SHD ages, the resulting slip rates are slightly higher than for other central South Island reverse faults. Perhaps more notably, the amount of slip on the Paddle Hill Creek fan is approximately the same as that on T5 and T3, which may be indicative of an earthquake cluster following deposition of the Paddle Hill Creek fan. More work should be conducted to establish terrace ages, offset, and the LHF's relationship with the FCF.

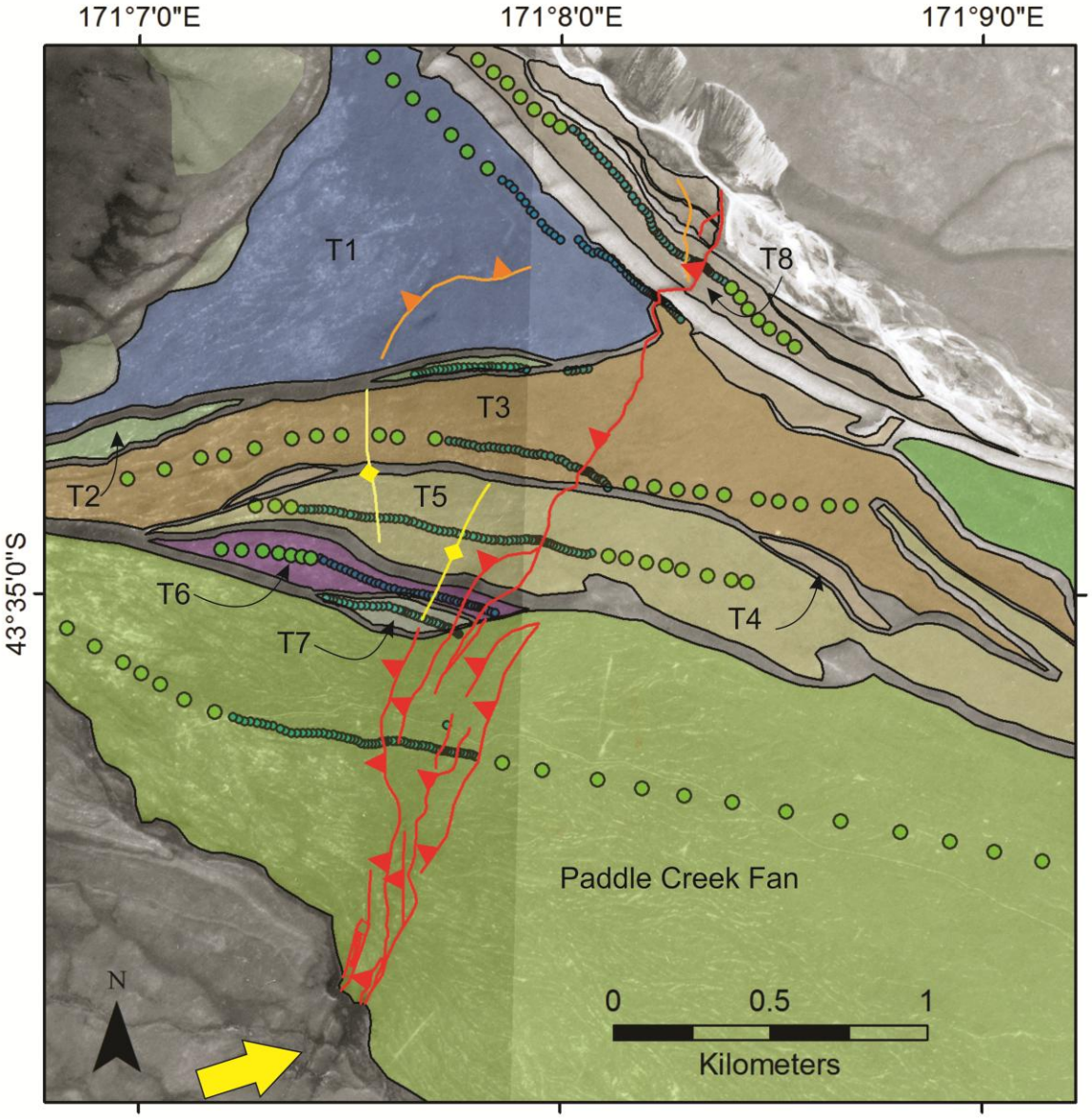

Figure 6.1: Map of the Lake Heron Fault at the Paddle Hill Creek fan. Dark green dots are RTK survey positions; light green are extracted from a 15 m DEM. Red lines are active fault traces; yellow lines are anticline axes; orange lines are possible fault traces. The yellow arrow is pointing at discrete fault traces south of the field area.

Table 6.2: Preliminary slip rate calculations from the Paddle Hill Creek fan area.

Terrace Surface	**SH Age**	**Net Slip**	**Slip Rate**
Paddle Hill Creek fan	N/A	19.5 ± 3 m	--
T5	9.9 ± 4.5 ka	22.5 ± 6 m	2.3, +2.2, -0.9 mm yr^{-1}
T3	12.8 ± 5 ka	18.7 ± 6 m	1.5, +1.1, -0.7 mm yr^{-1}
T1	20.5 ± 6 ka	N/A	--

6.4.2 Nevis-Cardrona Fault and the Terrace Spur Landslide

The Nevis-Cardrona Fault (NCF) was addressed in Chapter 2 as an active fault just south of Lake Wakatipu. It is an important structure because it has demonstrable late Quaternary activity and could produce M_W 7+ earthquakes relatively frequently. Unlike the nearby Dunstan Fault, which has been the focus of many GNS paleoseismic studies, the timing of past earthquakes on the NCF are only loosely constrained. Furthermore, the location of the fault and the timing of earthquakes on its most northern segment near Lake Hawea are only inferred.

On the western shores of Lake Hawea at Terrace Spur, a wind gap straddles an anticline that roughly coincides with the northern projection of the NCF (Fig. 6.2). Here, a train of sackung scarps (Fig. 6.2, 6.3 & 6.4) running parallel to the fold axis of the anticline and cross-cutting the wind gap create a crestal graben. While these are sackung features, they are most likely directly related to folding and shaking above the anticline, and presumably the NCF. A young scarp that ponds local drainages is an ideal location for trenching (Fig. 6.3).

This location is an ideal laboratory for distinguishing between spreading features and bending moment faults (e.g. McCalpin et al. 2011). It is also an example where landslide features may confidently record evidence for earthquakes on kinematically-related faults (Chapter 5). The timing of events in trenches can be compared to those in adjacent segments of the NCF to establish their reliability. I visited the location to map and collect GPR to determine the suitability of a paleoseismic excavation (Fig. 6.5).

Figure 6.2: Google Earth image of the Terrace Spur Landslide. The NCF runs strikes right to left in this image, and underlies the anticline that strands the wind gap in the middle of the image. The ridges surrounding the wind gap are cut by oppositely-facing sackung scarps; the wind gap is cut by a prominent scarp at its modern drainage divide.

Figure 6.3: Field photo looking South along the scarp in the Terrace Spur wind gap. The swampy area to the left is an ideal place to obtain datable material in an excavation.

Figure 6.4: Field photograph of the main landslide body at Terrace Spur. Scarps and anti-scarps have probably formed in response to shaking, uplift, or both.

6.4.3 Lake shoreline uplift gradients

As the results of Chapter 2 show, shoreline elevations can provide information on how plate boundary strain is distributed over long distances. The methods used in Chapter 2 to determine lake shoreline ages, correlation and offset can be applied elsewhere in the central South Island. The quantity and quality of uplift rate determinations have been refined by GPS and new dating techniques since Wellman's (1979) initial study of these lakes. However, there is a general lack of slip and uplift rate data over the late Quaternary despite several potentially active faults in the region (Cox et al. 2012). Additionally, Wellman's shoreline correlations are questionable. Unlike the Wakatipu basin, there is dense GPS coverage in the central lakes region that shows large uplift gradients tailing away from the Main Divide. Shoreline surveying and correlations across Lakes Ohau, Pukaki and Tekapo could fill in a crucial gap in the recent geologic uplift record and corroborate the accuracy and stability of GPS-derived uplift rates.

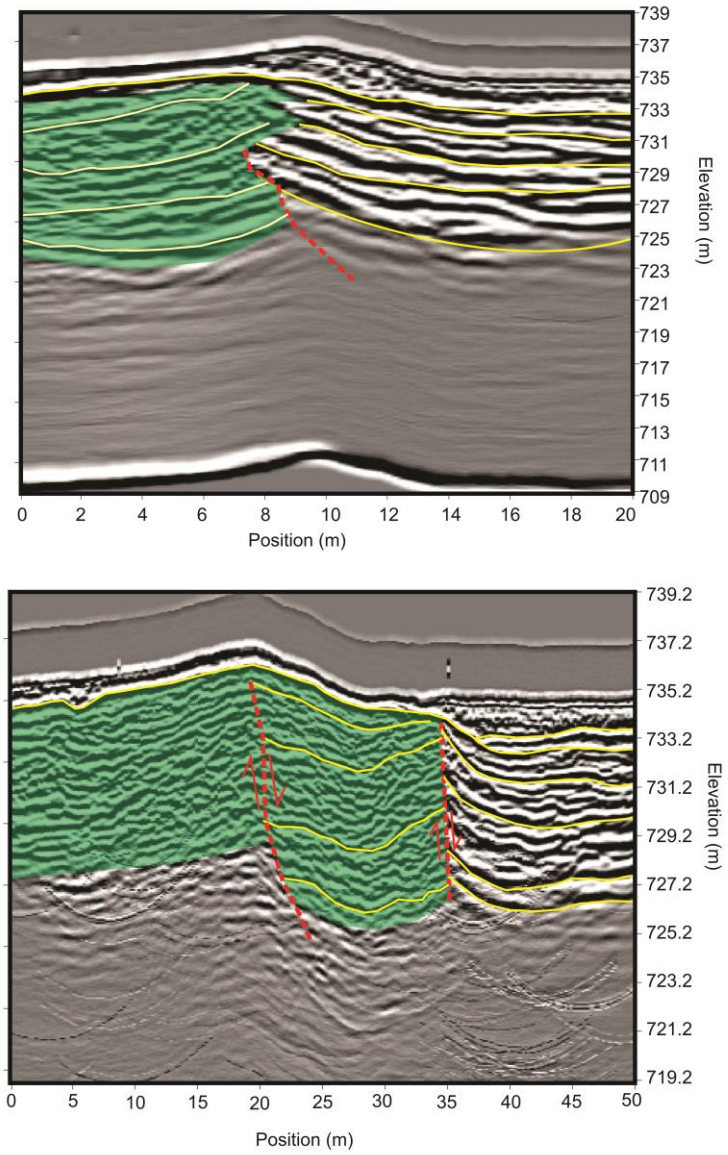

Figure 6.5: GPR profile across the scarp seen in Fig. 6.3. Frequencies of 50 and 100 MHz (top and bottom, respectively) profiles are of two separate locations along the scarp, with both showing evidence for folding and warping of reflectors.

6.5 Conclusion

Detailed field studies and numerical modelling have revealed useful information about reverse fault geohazards in New Zealand. A new exposure-age dating tool (SHD) was developed that allows collection of calibrated-age data in reverse faulting terrain not otherwise conducive to dating. SHD, field surveying and LiDAR, and a novel cross-correlation technique were used to determine the ages and magnitude of uplift around the Wakatipu Basin. From this data, it is evident that the Moonlight Fault has not been active or accumulating interseismic strain over at least the Holocene, which is consistent with models of periodic strain accumulation on Otago faults but not with the most current geodetic and seismic hazard models. The paleoseismicity of the Fox Peak and Forest Creek Faults was investigated using a range of field techniques and Monte Carlo simulations of fault slip rates and

earthquake magnitudes. My results show that the seismic hazard model must allow for fault-to-fault rupture and listric fault geometries to fully predict expected magnitudes. Landslides that fail with individual rupture scenarios may prove to be a useful supplement in predicting multi-fault and multi-segment earthquake magnitudes. This thesis improves upon the current understanding of the paleoseismicity of individual faults in New Zealand and the nature of reverse fault geohazards.

REFERENCES

Aa AR, Sjåstad J, Sønstegaard E, Blikra LH 2007. Chronology of Holocene rock-avalanche deposits based on Schmidt-hammer relative dating and dust stratigraphy in nearby bog deposits, Vora, inner Nordfjord, Norway. The Holocene 17: 955-964. DOI: 10.1177/0959683607082411.

Abdi H 2007. The Bonferroni and Sidak corrections for multiple comparisons, In: Salkind N ed. Encyclopedia of Measurement and Statistics. Thousand Oaks, Sage. 1416 p.

Abrahamson NA, Somerville PG 1996. Effects of the hanging wall and footwall on ground motions recorded during the Northridge earthquake. Bulletin of the Seismological Society of America 86: S93-S99.

Agliardi F, Crosta G, Zanchi A 2001. Structural constraints on deep-seated slope deformation kinematics. Engineering Geology 59: 83-102.

Alloway BV, Lowe DJ, Barrell DJA, Newnham RM, Almond PC, Augustinus PC, Bertler NAN, Carter L, Litchfield NJ, McGlone MS, Shulmeiter J, Vandergoes MJ, Williams PW 2007. Towards a climate event stratigraphy for New Zealand over the past 30000 years (NZ-INTIMATE project). Journal of Quaternary Science 22: 9-35.

Amos CB, Burbank DW 2007. Channel width response to differential uplift. Journal of Geophysical Research: Earth Surface 112(F2): F02010.

Amos CB, Burbank DW, Nobes DC, Read SAL 2007. Geomorphic constraints on listric thrust faulting: implications for active deformation in the Mackenzie Basin, South Island, New Zealand. Journal of Geophysical Research 112: DOI:10.1029/2006JB004291.

Amos CB, Burbank DW, Read SAL 2010. Along-strike growth of the Ostler Fault, New Zealand: consequences for drainage deflection above active thrusts. Tectonics 29: DOI:10.1029/2009TC002613.

Amos CB, Lapwood JJ, Nobes DC, Burbank DW, Rieser U, Wade A 2011. Palaeoseismic constraints on Holocene surface ruptures along the Ostler Fault, southern New Zealand. New Zealand Journal of Geology and Geophysics 54: 367-378.

Amos CB, Brownlee SJ, Rood DH, Fisher GB, Bürgmann R, Renne PR, Jayko AS 2013. Chronology of tectonic, geomorphic, and volcanic interactions and the tempo of fault slip near Little Lake, California. Geological Society of America Bulletin 125: 1187-1202.

Amos M 2010. New Zealand Vertical Datum 2009. New Zealand Surveyor, 300: 5-16.

André MF 1996. Rock weathering rates in arctic and subarctic environments (Abisko Mts., Swedish Lapland). Zeitschrift für Geomorphologie 40: 499-517.

Arrowsmith JR, Crosby CJ, Korjenkov AM, Mamyrov E, Povolotskaya IE 2005. Surface rupture of the 1911 Kebin (Chon-Kemin) earthquake, Northern Tien Shan, Kyrgyzstan, Eos Trans. AGU, , Fall Meet. Supplement 86: Abstract T51F-05.

Arrowsmith JR, Strecker MR 1999. Seismotectonic range-front segmentation and mountain-belt growth in the Pamir-Alai region, Kyrgyzstan (India-Eurasia collision zone). GSA Bulletin 111: 1665-1683.

Arvidsson R 1996. Fennoscandian earthquakes: whole crustal rupturing related to post-glacial rebound. Science 274: 744-746.

Awasthi DD, Bali R, Tewari NK 2005. Relative dating of moraines by lichenometric and Schmidt hammer techniques in the Gangotri glacier valley, Uttarkashi District, Uttaranchal. Special Publication of the Palaeontological Society of India 2: 201-206.

Baltay A, Ide S, Prieto G, Beroza G 2011. Variability in earthquake stress drop and apparent stress. Geophysical Research Letters 38: L06303.

Barka A 1996. Slip distribution along the North Anatolian fault associated with the large earthquakes of the period 1939 to 1967. Bulletin of the Seismological Society of America 86: 1238-1254.
Barnes PM, Sutherland R, Delteil J 2005. Strike-slip structure and sedimentary basins of the southern Alpine Fault, Fiordland, New Zealand. Geological Society of America Bulletin 117: 411-435.
Barnes, PM 1990. Provenance of Cretaceous accretionary wedge sediments: the Mangapokia Formation, Wairarapa, New Zealand. New Zealand Journal of Geology and Geophysics 33: 125-135.
Barrell DJA, Andersen BG, Denton GH 2011. Glacial geomorphology of the central South Island, New Zealand. Lower Hutt: GNS Science. GNS Science monograph 27. 2v.
Barrell DJA, Cox S 2003. Southern Alps tectonics and Quaternary geology. Geological Society of New Zealand Annual Conference Field Trip Guide FT6, Cox S, Lyttle, BS ed. Geological Society of New Zealand Miscellaneous Publication 116B. 40 p.
Barrell DJA 2011. Quaternary glaciers of New Zealand. In: Quaternary Glaciations-Extent and Chronology: A Closer Look. Ehlers J, Gibbard PL, Hughes PD eds. Developments in Quaternary Science 15: Amsterdam: 1047-1064.
Barrell DJA 1994. Surficial geology of the Wakatipu Basin, Central Otago, New Zealand. Institute of Geological and Nuclear Sciences Report 94/39. 31 p.
Barrell DJA, Litchfield NJ, Townsend DB, Quigley M, Van Dissen RJ, Cosgrove R, Cox SC, Furlong K, Villamor P, Begg JG, Hemmings-Sykes S, Jongens R, Mackenzie H, Noble D, Stahl T, Bilderback E, Duffy B, Henham H, Klahn A, Lang EMW, Moody L, Nicol R, Pedley K, Smith A2011. Strike-slip ground-surface rupture (Greendale Fault) associated with the 4 September 2010 Darfield earthquake, Canterbury, New Zealand. Quarterly Journal of Engineering Geology and Hydrogeology 44: 283-291.
Barrell DJA, Strong DT 2012. Geological contours for groundwater modelling, South Canterbury. GNS Science Consultancy Report 2012/245. 11 p.
Barth NC, Boulton C, Carpenter BM, Batt GE, Toy VG 2013. Slip localization on the southern Alpine Fault, New Zealand. Tectonics 32: 620-640.
Basu A**,** Celestino TB, Bortolucci AA. 2007. Predicting weathering grades by Schmidt hammer test: an investigation on granitic rock materials from Southeastern Brazil. Proceedings of the 11th Congress of the International Society for Rock Mechanics (ISRM), Lisbon, Portugal: 385-390.
Beanland S 1987. Field guide to sites of active earth deformation: South Island, New Zealand. NZ Geological Survey Record 19.
Beanland S, Barrow-Hurlbert SA 1988. The Nevis-Cardrona Fault System, Central Otago, New Zealand: Late Quaternary tectonics and structural development. New Zealand Journal of Geology and Geophysics 31: 337-352.
Beanland, S, Berryman KR, Hull AG, Wood, PR 1986. Late Quaternary deformation at the Dunstan Fault, Central Otago, New Zealand. Bulletin of the Royal Society of New Zealand 24: 293-306.
Beavan J, Haines J, 2001. Contemporary horizontal velocity and strain rate fields of the Pacific-Australian plate boundary zone through New Zealand. Journal of Geophysical Research 106: 741-770.
Beavan J., Motagh M, Fielding EJ, Donnelly N, Collett D 2012. Fault slip models of the 2010–2011 Canterbury, New Zealand, earthquakes from geodetic data and observations of postseismic ground deformation. New Zealand Journal of Geology and Geophysics 55: 207-221.
Beavan J, Ellis S, Wallace L 2007. Kinematic constraints from GPS on oblique convergence of the Pacific and Australian plates, central South Island, New Zealand. In: Okaya DA, Stern TA, Davey FJ eds. A Continental Plate Boundary: Tectonics at South Island, New Zealand. Washington, DC, American Geophysical Union. 369 p.

Beavan J, Samsonov S, Motagh M, Wallace L, Ellis S, Palmer, N 2010. The Darfield (Canterbury) earthquake: geodetic observations and preliminary source model. Bulletin of the New Zealand Society for Earthquake Engineering 43: 228-235.
Bebbington M, Harte D 2003. The linked stress release model for spatio-temporal seismicity: formulations, procedures and applications. Geophysical Journal International 154:925-946.
Bell DH 1992. Geomorphic evolution of a valley system: the Kawarau Valley, Central Otago. In: Soons JM, Selby MJ eds. Landforms of New Zealand. Auckland, Longman: 456-481.
Benedict, JB 1985. Arapaho Pass, glacial geology and archaeology at the crest of the Colorado Front Range. Center for Mountain Arachaeology (Ward, Colorado) Research Report 3. 197 p.
Berryman KR, Cochran UA, Clark KJ, Biasi G P, Langridge RM, Villamor P 2012. Major Earthquakes Occur Regularly on an Isolated Plate Boundary Fault. Science 336: 1690-1693.
Berryman K, Beanland S 1991. Variation in fault behaviour in different tectonic provinces of New Zealand. Journal of Structural Geology 13: 177-189.
Berryman KR, Webb T, Hill N, Stirling M, Rhoades DJ Beavan J, Darby D 2002. Seismic loads on Dams, Waitaki system: Earthquake source characterisation. GNS Client report 2001/129. 80 p.
Betts MW, Latta MA 2000. Rock surface hardness as an indication of exposure age: an archaeological application of the Schmidt hammer. Archaeometry 42: 209-223.
Biasi G P, Weldon RJ 2009. San Andreas Fault Rupture Scenarios from Multiple Paleoseismic Records: Stringing Pearls. Bulletin of the Seismological Society of America 99: 471-498.
Bienawski ZT 1989. Engineering Rock Mass Classifications: A Complete Manual for Engineers and Geologists in Mining, Civil, and Petroleum Engineering. Wiley-Interscience, Chichester. 272 p.
Birkeland PW, Noller JS 2000. Rock and mineral weathering. In: Noller JS, Sowers JM, Lettis WR eds. Quaternary Geochronology: Methods and Applications. Washington, American Geophysical Union: 293-312.
Bockheim JG, Hartemink AE 2013. Soils with fragipans in the USA. Catena 233-242.
Boker SM, Xu Minquan, Rotondo JL, King K 2002. Windowed cross-correlation and peak picking for the analysis of variability in the association between behavioral time series. Psychological Methods 7: 338-355.
Botsford JW 1983. The Esk Head melange in the Eske Head/Okuku area, North Canterbury. Unpublished MSc thesis, University of Canterbury, New Zealand. 247 p.
Bourguignon S, Stern TA, Savage MK 2007. Crust and mantle thickening beneath the southern portion of the Southern Alps, New Zealand. Geophysical Journal International 168: 681-690.
Bradley BA 2012. Strong ground motion characteristics observed in the 4 September 2010 Darfield, New Zealand earthquake. Soil Dynamics and Earthquake Engineering 42: 32-46.
Brady PV, Carroll SA 1994. Direct effects of CO_2 and T on silicate weathering: Possible implications for climate control. Geochimica et Cosmochimica Acta 58: 1853-1856.
Brady PV,Carroll SA 1994. Direct effects of CO_2 and T on silicate weathering: possible implications for climate control. Geochimica et Cosmochimica Acta 58: 1853-1856.
Bray JD, Seed RB, Cluff LS, Seed HB 1994. Earthquake fault rupture propagation through soil. Journal of Geotechnical Engineering 120: 543-561.
Browne GH 1983. A new interpretation of brecciation in the Sandpit Tuff, Harper Hills, Canterbury. New Zealand Journal of Geology and Geophysics 26: 429-434.
Brune JN 1999. Precarious rocks along the Mojave section of the San Andreas Fault: Constraints on ground motions from great earthquakes. Seismological Research Letters 70: 29-33.
Brune JN, Anooshehpoor A, Purvance MD, Brune RJ 2006. Band of precariously balanced rocks between the Elsinore and San Jacinto, California, fault zones: Constrains on ground motion for large earthquakes. Geology 34: 137-140.

Buech F, Davies TR, Pettinga JR 2010. The Little Red Hill Seismic Experimental Study: Topographic Effects on Ground Motion at a Bedrock-Dominated Mountain Edifice. Bulletin of the Seismological Society of America 100: 2219-2229.
Bull WL, Knuepfer PLK. 1987. Adjustments by the Charwell River, New Zealand, to uplift and climatic changes. Geomorphology 1: 15-32.
Bull WL. 1990. Stream-terrace genesis: Implications for soil development. Geomorphology 3: 351-367.
Busenberg E, Clemency CV. 1976. The dissolution kinetics of feldspars at 25°C and 1 atm CO_2 partial pressure. Geochimica et Cosmochimica Acta 40: 41-49.
Campbell JK, Nicol A, Howard ME. 2003. Long-term changes to river regimes prior to late Holocene coseismic faulting, Canterbury, New Zealand. Journal of Geodynamics 36: 147-168.
Campbell JK, Pettinga JR, Jongens R 2012. The tectonic and structural setting of the 4 September 2010 Darfield (Canterbury) earthquake sequence, New Zealand. New Zealand Journal of Geology and Geophysics 55: 155-168.
Carbonel D, Gutiérrez F, Linares R, Roqué C, Zarroca M, McCalpin J, Guerrero J, Rodríguez V 2013. Differentiating between gravitational and tectonic faults by means of geomorphological mapping, trenching and geophysical surveys: The case of the Zenzano Fault (Iberian Chain, N Spain). Geomorphology 189: 93-108.
Carlson JR, Grant-Mackie JA, Rodgers KA 1980. Stratigraphy and sedimentology of the Coalgate area, Canterbury, New Zealand. New Zealand Journal of Geology and Geophysics 23: 179-192.
Carpenter NS, Payne, SJ, Schafer AL 2012. Toward Reconciling Magnitude Discrepancies Estimated from Paleoearthquake Data. Seismological Research Letters 83: 555-565.
Caskey SJ, Ramelli AR 2004. Tectonic displacement and far-field isostatic flexure of pluvial lake shorelines, Dixie Valley, Nevada. Journal of Geodynamics 38: 131-145.
Caskey SJ, Wesnousky SG 1997. Static stress changes and earthquake triggering during the 1954 Fairview Peak and Dixie Valley earthquakes, central Nevada. Bulletin of the Seismological Society of America 87: 521-527.
Černá B, Engel Z 2011. Surface and subsurface Schmidt hammer rebound value variation for a granite outcrop. Earth Surface Processes and Landforms 36: 170-179.
Challis GA 1966. Cretaceous stratigraphy and structure of the Lookout area, Awatere Valley. Transactions of the Royal Society of New Zealand 4: 119-137.
Chinn TJH 1981. Use of rock weathering-rind thickness for Holocene numerical age-dating in New Zealand. Arctic and Alpine Research 13: 33-45.
Ciolkosz EJ, Waltman WJ 2000. Pennsylvania's Fragipans. Pennsylvania State University Agronomy Series 147. 12 p.
Ciolkosz EJ, Waltman WJ, Thurman NC 1992. Fragipan in Pennsylvania Soils. Pennsylvania State University Agronomy Series 119. 14 p.
Cook SJ, McColl ST, Stahl T 2013. Surveying and dating post-glacial lake shorelines in New Zealand. RICS Research Trust Report: 27 p.
Cook SJ, Swift DA 2012. Subglacial basins: Their origin and importance in glacial systems and landscapes. Earth-Science Reviews 115: 332-372.
Cox SC, Stirling MW, Herman F, Gerstenberger M.,Ristau J 2012. Potentially active faults in the rapidly eroding landscape adjacent to the Alpine Fault, central Southern Alps, New Zealand. Tectonics 31: *TC2011. DOI:10.1029/2011TC003038.*
Cox, SC, Barrell DJA 2007. Geology of the Aoraki area : scale 1:250,000. Lower Hutt: GNS Science. Institute of Geological & Nuclear Sciences 1:250,000 Geological map 15. 71 p. + 1 folded map.
Cremeens, DL, Hart JP, Darmody RG 1998. Complex pedostratigraphy of a terrace fragipan at the Memorial Park site, central Pennsylvania. Geoarchaeology: An International Journal 13: 339-359.

Crone AJ, Machette MN, Bowman JR 1992. Geologic investigations of the 1988 Tennant Creek, Australia, earthquakes – implications for paleoseismicity in stable continental regions: U.S. Geological Survey Bulletin 2032-A. 60 p.
Crook R, Gillespie AR 1986. Weathering rates in granitic boulders measured by P-wave speeds. In: Colman SM, Dethier DP eds. Rates of Chemical Weathering of Rocks and Minerals. Orlando, Academic Press: 395-417.
Cutten H 1990. Reconnaissance of faulting in the Fairlie Basin, Burke Pass, Lake Tekapo area. NZ Geological Survey Earth Deformation Section unpublished Immediate Report 90/2.
Davis K, Burbank DW, Fisher D, Wallace S, Nobes D 2005. Thrust-fault growth and segment linkage in the active Ostler fault zone, New Zealand. Journal of Structural Geology 27: 1528-1546.
Day MJ, Goudie AS 1977. Field assessment of rock hardness using the Schmidt test hammer. British Geomorphology Research Group Technical Bulletin 18: 19-29.
Day MJ 1980. Rock hardness: Field assessment and geomorphic importance. Professional Geographer 32: 72-81.
De Pascale GP, Quigley MC, Davies TRH 2014. Lidar reveals uniform Alpine fault offsets and bimodal plate boundary rupture behavior, New Zealand. Geology 42: 411-414.
Del Gaudio V, Wasowski J 2007. Directivity of slope dynamic response to seismic shaking. Geophysical Research Letters 34: L12301. DOI:10.1029/2007GL029842.
DeMets C, Gordon RG, Argus DF 2010. Geologically current plate motions. Geophysical Journal International 181: 1-80.
Demoulin A, Bovy B, Rixhon G, Cornet Y 2009. An automated method to extract fluvial terraces from digital elevation models: the Vesdre Valley, a case study in eastern Belgium. Geomorphology 91: 51-64.
Densmore AL, Ellis MA, Li Y, Zhou R, Hancock GS, Richardson N 2007. Active tectonics of the Beichuan and Pengguan faults at the eastern margin of the Tibetan Plateau. Tectonics 26: TC4005.
Densmore AL, Li Y, Richardson NJ, Zhou RJ, Ellis M, Zhang Y 2010. The Role of Late Quaternary Upper-Crustal Faults in the 12 May 2008 Wenchuan Earthquake. Bulletin of the Seismological Society Of America 100: 2700-2712.
DePolo CM, Clark DG, Slemmons DB, Ramelli, AR 1991. Historical surface faulting in the Basin and Range province, western North America: implications for fault segmentation. Journal of Structural Geology 13: 123-136.
Dietrich R, Ivins ER, Casassa G, Lange H, Wendt J, Fritsche M 2010. Rapid crustal uplift in Patagonia due to enhanced ice loss. Earth and Planetary Science Letters 289: 22-29.
Dixon TH, Norabuena E, Hotaling L 2003. Paleoseismology and Global Positioning System: Earthquake-cycle effects and geodetic versus geologic fault slip rates in the Eastern California shear zone. Geology 31: 55-58.
Dolan JF, Sieh K, Rockwell TK, Yeats RS, Shaw J, Suppe J, Huftile GJ, Gath EM 1995. Prospects for larger or more frequent earthquakes in the Los Angeles metropolitan region. Science 267: 199.
Dolan JF, Bowman DD, Sammis CG 2007. Long-range and long-term fault interactions in Southern Calirfornia Science 35: 855-858.
Dramis F, Blumetti AM 2005. Some considerations concerning seismic geomorphology and paleoseismology. Tectonophysics 408: 177-191.
Duffy B, Quigley M, Barrell D, Van Dissen R, Stahl T, Leprince S, McInnes C, Bilderback E 2013. Fault kinematics and surface deformation across a releasing bend during the 2010 M_w 7.1 Darfield, New Zealand, earthquake revealed by differential LiDAR and cadastral surveying. Geological Society of America. Geological Society of America Bulletin 125: 420-431.

Elliott AJ, Dolan JF, Oglesby DD 2009. Evidence from coseismic slip gradients for dynamic control on rupture propagation and arrest through stepovers. Journal of Geophysical Research - Solid Earth 114:B02313.

Elliott, JR, Nissen EK, England PC, Jackson JA, Lamb S, Li Z, Oehlers M, Parsons B 2012. Slip in the 2010–2011 Canterbury earthquakes, New Zealand. Journal of Geophysical Research 117: *B03401. DOI:10.1029/2011JB008868.*

Elliott JR, Parsons B, Jackson JA, Shan X, Sloan RA, Walker RT 2011. Depth segmentation of the seismogenic continental crust: The 2008 and 2009 Qaidam earthquakes. Geophysical Research Letters 38: L06305.

Engel Z 2007. Measurement and age assignment of intact rock strength in the Krkonoše Mountains, Czech Republic. Zeitschrift für Geomorphologie 51: 69-80.

Ericson K 2004. Geormorphological surfaces of different age and origin in granite landscapes: An evaluation of the Schmidt hammer test. Earth Surface Processes and Landforms 29: 495-509. DOI: 10.1002/esp.1048.

Feary DA 1979. Geology of the Urewera Greywacke in Waioeka Gorge, Raukumara Peninsula, New Zealand. New Zealand Journal of Geology and Geophysics 22: 693-708.

Field EH, Page MT 2011. Estimating Earthquake-Rupture Rates on a Fault or Fault System. Bulletin of the Seismological Society of America 101: 79-92.

Field EH, Biasi GP, Bird P, Dawson TE, Felzer KR, Jackson DD, Johnson KM, Jordan TH, Madden C, Michael AJ, Milner KR, Page MT, Parsons T, Powers PM, Shaw BE, Thatcher WR, Weldon RJ II, Zeng Y 2013. Uniform California earthquake rupture forecast, version 3 (UCERF3)—The time-independent model. U.S. Geological Survey Open-File Report 2013–1165, California Geological Survey Special Report 228, and Southern California Earthquake Center Publication 1792. 97 p.

Forsyth PJ, Barrell DJA, Jongens R 2008. Geology of the Christchurch area. Institute of Geological and Nucelear Sciences 1:250000 Geological map 16. 1 sheet + 67 p.

Fox AN 1987. The neotectonic history of the Lake Tekapo region, Mackenzie Basin, New Zealand. Unpublished MSc Thesis, University of Canterbury, Christchurch, New Zealand. 222 p.

Freed AM 2005. Earthquake triggering by static, dynamic, and postseismic stress transfer. Annual Review Of Earth And Planetary Sciences 33:335-367.

Fukuyama E, Hao KX 2013. Subparallel Dipping Faults that Ruptured during the 2008 Wenchuan Earthquake. Bulletin Of The Seismological Society Of America 103:2128-2134.

Gerbault M, Davey F, Henrys S 2002. Three-dimensional lateral crustal thickening in continental oblique collision: an example from the Southern Alps, New Zealand. Geophysical Journal International 150: 770-779.

Ghisetti FC, Sibson RH 2012. Compressional reactivation of E–W inherited normal faults in the area of the 2010–2011 Canterbury earthquake sequence. New Zealand Journal of Geology and Geophysics 55: 177-184.

Ghisetti FC, Gorman AR, Sibson RH 2007. Surface breakthrough of a basement fault by repeated seismic slip episodes: The Ostler Fault, South Island, New Zealand. Tectonics 26: TC6004.

Gledhill K, Ristau J, Reyners M, Fry B, Holden C 2011. The Darfield (Canterbury, New Zealand) Mw 7.1 Earthquake of September 2010: A Preliminary Seismological Report. Seismological Research Letters 82: 378-386.

Gold RD, Cowgill E, Wang XF, Chen XH 2006. Application of trishear fault-propagation folding to active reverse faults: examples from the Dalong Fault, Gansu Province, NW China. Journal of Structural Geology 28: 200-219.

Goldfinger C, Nelson CH, Morey AE, Johnson JE, Patton JR, Karabanov E, Gutiérrez-Pastor J, Eriksson AT, Gràcia E, Dunhill G, Enkin RJ, Dallimore A, Vallier T 2012. Turbidite event history—Methods and implications for Holocene paleoseismicity of the Cascadia subduction zone. U.S. Geological Survey Professional Paper 1661–F. 170 p.

Golledge NR, Mackintosh AN, Anderson BM, Buckley KM, Doughty AM, Barrell DJA, Denton GH, Vandergoes MJ, Andersen BG, Schaefer JM 2012. Last Glacial Maximum climate in New Zealand inferred from a modelled Southern Alps icefield. Quaternary Science Reviews 46: 30-45.

Goudie AS 2006. The Schmidt hammer in geomorphological research. Progress in Physical Geography 30: 703-718. DOI: 10.1177/0309133306071954.

Gradwell MW 1974. The available-water capacities of some southern and central zonal soils of New Zealand. New Zealand Journal of Agricultural Research 17: 465-478.

Gupta V, Sharma R, Sah MP 2009. An evaluation of surface hardness of natural and modified rocks using Schmidt hammer: Study from Northwestern Himalaya, India. Geografiska Annaler 91: 179-188.

Gutiérrez F, Linares R, Roque C, Zarroca M, Rosell J, Galve JP, Carbonel D 2012. Investigating gravitational grabens related to lateral spreading and evaporite dissolution subsidence by means of detailed mapping, trenching, and electrical resistivity tomography (Spanish Pyrenees). Lithosphere 4: 331-353.

Gutiérrez F, Lucha P, Galve JP 2010a. Reconstructing the geochronological evolution of large landslides by means of the trenching technique in the Yesa Reservoir (Spanish Pyrenees). Geomorphology 124: 124-136.

Gutiérrez F, Ortuño M, Lucha P, Guerrero J, Acosta E, Coratza P, Piacentini D, Soldati M 2008. Late Quaternary episodic displacement on a sackung scarp in the central Spanish Pyrenees. Secondary paleoseismic evidence? Geodinamica Acta 21: 187-202.

Gutiérrez F, Soldati M, Audemard F, Bălteanu D 2010b. Recent advances in landslide investigation: Issues and perspectives. Geomorphology 124: 95-101.

Hampel A, Hetzel R, Densmore AL 2007. Postglacial slip-rate increase on the Teton normal fault, northern Basin and Range Province, caused by melting of the Yellowstone ice cap and deglaciation of the Teton Range? Geology 35: 1107-1110.

Hampel A, Hetzel R, Maniatis G, Karow T 2009. Three-dimensional numerical modeling of slip rate variations on normal and thrust fault arrays during ice cap growth and melting. Journal of Geophysical Research 114: B08406.

Hampel A, Karow T, Maniatis G, Hetzel R 2010. Slip rate variations on faults during glacial loading and unloading: Implications for the viscosity structure of the lithosphere. Journal of the Geological Society of London 167: 383-399.

Hanks TC, Kanamori H 1979. A moment magnitude scale. Journal of Geophysical Research: Solid Earth 84:2348-2350.

Harden JW 1982. A quantitative index of soil development from field descriptions: Examples from a chronosequence in central California. Geoderma 28: 1-28.

Hart MW, Shaller PJ, Farrand GT 2012. When landslides are misinterpreted as faults: Case studies from the western United States. Environmental and Engineering Geoscience 18: 313-325.

Haupt F 2012. Anwendungsorientierte Bewertung zweier Methoden zur relativen Altersdatierung Holozäner Moränen an Hochgebirgsgletschern. Unpublished Diploma thesis, University of Würzburg. 126 p.

Heddar A, Authemayou C, Djellit H, Yelles AK, Déverchère J, Gharbi S, Boudiaf A, Van Vliet Lanoe B 2013. Preliminary results of a paleoseismological analysis along the Sahel fault (Algeria): New evidence for historical seismic events. Quaternary International 302: 210-223.

Hetzel R, Hampel A 2005. Slip rate variations on normal faults during glacial-interglacial changes in surface loads. Nature 435: 81-84.

Hodder APW, Hetherington JR 1991. A quantiative study of the weathering of greywacke. Engineering Geology 31: 353-368.

Hogg AG, Quan H, Blackwell PG, Mu N, Buck CE, Guilderson TP, Heaton TJ, Palmer JG, Reimer PJ, Reimer RW, Turney CSM, Zimmerman SRH 2013. SHCal13 Southern hemisphere calibration, 0-50,000 years cal BP. Radiocarbon 55: 1889-1903.

Hojo T 1931. Distribution of the median, quartiles and interquartile distance in samples from a normal population. Biometrika 23: 315-360.

Holden C, Beavan J, Fry B, Reyners M, Ristau J, Van Dissen R, Villamor P, Quigley M 2011. Preliminary source model of the Mw 7.1 Darfield earthquake from geological, geodetic and seismic data. Proceedings of the Ninth Pacific Conference on Earthquake Engineering. Auckland, New Zealand, 8.

Hornblow S, Quigley MC, Nicol A, Van Dissen RJ. Unpublished results, Paleoseismology of the 2010 Mw 7.1 Darfield (Canterbury) earthquake source, Greendale Fault, New Zealand.

Huang CC, Lee YH, Liu HP, Keefer DK, Jibson RW 2001. Influence of Surface-Normal Ground Acceleration on the Initiation of the Jih-Feng-Erh-Shan Landslide during the 1999 Chi-Chi, Taiwan, Earthquake. Bulletin of the Seismological Society of America 91: 953-958.

Hubbard J, Shaw JH, Dolan J, Pratt TL, McAuliffe L, Rockwell TK 2014. Structure and Seismic Hazard of the Ventura Avenue Anticline and Ventura Fault, California: Prospect for Large, Multisegment Ruptures in the Western Transverse Ranges. Bulletin of the Seismological Society of America 104: 1070-1087.

Ingles J, Darrozes J, Soula JC 2006. Effects of the vertical component of ground shaking on earthquake-induced landslide displacements using generalized Newmark analysis. Engineering Geology 86: 134-147.

Ishiyama T, Mueller K, Togo M, Okada A, Takemura K 2004. Geomorphology, kinematic history, and earthquake behavior of the active Kuwana wedge thrust anticline, central Japan. Journal of Geophysical Research: Solid Earth 109(B12): B12408.

Jackson J, Norris R, Youngson J 1996. The structural evolution of active fault and fold systems in central Otago, New Zealand: evidence revealed by drainage patterns. Journal of Structural Geology 18: 217-234.

Jackson J, Ritz JF, Siame L, Raisbeck G, Yiou F, Norris R, Youngson J, Bennett E 2002. Fault growth and landscape development rates in Otago, New Zealand, using in situ cosmogenic Be-10. Earth and Planetary Science Letters 195: 185-193.

James ZE 1998. Geology, Quaternary structure, fault rocks and fluid flow, Fox Peak Range, Eastern Southern Alps. Unpublished MSc Thesis, University of Otago, Dunedin, Otago.

Lin J, Stein R 2004. Stress triggering in thrust and subduction earthquakes and stress interaction between the southern San Andreas and nearby thrust and strike-slip faults. Journal of Geophysical Research - Solid Earth 109: B02303.

Jibson RW 1996. Use of landslides for paleoseismic analysis. Engineering Geology 43: 291-323.

Jibson RW 2011. Methods for assessing the stability of slopes during earthquakes—A retrospective. Engineering Geology 122: 43-50.

Jibson RW, Harp EL, Schulz W, Keefer DK 2004. Landslides Triggered by the 2002 Denali Fault, Alaska, Earthquake and the Inferred Nature of the Strong Shaking. Earthquake Spectra 20: 669-691.

Jibson RW, Keefer DK 1993. Analysis of the seismic origin of landslides: Examples from the New Madrid seismic zone. Geological Society of America Bulletin 105: 521-536.

Jibson RW, Rathje EM, Jibson MW, Lee YW 2013. SLAMMER—Seismic LAndslide Movement Modeled using Earthquake Records: US Geological Survey Techniques and Methods 12-B1.

Johnson PL, Cotton WR 2005. The Santiago Landslide and Associated Ridge-top Graben (Sackungen): Implications for Paleoseismic Landslide Studies. Environmental and Engineering Geoscience 11: 5-15.

Jones CH, Wesnousky SG 1992. Variations in Strength and Slip Rate Along the San Andreas Fault System. Science 256: 83-86.

Jongens R, Barrell DJA, Campbell JK, Pettinga JR 2012. Faulting and folding beneath the Canterbury Plains identified prior to the 2010 emergence of the Greendale Fault. New Zealand Journal of Geology and Geophysics 55: 169-176.
Joshi VA, Bradley BA2014. Explicit consideration of near-fault directivity effects in NZ-specific probabilistic seismic hazard analysis. New Zealand Society for Earthquake Engineering Conference (NZSEE), 21-23 Mar 2014. Auckland, New Zealand. 12 p.
Kammler DW 2007. A First Course in Fourier Analysis: Cambridge, Cambridge University Press. 862 p.
Kaneko Y, Fialko Y 2011. Shallow slip deficit due to large strike-slip earthquakes in dynamic rupture simulations with elasto-plastic off-fault response. Geophysical Journal International 186: 1389-1403.
Kato N 2001. Simulation of seismic cycles of buried intersecting reverse faults, Journal Of Geophysical Research-Solid Earth 106:4221-4232.
Kellerer-Pirklbauer A, Wangensteen B, Farbrot H, Etzelmüller B 2008. Relative surface age-dating of rock glacier systems near Hólar, Hjaltadalur, northern Iceland. Journal of Quaternary Science 23: 137-151. DOI: 10.1002/jqs.1117.
Kerr LC, Craw D, Norris RJ, Youngson JH, Wopereis R 2000. Structure, geomorphology, and gold concentration in the Nokomai valley, Southland, New Zealand. New Zealand Journal of Geology and Geophysics 43: 425-433.
Khajavi N, Quigley M, Langridge R Influence of topography and basement depth on surface rupture morphology revealed from LiDAR and field mapping, Hope Fault, New Zealand. Tectonophysics (in press).
Khajavi N, Quigley M, McColl ST, Rezanejad A 2012. Seismically induced boulder displacement in the Port Hills, New Zealand during the 2010 Darfield (Canterbury) earthquake. New Zealand Journal of Geology and Geophysics 55: 271-278.
King G, Yielding G 1984. The evolution of a thrust fault system: processes of rupture initiation, propagation and termination in the 1980 El Asnam (Algeria) earthquake. Geophysical Journal of the Royal Astronomical Society 77: 915-933.
Knuepfer PLK 1984. Tectonic geomorphology and present-day tectonics of the Alpine shear system, South Island, New Zealand. Unpublished Ph.D. thesis, Univ. of Arizona, Tucson, AZ. 489 p.
Knuepfer PLK. 1988. Estimating ages of late Quaternary stream terraces from analysis of weathering rinds and soils. GSA Bulletin 100: 1224-1236.
Knuepfer PLK 1989. Implications of the characteristics of endpoints of historical surface fault ruptures for the nature of fault segmentation. In: Schwartz DP, Sibson RH eds. Fault Segmentation and Controls of Rupture Initiation and Termination, Palm Springs California USGS Open File report 89-315. 458 p.
Kowallis BJ, Jones LEA, Wang HF 1984. Velocity-porosity-clay content systematics of poorly consolidated sandstones. Journal of Geophysical Research 89: 10355-10364.
Kruskal WH, Wallis WA 1952. Use of ranks in one-criterion variance analysis. Journal of the American Statistical Association 47: 583–621.
Lambeck K 1995. Late Devensian and Holocene shorelines of the British Isles and North Sea from models of glacio-hydro-isostatic rebound. Journal of the Geological Society of London 152: 437-448.
Langridge RM, Berryman KR, Van Dissen RJ 2005. Defining the geometric segmentation and Holocene slip rate of the Wellington Fault, New Zealand: The Pahiatua section. New Zealand Journal of Geology and Geophysics 48: 591-607.
Laustela M, Egli M, Frauenfelder R, Kääb A, Maisch M, Haeberli W 2003. Weathering rind measurements and relative age dating of rock-glacier surfaces in crystalline regions of the Eastern Swiss Alps. In: Phillips M, Springman S, Arenson L eds. Permafrost: Proceedings of the Eighth International Conference on Permafrost, July 2003, Zurich, Switzerland: 627-632.

Leitner B, Eberhart-Phillips D, Anderson H, Nabelek JH 2001. A focused look at the Alpine Fault, New Zealand: Seismicity, focal mechanisms, and stress observations. Journal of Geophysical Research 106: 2193-2220.

Litchfield NJ, Norris RJ 2000. Holocene motion on the Akatore Fault, south Otago coast, New Zealand. New Zealand Journal of Geology and Geophysics 43: 405-418.

Litchfield NJ, Lian OB 2004. Luminescence age estimate of Plesitocene marine terrace and alluvial fan sediments associated with tectonic activity along coastal Otago, New Zealand. New Zealand Journal of Geology and Geophysics 47: 29-37.

Little TA, Van Dissen R, Rieser U, Smith EGC, Langridge RM 2010. Coseismic strike slip at a point during the last four earthquakes on the Wellington fault near Wellington, New Zealand. Journal of Geophysical Research: Solid Earth 115(B5): B05403.

Long DT, Cox SC, Bannister S, Gerstenberger MC, Okaya D 2003. Upper crustal structure beneath the eastern Southern Alps and the Mackenzie Basin, New Zealand, derived from seismic reflection data. New Zealand Journal of Geology and Geophysics 46: 21-39.

Mabin MCG 1980. The glacial sequences in the Rangitata and Ashburton valleys, South Island, New Zealand. Unpublished PhD Thesis, University of Canterbury, Christchurch, New Zealand.

Machette MN, Personius SF, Nelson AR, Schwartz DP, Lund WR 1991. The Wasatch fault zone, utah—segmentation and history of Holocene earthquakes. Journal of Structural Geology 13: 137-149.

MacKinnon TC 1983. Origin of the Torlesse terrane and coeval rocks, South Island, New Zealand. Geological Society of America Bulletin 93: 625-634.

Maizels J 1989. Differentiation of late Pleistocene terrace outwash deposits using geomorphic criteria: Tekapo valley, South Island, New Zealand. New Zealand Journal of Geology and Geophysics 32: 225-241.

Mason DPM, Little TA, Van Dissen RJ 2006. Rates of active faulting during late Quaternary fluvial terrace formation at the Saxton River, Awatere Fault, New Zealand. GSA Bulletin 118: 1431-1446. DOI: 10.1130/B25961.1.

Matthews JA, Owen G 2010. Schmidt hammer exposure-age dating: developing linear age-calibration curves using Holocene bedrock surfaces from the Jotunheimen-Jostedalsbreen regions of southern Norway. Boreas 39: 105-115. DOI 10.1111/j.1502-3885.2009.00107.x.

Matthews JA, Shakesby RA 1984. The status of the 'Little Ice Age' in southern Norway: Relative-age dating of neoglacial moraines with Schmidt hammer and lichenometry. Boreas 13: 333–346.

Matthews JA, Winkler S 2011. Schmidt-hammer exposure-age dating (SHD): application to early Holocene moraines and a reappraisal of the reliability of terrestrial cosmogenic-nuclide dating (TCND) at Austanbotnbreen, Jotunheimen, Norway. Boreas 40: 256 - 270.

McCalpin JP 1987. Recommended setback distances from active normal faults. Proceedings of the Symposium on Engineering Geology and Soils Engineering 23: 35-56.

McCalpin JP, Irvine JR 1995. Sackungen at the Aspen Highlands ski area, Pitkin County, Colorado. Environmental and Engineering Geoscience 1: 277-290.

McCalpin JP 1996. Tectonic geomorphology and Holocene paleoseismicity of the Molesworth section of the Awatere fault, South Island, New Zealand. New Zealand Journal of Geology and Geophysics 39: 33–50.

McCalpin JP 1999. Episodic earthquake-induced movement on the Stillwater scarp sackung, central Nevada Geological Society of America Abstracts with Programs 31.

McCalpin JP, Hart EW 2002. Ridge-top spreading features and relationship to earthquakes, San Gabriel Mountains region, Southern California- Parts A & B. National Earthuake Hazards Reduction Program, USGS, Final Technical Report 51.

McCalpin JP 2009. Paleoseismology. 2nd ed. Burlington, MA, Academic Press.

McCalpin JP, Bruhn RL, Pavlis TL, Gutierrez F, Guerrero J, Lucha P 2011. Antislope scarps, gravitational spreading, and tectonic faulting in the Western Yakutat microplate, south coastal Alaska. Geosphere 7: 1143-1158.
McCarroll D, Nesje A 1993. The vertical extent of ice sheets in Sunnmøre, Western Norway: Measuring degree of rock surface weathering. Boreas 22: 255-265.
McCarroll D 1987. The Schmidt hammer in geomorphology: Five sources of instrument error. British Geomorphology Research Group Technical Bulletin 36: 16-27.
McCarroll D 1989. Potential limitations of the Schmidt hammer for relative-age dating: Field tests on Neoglacial moraines, Jotunheimen, southern Norway. Arctic and Alpine Research 21: 268-275.
McCarroll D 1991a. The Schmidt hammer, weathering and rock surface roughness. Earth Surface Processes and Landforms 16: 477-480.
McCarroll D 1991b.The age and origin of Neoglacial moraines in Jotunheimen, southern Norway: New evidence from weathering-based data. Boreas 20: 283-295.
McCarroll D 1991c. Relative-age dating of inorganic deposits: The need for a more critical approach. The Holocene 1: 174-180.
McCarroll D 1994. The Schmidt hammer as a measure of degree of rock surface weathering and terrain age. In: Beck C ed. Dating in Exposed and Surface Contexts. Albuquerque, University of New Mexico Press: 29-46.
McCarroll D, 1987. The Schmidt Hammer in geomorphology: five sources of instrumental error: British Geomorpholgical Research Group Technical Bulletin 36: 16-27.
McGill SF, Sieh K 1991. Surficial offsets on the Central and Eastern Garlock Fault associated with prehistoric earthquakes. Journal of Geophysical Research: Solid Earth 96: 21597-21621.
McGlone MS, 1989. The Polynesian settlement of New Zealand in relation to environmental and biotic changes. New Zealand Journal of Ecology 12: 115-129.
McGlone MS, Wilmshurst JM 1999. Dating initial Maori environmental impact in New Zealand. Quaternary International 59: 5-16.
McMartin I 2000. Paleogeography of Lake Agassiz and regional post-glacial uplift history of the Flin Flon region, central Manitoba and Saskatchewan. Journal of Paleolimnology 24: 293-315.
McSaveney M 1992. A manual for weathering-rind dating of grey sandstones of the Torlesse supergroup, New Zealand. Lower Hutt: Institute of Geological and Nuclear Sciences. GNS Science Report 92/04. 52 p.
McVerry GH, Zhao JX, Abrahamson NA, Somerville PG 2006. New Zealand acceleration response spectrum attenuation relations for crustal and subduction zone earthquakes. Bulletin of the New Zealand Society for Earthquake Engineering 39: 1-58.
McWethy DB, Whitlock C, Wilmshurst JM, McGlone MS, Li X 2009. Rapid deforestation of South Island, New Zealand, by early Polynesian fires. The Holocene 19: 883-897.
Merritts DJ, Vincent KR, Wohl EE 1994. Long river profiles, tectonism, and eustasy: A guide to interpreting fluvial terraces. Journal of Geophysical Research: Solid Earth 99: 14031-14050.
Meunier P, Hovius N, Haines AJ 2007. Regional patterns of earthquake-triggered landslides and their relation to ground motion. Geophysical Research Letters 34: L20408. DOI:10.1029/2007GL031337.
Meunier P, Hovius N, Haines JA 2008. Topographic site effects and the location of earthquake induced landslides. Earth and Planetary Science Letters 275: 221-232.
Molloy BPJ, Burrows CJ, Cox JE, Johnston JA, Wardle P 1963. Distribution of subfossil forest remains, eastern South Island, New Zealand. New Zealand Journal of Botany 1: 68-77.
Molnar P, Brown ET, Burchfiel BC, Qidong D, Xianyue F, Jun L, Raisbeck GM, Jianbang S, Zhangming W, Yiuo F, Huichuan Y 1994. Quaternary climate change and the formation of river terraces across growing anticlines on the North Flank of the Tien Shan, China. The Journal of Geology 102: 583-602.

Mörner NA 1978. Faulting, fracturing, and seismicity as functions of glacio-isostasy in Fennoscandia. Geology 6: 41-45.
Moro M, Saroli M, Gori S, Falcucci E, Galadini F, Messina P 2012. The interaction between active normal faulting and large scale gravitational mass movements revealed by paleoseismological techniques: A case study from central Italy. Geomorphology 151/152: 164-174.
Moss RES, Ross ZE 2011. Probabilistic Fault Displacement Hazard Analysis for Reverse Faults: Bulletin of the Seismological Society of America 101: 1542-1553.
Mountjoy J, Pettinga J 2006. Controls on large deep-seated landslides in soft rock terrain: rock mass defects and seismic triggering. Proceedings of Technical Groups, New Zealand Geotechnical Society 2006 Symposium: Earthquakes and Urban Development. Nelson, New Zealand. 10 p.
Muirson, JS 2003. An engineering geological investigation into slope movement at the Coalgate bentonite quarry, inland Canterbury. Unpublished MSc Thesis, University of Canterbury, Christchurch, New Zealand.
Muir-Wood R 2000. Deglaciation seismotectonics: a principal influence on intraplate seismogenesis at high latitudes. Quaternary Science Reviews 19: 1399-1411.
Muller JR, Martel SJ 2000. Numerical Models of Translational Landslide Rupture Surface Growth. Pure and Applied Geophysics 157: 1009-1038.
Nesje A, Blikra LH, Anda E 1994a. Dating rockfall-avalanche deposits from degree of weathering by Schmidt-hammer tests: a study from Norangsdalen, Sunnmøre, Norway. Norsk Geologisk Tidsskrift 74: 108-113.
Nesje A, McCarroll D, Dahl SO 1994b. Degree of rock surface weathering as an indicator of ice-sheet thickness along an east-west transect across southern Norway. Journal of Quaternary Sciences 9: 337-347.
Nicholas JW, Butler DR 1996. Application of relative-age dating techniques on rock glaciers of the La Sal Mountains, Utah: An interpretation of Holocene paleoclimates. Geografiska Annaler 78: 1-18.
Nicol A 1993. Conical folds produced by dome and basin fold interference and their application to determining strain: examples from North Canterbury, New Zealand. Journal of Structural Geology 15: 785-792.
Nicol A, Campbell JK 2001. The impact of episodic fault-related folding on late Holocene degradation terraces along Waipara River, New Zealand. New Zealand Journal of Geology and Geophysics 44: 145-156. DOI: 0028-8306/01/4401-0145.
Nicol A, Wallace LM 2007. Temporal stability of fault slip rates: Comparison of geologic and geodetic observations, Hikurangi subduction margin, New Zealand. Earth and Planetary Science Letters 238: 397-413.
Nicol A, Van Dissen R, Robinson R, Harvison A 2012. Variability in single event slip and recurrence intervals for large magnitude paleoearthquakes on New Zealand's active faults. GNS Science Report 2012/41. 57 p.
Niedzielski T, Migoń P, Placek A 2009. A minimum sample size required from Schmidt hammer measurements. Earth Surface Processes and Landforms 34: 1713-1725. DOI: 10.1002/esp.1851.
Nikonov AA 1988. Reconstruction of the main parameters of old large earthquakes in Soviet Central Asia using the paleoseismogeological method. Tectonophysics 147: 297-312.
Nolan JM, Weber GE 1992. Evaluation of surface cracking caused by the 1989 Loma Prieta earthquake, Santa Cruz County, California: case histories. In: Sharma S ed. Proceedings of the 28th Symposium on Engineering Geology and Geotechnical Engineering. University of Idaho, Moscow, ID: 272-286.

Nolan JM, Weber GE 1998. Evaluation of coseismic ground cracking accompanying the earthquake: Trenching studies and case histories in The Loma Prieta, California, earthquake of October 17, 1989 landslides. U.S. Geological Survey Professional paper 1551-C, 145-163.
Norris RJ, Cooper AF 2001. Late Quaternary slip rates and slip partitioning on the Alpine Fault, New Zealand. Journal of Structural Geology 23: 507-520.
Norris RJ, Nicolls R 2004. Strain accumulation and episodicity of fault movements in Otago: Earthquake Commission Research Report 01/445, University of Otago. 146 p.
Norris RJ, Koons PO, Cooper AF 1990. The obliquely-convergent plate boundary in the South Island of New Zealand: Implications for ancient collision zones. Journal of Structural Geology 12: 715-725.
Norton DA 1985. A multivariate technique for estimating New Zealand temperature normals. Weather and Climate 5: 64-74.
Officers of the Geological Survey 1983. Seismotectonic hazard evaluation of the Clyde Dam site. New Zealand Geological Survey /EG Report 375.
Oglesby, DD, Day SM, O'Connell DRH 2003. Dynamic and static interaction of two thrust faults: A case study with general implications. Journal of Geophysical Research: Solid Earth 108: 2489. DOI*:10.1029/2002JB002228.*
Oguchi CT, Matsukura Y 1999. Effect of porosity on the increase in weathering-rind thickness of andesite gravel. Engineering Geology 55: 77-89.
Oldow JS, Singleton ES 2008. Application of terrestrial laser scanning in determining the pattern of late Plesitocene and Holocene fault displacement from the offset of pluvial lake shorelines in the Alvord extensional basin, northern Great Basin, USA. Geosphere 4: 536-563.
Onida M, Galadini F, Forcella F 2001. Application of paleoseismological techniques to the study of Late Pleistocene-Holocene deep-seated gravitational movements at the Mortirolo Pass (central Alps, Italy). Netherlands Journal of Geosciences 80: 209-227.
Oskin ME, Arrowsmith JR, Corona AH, Elliott AJ, Fletcher JM, Fielding EJ, Gold PO, Garcia JJG, Hudnut KW, Liu-Zeng J, Teran OJ 2012. Near-Field Deformation from the El Mayor–Cucapah Earthquake Revealed by Differential LIDAR: Science 335: 702-705.
Oskin M, Perg L, Shelef E, Strane M, Gurney E, Singer B, Zhang X 2008. Elevated shear zone loading rate during an earthquake cluster in eastern California. Geology 36: 507-510.
Ozbek A, Gul M 2011. Variation of Schmidt hammer rebound values depending on bed thickness and discontinuity surfaces. Scientific Research and Essays 6: 2201-2211.
Pace B, Stirling MW, Litchfield NJ, Rieser U 2005. New active fault data and seismic hazard estimates for west Otago, New Zealand. New Zealand Journal of Geology and Geophysics 48: 75-83.
Papanikolaou ID, Roberts GP, Michetti AM 2005. Fault scarps and deformation rates in Lazio-Abruzzo, Central Italy: Comparison between geological fault slip-rate and GPS data. Tectonophysics 408: 147-176.
Parsons TE, Field H, Page MT, Milner K 2012. Possible Earthquake Rupture Connections on Mapped California Faults Ranked by Calculated Coulomb Linking Stresses. Bulletin of the Seismological Society of America 102: 2667-2676.
Pettinga JR 1987. Ponui Landslide: A deep-seated wedge failure in Tertiary weak-rock flysch, Southern Hawke's Bay, New Zealand. New Zealand Journal of Geology and Geophysics 30: 415-430.
Pettinga JR, Wise DU 1994. Paleostress adjacent to the Alpine Fault: Broader implications from fault analysis near Nelson, South Island, New Zealand. Journal of Geophysical Research 99: 2727-2736.
Pierce KL, Cannon KP, Meyer GA, Trebesch MJ, Watts RD 2007. Postglacial inflation-deflation cycles, tilting, and faulting in the Yellowstone caldera based on Yellowstone Lake Shorelines. In: Morgan LA ed. Integrated Geoscience Studies in the Greater Yellowstone Area— Volcanic,

Tectonic, and Hydrothermal Processes in the Yellowstone Geoecosystem. US Geological Survey Professional Paper 1717: 131-164.
Pollitz F, Vergnolle M, Calais E 2003. Fault interaction and stress triggering of twentieth century earthquakes in Mongolia. Journal of Geophysical Research: Solid Earth 108: 2503.
Pradel D, Smith PM, Stewart JP, Raad G 2005. Case history of landslide movement during the Northridge earthquake. Journal of Geotechnical and Geoenvironmental Engineering 131: 1360-1369.
Preusser F, Ramseyer K, Schlüchter C 2006. Characterisation of low OSL intensity quartz from the New Zealand Alps. Radiation Measurements 41: 871-877.
Proceq SA. 2004. Concrete test hammer- operating instructions. Schwerzenbach (Proceq SA). 14 p.
Qi W, Qiao X, Lan Q, Freymueller J, Shaomin Y, Caijun X, Yang Y, You X, Tan K, Chen G 2011. Rupture of deep faults in the 2008 Wenchuan earthquake and uplift of the Longmen Shan. Nature Geoscience 4: 634-640.
Quigley M, Noble D, Van Dissen R, Litchfield N, Villamor P, Duffy B, Barrell D, Furlong K, Stahl T, Bilderback E 2012. Surface rupture during the 2010 M_w 7.1 Darfield (Canterbury) earthquake: implications for fault rupture dynamics and seismic-hazard analysis. Geology 40: 55-58.
Quigley MC, Sandiford M, Cupper ML 2007. Distinguishing tectonic from climatic controls on range-front sedimentation. Basin Research 19: 491-505.
Quigley M, Villamor P, Furlong K, Beavan J, Van Dissen R, Litchfield N, Stahl T, Duffy B, Bilderback E, Noble D, Barrell D, Jongens R, Cox S 2010. Previously Unknown Fault Shakes New Zealand's South Island. Eos, Transactions American Geophysical Union 91: 469-470.
Raeside JD 1964. Loess Deposits of the South Island, New Zealand, and Soils Formed on them. New Zealand Journal of Geology and Geophysics 7: 811-838.
Read SAL, Richards LR, Perrin ND 1999. Applicability of the Hoek-Brown failure criterion to New Zealand greywacke rocks. Proceedings 9th International Congress on Rock Mechanics, Paris, 1999 2: 655-660.
Reyners MD, Eberhart-Phillips D, Bannister D 2011. Tracking repeated subduction of the Hikurangi Plateau beneath New Zealand. Earth and Planetary Science Letters 311: 165-171.
Rhoades DA, Van Dissen RJ 2003. Estimates of the time-varying hazard of rupture of the Alpine Fault, New Zealand, allowing for uncertainties. New Zealand Journal of Geology and Geophysics 46: 479-488.
Riebe CS, Kirchner JW, Finkel RC 2004. Erosional and climatic effects on long-term chemical weathering rates in granitic landscapes spaning diverse climate regimes. Earth and Planetary Science Letters 224: 547-562.
Robinson R 2004. Potential earthquake triggering in a complex fault network: the northern South Island, New Zealand. Geophysical Journal International 159:734-748.
Rockwell T 1988. Neotectonics of the San Cayetano fault, Transverse Ranges, California. Geological Society of America Bulletin 100: 500-513.
Rockwell T, Ragona D, Seitz G, Langridge R, Aksoy ME, Ucarkus G, Ferry M, Meltzner AJ, Klinger Y, Meghraoui M, Satir D, Barka A, Akbalik B 2009. Palaeoseismology of the North Anatolian Fault near the Marmara Sea: implications for fault segmentation and seismic hazard. Geological Society, London, Special Publications 316: 31-54.
Rode M, Kellerer-Pirklbauer A 2011. Schmidt-hammer exposure-age dating (SHD) of rock glaciers in the Schöderkogel-Eisenhut area, Schladminger Tauern Range, Austria. The Holocene 22: 761-771.
Roser BP, Korsch RJ 1999. Geochemical characterization, evolution and source of a Mesozoic accretionary wedge: the Torlesse terrane, New Zealand. Geology Magazine 136: 493-512.
Rubin CM 1996. Systematic underestimation of earthquake magnitudes from large intracontinental reverse faults: Historical ruptures break across segment boundaries. Geology 24:989-992.

Sánchez J, Mosquera DF, Romaní JRV 2009. Assessing the age-weathering correspondence of cosmogenic ^{21}Ne dated Pleistocene surfaces by the Schmidt hammer. Earth Surface Processes and Landforms 34: 1121-1125. DOI: 10.1002/esp.1802

Sánchez G, Rolland Y, Corsini M, Braucher R, Bourlès D, Arnold M, Aumaître G 2010. Relationships between tectonics, slope instability and climate change: Cosmic ray exposure dating of active faults, landslides and glacial surfaces in the SW Alps. Geomorphology 117: 1-13.

Sauber JM, Molnia BF 2004. Glacier ice mass fluctuations and fault instability in tectonically active Southern Alaska. Global and Planetary Change 42: 279-293.

Schaefer JM, Denton GH, Kaplan M, Putnam A, Finkel RC, Barrell DJA, Andersen BG, Schwartz R, Mackintosh A, Chinn T, Schlüchter, C 2009. High frequency Holocene glacier fluctuations in New Zealand differ from the northern signature. Science 324: 622-625. DOI: 10.1126/science.1169312

Schaetzl, RJ, Drzyzga SA, Weisenborn BN, Kincare KA, Lepczyk XC, Shein K, Dowd C, Linker J 2002. Measurement, correlation, and mapping of glacial Lake Algonquin shorelines in Northern Michigan. Annals of the Association of American Geographers 92: 399-415.

Scherwath, M, Stern T, Davey F, Davies R 2006. Three-dimensional lithospheric deformation and gravity anomalies associated with the oblique continetnal collision in South Island, New Zealand. Geophysical Journal International 167: 906-916.

Schmidt E 1951. A non-destructive concrete tester. Concrete 59: 34–35.

Scholz CH 2010. Large Earthquake Triggering, Clustering, and the Synchronization of Faults. Bulletin of the Seismological Society of America 100: 901-909.

Schwartz DP, Haeussler PJ, Seitz GG, Dawson TE 2012. Why the 2002 Denali fault rupture propagated onto the Totschunda fault: Implications for fault branching and seismic hazards. Journal of Geophysical Research B: Solid Earth 117.

Shakesby RA, Matthews JA, Owen G 2006. The Schmidt hammer as a relative-age dating tool and its potential for calibrated-age dating in Holocene glaciated environments. Quaternary Science Reviews 25: 2846-2867.

Shakesby RA, Matthews, JA, Karlén W, Los SO 2011. The Schmidt hammer as a Holocene calibrated-age dating technique: Testing the form of the R-value-age relationship and defining the predicted-age errors. The Holocene 21: 615-628. DOI: 10.1177/0959683610391322.

Sharma PK, Khandelwal M, Singh TN 2011. A correlation between Schmidt hammer rebound numbers with impact strength, slake durability index and P-wave velocity. International Journal of Earth Science 100: 189-195. DOI 10.1007/s00531-009-0506-5.

Shaw BE, Dieterich JH 2007. Probabilities for jumping fault segment stepovers. Geophysical Research Letters 34.

Shen ZK, Sun J, Zhang P, Wan Y, Wang M, Burgmann R, Zeng Y, Gan W, Liao H, Wang Q 2009. Slip maxima at fault junctions and rupturing of barriers during the 2008 Wenchuan earthquake. Nature Geoscience 2: 718-724.

Sidak Z 1967. Rectangular confidence regions for the means of multivariate normal distributions. Journal of the American Statistical Association 62: 626-633.

Sleep NH 2011. Deep-seated downslope slip during strong seismic shaking. Geochemistry, Geophysics, Geosystems 12: Q12001. DOI:10.1029/2011GC003838.

Stahl T, Winkler S, Quigley, M, Bebbington M, Duffy B, Duke D 2013. Schmidt hammer exposure-age dating (SHD) of late Quaternary fluvial terraces in New Zealand. Earth Surface Processes and Landforms. DOI:10.1002/esp.3427.

Stahl T, Bilderback EL, Quigley MC, Nobes DC, Massey CI 2014. Coseismic landsliding during the Mw 7.1 Darfield (Cantebury) earthquake: implications for paleoseismic studies of landslides. Geomorphology 214: 114-127.

Steacy SJ, McCloskey JJ 1998. What controls an earthquake's size? Results from a heterogeneous cellular automaton. Geophysical Journal International 133: F11-F14.

Stein RS, King GCP, Rundle JB 1988. The growth of structures by repeated earthquakes 2. Field examples of continental dip-slip faults. Journal of Geophysical Research 93: 13319-13331.
Stein RS, Thatcher W 1981. Seismic and aseismic deformation associated with the 1952 Kern County, California, earthquake and relationship to the Quaternary history of the White Wolf Fault. Journal of Geophysical Research 86: 4913-4928.
Stewart IS, Sauber J, Rose J 2000. Glacio-seismotectonics: ice sheets, crustal deformation and seismicity. Quaternary Science Reviews 19: 1367-1389.
Stirling M, Gerstenberger M, Litchfield N, McVerry G, Smith W, Pettinga JR, Barnes P 2008. Seismic hazard of the Canterbury Region, New Zealand: New earthquake source model and methodology. Bulletin of the New Zealand Society of Earthquake Engineering 41: 51-67.
Stirling M, McVerry G, Gerstenberger M, Litchfield N, Van Dissen R, Berryman KR, Barnes P, Wallace L, Villamor P, Langridge R, Lamarche G, Nodder S, Reyners M, Bradley B, Rhoades D, Smith W, Nicol N, Pettinga JR, Clark K, Jacobs K 2012. National seismic hazard model for New Zealand: 2010 update. Bulletin of the Seismological Society of America 102: 1514-1542.
Stirling M, Pettinga JR, Berryman KR, Yetton M 2001. Probabilistic seismic hazard assessment of the Canterbury region, New Zealand. Bulletin of the New Zealand Society of Earthquake Engineering 34: 318-333.
Suggate RP 1958. Geology of the Clarence Valley from Gore Stream to Bluff Hill. Transactions of the Royal Society of New Zealand 85: 397-408.
Sumner P, Nel W 2002. The effect of rock moisture on Schmidt hammer rebound: Tests on rock samples from Marion Island and South Africa. Earth Surface Processes and Landforms 27: 1137-1142. DOI: 10.1002/esp.402.
Sutherland R, Berryman KR, Norris RJ 2006. Quaternary slip rate and geomorphology of the Alpine fault: Implications for kinematics and seismic hazard in southwest New Zealand. Geological Society of America Bulletin 118: 464-474.
Taylor A, Blum JD 1995. Relation between soil age and silicate weathering rates determined from the chemical evolution of a glacial chronosequence. Geology 23: 979-982.
Technical Advisory Group on the Santa Cruz Geologic Hazard Investigation 1991. Geologic hazards in the Summit Ridge area of the Santa Cruz Mountains, Santa Cruz County, California, evaluated in response to the 17 October 1989 Loma Prieta earthquake. Report of Technical Advisory Group: U.S. Geological Survey Open-File Report 91-618. 427 p.
Thompson SC, Weldon RJ, Rubin CM, Abdrakhmatov K, Molnar P, Berge GW 2002. Late Quaternary slip rates across the central Tien Shan, Kyrgyzstan, central Asia. Journal of Geophysical Research 107: *2203, DOI:10.1029/2001JB000596.*
Thomson R 1985. A discussion of some evidence for a pre-historic natural damming of Lake Wakatipu. New Zealand Geological Survey Enginnering Geology Immediate Report EGI 84/047.
Thomson R 1996. Prehistoric changes in the level of Lake Wakatipu: An unpublished outline study prepared for the Otago Regional Council. 4 p.
Thorson RM 1996. Earthquake recurrence and glacial loading in Western Washington. Geological Society of America Bulletin 108: 1181-1191.
Tonkin PJ, Basher LR 1990. Soil-stratigraphic techniques in the study of soil and landform evolution across the Southern Alps, New Zealand. Geomorphology 3: 547-575.
Tsuboi S, Kikuchi M, Yamanaka Y, Kanao M, 2000. The March 25, 1998 Antarctic Earthquake: Great earthquake caused by postglacial rebound. Earth Planets Space 52: 133-136.
Turnbull IM 1980. Structure and interpretation of the Caples terrane of the Thomson Mountains, northern Southland, New Zealand. New Zealand Journal of Geology and Geophysics 23: 43-62.
Turnbull 2000. Geology of the Wakatipu area: Institute of Geological and Nuclear Sciences limited, 1 sheet + 72 p.

Turnbull IM, Barry JM, Carter RM, Norris RJ 1975. The Bobs Cove Beds and their relationship to the Moonlight Fault Zone. Journal of the Royal Society of New Zealand 5: 355-394.
Upton P, Koons PO 2007. Three-Dimensional Geodynamic Framework for the Central Southern Alps, New Zealand. In: Okaya DA, Stern TA, Davey FJ eds. Integrating Geology, Geophysics and Mechanical Observations, A Continental Plate Boundary: Tectonics at South Island, New Zealand, American Geophysical Union: 253-270.
Upton P, Osterberg EC 2007. Paleoseismicity and mass movements interpreted from seismic-reflection data, Lake Tekapo, South Canterbury, New Zealand. New Zealand Journal of Geology and Geophysics 50: 343-356.
Upton P, Craw D, James ZE, Koons PO 2004. Structure and late Cenozoic tectonics of the southern Two Thumb range, mid Canterbury, New Zealand. New Zealand Journal of Geology and Geophysics 47: 141-153.
Upton P, Craw D, James ZE, Koons PO 2004. Structure and late Cenozoic tectonics of the southern Two Thumb range, mid Canterbury, New Zealand. New Zealand Journal of Geology and Geophysics 47:141-153.
Upton P, Koons PO, Craw D, Henderson CM, Enlow R 2009. Along-strike differences in the Southern Alps of New Zealand: Consequences of inherited variation in rheology. Tectonics 28: TC2007. DOI*:10.1029/2008TC002353.*
Ustaszewski ME, Hampel A, Pfiffner OA 2008. Composite faults in the Swiss Alps formed by the interplay of tectonics, gravitation and postglacial rebound: an integrated field and modelling study. Swiss Journal of Geosciences 101: 223-235.
Van Dissen R, Barrell D, Litchfield N, Villamor P, Quigley M, King A, Furlong K, Begg J, Townsend D, Mackenzie H, Stahl T, Noble D, Duffy B, Bilderback E, Claridge J, Klahn A, Jongens R, Cox S, Langridge R, Ries W, Dhakal R, Smith A, Horblow S, Nicol R, Pedley K, Henham H, Hunter R, Zajac A, Mote T 2011. Surface rupture displacement on the Greendale Fault during the Mw 7.1 Darfield (Canterbury) earthquake, New Zealand, and its impact on man-made structures. Ninth Pacific Conference on Earthquake Engineering: Building an Earthquake-Resilient Society, 14-16 Apr 2011. Auckland, New Zealand. 8 p.
Van Dissen RJ, Hull AG, Read SAL 1994.Timing of some large Holocene earthquakes on the Ostler Fault, New Zealand. In:Proceedings of the Eighth International Symposium on Recent Crustal Movements (CRCM '93), Kobe, December 6-11, 1993. Japan: Geodetic Society of Japan: 381-386.
Vance D, Teagle DAH, Foster GL 2009. Varying Quaternary chemical weathering fluxes and imbalances in marine geochemical budgets. Nature Letters 458: 493-496.
Velbel MA 1990. Influence of temperature and mineral surface characteristics on feldspar weathering rates in natural and artificial systems: A first approximation. Water Resources Research 26: 3049-3053.
Viles H, Goudie A, Grab S, Lalley J 2011. The use of the Schmidt Hammer and Equotip for rock hardness assessment in geomorphology: A comparative analysis. Earth Surface Processes and Landforms 36: 320-333.
Villamor P, Litchfield N, Barrell D, Van Dissen R, Hornblow S, Quigley M, Levick S, Ries W, Duffy B, Begg J and others 2012. Map of the 2010 Greendale Fault surface rupture, Canterbury, New Zealand: application to land use planning. New Zealand Journal of Geology and Geophysics 55: 223-230.
Villamor P, Van Dissen RJ, Alloway BV, Palmer AS, Litchfield NJ 2007. The Rangipo fault, Taupo rift, New Zealand: An example of temporal slip-rate and single-event displacement variability in a volcanic environment. Geological Society of America Bulletin 119: 529-547.
Walcott RI 1998. Modes of oblique compression: Late Cenozoic tectonics of the south island of New Zealand. Reviews of Geophysics 36: 1-26.
Walker M 2005. Quaternary dating methods. Wiley, Chichester: 286 p.

Wallace LM, Beavan J, McCaffrey R, Berryman KR, Denys P 2007. Balancing the plate motion budget in the South Island, New Zealand using GPS, geological and seismological data. Geophysical Journal International 168: 332-352.

Wannamaker PE, Jiracek GR, Stodt JA, Caldwell TG, Gonzalez VM, McKnight JD, Porter AD 2002. Fluid generation and pathways beneath an active compressional orogen, the New Zealand Southern Alps, inferred from magnetotelluric data. Journal of Geophysical Research - Solid Earth 107, 2117: DOI*:10.1029/2001JB000186.*

Warton DI, Wright IJ, Falster DS, Westoby M 2006. Bivariate line-fitting methods for allometry. Biological Reviews 81: 259-291.DOI: 10.1017/S1464793106007007.

Watters WA, Soong CWR, Riddolls BW 1981. Weathering of greywacke sandstone, Wellington, New Zealand. In: Akai K, Hayashi M, Nishimatsu Y eds. Proceedings of the International Symposium on Weak Rock, 1981, Tokyo, Japan 1: 179-184.

Wellman HW 1979. An uplift map for the South Island of New Zealand, and a model for uplift of the Southern Alps. In: Walcott RI, Cresswell MM eds. The Origin of the Southern Alps. Bulletin of the Royal Society of New Zealand 18: 13-20.

Wells DL, Coppersmith KJ 1994. New empirical relationships among magnitude, rupture length, rupture width, rupture area, and surface displacement. Bulletin of the Seismological Society of America 84: 974-1002,A1-A4,B1-B11,C1-C49.

Wesnousky SG 2006. Predicting the endpoints of earthquake ruptures. Nature 444:358-360.

Wesnousky SG 2008. Displacement and Geometrical Characteristics of Earthquake Surface Ruptures: Issues and Implications for Seismic-Hazard Analysis and the Process of Earthquake Rupture. Bulletin of the Seismological Society of America 98:1609-1632.

White AF, Blum AE 1995. Effects of climate on chemical weathering in watersheds. Geochimica et Cosmochimica Acta 59: 1729-1747.

White AF, Brantley SL 2003. The effect of time on the weathering of silicate minerals: why do weathering rates differ in the laboratory and the field? Chemical Geology 202: 479-506.

White K, Bryant R, Drake N 1998. Techniques for measuring rock weathering: Application to a dated fan segment sequence in southern Tunisia. Earth Surface Processes and Landforms 23: 1031-1043.

Whitehouse IE, McSaveney MJ, Knuepfer PLK, Chinn TJ 1986. Growth of weathering rinds on Torlesse sandstone, Southern Alps, New Zealand. In: Colman SM, Dethier DP eds. Rates of Chemical Weathering of Rocks and Minerals. Orlando, Academic Press: 419-435.

Williams RBG, Robinson DA 1983. The effect of surface texture on the determination of the surface hardness of rock using Schmidt Hammer. Earth Surface Processes and Landforms 8: 289-292.

Winkler S 2005. The Schmidt hammer as a relative-age dating technique: Potential limitations of its application on Holocene moraines in Mt. Cook National Park, Southern Alps, New Zealand. New Zealand Journal of Geology and Geophysics 48: 105-116. DOI: 0028–8306/05/4801–0105.

Winkler S 2009. First attempt to combine terrestrial cosmogenic nuclide (^{10}Be) and Schmidt hammer relative-age dating: Strauchon Glacier, Southern Alps, New Zealand. Central European Journal of Geosciences 1: 274-290.

Xu X, Wen X, Yu G, Chen G, Klinger Y, Hubbard J, Shaw J 2009. Coseismic reverse- and oblique-slip surface faulting generated by the 2008 Mw 7.9 Wenchuan earthquake, China. Geology 37: 515-518.

Yeats RS 2000. The 1968 Inangahua, New Zealand, and 1994 Northridge, California, earthquakes: Implications for northwest Nelson. New Zealand Journal of Geology and Geophysics 43: 587-599.

Yu G, Guo T, Sun X, Tan X, An Y, Xu X, Klinger Y, Diao G, Chen G, Feng X, Li C, Zhu A, Yuan R 2010. Fault-Scarp Features and Cascading-Rupture Model for the Mw 7.9 Wenchuan Earthquake, Eastern Tibetan Plateau, China. Bulletin of the Seismological Society of America 100: 2590-2614.

Yu SB, Kuo LC, Hsu YJ, Su HH, Liu CC, Hou CS, Lee JF, Lai TC, Liu CC, Liu CL, Tseng TF, Tsai CS Shin TC 2001. Preseismic and coseismic displacements associated with the 1999 Chi-Chi, Taiwan, Earthquake. Bulletin of the Seismological Society of America 91: 995-1012.

Zhang PZ, Wen XZ, Shen ZK, Chen JH 2010. Oblique, high-angle, listric-reverse faulting and associated development of strain: The Wenchuan earthquake of May 12, 2008, Sichuan, China. Annual Review of Earth and Planetary Sciences 38:353-382.

Zhu SB, Zhang PZ 2010. Numeric modeling of the strain accumulation and release of the 2008 Wenchuan, Sichuan, China, Earthquake. Bulletin Of The Seismological Society Of America 100: 2825-2839.